

Cavity quantum electrodynamics with systems of site-controlled quantum dots and photonic crystal cavities

THÈSE N° 7039 (2016)

PRÉSENTÉE LE 15 JUILLET 2016

À LA FACULTÉ DES SCIENCES DE BASE
LABORATOIRE DE PHYSIQUE DES NANOSTRUCTURES
PROGRAMME DOCTORAL EN PHYSIQUE

ÉCOLE POLYTECHNIQUE FÉDÉRALE DE LAUSANNE

POUR L'OBTENTION DU GRADE DE DOCTEUR ÈS SCIENCES

PAR

Clément William Tendaï JARLOV

acceptée sur proposition du jury:

Prof. M. Q. Tran, président du jury
Prof. E. Kapon, directeur de thèse
Prof. A. Auffèves, rapporteuse
Prof. V. Zwiller, rapporteur
Prof. R. Houdré, rapporteur



ÉCOLE POLYTECHNIQUE
FÉDÉRALE DE LAUSANNE

Suisse
2016

En bas, les rouleaux s'éventraient sur les saillies. Le rocher déchirait la pulpe salée.
Des paquets d'embruns aspirés par l'ouragan explosaient contre le phare.
Le rai de lumière déchirait l'obscurité, indifférent.
—Sylvain Tesson
Le Phare, Une vie à coucher dehors

A mes parents et papi Bob...

Remerciements/Acknowledgements

L'accomplissement de ces quatre années de travail et de recherche, résumées dans cette thèse, aura nécessité bien plus qu'un effort personnel, et n'aurait pas été possible sans l'aide d'un grand nombre de personnes que je souhaite remercier ici.

Tout d'abord, je remercie le professeur Elyahou Kapon qui m'a donné la chance de pouvoir travailler au Laboratoire de Physique des Nanostructures (LPN) sur ce sujet de recherche passionnant. Il a supervisé mon travail avec patience et enthousiasme, et m'a transmis sa passion pour la physique. Son expertise, son intuition et ses conseils ont été indispensables à l'aboutissement de cette thèse mais ont aussi constitué une aide précieuse pour la rédaction de publications scientifiques et la préparation d'exposés oraux.

Je voudrais aussi exprimer ma gratitude aux membres du jury, Prof. Auffèves, Prof. Houdré et Prof. Zwiller pour l'intérêt qu'ils ont porté à ce travail, leur relecture minutieuse et leurs remarques très constructives.

Cette aventure n'aurait bien sûr pas été possible sans tous les collaborateurs du LPN. Je tiens à remercier Pascal Gallo qui m'a accueilli lors de mon premier stage il y a sept ans déjà et qui m'a accompagné pendant les premières années de ma thèse. Il m'a guidé lorsque j'ai fait mes premiers pas dans un laboratoire d'optique, toujours avec bonne humeur et bienveillance. Sa passion débordante pour la science et la recherche a été une inspiration pour moi, pendant ces quatre années passées au LPN à ses côtés. Un grand merci aussi à Milan Čalić pour son aide indispensable en "manip", la convivialité des journées en conférence et les instants de détente musicales. Merci aussi à Lydie Ferrier, voisine de bureau, pour sa gentillesse et sa spontanéité, ainsi que pour les bons moments passés dans les labos d'optique et en conférence. Un grand merci à Benjamin Dwir et Alok Rudra, sans qui les échantillons de boîtes ne verraient pas le jour, pour leur enthousiasme et leur bonne humeur. Merci aussi aux collègues doctorants avec qui j'ai partagé cette aventure : Romain Carron, Alessandro Surrente, Justyna Szeszko, Nicolas Volet, Alexey Lyasota, Mikhaïl Lazarev, Bruno Rigal et Antoine Delgoffe.

Je voudrais aussi saluer les collaborateurs et visiteurs du LPN (passé et présent) qui ont enrichi cette expérience : Irina Kulkova, Etienne Wodey, Stefan Keller, Yichen Ma,

Remerciements/Acknowledgements

Zlatko Mickovic, Ellafi Dalila, Fredrik Karlsson, Jakob Rosenkrantz de Lasson, Christopher Long, Marc-André Dupertuis, Moshe Judelewicz, Alexandru Mereuta, Andrei Caliman, Vladimir Iakoviev. Une pensée particulière à Gabriella Fuchs et Nadia Gauljoux que je remercie pour leur soutien et leur dynamisme.

Enfin, je salue tous mes amis EPFLiens qui m'ont soutenu pendant les périodes difficiles de la thèse et avec qui j'ai pu fêter, dignement, les moments plus heureux. C'est aussi grâce à eux que j'ai pu réussir les cinq années à l'EPFL qui ont précédé la thèse. Pour tout cela, merci à Kevin, Sascha, Jérôme, Ancelin, Samuel, Sébastien, Camille, Johnny, Hadrien, Angélique, Tak, Justin, Jonas, Xavier, Thomas, Adrien, Cédric. . . Merci aussi à Satellite et à son staff qui distille des particules de gaité dans le cœur des doctorants.

Pour finir, mille merci à ma famille et mes parents, Sylvie et Christian. Sans leur soutien et leur amour inconditionnels rien ne serait possible.

Abstract

The study of light-matter interactions holds an important place in physics and many fields of science including biology, medicine and chemistry. Understanding and exploiting light-matter interactions has become ever more relevant in our modern society which strives for sustainable energy sources and efficient transfer and storage of information. In this context, the realization of novel light harvesting or emitting devices, as well as novel information and computing platforms will demand a thorough understanding and control of nanoscale light-matter interactions. This involves studying the fundamental interactions between quantum emitters and modes of the electromagnetic field, which is undertaken by the field of cavity quantum electrodynamics (cavity-QED). Although initially interactions between isolated atoms and optical cavity modes were investigated, it has recently become possible to realize cavity-QED experiments with solid-state platforms, facilitating the transfer from fundamental studies to applications and device fabrication. In such solid-state platforms, atoms can be substituted by semiconductor quantum dots (QDs), which are nanostructures engineered to have atom-like optical and electronic properties, made to interact with semiconductor nanocavities. The subject of this thesis is the study of semiconductor QDs coupled to optical modes of photonic crystal (PhC) cavities.

One of the challenges faced when studying QD-cavity interactions is understanding the impact of the QD environment on its interaction with the cavity mode (CM). Unlike atoms, QDs are embedded in a crystal lattice with which it can interact, leading to quantum decoherence. In this work we rely on site-controlled pyramidal QDs integrated in PhC cavities to study the impact of decoherence on their photoluminescence (PL). Most previous experiments used self-assembled QDs that interact with delocalised electronic states formed in their vicinity during their growth process. This grants them complex electronic states that influence the QD-cavity interaction, overshadowing the impact of solid-state decoherence mechanisms. In contrast, pyramidal QDs possess simpler electronic states that are closer to ideal atom-like states. Using site-controlled pyramidal QDs, we probe the spectral features of a coupled QD-cavity system using PL measurements, and compare them to a theoretical model of a two-level system (TLS) coupled to a CM, providing new insights into the influence of the QD environment on its interaction with a confined CM.

Abstract

A prerequisite demanded of QD-photonic structures to realize on-chip quantum information and computing devices is the possibility to scale-up the system. This requires a good control of the QDs position within the photonic structure as well as a good control of the QDs emission energies. On the one hand this allows the coupling of several QD emitters with the same CM, enabling collective or lasing effects. On the other hand, the QDs can be precisely positioned in an extended photonic structure, permitting the transfer of information, mediated by light, between distant emitters. Within the framework of this thesis, we study such complex photonic structures comprising of multiple quantum emitters embedded in arrays of coupled PhC cavities. We demonstrate the coupling of site-controlled quantum wires (QWRs) to delocalized modes of linear and 2D arrays of cavities. Relying on the high uniformity of pyramidal QDs, we evidence the coupling of the delocalized mode of two coupled cavities to two site-controlled QDs, embedded in each cavity.

Key words: cavity quantum electrodynamics, nanophotonic, semiconductor, quantum dot, optical cavity, photonic crystal, Jaynes-Cummings model, Purcell effect, decoherence, dephasing, phonon, optical supermode.

Résumé

L'étude de l'interaction lumière-matière tient une place importante en physique et dans d'autres disciplines comme la biologie, la médecine ou la chimie. Comprendre et exploiter l'interaction entre la lumière et la matière est devenu primordial dans notre société qui est à la recherche d'énergies renouvelables et demande toujours plus d'espace de stockage et de rapidité de transfert pour l'information. Dans ce contexte, la fabrication de nouveaux dispositifs collectant ou émettant de la lumière, ainsi que le développement de nouvelles plateformes permettant le transfert d'informations et le calcul quantique, passera par une compréhension profonde de l'interaction entre la lumière et la matière à l'échelle nanoscopique. Cela nécessite d'étudier d'un point de vue fondamental, l'interaction entre des émetteurs quantiques et des modes optiques du champ électromagnétique, ce qui représente le domaine d'étude de l'électrodynamique quantique en cavité. Alors qu'à l'origine cette étude était pratiquée avec des atomes dans des cavités optiques, il est devenu possible de réaliser des expériences d'électrodynamique quantique en cavité à l'aide de constituants appartenant aux technologies cristallines, facilitant le passage de l'étude fondamentale à l'application pratique. L'atome est alors remplacé par une boîte quantique (BQ) semi-conductrice, une nanostructure modelée de façon à ce qu'elle ait des propriétés électroniques et optiques semblables à celles des atomes, interagissant avec une nanocavité semi-conductrice. Le sujet de cette thèse est l'étude de l'interaction entre une BQ semi-conductrice et les modes optiques d'une cavité à cristaux photoniques.

Lors de l'étude de l'interaction entre une BQ et une cavité optique, comprendre quel est l'impact de l'environnement de la BQ sur son interaction avec le mode optique de la cavité peut s'avérer être un défi. En effet, contrairement aux atomes, les BQs sont incorporées dans un environnement cristallin avec lequel elles peuvent interagir, entraînant des effets de décohérence quantique. Dans ce travail, nous utilisons des BQs *pyramidales*, dont la position spatiale est contrôlée, incorporées dans des cavités à cristaux photoniques afin d'étudier l'impact de la décohérence induite par l'environnement de la BQ sur la photoluminescence du système BQ-cavité. La majorité des expériences sur ce sujet repose sur l'utilisation de BQ auto-assemblées, interagissant avec des états électroniques délocalisés apparaissant lors de leur processus de croissance. Cela les dote d'états électroniques complexes qui peuvent avoir une influence sur les mécanismes d'interaction BQ-cavité, empêchant l'étude approfondie de l'im-

Résumé

pect des mécanismes de décohérence. En revanche, les BQs pyramidales possèdent des états électroniques se rapprochant de ceux d'atomes isolés. Ceci nous permet d'étudier, à l'aide de mesures spectrales, l'impact des mécanismes de décohérence sur l'interaction d'une BQ et d'un mode optique, en comparant les résultats expérimentaux à un modèle théorique.

La fabrication de dispositifs d'informations et de calcul quantique intégrés, à l'aide de BQs couplées à des systèmes photoniques, nécessite d'avoir la possibilité d'augmenter leur taille et leur complexité. Ceci demande un contrôle suffisant de la position des BQs au sein du dispositif photonique, ainsi qu'un contrôle de l'énergie d'émission des BQs. D'un côté cela permet de coupler plusieurs BQs au même mode optique, donnant la possibilité d'étudier l'émission collective d'objets quantiques ou d'atteindre le régime d'émission laser. D'un autre côté, cela rend possible la création de dispositifs permettant l'échange d'information entre des émetteurs quantiques distants, en utilisant la lumière comme vecteur d'information. Dans le cadre de cette thèse, nous étudions des structures photoniques constituées de plusieurs BQs incorporées dans des réseaux de cavités à cristaux photoniques. Nous démontrons le couplage de fils quantiques, dont la position spatiale est contrôlée, à des modes optiques délocalisés de réseaux de cavités unidimensionnels et bidimensionnels. De plus, à l'aide de l'importante uniformité des BQs pyramidales, nous mettons en évidence le couplage d'un mode optique délocalisé appartenant à un réseau formé de deux cavités, avec deux BQs incorporées dans l'une et l'autre des deux cavités formant le réseau.

Mots clefs : électrodynamique quantique en cavité, nanophotonique, semiconducteur, boîte quantique, cavité optique, cristal photonique, modèle de Jaynes-Cummings, effet Purcell, décohérence, déphasage, phonon, mode optique délocalisé.

List of abbreviations

cavity-QED	<i>cavity quantum electrodynamics</i>
QD	<i>quantum dot</i>
QWR	<i>quantum wire</i>
QW	<i>quantum well</i>
CM	<i>cavity mode</i>
PhC	<i>photonic crystal</i>
TLS	<i>two-level system</i>
VB	<i>valence band</i>
CB	<i>conduction band</i>
hh	<i>heavy-hole</i>
lh	<i>light-hole</i>
MOVPE	<i>metal-organic vapor phase epitaxy</i>
MBE	<i>molecular beam epitaxy</i>
PECVD	<i>plasma-enhanced chemical vapor deposition</i>
PMMA	<i>poly(methyl methacrylate)</i>
HSQ	<i>hydrogen silsesquioxane</i>
MIBK	<i>methyl isobutyl ketone</i>
EBL	<i>electron beam lithography</i>
RIE	<i>reactive ion etching</i>
ICP	<i>inductively-coupled-plasma</i>
TMGa	<i>trimethylgallium</i>
TEGa	<i>triethylgallium</i>
X	<i>neutral exciton</i>
2X	<i>biexciton</i>
X ⁻	<i>negatively charged exciton</i>
X ⁺	<i>positively charged exciton</i>
FWHM	<i>full width at half maximum</i>

Résumé

PL	<i>photoluminescence</i>
μ -PL	<i>micro-photoluminescence</i>
DOLP	<i>degree of linear polarization</i>
HBT	<i>Hanbury Brown and Twiss</i>
APD	<i>avalanche photodiode</i>
FDFD	<i>finite-difference-frequency-domain</i>
FDTD	<i>finite-difference-time-domain</i>
CCA	<i>coupled cavity array</i>

Contents

Remerciements/Acknowledgements	i
Abstract (English/Français)	iii
List of abbreviations	vii
1 Introduction	1
1.1 Nanophotonics	1
1.2 Cavity quantum electrodynamics	3
1.2.1 Semiconductor quantum dots and nanocavities	5
1.3 Semiconductor quantum dots	6
1.3.1 Semiconductors	7
1.3.2 Semiconductor heterostructures	8
1.3.3 Semiconductor quantum dot properties	10
1.3.4 Fabrication of semiconductor quantum dots	15
1.3.5 Linewidth broadening of semiconductor QDs	18
1.4 Photonic crystal cavities	21
1.4.1 Photonic crystal slab	23
1.5 Cavity quantum electrodynamics with semiconductor quantum dots	25
1.6 Thesis goals and outline	30
2 Experimental and modelling techniques	33
2.1 Photoluminescence spectroscopy	33
2.1.1 Principle of micro-photoluminescence measurements	33
2.1.2 Micro-photoluminescence setup	35
2.1.3 Photon correlation measurements	37
2.1.4 Time-resolved photoluminescence measurements	40
2.2 Photonic crystal numerical simulations	42
2.2.1 2D finite-difference method	42
2.2.2 3D finite-difference-time-domain method	44
2.2.3 L_3 photonic crystal cavities	44
2.3 Fabrication	48
2.3.1 Quantum dot fabrication process	48

Contents

2.3.2	QD integration in photonic crystal cavities	53
2.3.3	QD isolation using mesas	58
2.4	Chapter summary	59
3	Cavity quantum electrodynamics with semiconductor quantum dots	61
3.1	Jaynes-Cummings model	62
3.1.1	Two-level system Hamiltonian	62
3.1.2	Theoretical description of a cavity mode	63
3.1.3	Hamiltonian of the coupled system	64
3.2	Open-system Jaynes-Cummings model	68
3.2.1	Strong coupling	69
3.2.2	Weak coupling	70
3.3	Modeling semiconductor dephasing effects	72
3.3.1	Pure dephasing	73
3.3.2	Phonon cavity feeding	73
3.4	Simulating photoluminescence spectra	76
3.4.1	Photoluminescence spectra for N quantum dots	80
3.5	Chapter summary	83
4	Exciton complexes in site-controlled pyramidal quantum dots	85
4.1	Pyramidal quantum dots spectral properties	86
4.1.1	Power dependent measurements	89
4.1.2	Photon correlation spectroscopy	90
4.1.3	Exciton binding energies	94
4.1.4	Null binding energy biexciton	97
4.2	Exciton dynamics	100
4.3	Chapter summary	102
5	Site-controlled quantum dots in L_n photonic crystal cavities	105
5.1	One quantum dot coupled to an L_3 photonic crystal cavity	107
5.1.1	Detuning dependent photoluminescence	108
5.1.2	Modeling of photoluminescence	112
5.1.3	Detuning dependent QD-cavity dynamics	119
5.2	Two quantum dots coupled to an L_3 photonic crystal cavity	126
5.2.1	Detuning dependent photoluminescence	128
5.2.2	Modeling of photoluminescence	128
5.3	Chapter summary	132
6	Supermodes in 1D and 2D coupled cavity arrays	135
6.1	1D and 2D arrays of coupled cavities with site-controlled quantum wire light sources	136
6.1.1	Fabrication of photonic crystal cavity arrays with integrated quan- tum wire light sources	136

6.1.2 Supermode finite difference simulations	140
6.1.3 Photoluminescence measurements	148
6.1.4 Coupled cavity mode delocalization	154
6.2 Site-controlled quantum dots coupled to photonic crystal molecules .	159
6.2.1 Structure design and photonic molecule properties	159
6.2.2 Optical signatures of coupling between two quantum dots and the supermode of a photonic molecule.	161
6.3 Chapter summary	164
7 Conclusions and outlook	167
A Appendix	171
A.1 Effective phonon density of states calculation	171
A.2 Contributions	175
Bibliography	197
Publications and conferences	199
Curriculum Vitae	201

1 Introduction

The field of *photonics* is very broad and deals with the emission, absorption, harvesting, handling and processing of light. Photonics already had a great impact on our modern society by increasing data transmission rates to tens of Gbit/s with optical fiber technologies and memory storage capacities to 1000 Gbit/cm² with optical memory systems, leading to the advent of modern communication and modern internet. To keep up with the exponential expansion of internet and increasing demands of communication technologies, data transmission rates of tens of Tbit/s and memory storage capacities greater than tens of Tbit/cm² are needed, requiring the optical industry to process light on sub-wavelength scale. This has led to the recently emerged field of *nanophotonics* which studies the interaction of light and matter on a nanometer scale.

1.1 Nanophotonics

The present thesis is situated within *nanophotonics*, a field of science and technology that deals with light and matter on a nanoscale level, and engages many disciplines including optics, physics, chemistry, biology and material science. It is often defined as a field of study that aims to overcome Abbe's diffraction limit by developing innovative technologies that handle light on a deep sub-wavelength scale. Nanophotonics can be conceptually divided into three parts[1, 2] :

- *Nanoscale confinement of radiation*: inducing light-wave confinement at the nanoscale using near-field optical propagation, photonic crystals (PhC), surface plasmons, nanocavities etc.
- *Nanoscale confinement of matter*: inducing electron confinement at the nanoscale by developing nanostructured materials such as nanoparticles, semiconductor heterostructures etc.

Chapter 1. Introduction

- *Quantum optics of nanostructures*: inducing light-matter interactions in nanostructures with confined light-waves.

The research in these three directions has made a lot of progress in the past decades. We give here a non-exhaustive list of materials and devices involved in this research:

- **Metamaterials**: artificial materials composed of ordered or disordered arrays of nanoscale metallic or dielectric elements, used to generate superlenses, perfect absorbers or negative refractive index materials[3, 4].
- **Plasmonic materials**: noble metals with negative dielectric constants sustaining surface plasmon polaritons consisting of hybridised photons and electrons oscillations. These materials have been used to achieve ultra-strong light confinement[5] and exploited to realize plasmon nanolasers[6] and nanoantennas[7].
- **Photonic crystals**: high-refracting index materials engineered to have a periodic dielectric constant leading to the formation of photonic band gap prohibiting the propagation of light in chosen directions. These novel materials can be used to guide[8] or slow down light[9].
- **Nanocavities**: nanostructures designed to confine light on a nanometer scale. Nanocavities include nanodisk cavities[10], micropillar cavities[11], PhC cavities[12] and plasmonic cavities[13]
- **Semiconductor heterostructures**: nanostructures fabricated by juxtaposing semiconductors with different band gap energies, resulting in the confinement of electrons on a scale of the order of their De Broglie wavelength, leading to quantum effects. Such nanostructures are called quantum wells (QWs), quantum wires (QWRs) and quantum dots (QDs) when the confinement occurs in one, two or three dimensions of space. Their capacity to interact with light has been exploited to realize nanolasers[14, 15] or efficient sources of single indistinguishable photons[16].

The study presented in this thesis is related to the quantum optics of nanostructures. The possibility to confine both light and matter on a nanoscopic scale, enabled by the progress made in the field of nanophotonics, gave the opportunity to study the interaction of light and matter on a quantum level. Most notably, it became apparent that the possibility to control the confinement of light in nanostructures allowed to engineer the photon density of states in order to modify light-matter interactions. This aspect of nanophotonics was brought forward in 1946 by the seminal paper of E. Purcell[17] that predicted the modification of the spontaneous emission lifetime for an emitter placed in a cavity. In this work we investigate the interaction between semiconductor QD emitters and a PhC nanocavity. This study falls in the more general

field of *cavity quantum electrodynamics* (cavity-QED), presented in the next section, which deals with the interaction of a two-level system (TLS) emitter coupled to an optical cavity.

1.2 Cavity quantum electrodynamics

Cavity-QED is the study of the interaction between a TLS and the mode of an optical cavity (Fig. 1.1). It was after the initial discovery of E. Purcell that the spontaneous emission of an emitter could be modified by the presence of a resonator, that the need for a formalism describing the quantum interaction between an emitter and a quantized cavity electromagnetic field became apparent. In 1970, the theory of quantum electrodynamics was used to calculate the modified spontaneous emission of a TLS inside a Fabry-Perot cavity[18, 19], initiating a long series of papers on the subject. A detailed description of the theoretical formalism used to model the open quantum system formed by a TLS interacting with a cavity mode (CM) is given in chapter 3. We summarize here the most essential results.

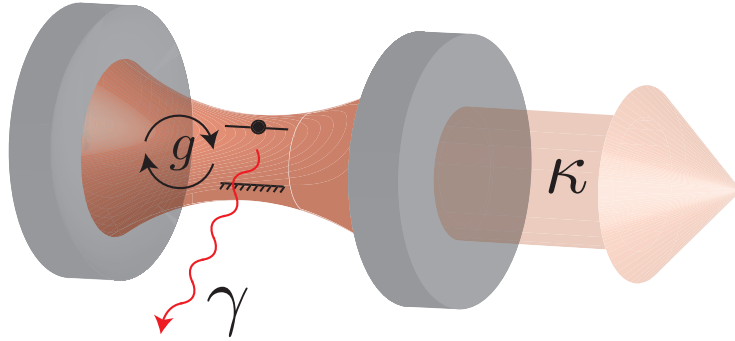


Figure 1.1: Schematic depiction of a TLS interacting with an optical mode of a mirror cavity. The coupling constant g describes the strength of the light-matter interaction. γ is the decay rate of the TLS in modes other than the cavity mode and κ the decay rate of the confined optical mode.

A simple model of a cavity-QED system consists of a TLS placed within the electromagnetic field confined between two reflective mirrors as sketched in Fig. 1.1. The interaction between the TLS and the field is described by a coupling constant

$$g \sim \mu \sqrt{\frac{\omega_c}{2\hbar V}} \quad (1.1)$$

with μ the TLS dipole moment, V the confined optical mode volume and ω_c its fre-

Chapter 1. Introduction

quency. The spontaneous emission of the isolated TLS is described by a decay rate γ , and the mirror losses of the cavity by a rate κ . Depending on the relative values of g , γ and κ , two main regimes can be observed:

- **weak coupling regime** ($\kappa \gg g, \gamma$): the cavity dissipative losses are greater than the coupling strength, leading to a modification of the TLS emission rate by a factor $F_p = \frac{3\lambda^3 Q}{4\pi^2 V}$, with $Q = \omega_c/\kappa$ the cavity quality factor and λ the wavelength of the emission. This modification factor is called the *Purcell factor* and first appeared in the paper of E. Purcell[17].
- **strong coupling regime** ($g \gg \kappa, \gamma$): the coherent interactions between the TLS and the confined field dominate over the system dissipations. This leads to a reversible exchange of energy between the TLS and CM known as Rabi oscillations. In the strong coupling regime, new entangled states of the system are formed, split in energy by $2\hbar g$ (vacuum Rabi splitting). In this regime the dynamics is dictated by single quanta, such that the interaction can be nonclassical and nonlinear on a single photon level[20].

The first cavity-QED experiments were carried by sending beams of Rydberg atoms through a millimeter-wave Fabry-Perot cavity. This led to the first experimental demonstration in the 1980s of spontaneous emission enhancement[21] and inhibition[22] for an atom weakly coupled to a CM. The increase of the Fabry-Perot cavities quality factor enabled in the 1990s to reach the strong coupling regime, leading to the first observation of vacuum Rabi splitting[23]. Shortly after, Rabi oscillation of Rydberg atoms in high-finesse cavities were observed and provided a direct evidence of field energy quantization in a cavity mode[24]. Since then many experiments, facilitated by atom trapping, led to the investigation of one-atom lasers[25] and single photon emission[26], and were extended to arrays of optically trapped atoms in cavities[27]. Although atom-cavity experiments provide an important resource for the investigation of fundamental cavity-QED aspects, the potential applications of cavity-QED in opto-electronics and quantum information science have led to an ongoing search for scalable, on-chip emitter-cavity systems.

An example of on-chip emitter-cavity system can be engineered using superconducting circuits. The atom is replaced by a Josephson-junction qubit and the cavity by a Josephson-junction microwave resonator. This constitutes the basic elements used to perform circuit-QED[28] experiments. This solid-state system provides emitter-cavity coupling strengths order of magnitude greater than atom-cavity structures, and was shown to undergo vacuum Rabi splitting[29], Rabi oscillations[30] and provide on demand single-photon emitters[31].

Another promising platform for realizing cavity-QED experiments uses surface plasmon polaritons to achieve subwavelength and subdiffraction confinement of light[32]. The small mode volumes of confined plasmonic mode have been used to increase the

spontaneous emission of various emitters such as molecules[33], QDs[34] or nitrogen-vacancy centers[35]. Although vacuum Rabi splitting has been observed with ensembles of molecules interacting with surface plasmon polaritons, the inherent large ohmic losses of confined plasmonic modes prevented up to now the observation of the strong coupling regime with single emitters. Theoretical predictions however suggest that this regime is not far from reach[36, 37].

The most studied solid-state cavity-QED platform consists of solid-state QDs incorporated in semiconductor nanocavities and is presented in the following section.

1.2.1 Semiconductor quantum dots and nanocavities

Cavity-QED experiments can be realized using solid-state QDs incorporated in semiconductor nanocavities. QDs are heterostructures that provide a three-dimensional confinement to electrons, resulting in a discrete, "atom-like" energy spectrum (see section 1.3). They can be incorporated in semiconductor nanocavities that provide a three-dimensional sub-micrometer confinement for optical modes. These cavities are generally fabricated using high refractive index semiconductor materials like GaAs or Si ($n \sim 3.5$). The main semiconductor cavities used in cavity-QED experiments are listed below[38]:

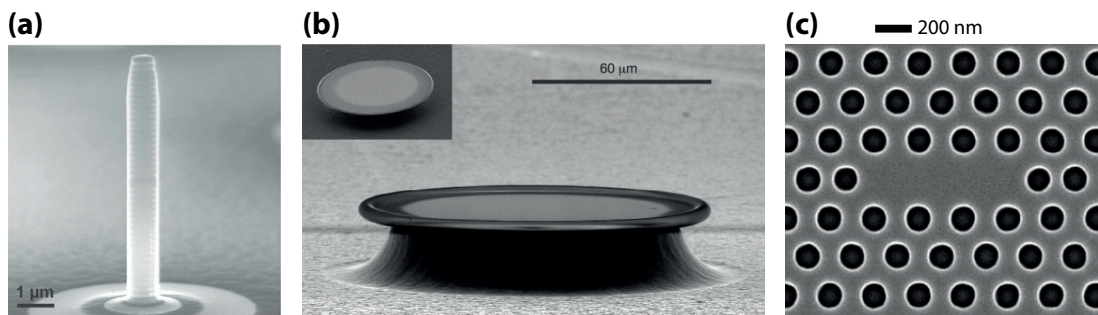


Figure 1.2: (a) Scanning electron micrograph image of a micropillar cavity with GaAs/AlAs distributed Bragg reflectors. Reprinted by permission from Macmillan Publishers Ltd: Nature [39], copyright (2004). (b) Scanning electron micrograph image of a silica microdisk. Reprinted by permission from Macmillan Publishers Ltd: Nature [40], copyright (2003). (c) Scanning electron micrograph image of a GaAs PhC slab defect cavity. Adapted from [41].

- Micropillar cavities:** Micropillars are Fabry-Perot style cavities that confine light between two high reflective mirrors made of distributed Bragg reflectors (DBRs) (Fig. 1.2 (a)). Lateral confinement is obtained using total internal reflexion on side walls of the etched cylinders. These cavities provide a highly directional output in the axial direction. Micropillar cavities have mode volumes $V \sim 16 (\lambda/n)^3$ and typical quality factors $Q \sim 10000$ although record values of $Q \sim 160000$ have been achieved[42].

- **Microdisk cavities:** In microdisk cavities (Fig. 1.2 (b)), the light is confined by continuous total internal reflection leading to the formation of whispering gallery modes. These cavities exhibit mode volumes $V \sim 8 (\lambda/n)^3$ and quality factors of $Q \sim 10000$ although record values of $Q = 10^9$ have been obtained[40, 43]. These cavities do not provide directional emission but light can be extracted using side coupling fiber-taper waveguides[44].
- **Photonic crystal cavities:** PhC cavities are formed by introducing a defect in the periodic dielectric constant of a PhC structure. The most commonly used PhC cavities consist of hole defects in 2D PhC slabs (Fig. 1.2 (c)). The light is confined inside the defect by the PhC band gap in the slab plane, and by total internal reflection in the out-of-plane direction (see section 1.4). These cavities provide directional output coupling[45] and are of particular interest due to their small mode volumes $V \sim 0.1 (\lambda/n)^3$ and high quality factors $Q \sim 20000$ with record values of $Q = 2 \cdot 10^6$ [46].

The first observation of the increased spontaneous emission of QDs weakly coupled to semiconductor nanocavities was realized in 1998 using micropillar cavities[47, 48]. The same effect was later observed with microdisk cavities[49] and PhC cavities[50]. The strong coupling regime was reached in 2004 with the first observation of vacuum Rabi splitting with single QD coupled to a micropillar cavity[39] and a microdisk[51] cavity. Soon after, vacuum Rabi splitting was observed with a single QD coupled to a PhC slab cavity[52]. Since then, multiple cavity-QED experiments have been performed using QDs and semiconductor nanocavities, bringing to light new phenomena specific to solid-state platforms. These are discussed in section 1.5.

1.3 Semiconductor quantum dots

In this thesis, the emitters used for performing cavity-QED experiments are semiconductor QDs[53]. The two main types of QDs are colloidal QDs[54] and epitaxial QDs[55]. The former is formed by evaporation and crystallization of colloidal solutions resulting in the synthesis of spherical nanocrystalline cores, typically composed of cadmium sulfide (CdS) or cadmium selenide (CdSe). Epitaxial QDs are formed using bottom up epitaxial growth of different semiconductor layers, relying on lattice-mismatch or patterned substrates to induce the formation of three dimensional QD islands. Colloidal QDs have been exploited to improve the emission of light-emitting diodes[56] and are of interest for applications in bio-imaging, displays[57] and solar power devices[58]. Although cavity-QED have been performed with colloidal QDs[59], they present large inhomogeneous broadenings ($\sim 100meV$) and additional steps are required to position them in semiconductor nanocavities, limiting their use for single QD experiments. On the other hand, epitaxial QDs can be straightforwardly incorporated in semiconductor nanocavities during the cavity fabrication process and present lower inhomogeneous

broadenings ($< 50 \text{ meV}$). Epitaxial QDs are the most extensively used emitters in solid-state cavity-QED experiments and their fundamental properties and fabrication process are summarized here.

1.3.1 Semiconductors

Semiconductors are the raw materials used in the fabrication of solid-state QDs. Semiconductors belong to the class of solid crystals, along with metallic and insulating solids. Solid crystals are formed by atoms tightly bound together and arranged in a periodic lattice. The orbital wave functions of the atoms forming the lattice overlap, resulting in the formation of energy bands separated by energy band gaps. The energy bands that govern important properties of the solid are the *valence band* (VB) and *conduction band* (CB). At 0 K the highest energy level occupied by crystal electrons is called the Fermi level. Metals have a Fermi level overlapping with the CB while the Fermi level of insulators is in between the valence and conduction bands. Semiconductors are a special kind of insulator, with a band gap energy sufficiently small to allow the promotion of electrons from the VB to the CB for finite temperatures. When an electron is excited to the CB, it leaves an empty state in the VB called a "hole". The electron in the CB (and the hole in the VB) have a sufficient amount of energy to escape the covalent bounds of the atoms and become mobile. The CB electron can relax into the VB annihilating a hole, which is commonly referred to as an electron-hole recombination. This energy relaxation can lead to the emission of a photon with an energy given approximately by the energy of the band gap.

Semiconductors are formed of elements belonging to the groups I to VII of the periodic table[60]. Silicon (Si) and Germanium (Ge) constitute the category of elemental semiconductors. Silicon is the most commonly used semiconductor with many applications in electronic circuits. However, like Germanium it possesses an indirect band gap which is not suited for optoelectronic applications. Two-element, *binary* or three-element, *ternary*, semiconductors can be formed by combining elements from different groups of the periodic table[61]. Binary compound materials can be constituted of II-VI elements like zinc selenide (ZnSe) or cadmium sulfide (CdS), I-VII elements like sodium chloride (NaCl) or lithium fluoride (LiF) and III-V elements like gallium arsenide (GaAs), indium phosphide (InP) or gallium nitride (GaN). The III-V semiconductor listed here have superior light-emitting properties compared to Si or Ge due to their direct band gaps, which makes them particularly suited for optoelectronic and photonic studies and applications. Ternary semiconductors are formed by combining three-elements from the periodic table and include $\text{In}_x\text{Ga}_{1-x}\text{As}$ and $\text{Al}_x\text{In}_{1-x}\text{As}$ where x denotes the indium (In) and aluminum (Al) mole fraction respectively[62]. These semiconductors are more flexible and allow the fabrication of more complex structures through band gap engineering. We focus here on structures based on GaAs for which the band structure is sketched in Fig. 1.3.

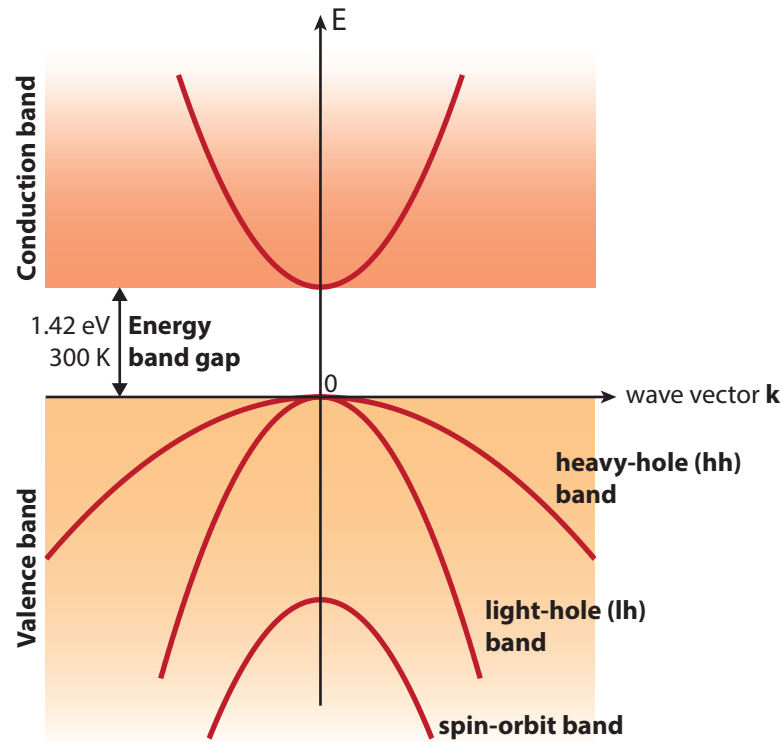


Figure 1.3: Illustration of band structure of GaAs in the effective mass approximation near the band extrema (wavevector $k = 0$).

Although the exact calculation of semiconductor band structures is extremely difficult to implement since it requires solving an N body problem, approximations such as the *effective mass approximation*[63] can be used to get a simplified picture of the electron energy dispersion. In the effective mass approximation, the electrons are modeled by free effective particles with a parabolic energy dispersion and an effective mass that accounts for the effect of the crystal's periodic potential. This approximation is valid when considering band extrema and is used to portray the band structure of GaAs in Fig. 1.3. For GaAs and most III-V semiconductors, the VB is composed of three sub-bands[64] (Fig. 1.3). The two bands degenerate at the VB extremum are the heavy-hole (hh) and light-hole (lh) bands. They are associated to holes with different effective masses. The third band is the spin-orbit split-off band which can be neglected if the spin-orbit interaction is important.

1.3.2 Semiconductor heterostructures

The progress of epitaxial growth techniques such as metal-organic vapor phase epitaxy (MOVPE) and molecular beam epitaxy (MBE) have made possible the fabrication of heterostructures using ternary compound semiconductors. During the epitaxial growth, the composition of the ternary semiconductor can be tuned to vary the band

1.3. Semiconductor quantum dots

gap profile along the growth direction. Using this technique, layers of different semiconductors with different energy band gaps can be grown on top of each other with atomically sharp interfaces. This requires the semiconductor layers to have similar lattice constants in order to avoid strain at the interfaces. The lattice constant a of a ternary alloy, for example $\text{Al}_x\text{Ga}_{1-x}\text{As}$, is given by Vegard's law[65]

$$a = a_{\text{AlAs}}x + a_{\text{GaAs}}(1 - x). \quad (1.2)$$

Given the similar lattice constants of GaAs ($a_{\text{GaAs}} = 0.565 \text{ nm}$) and AlAs ($a_{\text{AlAs}} = 0.566 \text{ nm}$) it is possible to grow alternative layers of GaAs and AlAs with nearly strain free interfaces. For $\text{In}_x\text{Ga}_{1-x}\text{As}$, however the difference in lattice constants of GaAs and InAs ($a_{\text{InAs}} = 0.606 \text{ nm}$) will induce strain during the growth.

This method is used to fabricate quantum confined semiconductor heterostructures such as QWs, QWRs and QDs. An example of QW heterostructure made of a $5 - 50 \text{ nm}$ InGaAs layer in between two GaAs semiconductor barriers is sketched in Fig. 1.4 (a). The associated variation in band gap energy along the z axis is shown in Fig. 1.4 (b).

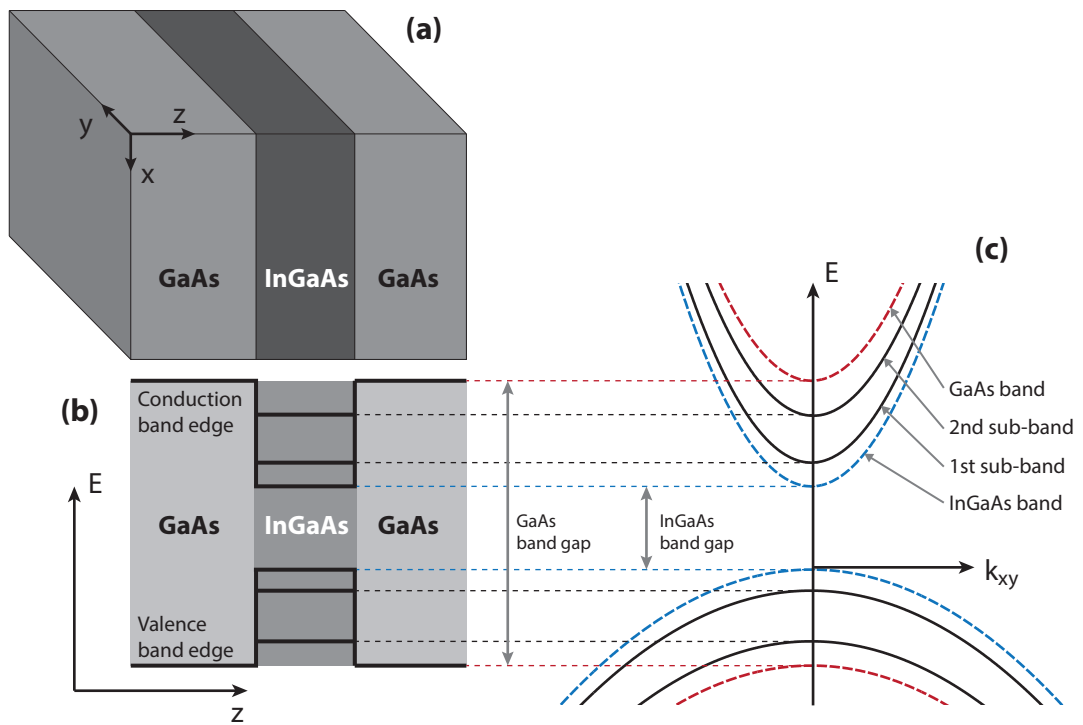


Figure 1.4: (a) Sketch of an GaAs/InGaAs/GaAs QW heterostructure. (b) Corresponding band diagram along the z axis of the QW. (c) Illustration of the QW band structure for carriers propagating in the xy plane. The confinement in the InGaAs layer leads to the formation of energy sub-bands.

Chapter 1. Introduction

When the effective mass approximation is valid, the electrons in the InGaAs layer can be seen as nearly free particles confined in a potential well. Since the De Broglie wavelength of electrons in the InGaAs layer (20 – 40 nm) is of the same order as the confinement length of the potential well, the electron motion is restricted in the z direction leading to quantum confinement. This results in the formation of energy sub-bands as illustrated in Fig. 1.4 (c). In addition, the strain induced by the lattice mismatch of the heterostructures modifies the band structure of the semiconductor. For uniaxial compression, the hh and lh bands split with the hh band above lh band. In general, mixing occurs between the two VBs leading to a deviation from parabolic dispersion relations[66].

The same principle applies to heterostructures confining the electrons in two directions of space (QWRs) and three directions of space (QDs). The quantum confinement leads to a redistribution of the number of states per interval of energy and per volume available for the electrons. This quantity is the electronic density of states and is shown in Fig. 1.5 for free electrons, 2D, 1D and 0D confinement. Interestingly, the 3D quantum confinement for QDs results in a discrete distribution of allowed energies, similar to the energy spectrum of atoms.

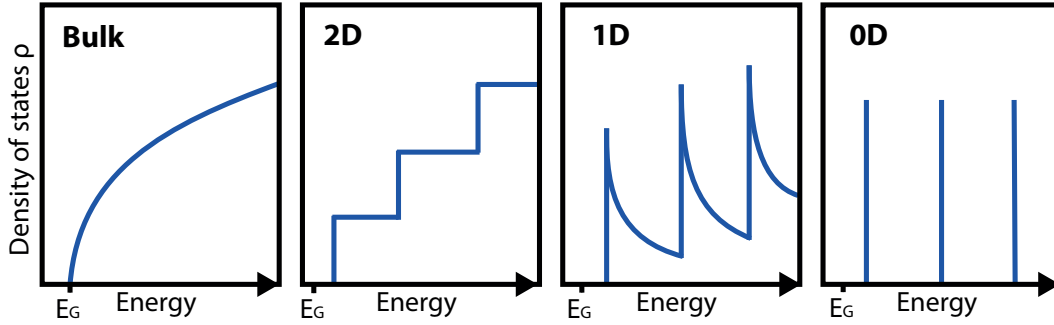


Figure 1.5: Illustration of the electronic density of states for carriers in the bulk, for 2D confinement (QW), 1D confinement (QWR) and 0D confinement (QD). E_G is the band gap energy.

1.3.3 Semiconductor quantum dot properties

For QDs, the energy of the confined particles can be estimated, in the effective mass approximation, by solving the following Schrödinger equation[66]

$$\left[-\frac{\hbar^2}{2m^*} \nabla^2 + W(\mathbf{r}) \right] \phi(\mathbf{r}) = E\phi(\mathbf{r}) \quad (1.3)$$

where $\phi(\mathbf{r})$ is the slow varying (compared to the crystal lattice) envelope wave function (the effect of the crystal lattice is included in the effective mass) and $W(\mathbf{r})$ is the confining potential which has, in most real cases, a complicated dependence on \mathbf{r} . Most

epitaxially grown QDs have an asymmetric shape leading to a stronger confinement in the growth direction. A simple but reasonably good approximation for the potential confinement of such QDs is an infinite barrier confinement along the growth axis (z -axis), and parabolic confinement in plane (x - y plane). The infinite barrier confinement gives a contribution to energy equal to

$$E_l^z = \frac{\hbar^2 \pi^2}{2m^*} \frac{l^2}{L_z^2}, \quad l = 1, 2, \dots \quad \text{for infinite rectangular barriers,} \quad (1.4)$$

with L_z the size of the confinement in the z direction. Since the confinement is stronger in the growth direction, we can restrict to the lowest energy level $l = 1$ and solve the Schrödinger equation separately for the transverse parabolic confinement. Note that, as a rough approximation, we consider here noninteracting electrons and holes (single particle picture). In the wafer plane the Schrödinger equation becomes[67]

$$\left[-\frac{1}{2m^*} (\hat{p}_x^2 + \hat{p}_y^2) + \frac{1}{2} \omega^2 (\hat{x}^2 + \hat{y}^2) \right] |\phi\rangle = E |\phi\rangle \quad (1.5)$$

with ω relates the strength of the confinement, \hat{x} is the position operator of the particle and \hat{p} its momentum operator. This is the Schrödinger equation of a 2D isotropic harmonic oscillator. The eigenvalues are given by $E_{n_+, n_-} = \hbar\omega(n_+ + n_- + 1)$. The corresponding eigenstates are $|n_+, n_-\rangle$, to which are associated the angular momentums $L_{n_+, n_-}^z = n_- - n_+$ due to the circular symmetry of the parabolic confinement. The energy states of the confined CB electrons are thus

$$\begin{aligned} E_{n_+, n_-}^e &= \frac{E_g}{2} + \hbar\omega_e(n_+ + n_- + 1) + \frac{\hbar^2 \pi^2}{2m_e^*} \frac{1}{L_z^2}, & L_{n_+, n_-}^{z,e} &= n_- - n_+ \\ n_+ &= 0, 1, 2, \dots \\ n_- &= 0, 1, 2, \dots \end{aligned} \quad (1.6)$$

where ω_e relates the strength of the confinement for the electrons and m_e^* is the effective mass of the CB electrons. $L_{n_+, n_-}^{z,e}$ denotes the angular momentum number of the electron. The energy reference is taken in the center of the band gap. If we assume a sufficiently large hh-lh band splitting, which is a reasonably good approximation for strongly confining heterostructures, the lh and spin-orbit split-off bands can be neglected and the energy states of the confined hh are

$$E_{n_+, n_-}^{hh} = \frac{E_g}{2} + \hbar\omega_{hh}(n_+ + n_- + 1) + \frac{\hbar^2 \pi^2}{2m_{hh}^*} \frac{1}{L_z^2}, \quad L_{n_+, n_-}^{z, hh} = n_+ - n_-.$$

These energy levels are indicated in figure 1.6 for $n = n_+ + n_- = 0$ (s-like states), 1 (p-

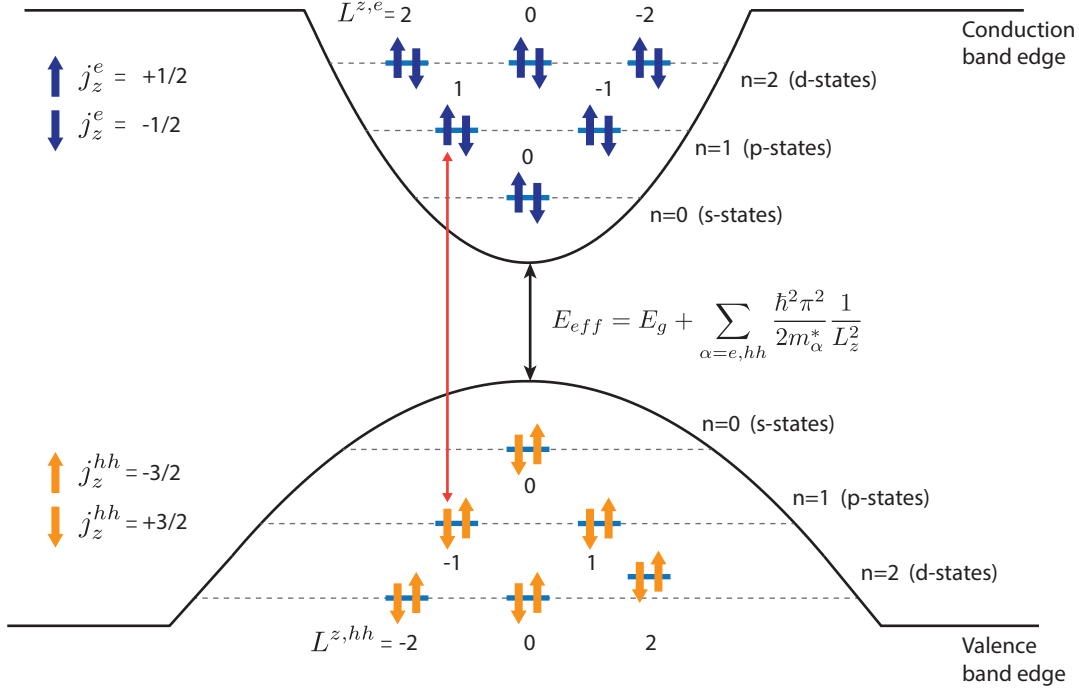


Figure 1.6: Energy level of electron and holes confined in a parabolic QD. They are equally spaced in energy and labeled by the quantum numbers n and L^z . The red arrow indicates an example of allowed optical transition.

like states) and 2 (d-like states)¹. The angular momentum number $L^{z,e}$ ($L^{z,hh}$) denotes a certain orbital symmetry of the envelope wave function $|\phi\rangle$. Each state is two-fold degenerate due to total angular momentum inherited from the semiconductor crystal. Indeed, the CB of III-V semiconductors with zincblend structure has, close to $\mathbf{k} = 0$, a total angular momentum $j = \frac{1}{2}$. The electrons can thus have total angular momentum projections of $j_z^c = \pm\frac{1}{2}$. The hh and lh bands have a total angular momentum of $j = \frac{3}{2}$. The holes total angular momentum projections are $j_z^{hh} = \pm\frac{3}{2}$ for the hh band, and $j_z^{lh} = \pm\frac{1}{2}$ for the lh band. The \pm are indicated in Fig. 1.6 by arrows pointing up or down. Radiative recombinations between electrons and holes can occur only if they follow certain selection rules. First of all, the overlap of the particles envelope wave functions must be non zero. This is the case only if they have the same quantum numbers n_+ and n_- , which is equivalent to say they must have opposite angular momentums L^z . The photon acquires the difference of the electron and hole total angular momentum given by $j_{ph} = j_z^c - j_z^{hh}$. Photons can only have total angular momentums projections equal to 0 (linear polarization) or ± 1 (circular polarization). Radiative recombination thus involves electron and heavy-holes of positive or negative angular momentum j_z . An example of allowed transition is indicated by an arrow in figure 1.6. The energy of

¹The s,p,d,... labels are chosen in analogy to atomic physics.

the emitted photon, in the single particle picture, is

$$E_{n_+,n_-}^{photon} = E_g + \sum_{\alpha=e,hh} \frac{\hbar^2 \pi^2}{2m_\alpha^*} \frac{1}{L_z^2} + \sum_{\alpha=e,hh} \hbar \omega_\alpha (n_+ + n_- + 1) \quad (1.7)$$

where $E_{eff} \equiv E_g + \sum_{\alpha=e,hh} \frac{\hbar^2 \pi^2}{2m_\alpha^*} \frac{1}{L_z^2}$ can be treated as an effective band gap.

QD excitonic species

The above discussion is valid when considering a single particle picture. When more than one electronic particle is confined in the QD, Coulomb interactions between the charges will modify the the QD energy levels. The Coulomb interaction energy between two particles with charges $q_{1,2}$ at positions $r_{1,2}$ is given by

$$V_{Coul}^{1,2} = \frac{q_1 q_2}{4\pi \epsilon_0 \epsilon_r} \frac{1}{|r_1 - r_2|} \quad (1.8)$$

where ϵ_0 and ϵ_r are the vacuum and semiconductor dielectric constants respectively. In a bulk semiconductor a CB electron and a VB hole, excited for example by an optical intra-band transition, can form a bound state referred to as *exciton*. An exciton can also be formed in a QD structure either by trapping of diffusing bulk electron and hole particles in attractive QD potential or resonant excitation of a an electron-hole pair in the QD. If the effective Bohr radius[62] of the exciton is smaller than the QD confinement length (weak confinement regime), the Coulomb interaction energy dominates over the single particle energy levels, and the exciton is confined as a whole "quasiparticle". On the other hand, if the exciton effective Bohr radius is larger than the QD confinement length (strong confinement regime), the Coulomb interaction energy is small with respect to the single particle confinement energies. In other words, the electron and hole are bound by the QD confinement potential rather than by the Coulomb interaction. In the strong confinement regime, applicable to most small QD structures, the Coulomb interaction can be treated perturbatively, and the confined exciton (X) energy approximated by[66]

$$E_X = E_{0,0}^e + E_{0,0}^{hh} - V_{Coul}^{e,h} \quad (1.9)$$

An QD excitonic state composed of one electron and one hole is often referred to as the *neutral exciton*. In total, four bright excitonic states are allowed in the QD s-state energy levels depicted in Fig. 1.7. The arrows indicate the spin orientation of the particle (see Fig. 1.6). If in addition to the neutral exciton (Fig. 1.7 (a)) an additional electron (hole) is confined in the QD, the excitonic state is a *negatively (positively)*

Chapter 1. Introduction

charged exciton denoted X^- (X^+) (Fig. 1.7 (b) and (c)). If, as shown in Fig. 1.7 (d), an additional exciton is confined in the QD, the excitonic state is a *biexciton* ($2X$).

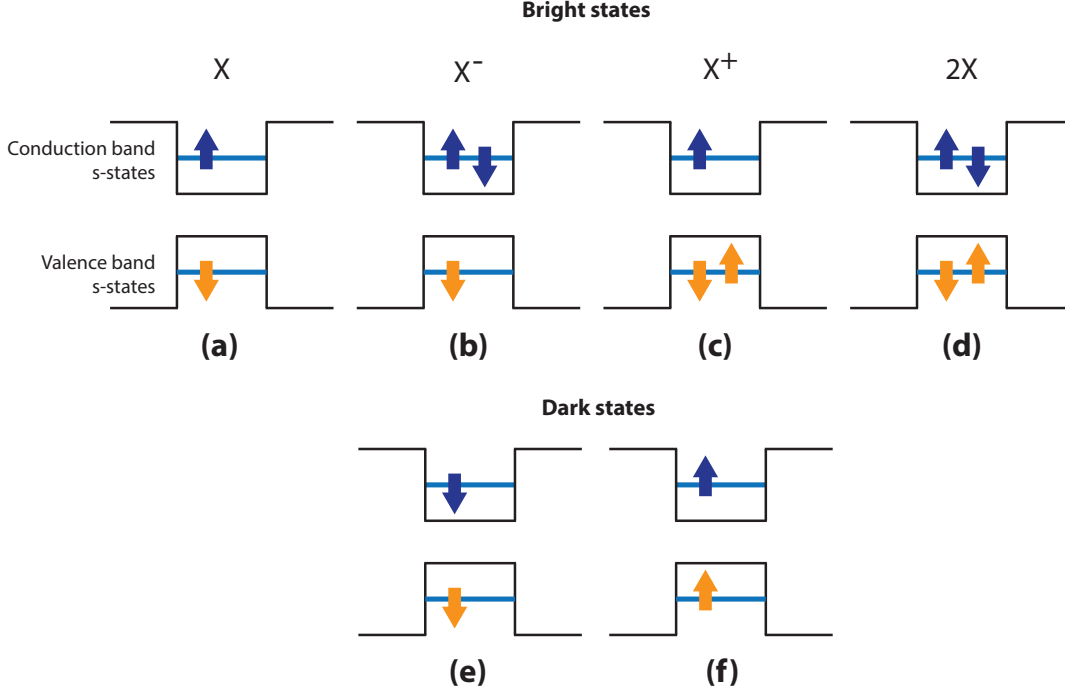


Figure 1.7: Bright excitonic states of the QD s-states levels. (a) Neutral exciton (X). (b) Negatively charged exciton (X^-). (c) Positively charged exciton X^+ . (d) Biexciton ($2X$). (e) and (f) Dark excitonic states.

The energies associated with these excitonic species are[66]

$$E_{X^-} = 2E_{0,0}^e + E_{0,0}^{hh} + V_{Coul}^{e,e} - 2V_{Coul}^{e,h} \quad (1.10)$$

$$E_{X^+} = E_{0,0}^e + 2E_{0,0}^{hh} + V_{Coul}^{h,h} - 2V_{Coul}^{e,h} \quad (1.11)$$

$$E_{2X} = 2E_{0,0}^e + 2E_{0,0}^{hh} + V_{Coul}^{e,e} + V_{Coul}^{h,h} - 4V_{Coul}^{e,h}. \quad (1.12)$$

The corresponding radiative energy transitions are given by the difference in energy between the initial and final excitonic states (conservation of energy)

$$E_X^{photon} = E_X \quad (1.13)$$

$$E_{X^-}^{photon} = E_{X^-} - E_{0,0}^e = E_{0,0}^e + E_{0,0}^{hh} + V_{Coul}^{e,e} - 2V_{Coul}^{e,h} \quad (1.14)$$

$$E_{X^+}^{photon} = E_{X^+} - E_{0,0}^{hh} = E_{0,0}^e + E_{0,0}^{hh} + V_{Coul}^{h,h} - 2V_{Coul}^{e,h} \quad (1.15)$$

$$E_{2X}^{photon} = E_{2X} - E_X = E_{0,0}^e + E_{0,0}^{hh} + V_{Coul}^{e,e} + V_{Coul}^{h,h} - 3V_{Coul}^{e,h}. \quad (1.16)$$

This leads to an s-state energy spectrum with four discrete transitions having in general different energies. The shift in energy of the excitonic species transition energy with respect to the neutral exciton transition energy is called the binding energy, and is given by

$$E_{X^-}^B = E_X^{photon} - E_{X^-}^{photon} = V_{Coul}^{e,h} - V_{Coul}^{e,e} \quad (1.17)$$

$$E_{X^+}^B = E_X^{photon} - E_{X^+}^{photon} = V_{Coul}^{e,h} - V_{Coul}^{h,h} \quad (1.18)$$

$$E_{2X}^B = E_X^{photon} - E_{2X}^{photon} = 2V_{Coul}^{e,h} - V_{Coul}^{e,e} - V_{Coul}^{h,h}. \quad (1.19)$$

In addition to these four bright state excitons, two "dark state" excitons can populate the QD s-states. They are obtained from the excitonic state of Fig. 1.7 (a) by inverting either the electron or hole spin (Fig. 1.7 (e) and (f)). These dark states have total angular momenta of ± 2 which makes them nonradiative.

1.3.4 Fabrication of semiconductor quantum dots

A large number of methods are used to fabricate QD structures. The most commonly used QDs are *self-assembled* In(Ga)As QDs, fabricated using the Stranski-Krastanov growth mode. This fabrication method relies on the $\sim 7\%$ lattice mismatch between the InAs and GaAs bulk semiconductors. A thin wetting layer of InAs is grown on a GaAs substrate (typically with a (100) orientation), using MBE or MOVPE. As the thickness of the InAs layer increases, the lattice mismatch induces a build up of strain, increasing the elastic energy of the crystal. Once a critical thickness is reached (typically a few monolayers), the crystal minimizes its energy by forming small InAs islands randomly distributed on a 2D wetting layer. The InAs islands are finally capped with a GaAs upper layer forming In(Ga)As/GaAs QD structures. These QDs have typical heights of $5 - 10 \text{ nm}$ and in-plane diameters of $20 - 30 \text{ nm}$.

Self-assembled QDs are widely used in cavity-QED experiments because they can be easily fabricated and exhibit thin QD spectral linewidths below $10 \mu\text{eV}$. The size distribution of self-assembled QDs leads to poor control of the QD emission energy, characterized by an inhomogeneous broadenings of $30 - 50 \text{ meV}$. Along with their inherent random nucleation, this prevents a straightforward deterministic integration of self-assembled QDs in photonic structures. Current QD-cavity experiments rely either on large or low densities of self-assembled QDs. The former case ensures that at least one QD will couple to the optical field of the cavity but is not suitable for single QD experiments. The latter case requires the fabrication of a large number of structures, relying on statistics and long systematic measurements to find a QD with a sufficient spatial and spectral overlap with the optical field of the cavity.

The deterministic integration of single self-assembled QDs can be achieved by posi-

Chapter 1. Introduction

tioning the cavity structure around a randomly positioned QD[68–70]. This requires a pre-characterization step to locate the QD, followed by a lithography step to align the cavity structure with the designated QD. Although these methods are suited for fundamental cavity-QED studies, they are not viable for applications in quantum information science which require the upscaling of nanophotonic devices. Note that growth modes other than Stranski-Krastanov exist such as droplet epitaxy[71] or monolayer fluctuation control in quantum wells[72], but they suffer from the same drawbacks.

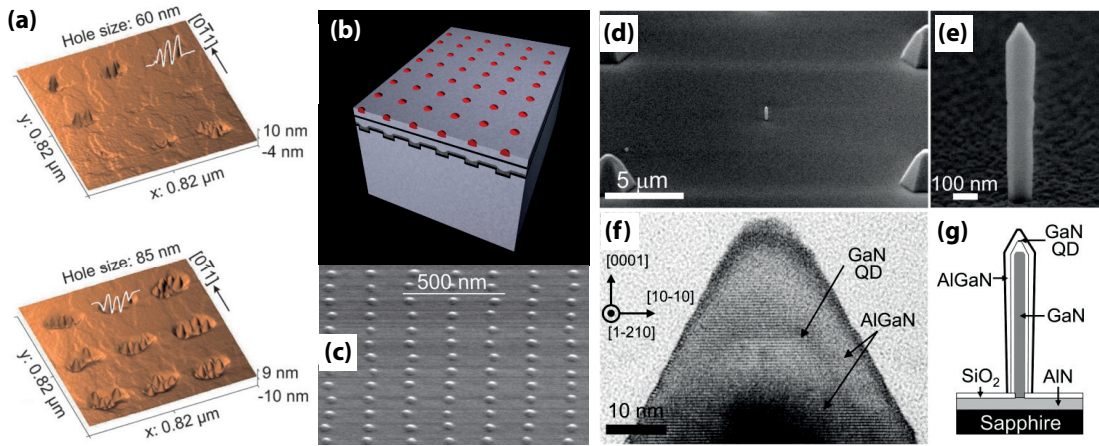


Figure 1.8: (a) Atomic force microscopy image showing part of a QD array in which the original hole diameter before buffer layer growth was 60 nm (top), and 85 nm (bottom). Representative height profiles reveal the formation of QDs inside the holes. (b) Growth scheme of the vertically coupled site-controlled QDs. The seeding layer is shown in medium grey. The site-controlled QDs on the surface are shown in red. GaAs is light grey and the AlGaAs barrier is dark grey. (c) Scanning electron microscope image of an array of site-controlled QDs (see (b)) with a period of 500 nm. This image was acquired under a tilted angle of view to increase the contrast. (d)-(e) Scanning electron microscope images of a GaN/AlGaN nanowire containing a single GaN QD grown on a patterned AlN/sapphire substrate. (f) High-resolution transmission electron microscopy image of a GaN QD embedded in a nanowire. (g) Schematic illustration of a GaN/AlGaN nanowire. (a) Reprinted with permission from [73]. 2012 WILEY-VCH Verlag GmbH & Co. KGaA, Weinheim. (b)-(c) Reprinted from Publication [74], Copyright (2011), with permission from Elsevier. (d)-(g) Reprinted with permission from [75]. Copyright [2013], AIP Publishing LLC.

The fabrication of high yield, scalable photonic devices requires a nearly perfect control of the QD position. Several strategies have been developed to control the position of QDs on a substrate. The most commonly used methods involve epitaxial growth of InAs self-assembled QDs on patterned GaAs substrates with (100) orientation. Regular arrays of holes are defined on the substrates using either electron beam lithography (EBL) combined with ion etching, nano-imprint lithography or atomic force lithography. The holes can be used as surface deformations that localize diffusing indium atoms during the growth, inducing the spontaneous nucleation of QDs inside the holes[73] (Fig. 1.8 (a)). Using this method, site-controlled QDs with linewidths as low as $60 \mu\text{eV}$ were fabricated[76]. Another approach is to overgrow the patterned

substrate with a GaAs layer, partly filling the holes. This induces strain in the regions of the overgrown layer located above a nano-hole of the substrate. By growing a subsequent InAs layer, self-assembled QDs form preferential above a filled nano-hole due to vertical strain coupling[74] (Fig. 1.8 (b) and (c)). This method presents the advantage of distancing the QDs from the defects of the hole's etched surface, leading to improved QD linewidth of $10 - 40 \mu eV$ [77, 78]. This controlled QD nucleation also improves the size distribution of the QDs leading to inhomogeneous broadenings as low as $15 meV$ for the emission of ensembles of QDs[79]. Although these site-controlled QDs present good optical properties, their nucleation, like self-assembled QDs, relies on strain. Strain being orientation dependent on the substrate, self-assembled QDs form with an asymmetric, elongated shape. This induces polarization anisotropy of the emission and fine-structure splitting of the exciton state ($\sim 60 \mu eV$), which can be detrimental for certain applications including the emission of entangled or indistinguishable photons. In addition, the presence of a 2D wetting layer adds spurious effects in cavity-QED experiments as discussed in more details in section 1.5.

Although we focus here on arsine based semiconductors, other semiconductor materials can be used to fabricate QDs. An example is given by GaN QDs embedded in site-controlled nanowires[75, 80] (Fig. 1.8 (d)-(g)). The nanowires can be fabricated using either a top-down or bottom-up approach to incorporate InGaN/GaN or GaN/AlGaIn QDs near the top of the nanowire. The large band energies of nitride based ternary alloy allows to reach QD emission energies above $4 eV$. Furthermore, emission from single QDs was observed up to room temperature with these structures[75].

The site-controlled QDs used in this work are obtained by MOVPE growth of InGaAs/-GaAs on a (111)B-oriented GaAs substrate patterned with pyramidal pits[81, 82]. The QDs obtained with this method are referred to as *pyramidal* QDs. Regular arrays of pyramidal recesses are etched on the GaAs substrate by means of EBL and wet chemical etching. This results in the formation of uniform inverted pyramids with well defined (111)A facets (Fig. 1.9 (a)). What distinguishes these QDs from site-controlled self-assembled QDs is that their nucleation process is not governed by strain. During MOVPE growth, the forces driving the nucleation of the pyramidal QDs are growth rate anisotropy and capillarity effects, resulting in the formation of lens-shaped QDs at the apex of the pyramidal pits. These QDs have a height to width ratio similar to self-assembled QDs ($\sim 20 nm$ in plane and $\sim 5 nm$ in the growth direction), but present a high hexagonal symmetry induced by the self-limited growth mechanism[83, 84] and symmetry of the inverted pyramids (Fig. 1.9 (b)-(d)). Furthermore, no 2D wetting layer is formed during the growth of the QD. However, under certain growth conditions, InGaAs/GaAs QWRs can form on the three wedges of the inverted pyramid.

Using this technique, highly uniform site-controlled QDs with promising optical properties were fabricated, yielding reproducible single QD spectra (Fig. 1.9 (e)). The emission of pyramidal QD ensembles is characterized by an average inhomogeneous

broadening of 10 meV with record low spread of the neutral exciton line of $\sim 1\text{ meV}$ from QD to QD[85] (Fig. 1.9 (f)). Single QDs exhibit thin excitonic lines with linewidths of $80 - 100\ \mu\text{eV}$ [86]. The high symmetry of pyramidal QDs results in low fine-structure splitting of the exciton state[82] ($20\ \mu\text{eV}$ in average).

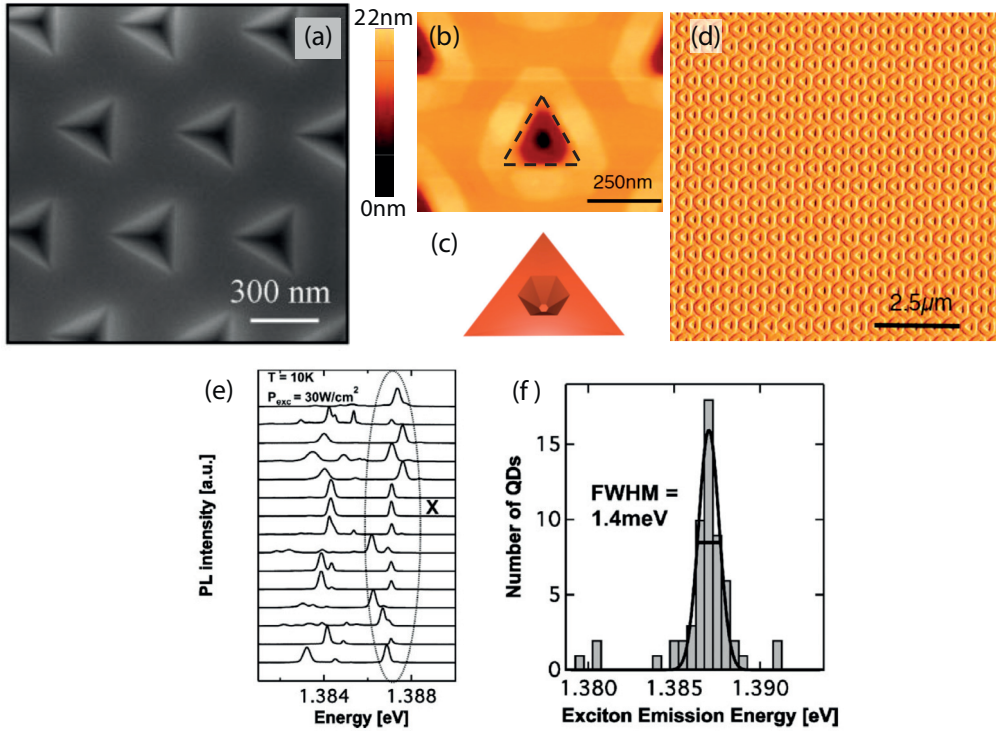


Figure 1.9: (a) Scanning electron microscope image of an ensemble of etched pyramids prior to growth. (a)-(d) Arrays of site-controlled pyramids with a 300 nm base side, overgrown with a nominally 27 nm thick GaAs layer. (b) Top-view tapping mode atomic force microscopy image of a single pyramid. The dashed lines indicate the initial boundaries of the pyramid. (c) Schematic illustration of the overgrown pyramid. (d) Top-view phase mode atomic force microscopy image of a 500 nm pitch array of overgrown pyramids. (e) Low-temperature (10 K) photoluminescence spectra from 15 different single QDs, which show the ground-state emission from different excitonic species (identified by excitation- and temperature-dependence studies[87]). (f) Statistical distribution of X emission energies from 60 different QDs, with a fit to a Gaussian distribution revealing a narrow FWHM of only 1.4 meV. (a) Reprinted with permission from[81]. 2009 Wiley-VCH Verlag GmbH & Co. KGaA, Weinheim.. (b)-(d) Reprinted with permission from [88]. Copyright [2008], AIP Publishing LLC.. (e) and (f) Reprinted with permission from[85]. 2010 Wiley-VCH Verlag GmbH & Co. KGaA, Weinheim..

1.3.5 Linewidth broadening of semiconductor QDs

The spectral signature of an isolated ideal atom is given by a sharp Lorentzian function with a full width at half maximum (FWHM) γ (Fig. 1.10 (a)) given by the inverse of the atom radiative lifetime τ . This natural broadening is a consequence of the uncertainty principle and is often referred to as *lifetime broadening*. All quantum emitters,

including atoms, are never truly isolated from their environment. Interactions with the environment leads to quantum decoherence which destroys quantum mechanical interference effects. It is convenient to describe a quantum emitter and its environment by a Hamiltonian made of three parts[89]: the system Hamiltonian (the emitter), the bath Hamiltonian (the environment) and the system-bath coupling Hamiltonian. The latter can be composed of off-diagonal and diagonal elements. Off-diagonal coupling terms lead to a population relaxation of the emitter. An example is given by the coupling of an atom to the electromagnetic field that induces radiative emission. Diagonal coupling terms do not produce population relaxation but lead to *pure dephasing* which introduces additional linewidth broadening. These coupling terms can be viewed as providing time-dependent fluctuations to the system eigenenergies, introducing a "dephasing" between the phases of the system states.

For semiconductor QD emitters, which are embedded in a crystal lattice, the interaction with the environment can be important, leading to linewidth broadening beyond the radiative lifetime limit. We review here the two main decoherence mechanisms responsible for linewidth broadening in semiconductor QDs.

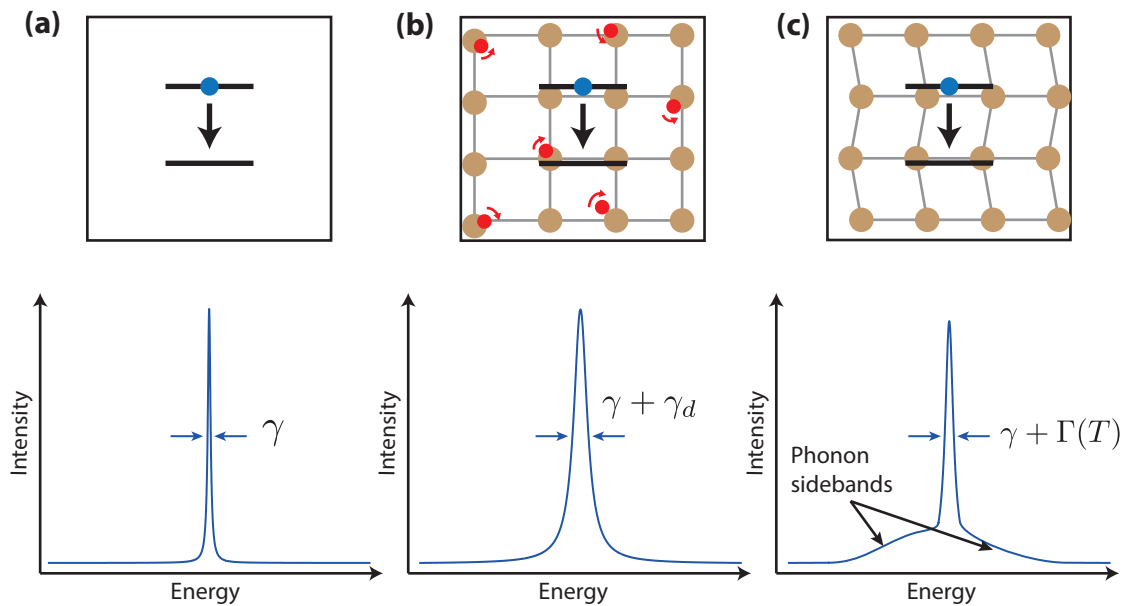


Figure 1.10: Illustration of decoherence processes in semiconductor QDs. (a) Lifetime limited spectral signature of a QD isolated from its environment. (b) Spectral signature of a QD broadened by pure dephasing- γ_d is the pure dephasing rate. (c) Spectral signature of a QD modified by the interaction of the QD with LA phonons.

Pure dephasing induced by fluctuating charges

The typical lifetime measured for InAs QDs are on the order of 1 ns . This corresponds to a lifetime broadening of $0.7\ \mu\text{eV}$. This is well below the $10 - 100\ \mu\text{eV}$ linewidths reported in the literature for these QDs. This discrepancy is explained by the interaction of the

QD excitonic states with the fluctuating electric field generated by charges in the vicinity of the QD. Defects present in the bulk material or generated during the growth of the QDs can capture and release charges at a given rate, generating a fluctuating field, which modifies the energy of the excitonic states. As explained by Berthelot et al.[90], if these energy shifts occur at rate slower than the QD radiative decay rate, this leads to spectral jumps of the emission known as *spectral diffusion*. When the integration time of the luminescence signal is much longer than the time scale on which these spectral jumps occur, the recorded QD emission has a Gaussian line-shape, with a width determined by the density of defects surrounding the QD. However if the energy shift induced by the fluctuating charges occur at a rate faster than the QD radiative lifetime, spectral jumps are inhibited and the QD Lorentzian spectral feature is homogeneously broadened. This situation corresponds to a pure dephasing of the QD transition, which is broadened by γ_d (Fig. 1.10 (b)).

Spectral diffusion of the QD emission has been observed with energy shifts occurring on a time scale of 1 s[91] up to 100 s[92] for CdSe self-organized QDs. For InAs QDs, the energy shifts occur on a much more smaller time scale of ~ 10 ps[93, 94], leading to pure dephasing induced broadening. In general, the effects of spectral diffusion and pure dephasing are pronounced when the QD is excited non-resonantly, resulting in the generation of diffusing charges in the QD barrier material which can be trapped and released by neighboring defects[74] or wetting layer states[95]. Pure dephasing can be inhibited by exciting the QD resonantly and thus preventing the generation of carriers in the QD barriers[96]. However it was recently shown that fluctuations of the QD electrostatic environment can persist even under resonant excitation, leading to pure dephasing[16]. In this experiment, non-resonant excitation was used as a mean to stabilize the electrostatic environment by filling the traps in the QD vicinity.

The decoherence induced by pure dephasing can hinder the observation of cavity-QED effects. Observing the strong coupling regime can then be more difficult since pure dephasing induces a damping of the Rabi oscillations and broadens the emitter emission, smearing out the vacuum Rabi splitting[97, 98]. On the other hand, as emphasised by Auffèves et al. [99], pure dephasing can also enhance the effective coupling between a QD and the optical mode of a cavity when they are detuned in energy. Pure dephasing can also be used to increase the indistinguishability of photons emitted by a QD coupled to a CM[100, 101], serving as an additional degree of freedom that can prove beneficial for cavity-QED experiments.

Phonon scattering

An important source of decoherence in semiconductor QDs comes from their interaction with the crystal lattice vibrations known as phonons. The impact of QD-phonon interaction on the spectra of semiconductor QDs has been observed in several photoluminescence experiments[102–107]. It translates into a temperature dependent broadening of the QD Lorentzian feature, referred to as the zero phonon line (ZPL), as

well as the appearance of an asymmetric broadband emission superposed on the ZPL (Fig. 1.10 (c)).

There have been many attempts to describe theoretically these observations of phonon induced QD dephasing. The most successful ones use a generalized Huang-Rhys theory of localized exciton-phonon interactions[102, 108, 109]. In these theoretical descriptions, longitudinal acoustic (LA) phonon scattering is described by an exciton-phonon interaction Hamiltonian with diagonal and off-diagonal elements. The diagonal elements are responsible for a fast decay of the coherence on a few picosecond time scale[110]. This pure dephasing mechanism is the result of the coupling of the QD excitonic states with a continuum of acoustic phonons. In essence, the phonon interaction induces a shift of the excitonic state to lower and higher energies, corresponding to the "emission" and "absorption" of a phonon respectively. At low temperatures, the broadband emission, often referred to as *phonon sidebands*, is thus asymmetric due to the low population of the phonon bath, which inhibits the absorption of a phonon. When the temperature is increased this asymmetry becomes less pronounced. The energy of the acoustic phonons interacting efficiently with the confined exciton states is proportional to the inverse of the QD confinement length[102]. For QDs with a size of $5 - 10 \text{ nm}$, this leads to sidebands extending up to $\pm 3 \text{ meV}$. On the other hand, the off-diagonal elements induce both population relaxation and pure dephasing that mainly result in a long time decay of the excitonic population, resulting in a temperature dependent broadening of the ZPL given by $\Gamma(T)$. This broadening is negligible at low temperatures ($< 1 \text{ } \mu\text{eV}$) and increases to $\sim 50 \text{ } \mu\text{eV}$ at 50 K [109]. Phonon scattering has recently been shown to play an important role in cavity-QED experiments by increasing the effective coupling of an off-resonant CM and a QD[111–115].

1.4 Photonic crystal cavities

A photonic crystal (PhC) is a macroscopic medium with a periodic dielectric function that modifies the propagation of light. The periodicity of the dielectric material can be one, two or three dimensional as illustrated in Fig. 1.11. In a macroscopic, isotropic dielectric medium in the linear regime, the electric field $\mathbf{E}(\mathbf{r})$ and magnetic field $\mathbf{H}(\mathbf{r})$ are governed by

$$\nabla \times \left(\frac{1}{\epsilon(\mathbf{r})} \nabla \mathbf{H}(\mathbf{r}) \right) = \frac{\omega^2}{c^2} \mathbf{H}(\mathbf{r}) \quad (1.20)$$

$$\nabla \cdot \mathbf{H}(\mathbf{r}), \quad \nabla \cdot [\epsilon(\mathbf{r}) \mathbf{E}(\mathbf{r})] \quad (1.21)$$

Chapter 1. Introduction

with ω and c the frequency and speed of light and $\epsilon(\mathbf{r})$ the dielectric function of the medium. Equation (1.20) is the *master equation* and constitutes an eigenvalue problem. When the dielectric function is periodic in space, the master equation presents

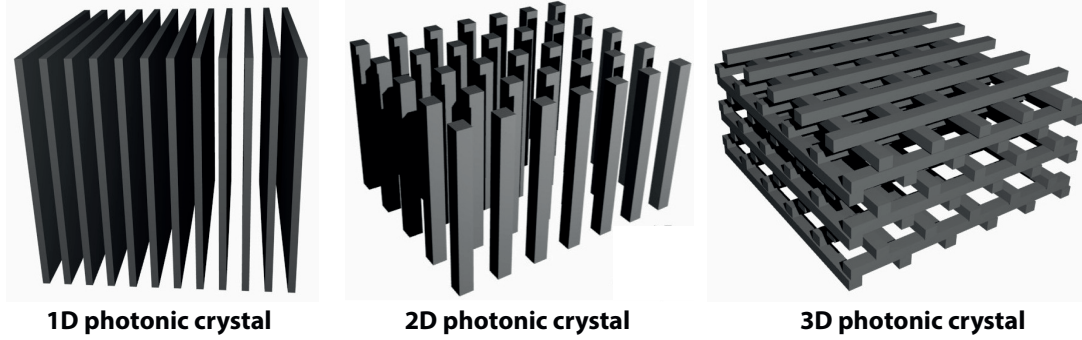


Figure 1.11: illustration of 1D, 2D and 3D PhCs formed of a dielectric material (grey) surrounded by air.

similitudes to the Schrödinger equation describing the motion of electrons in the periodic potential of a crystal. In essence, given the wavelike properties of electrons in the quantum regime, these two problems describe the motion of waves in a periodic medium. In crystals, the electrons scatter coherently on the periodic potential of the crystal lattice leading to formation of a band structure describing the directions of propagation allowed for given electron energies. This leads to a set of continuous band functions $E_n(\mathbf{k})$ that specifies the energies of the electrons as a function of their wave vectors. In between two bands, there is a range of energies for which the propagation is forbidden regardless of the direction of propagation. Such an energy band gap can be found for example between the conduction and valence bands of a crystal. In PhCs, the electrons are substituted by electromagnetic waves and the crystal lattice by a periodic dielectric medium. The electromagnetic field then scatters coherently at the interface of two dielectric regions of different refractive index. The periodicity of the dielectric medium allows to write the solutions of equation (1.20) in the Bloch form, in analogy to the Bloch functions of electrons in a periodic crystal

$$H_{\mathbf{k}}(\mathbf{r}) = \mathbf{u}_{\mathbf{k}}(\mathbf{r})e^{i\mathbf{k}\cdot\mathbf{r}} \quad (1.22)$$

where $\mathbf{u}_{\mathbf{k}}(\mathbf{r})$ has the same periodicity as the dielectric function. The energies of the these harmonic modes are given by continuous band functions $\omega_n(\mathbf{k})$ that specify the energies of the electromagnetic field as a function of its direction of propagation. The range of energies for which the propagation is forbidden are called *photonic band gaps*. An example of a band structure for a 3D PhC is shown in Fig. 1.12 (a). Photonic band gaps can only appear for light propagating in the direction of the medium's periodicity. This means that complete photonic band gaps preventing the propagation of light in

all three directions of space can only occur in 3D PhCs.

The initial mentions of the possibility to control light propagation with periodic dielectric date back to 1887[116] and 1972[117]. However the intensive study of PhC structures was initiated by the papers of E. Yablonovitch[118] and S. John[119] in 1987. Soon after, the first 3D PhCs with a complete photonic band gap were realized experimentally in the microwave[120] and infrared[121] energy regions. Despite these achievement it was clear that the fabrication of 3D PhCs is technologically challenging. Lower dimensional, easier to fabricate, PhC structures have thus triggered some interest. Among those are PhC slabs that are presented in the following section.

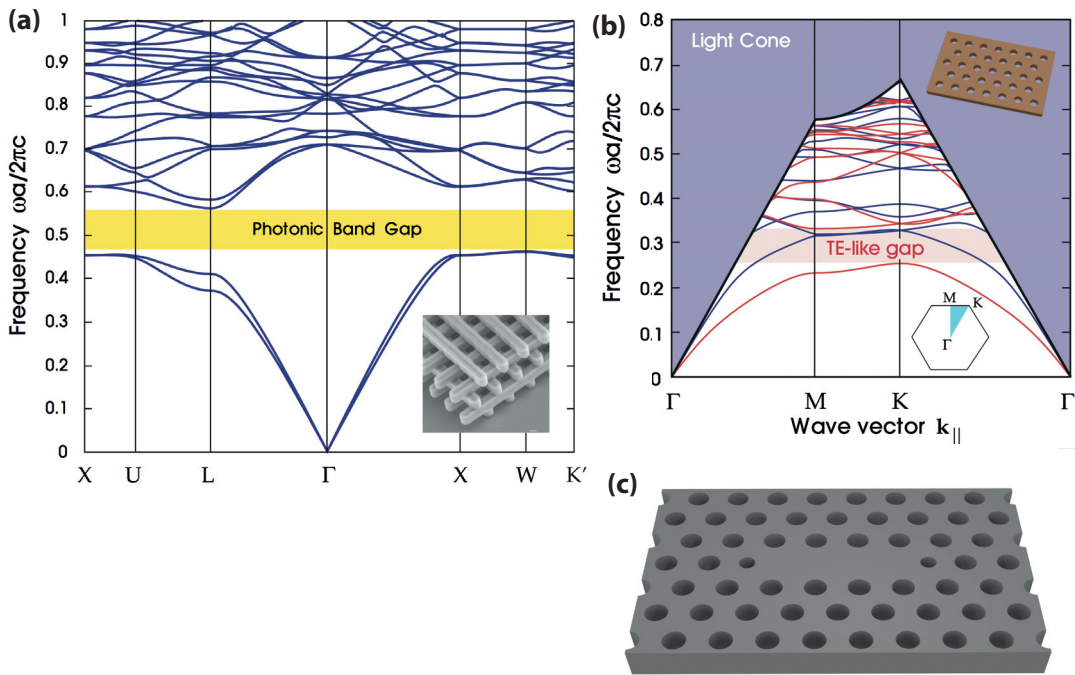


Figure 1.12: (a) The photonic band structure for the lowest bands of a woodpile structure (inset) with $\epsilon = 13$ logs in air. The photonic band gap is indicated in yellow. (b) Band diagrams for photonic crystal hole slab suspended in air (inset). The blue shaded area is the light cone. TE-like bands are shown in red and TM-like bands in blue. The TE-like photonic band gap is indicated by the red shaded region. (c) Illustration of an L_3 PhC slab cavity. (a) and (b) Republished with permission of Princeton University Press, from [122]; permission conveyed through Copyright Clearance Center, Inc.

1.4.1 Photonic crystal slab

Photonic crystal slabs rely on a 2D PhC and index guiding to confine light. A PhC crystal slab consisting of a triangular lattice of holes in a dielectric material of finite thickness surrounded by air is illustrated in the inset of Fig. 1.12 (b). In this geometrical configuration, the propagation of electromagnetic waves with certain energies will be forbidden in plane by the 2D PhC. In addition, the finite thickness of the slab will limit

the propagation of electromagnetic waves in certain directions due to total internal reflexions. This leads to the band structure shown in Fig. 1.12 (b) that displays an incomplete band gap. The band gap is incomplete because the slab confines only modes satisfying $\omega < ck_{\parallel}$, where k_{\parallel} is the component of the wavevector parallel to the PhC slab. When $\omega > ck_{\parallel}$, Snell's law is satisfied, leading to a continuum of modes indicated by the shaded region in Fig. 1.12 (b) that can escape the slab. These modes are said to be in the light cone. The limit of the light cone corresponding to $\omega = ck_{\parallel}$ is indicated by a thick dark line. Below the light line is the band structure corresponding to modes localized within the PhC slab. These modes can be classified according to their mirror symmetry with the $z = 0$ plane into TE-like (even) and TM-like (odd) modes[122]. As can be seen in Fig 1.12 (b), a band gap exists only for TE-like modes. The TE bands located above and below the band gap are generally referred to as the dielectric and air bands because they correspond to modes with electric field localized in the dielectric and air regions of the PhC respectively.

Photonic crystal slab defect cavities

Localization of light can be achieved in PhCs by introducing a defect in the periodicity of the dielectric function. In a PhC slab, this can be achieved for example by removing one or several holes of the triangular lattice as illustrated in Fig. 1.12 (c), forming a cavity-like structure. Due to the additional dielectric material present where the hole was removed, a mode from the air band will be pulled down into the band gap. This implies that the cavity mode electromagnetic field will be bound to the defect since its propagation is prohibited by the PhC and index guiding. For a perfect 3D PhC, a defect mode is completely confined. For a 2D PhC slab however, the localized mode has intrinsic radiative losses due to the incomplete PhC band gap. The losses of such a defect cavity mode are generally described by the ratio of the mode frequency ω_m to its loss rate κ_m , known as the cavity quality factor $Q = \omega_m/\kappa_m$. Q represents a dimensionless number that quantifies the number of optical periods occurring before the mode energy decays by $e^{-2\pi}$. A large quality factor thus characterises a cavity with low radiative losses. PhC slab defect cavities are appealing for cavity-QED experiments because of their small mode volumes and high quality factors. Reaching high quality factors requires an optimization of the cavity design to reduce losses[46, 123].

In this work we coupled pyramidal QDs to L_3 defect cavity modes[124]. L_3 cavities are obtained by removing three holes of a triangular PhC slab as depicted in Fig. 1.12 (c). The properties and mode structures of the L_3 cavities used in this work are presented in subsection 2.2.3.

1.5 Cavity quantum electrodynamics with semiconductor quantum dots

The important progress in the fabrication of semiconductor QDs and nanocavities have enabled the study of cavity-QED effects in solid-state based devices. After the initial observation of enhanced QD spontaneous emission in micropillar cavities, multiple experiments studied the influence of the Purcell effect on QDs in PhC[69, 111, 125–132] or micropillar[16, 133–137] cavities by measuring the lifetime dynamics or spectra of QDs interacting with a CM. Time-resolved measurements give a direct estimation of the Purcell enhancement by comparing the QD lifetime when coupled to the CM to the QD lifetime in the bulk semiconductor. On the other hand, measuring the intensity of the QD spectra for different QD-cavity energy detunings can also give access to the Purcell factor; but this is not straightforward since the increased intensity of the QD emission when in resonance with the CM can be dependent on the structure geometry and QD pumping rate[133].

In section 1.2, the Purcell factor was defined as $F_p = \frac{3\lambda^3 Q}{4\pi^2 V}$, which describes the ratio between the bare emitter lifetime τ_0 and the lifetime τ_{cav} of the emitter optimally coupled to the CM: $F_p = \tau_0/\tau_{cav}$. This expression assumes an ideal cavity, and results in a Purcell factor of 0 (complete suppression of the emitter emission) when the emitter is not coupled to the CM, for example if it is placed on a node of the cavity confined electric field. Real cavities, in particular semiconductor nanocavities, can support leaky modes, which allow for the emitter to emit even when uncoupled to the CM[138]. This leaky mode emission is characterised by a lifetime τ_{leak} and leads to modified ratio between the bare and coupled emitter lifetimes[47, 133].

$$\frac{\tau_0}{\tau(\delta)} = \frac{\tau_0}{\tau_{cav}(\delta)} + \frac{\tau_0}{\tau_{leak}} = F_p(\delta) + \frac{\tau_0}{\tau_{leak}} \quad (1.23)$$

where a dependence on the emitter-CM detuning δ is introduced. Note that for $\delta \rightarrow \infty$, $F_p = 0$ and $\tau(\delta = \infty) = \tau_{leak}$.

Table 1.1 summarizes measured decay times τ , τ_0 and τ_{leak} for QDs coupled to PhC and micropillar cavities reported in the literature. The corresponding Purcell factor calculated with (1.23) and the inhibition factor τ_{leak}/τ_0 are also indicated in table 1.1. For PhC cavities the inhibition factor varies from 2 – 9, indicating an important inhibition of the QD spontaneous emission by the PhC band gap. For self-assembled QDs, controlling the inhibition of the spontaneous emission is difficult because it is highly dependent on the position of the QD in the cavity. Inhibition factors > 1000 have been predicted for H1 cavities but require specific positioning of the emitter dipole inside the cavity[139]. In these experiments the enhancement of the emission by the CM was observed on single QD spectral lines, with Purcell factors up to ~ 15 . Although these values are encouraging, they are well below the theoretical maximal Purcell

Chapter 1. Introduction

Table 1.1: Non exhaustive list of QD decay rates reported in the literature measured for QDs coupled to PhC and micropillar cavities. τ_0 is the bulk QD decay rate, $\tau(\delta = 0)$ the decay rate of the QD in resonance with the CM transition and τ_{leak} the decay of the QD when far-off resonant from the CM. The last two columns show the corresponding Purcell factors and inhibition factor τ_{leak}/τ_0 .

PhC cavity					
	τ_0 [ns]	$\tau(\delta = 0)$ [ns]	τ_{leak} [ns]	$F_p(\delta = 0)$	τ_{leak}/τ_0
Chang et al. [126]	0.65	0.21	2.52	2.8	3.9
Gevaux et al. [127]	0.98	0.086	4.38	11.2	4.5
Balet et al. [128]	1.2	0.15	3.6	7.7	3
Hennessy et al. [69]	1	0.06	8.7	16.5	8.7
Luxmoore et al. [130]	1.1	0.64	2.5	1.3	2.3
Micropillar cavity					
Munsch et al. [133]	0.8	0.2	-	3	-
Jakubczyk et al. [135]	0.422	0.063	-	5.7	-
Gazzano et al. [16]	1.3	0.265	-	3.9	-

factors for PhC defect cavities ($F_p \sim 400$ for $Q \sim 6000$ and mode volume $0.04(\lambda/n)^3$). This discrepancy is generally explained by a non-ideal alignment of the QD exciton dipole and cavity electric field vector or a poor spatial overlap between the QD and CM field pattern[125, 128]. For micropillar cavities, the inhibition factor is not indicated because the decay times into the leaky modes is generally assumed to be equal to bulk QD decay time, which signifies that the micropillar structure does not alter the uncoupled QD emission significantly[133]. For micropillar cavities the Purcell factor is expected to be lower than for PhC cavities, due to the larger optical mode volumes of micropillar structures. This can explain the slightly lower Purcell factors reported in table 1.1.

The strong coupling regime has also been studied in semiconductor QD-nanocavity systems[44]. This was an important step since it allowed to enter the single quanta regime in which single-photon non-linear effect arise, and was an opportunity to get direct measurements of QD-cavity coupling strengths. In the strong coupling regime, an anti-crossing is observed between the QD and CM transitions when the QD-CM detuning is varied. This minimum splitting between the two transitions corresponds to the vacuum Rabi splitting ΔE_{RS} and is related to the coupling strength g by[147]

$$g = \sqrt{\frac{\Delta E_{RS}^2}{4\hbar^2} + \frac{(\kappa - \gamma)^2}{16}} \quad (1.24)$$

with κ and γ the cavity and QD decay rates. Table 1.2 summarizes coupling strength values reported in the literature, extracted from measurements of vacuum Rabi splitting, along with the cavity Q factors and QD linewidths. The coupling strength values

1.5. Cavity quantum electrodynamics with semiconductor quantum dots

Table 1.2: Non exhaustive list of Q factors, QD linewidths and QD-cavity coupling strength g reported in the literature and obtained experimentally in the strong coupling regime.

PhC cavity			
	Q factor	QD linewidth [μeV]	g [μeV]
Yoshie et al. [52]	6000	89	85
Hennessy et al. [69]	13300	35	76
Thon et al. [140]	9200	53	71
Laucht et al. [141]	17600	20	59
Englund et al. [142]	11200	9	86
Luxmoore et al. [130]	8000	30	106
Ota et al. [143]	20000	3	40
Micropillar cavity			
Reithmaier et al. [39]	7350	72	80
Press et al. [144]	15200	54	35
Münch et al. [145]	11000	37	43
Keldysh et al. [146]	12000	50	60

range from $40\mu eV$ to $100\mu eV$ and are higher in average for PhC cavities. The coupling strength being proportional to the inverse of the cavity mode volume, higher values are easier to reach with the smaller mode volumes of PhC cavities.

These weak coupling and strong coupling cavity-QED effects observed with semiconductor QD-cavity systems were an indication that they are, at least to some extent, analogous to atom-cavity systems. However, significant differences with atomic systems were observed in experiments. One of the most striking features of solid-state QD-cavity systems is the pronounced spectral signature of the CM that persists even when the spectral overlap of the QD and CM transitions become negligible[148–152]. Furthermore, in the strong coupling regime, some experiments reported the observation of a triplet in the QD-cavity spectrum[69, 143] instead of the usual vacuum Rabi splitting doublet observed in atom-cavity experiments. These surprising results sparked a series of ongoing theoretical and experimental investigations to find explanations for these puzzling novel phenomena.

The off-resonant CM emission was found to be persistent for detunings extending to $45 meV$ [153] for self-assembled QD systems. In addition, this *far-off resonant* CM emission was found to be anti-correlated with the QD emission, proving that the CM feeding is mediated by the QD transition[69, 148]. However, the CM emission did not show any significant quantum correlations[153]. The ideal representation of a QD with a discrete density of states owing to its 3D confinement fails to account for these observations. Indeed, the QD can host a large number of electron-hole pairs in its higher energy state (for example p-states or d-states), that undergo Coulomb

interactions. For self-assembled QDs, the 3D-confined carriers can efficiently interact with delocalized electrons and holes in the 2D wetting layer. This interaction leads to the formation of extended QD excitonic states that go beyond the atomistic picture[154]. The hybridisation of localized QD states with delocalized wetting layer states leads to the formation of a broadband quasi-continuum of states that give rise to a QD background emission[148, 153, 155]. This broadband background emission can sustain the CM emission for large detunings and also manifests in the time-domain by a fast decaying CM emission, uncorrelated with the s-state transitions, that decays with a rate of the same order as QD excited states[152]. The hybridisation of QD and wetting layer state is an elaborate N-body problem that complicates the interpretation of cavity-QED experiments. In order to diminish its effects the QD s-states or p-states can be pumped resonantly without populating the 2D wetting layer[115, 142]. The application of a electric field bias to the QD-cavity structure has also been shown to strongly suppress off-resonant CM emission by depopulating high energy and wetting layer states[156].

This far-off resonant CM emission is not intrinsic to semiconductor QDs. It is a feature specific to self-assembled QDs nucleating on top of a 2D wetting layer. As mentioned earlier, no 2D wetting layer is formed during the growth of the pyramidal QDs used in this work. This results in the absence of QD background emission and far-off resonant QD-cavity coupling in their photoluminescence spectra[113]. In section 5.1.3 we show that this absence of background emission also manifests in the dynamics of the coupled QD-cavity system, in the form of a strong temporal correlation between the CM and s-states QD transitions emission[157]. Although pyramidal QDs nucleate in the vicinity of 1D QWR states, their influence of the QD emission is shown to be nonexistent for low excitation powers, owing to the large energy difference and absence of hybridization between the localised QD states and 1D delocalized state.

Although the continuum of states generated by the interaction of self-assembled QD states with wetting layer states has been shown to be beneficial to achieve lasing with single QD-cavity structures, it overshadows other interesting effects intrinsic to solid-state QD-cavity systems. In particular, the pure dephasing and phonon scattering decoherence mechanisms mentioned in subsection 1.3.5 are expected to greatly impact the QD-cavity interaction, leading to optical properties differing from atomic-cavity systems. Even in the weak coupling regime, decoherence effects lead to off-resonant CM emission and influence the QD polarization. Working with wetting-layer free semiconductor QDs is thus a necessity to conduct a proper investigation of these solid-state effects.

The pure dephasing induced by rapidly fluctuating electrical charges in the vicinity of the QD (see subsection 1.3.5) was predicted to alter the QD-cavity coupling mechanism[97–100, 158]. Several theoretical studies showed that pure dephasing modifies the spectrum of a QD-cavity system in the weak coupling regime, shifting the intensity

1.5. Cavity quantum electrodynamics with semiconductor quantum dots

distribution from the QD peak to the off-resonant CM peak[98, 100]. The QD-cavity effective coupling rate is increased by pure dephasing, leading to a more efficient off-resonant cavity feeding[99]. This results in a pronounced CM off-resonant emission for detunings extending to a few meV . In the strong coupling regime, the vacuum Rabi splitting is blurred by the damping of the coherent Rabi oscillations induced by pure dephasing[97, 98], and the emission intensity is shifted towards the cavity energy for finite detunings. Pure dephasing combined with the multi-excitonic nature of semiconductor QDs was also brought forward as an explanation for the observation of a spectral triplet at resonance in the strong coupling regime[158, 159]. Pure dephasing induced by the charged environment of the QD thus plays an important role in the QD-cavity interactions. A quantitative analysis of its impact remains however difficult with self-assembled QDs as additional decoherence mechanisms related to wetting layer continuum states can come into play even when pumping the system resonantly[160].

Another source of off-resonant cavity feeding comes from the interaction of the QD states with acoustic phonons. As mentioned in subsection 1.3.5, phonon scattering generates a broadband background emission around the discrete QD transition. This broadband emission can be enhanced by the Purcell effect, leading to a significant off-resonant CM emission. In some studies, phonon-mediated cavity feeding was taken into account in an effective manner by adding a pure dephasing rate to the QD dynamics[142, 161]. This effective treatment however is not sufficient to explain the asymmetry of phonon scattering with respect to detuning. As mentioned in subsection 1.3.5, this asymmetry stems from different efficiencies of phonon absorption and emission at low temperatures. In a coupled QD-cavity system, a detuned QD transition can overcome the energy mismatch by absorbing or emitting a phonon leading to the emission of a photon at the CM frequency[115]. At low temperatures, this process is less efficient when the QD is red-shifted from the CM since the absorption of a phonon is inhibited by the low population of the phonon bath. The off-resonant CM emission is limited by the extent of the phonon sidebands resulting in cavity feeding over a small detuning range of $\pm 3 meV$. The influence of phonon scattering on the off-resonant CM emission was observed in several semiconductor QD-cavity experiments[113–115, 162] and thoroughly investigated theoretically[112, 163–170]. This phonon scattering was shown to induce a pulling of the cavity frequency towards the QD transition energy[171] and give rise to an asymmetry with respect to detuning of the QD decay rate[111, 131]. In recent works, phonon scattering was shown to assist the population inversion of a single QD[131] and relax the QD-cavity resonant condition required to obtain high brightness single photon sources in micropillars[172]. As emphasized by the work of Valente et al. [171], observing the fine features of phonon scattering requires a full control of the QD-cavity coupling. Wetting-layer-free site-controlled emitter such as pyramidal QDs are thus promising candidates to continue the investigation of QD-cavity phonon-mediated coupling.

1.6 Thesis goals and outline

The goal of this thesis is to present an experimental study of a solid-state cavity-QED platform comprising of site-controlled QDs and PhC cavities. This study was initiated by the article of Gallo et al.[88] that demonstrated the coupling of a site-controlled pyramidal QD to an L_3 PhC cavity. The fabrication technique was then optimized by M. Calic, enabling a statistical optical study of up to two or more site-controlled QDs embedded in a PhC cavity[173–175]. In this work we continue the investigation of these promising structures, starting with the fundamental component of cavity-QED system: a single quantum emitter inside an optical cavity. As reported by M. Calic et al.[113], unlike previous cavity-QED systems based on self-assembled QDs, site-controlled QDs embedded in PhC cavities corresponds to a single confined exciton interacting with a CM, making it closer to an ideal TLS emitter interacting with an optical mode. We rely on this feature to investigate the impact of solid-state decoherence mechanisms on QD-cavity coupling. The study is then extended to more complex QD-cavity structures. This is made possible by the deterministic fabrication approach that enables a controlled positioning of each QDs in the photonic structure, as well as a record control of the QD emission energy. This gives the opportunity to study structures with multiple QDs coupled to the same CM or multiple QDs coupled to arrays of optical cavities. The thesis is therefore organized as follows.

Chapter 2 provides a description of the experimental and modelling techniques used in this work. The optical setups used to perform photoluminescence measurements are presented, along with the modeling tools used to analyse the optical properties of PhC structures. This chapter also provides a description of the fabrication steps involved in the realization of pyramidal QDs and their integration in PhC cavities.

Chapter 3 briefly reviews the theoretical formalism used in cavity-QED to describe the interaction of a TLS with a CM. The extension of the ideal TLS-cavity model to a more realistic model describing the interaction of a QD with a CM in the presence of solid-state decoherence mechanisms is discussed. Owing to the TLS-like properties of pyramidal QDs, a theoretical model including QD dephasing processes and aiming to reproduce the spectra of one or more pyramidal QDs embedded in L_3 PhC cavities is proposed.

Chapter 4 presents an optical study of single, isolated site-controlled pyramidal QDs that aims to establish the characteristics of their luminescence. The QD spectral features are probed with photon-correlation and time-resolved measurements and particular attention is paid to the binding energies of QD excitons. This study provides a rigorous identification of the QD s-state features and demonstrates the high reproducibility of the QD emission. The $2X$ binding energy is found to be either positive or negative depending on the QD size and QDs with vanishing $2X$ binding energies are evidenced.

Chapter 5 presents a study of site-controlled pyramidal QDs embedded in the same PhC cavity. The polarization resolved emission of a single QD coupled to a PhC cavity mode is investigated as a function of QD-cavity detuning. Although this experiment is performed in the weak coupling regime, the emission of the coupled system exhibits complex polarization features that are influenced by solid-state decoherence mechanisms. The emission spectra is compared to the theoretical model exposed in chapter 3, giving important insights into the impact of pure dephasing and phonon scattering on the QD-cavity coupling mechanism. A structure comprising of two QDs embedded in the same PhC cavity is then investigated showing that although both QDs are simultaneously coupled to the CM, no collective effects are registered.

Chapter 6 explores more complex photonic structures comprising of linear and 2D arrays of PhC cavities. Delocalized optical modes are evidenced by using a novel approach that consists in exciting the photonic structure with site-controlled QWR light sources. The impact of fabrication-induced disorder in these structures is discussed. The coupling of two site-controlled QDs embedded in two coupled PhC cavity is demonstrated.

2 Experimental and modelling techniques

This chapter presents the experimental and modelling tools used in this work, as well as the fabrication process of the QD-cavity structures investigated in chapters 4, 5 and 6. Section 2.1 details the photoluminescence measurement techniques used to study the QD-cavity structures. The numerical simulation methods used to calculate the field pattern and energies of photonic crystal (PhC) cavity modes are briefly presented in section 2.2. Finally, the fabrication of site-controlled pyramidal QDs and their integration in L_3 PhC cavities are explained in section 2.3.

2.1 Photoluminescence spectroscopy

Optical spectroscopy relies on the interaction of a sample or structure with light to extract the structure's spectral or dynamical characteristics. A commonly employed technique to study semiconductor nanostructures is *photoluminescence (PL) spectroscopy*. It requires the excitation of the nanostructure by a resonant or off-resonant laser source followed by the collection of the structure's luminescence, thus gaining insights on its optical properties.

2.1.1 Principle of micro-photoluminescence measurements

The study of sub-micron sized semiconductor nanostructures such as QDs, QWRs or nanocavities requires the possibility to address individual devices, which is achieved by focusing the laser-source to a μm sized spot using a microscope objective. The photons emitted by the nanostructure are then collected through the same objective. This procedure is called *micro-photoluminescence (μ -PL)* and is detailed here for the specific case of semiconductor QDs.

The excitation of the QD can be done using either a resonant or non-resonant laser source. The former presents the advantage of targeting specific electronic states

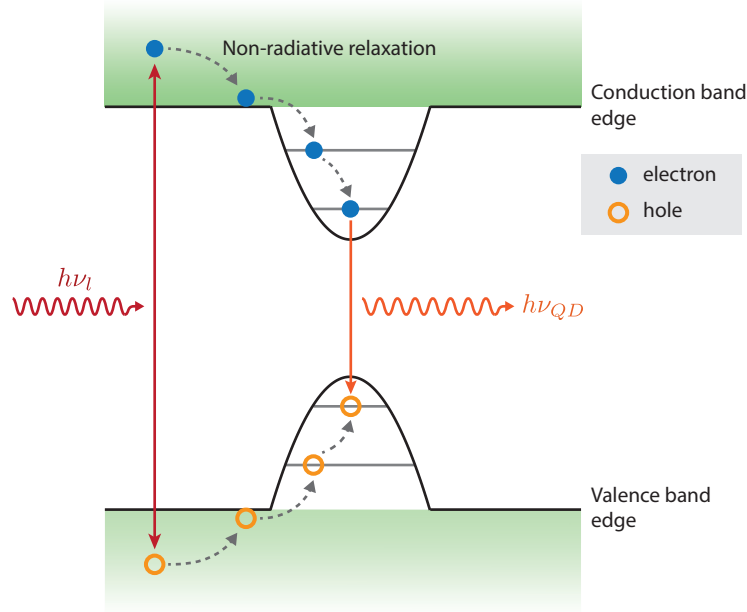


Figure 2.1: Single QD photoluminescence measurement. Electron and hole pairs are excited above band gap with an incident laser beam of energy $h\nu_l$. The electron and holes relax non-radiatively in the lower energy states of the QD and recombine emitting a photon of energy $h\nu_{QD}$.

and allows the coherent manipulation of states[176, 177]. In this thesis we rely on non-resonant excitation which uses a laser source with incident photon energy $h\nu_l$ greater than the band gap of the QD barrier material (Fig. 2.1). In this way electronic carriers are generated in the vicinity of the QD nanostructure. Those free electrons and holes relax to the QD band edge with a 1 ps time scale by interacting with lattice phonons[178]. The carriers can then be captured by the QD, and thermalize through phonon interaction into the low energy QD states. The intra-QD relaxation of carriers occurs at a slower rate because of the mismatch between the spacing of the discrete QD levels ($\sim 10\text{ meV}$) and the phonon energy dispersion. Indeed longitudinal-acoustic (LA) phonons efficiently interacting with the QD carriers have energies in the meV range (related to the inverse of the QD size) and longitudinal-optical (LO) phonons have an energy peak around 37 meV (in GaAs based materials). This was believed to lead to a large reduction of the relaxation rate referred to as the phonon-bottleneck effect[179]. However, it was shown that the interaction of LO phonons and carriers leads to the formation of polarons that relax efficiently inside the QD[180] on time scales of $\sim 10\text{ ps}$. This is consistent with most QD PL experiments that observed a rapid turn-on of the luminescence after non-resonant excitation.

Once the electrons and holes occupy the lower energy states of the QD, they recombine and a photon with energy $h\nu_{QD}$ is emitted by the structure (Fig. 2.1). This light is collected by the microscope objective and sent towards the detection path, where the

2.1. Photoluminescence spectroscopy

luminescence can be analyzed in different ways. The light frequency spectrum can be analyzed with the help of a spectrometer (subsection 2.1.2) or its photon statistics and temporal evolution can be investigated with photon correlation measurements (subsection 2.1.3) and time-resolved PL measurements (subsection 2.1.4), respectively.

2.1.2 Micro-photoluminescence setup

The experimental setup used for μ -PL measurements is sketched in Fig. 2.2. The excitation path consists of a Ti:sapphire laser (Spectra Physics Tsunami) in continuous wave (cw) mode optically pumped at 532 nm by a Nd:Yag laser (Spectra Physics Millennia). The Ti:sapphire laser beam set at $\lambda_l = 730\text{ nm}$ passes through a set of neutral density filters that allow a precise control of the laser beam power ($\sim 0.1\mu\text{W}$ resolution). The laser beam is then reflected on a 50:50 beam splitter, passes through a 90:10 beam splitter and is then focused on the sample's surface by a microscope objective (Zeiss, $50\times$ magnification, numerical aperture $\text{NA} = 0.55$ and focal length $f = 3.6\text{ mm}$), to a circular spot with a $1\mu\text{m}$ radius.¹

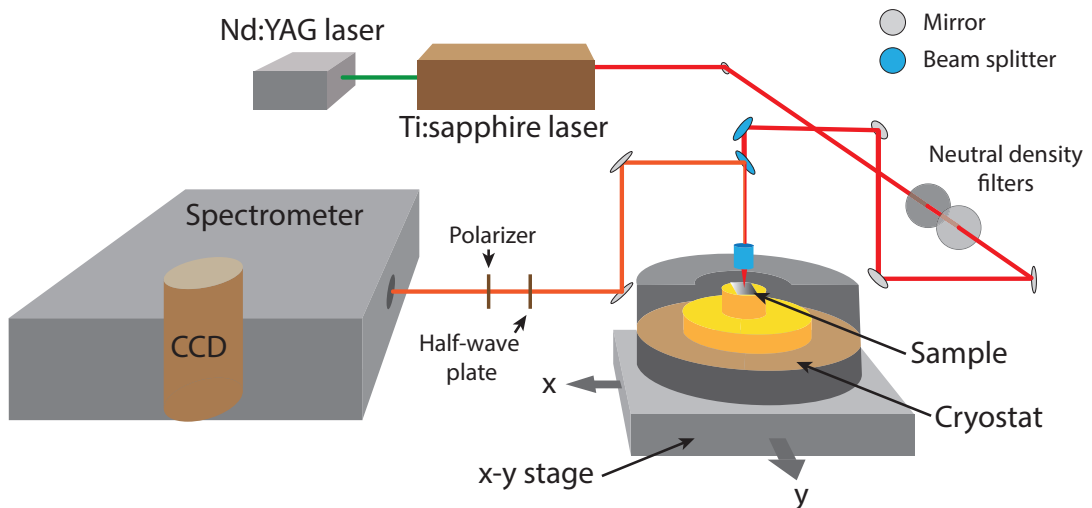


Figure 2.2: Schematic of our μ -PL setup. The optical excitation path is indicated in red and the optical detection is indicated in orange.

The sample is glued using silver paste to the cold finger of a helium flow cryostat (Janis ST-500 or Cryo Vac). The sample temperature is adjusted using a temperature controller (Lakeshore 331). The cryostat is placed on an XY stage which allows to control the sample's position in the horizontal plane with a spatial resolution better than $0.1\mu\text{m}$. A camera placed above the beam splitters and microscope objective allows to monitor the magnified image of the sample, helping with the in-plane alignment of

¹The excitation powers in this thesis are measured after the set of neutral densities, such that an indicated power of $1\mu\text{W}$ corresponds to a power density of 0.5 W/cm^2 on the sample's surface.

Chapter 2. Experimental and modelling techniques

the sample and focused laser beam spot.

The sample's luminescence is collected by the same microscope objective and sent to the detection path. The signal is analysed by a spectrometer (Jobin Yvon Triax 550 - 55 cm focal length, 1200 grooves/mm grating and 1.55 nm/mm dispersion) equipped with a nitrogen-cooled CCD (Jobin Yvon Spex Spectrum One - silicon photon detector with a 2048 × 512 pixel array), giving the PL signal's energy spectrum with a 80 μeV resolution.

Polarization resolved PL measurements

The PL spectrum can be resolved in linear polarization by placing a half-wave plate followed by a linear polarizer on the detection path. Given a polarized plane wave with electric field described by the Jones vector

$$\mathbf{E} = \begin{bmatrix} E_V e^{i\phi} \\ E_H \end{bmatrix} \quad (2.1)$$

where ϕ the phase difference between the vertical and horizontal field components E_V and E_H , respectively. The electric field intensity after it propagates through the half-wave plate and polarizer, with the half-wave plate fast axis forming an angle θ with the axis of the polarizer (see Fig. 2.3), is given by

$$I(\theta) = \frac{1}{2}(|E_V|^2 - |E_H|^2) \cos(4\theta) + \frac{1}{2}(|E_V|^2 + |E_H|^2) + E_V E_H^* \cos(\phi) \sin(4\theta). \quad (2.2)$$

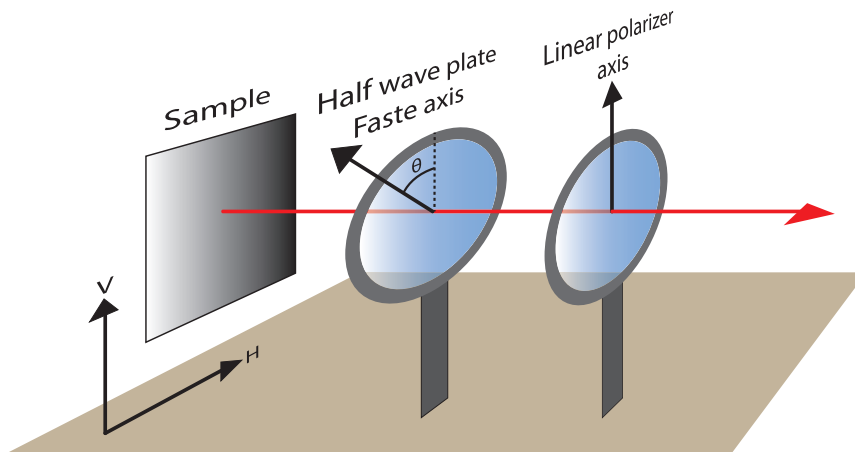


Figure 2.3: Schematic drawing of the polarization setup used to perform PL measurements resolved in linear polarization. The light path is indicated in red.

2.1. Photoluminescence spectroscopy

In the experiment, the spectra are resolved in linear polarization by measuring the spectrum for $\theta = 0$ and $\theta = \pi/4$

$$I_V \equiv I(0) = |E_V|^2 \quad \text{and} \quad I_H \equiv I(\pi/4) = |E_H|^2 \quad (2.3)$$

giving access to the vertical and horizontal electric field intensities. The degree of linear polarization (DOLP) is defined as

$$DOLP = \frac{I_V - I_H}{I_V + I_H}. \quad (2.4)$$

Note that $DOLP = 1$ if the light is fully vertically polarized and $DOLP = -1$ if it is horizontally polarized.

2.1.3 Photon correlation measurements

Studying the statistic of the light emitted by QDs provides an additional way to investigate their complex behaviour. The statistic nature of the light can be quantified by the *second order correlation* function which is introduced below[181, 182].

The second order correlation function

The second order correlation function is introduced as a way to quantify intensity correlations or intensity fluctuations. It is defined as

$$g^{(2)}(\tau) = \frac{\langle E^*(t)E^*(t+\tau)E(t)E(t+\tau) \rangle}{\langle E^*(t+\tau)E(t+\tau) \rangle \langle E^*(t)E(t) \rangle} = \frac{\langle I(t+\tau)I(t) \rangle}{\langle I(t+\tau) \rangle \langle I(t) \rangle} \quad (2.5)$$

where $E(t)$ and $I(t)$ are respectively the electric field and the intensity of the light at time t . This expression of $g^2(\tau)$ serves to quantify temporal coherence of a classical light beam. It can be shown that this function has to satisfy the following conditions

$$g^{(2)}(\tau = 0) \geq 1 \quad \text{and} \quad g^{(2)}(0) \geq g^{(2)}(\tau). \quad (2.6)$$

However, to describe the emission of quantum emitters such as atoms or QDs, this classical framework is not sufficient. To account for the quantum nature of light, the correlation function has to be rewritten in terms of quantum electric field operators $\hat{\varepsilon}^\pm(r, t)$ with positive and negative frequencies. The second order correlation function becomes

$$g^{(2)}(r_1, r_2; t_1, t_2) = \frac{\langle \hat{\varepsilon}^-(r_1, t_1) \hat{\varepsilon}^-(r_2, t_2) \hat{\varepsilon}^+(r_1, t_1) \hat{\varepsilon}^+(r_2, t_2) \rangle}{\langle \hat{\varepsilon}^-(r_2, t_2) \hat{\varepsilon}^+(r_2, t_2) \rangle \langle \hat{\varepsilon}^-(r_1, t_1) \hat{\varepsilon}^+(r_1, t_1) \rangle}. \quad (2.7)$$

This expression can be qualitatively understood as the probability of joint detection of one photon at space-time point (r_1, t_1) and one photon at space time point (r_2, t_2) . If

Chapter 2. Experimental and modelling techniques

we consider the simple case of a single mode of the quantized electric field with corresponding creation and annihilation operators \hat{a}^\dagger and \hat{a} , the second order correlation function for $\tau = t_2 - t_1 = 0$ reads

$$g^{(2)}(0) = \frac{\langle n | \hat{a}^\dagger \hat{a}^\dagger \hat{a} \hat{a} | n \rangle}{n^2} = 1 - \frac{1}{n} \quad (2.8)$$

where n is the number of photons in the mode corresponding to the Fock state $|n\rangle$. It becomes apparent from (2.8) that the second order quantum correlation function can take values smaller than one, in contrast to its classical counterpart.

The statistical nature of non classical light can be classified according to the value of $g^{(2)}(\tau)$ as follows

- $g^{(2)}(0) = 1$ coherent light,
- $g^{(2)}(0) > 1$ bunched light,
- $g^{(2)}(0) < 1$ antibunched light.

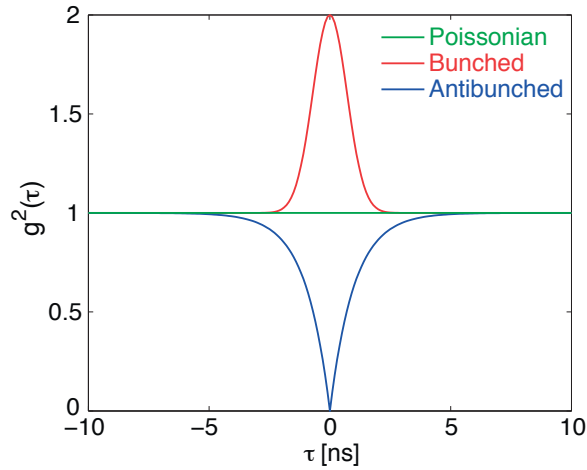


Figure 2.4: Second order photon correlation function $g^2(\tau)$ for Poissonian, bunched and antibunched light.

The corresponding second order functions are illustrated in Fig. 2.4. Perfectly coherent light has Poissonian photon statistics, meaning that the time interval between the detection of two photons is random. Bunched light on the other hand has photons clamped together in bunches. The probability to detect a photon is then greater short times after the detection of a previous photon. This is the case for thermal light emitted by, for examples, candles or gaz discharge lamps. The second order correlation functions of coherent and bunched light satisfy the classical limitations given by (2.6) and can thus be explained by considering only classical electromagnetic waves. Antibunched light, which has no classical counterpart, is characterised by a stream of

2.1. Photoluminescence spectroscopy

photons spread out in regular time intervals. This reduces the probability of detecting simultaneously two photons, leading to $g^{(2)}(0) < 1$. Single photon emitters like atoms or QDs exhibit antibunched light statistics[183–186]. Indeed, after the emission of a photon by an atom (or QD), it takes a finite duration of time to re-excite the atom and for the atom to emit the next photon. The rate at which the photons are emitted is thus the sum of the capture and emission rates, leading to a stream of photons separated by regular time intervals. For an ideal single photon emitter, the second order correlation function vanishes at $\tau = 0$.

Correlation measurement setup

The second order correlation function can be measured using a Hanbury Brown and Twiss (HBT) detection setup[187]. The HBT setup used for the measurements presented in this thesis is sketched in Fig. 2.5. Only the detection path of the setup described in subsection 2.1.2 is modified. The detection path now consists of 50:50 beam splitter that divides the QD emission into two output channels. Each channel leads to a spectrometer² equipped with an avalanche photodiode (APD) used for single photon detection (Perkin Elmer AQR series with a dark count rate of ~ 200 Hz and a detection efficiency of approximately 45%). Each APD is connected to a modulation domain analyser (Hewlett Packard 53310A) that generates a cumulative correlation histogram. The setup time response is ~ 700 ps.

During an HBT experiment, the stream of photons generated by the emitter is divided equally by the beam splitter such that half the photons impinge on APD_A and the other half on APD_B. Once a photon is detected by one of the APDs, the module domain

²The second spectrometer used in this experiment is a Jobin Yvon Triax 320 with 32 cm focal length, 1200 grooves/mm grating and a dispersion of 2.64 nm/mm.

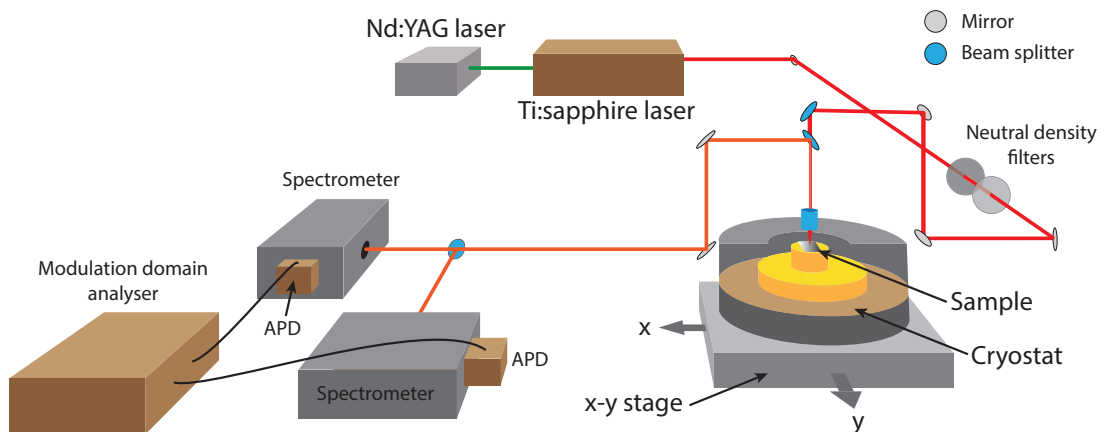


Figure 2.5: Schematic of the HBT setup used for photon correlation measurements. The optical excitation path is indicated in red and the optical detection is indicated in orange.

Chapter 2. Experimental and modelling techniques

analyser records the time before a photon is detected by the other APD. The number of events corresponding to the detection of a photon on APD_A at time t followed by the detection of photon by APD_B at time $t + \tau$ is registered by the module domain analyser. These events are accumulated in a histogram for each delay τ , giving a quantity proportional to the second order correlation function.

2.1.4 Time-resolved photoluminescence measurements

The time-resolved measurements shown in this thesis were obtained by modifying the PL setup described in section 2.1.2 in the following manner. The Ti:sapphire laser was operated in mode-locked mode, generating laser pulses at 80 MHz repetition rate and 3 ps pulse width. With the help of a beam splitter, a part of the excitation laser beam was sent to a photodiode. On the detection path, the spectrometer was equipped with a Picoquant APD (τ -SPAD-FAST with $150 - 200\text{ ps}$ photon timing resolution and a detection efficiency of 20% at 890 nm) for single photon counting. The APD and photodiode are both connected to a time-correlated single photon counting unit (Time Harp 260 TCSPC board with a 25 ps time bin width). This optical setup is sketched in Fig. 2.6

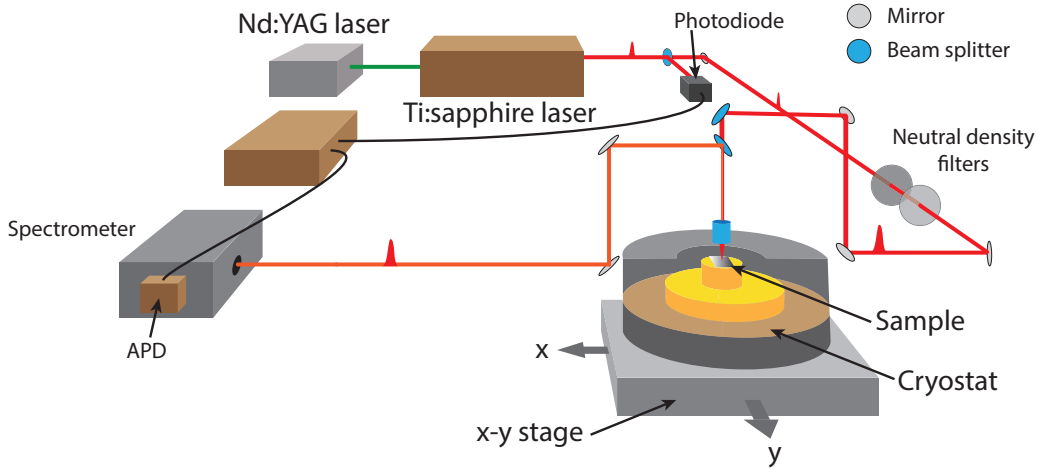


Figure 2.6: Schematic of our time-resolved PL setup. The optical excitation path is indicated in red and the optical detection is indicated in orange.

This setup allows to record the time dependent profile of the light emitted by the QD. After excitation of the QD by the laser pulse, the APD records the emission of a photon by the QD. The APD is synchronised with the photodiode that provides a reference timing for the laser pulse. The time-correlator unit records the delay between the laser pulse and the detection of a photon by the APD. This process is repeated many times during the integration window due to the high repetition rate of the laser, forming a histogram of the number of photon arrivals per time bin, which represents

2.1. Photoluminescence spectroscopy

the time-resolved emission of the emitter. This requires a low probability of registering more than one photon per cycle, which is generally the case for QDs. This process is schematised in Fig. 2.7.

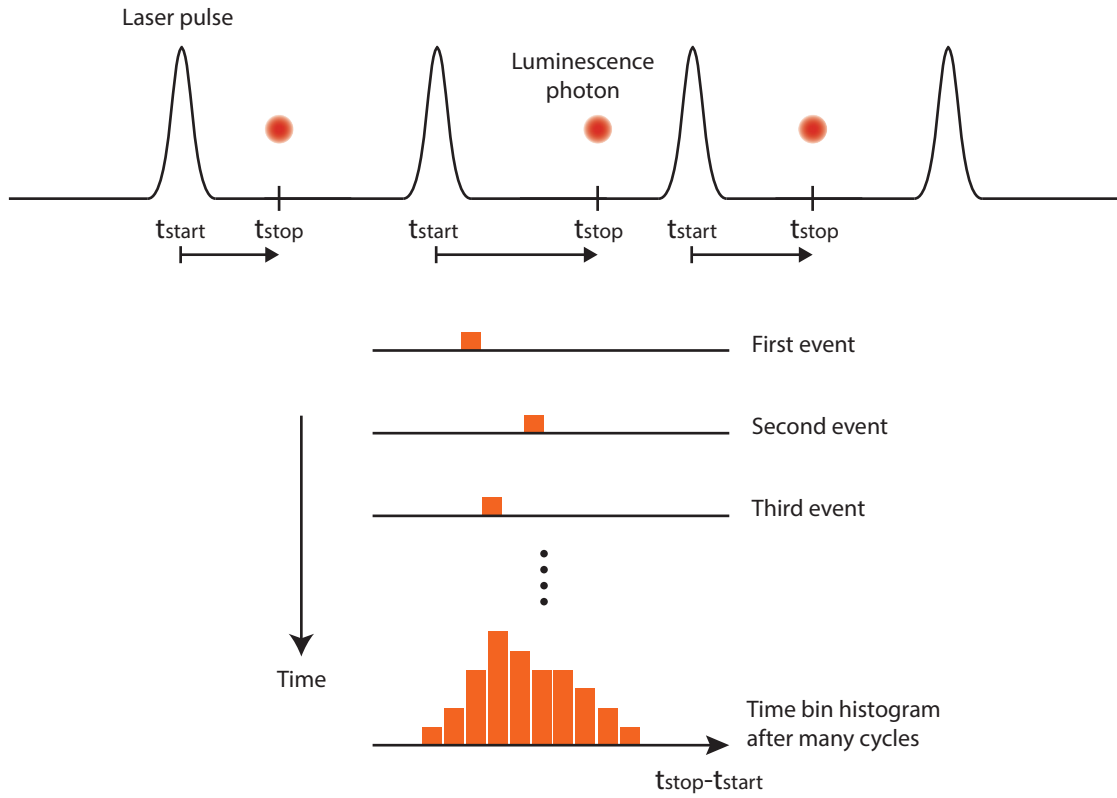


Figure 2.7: Schematic of the time-correlated single photon counting method used to measure the time-resolved emission of QDs.

2.2 Photonic crystal numerical simulations

The fabrication of QD-PhC cavity structures and the interpretation of their spectral features requires some knowledge of the PhC cavities properties. In particular, it is necessary to know the CM energies and electric field distributions. This can be achieved using several computational methods which can be separated in two main categories:

- **Frequency domain eigenproblems:** the problem is expressed as an eigenvalue problem $Mx = \omega^2 x$ which is solved to obtain the band structure $\omega(k)$ and associated electric fields for a given PhC geometry.
- **Time-domain problems:** the solutions of the problem are obtained by iterating the Maxwell equations to find the time evolution of the electromagnetic fields for a given PhC geometry.

In this thesis the PhC simulations are performed in the frequency domain for 2D problems and in the time-domain for 3D problems as detailed below.

2.2.1 2D finite-difference method

We apply the finite-difference method[188] to a PhC slab defect cavity surrounded by air (Fig. 2.8 (a)). The electromagnetic field is calculated only on the $z = 0$ symmetry plane of the slab (the calculation is limited to a 2D plane; see Fig. 2.8 (b)). The effect of the slab thickness is then accounted for by an effective dielectric constant $\epsilon_{eff}(\mathbf{r})$ for the dielectric material of the $z = 0$ symmetry plane, which is approximated by calculating the effective index of TE modes guided by a 1D slab with the same thickness as the PhC slab[189].

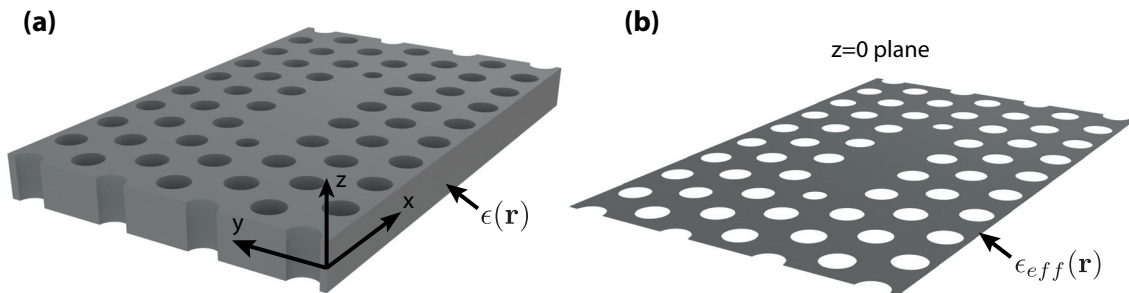


Figure 2.8: (a) Illustration of a PhC slab defect cavity. (b) $z = 0$ plane of the PhC slab.

The mirror symmetry with respect to the $z = 0$ plane implies that for $\mathbf{r} = (x, y, 0)$, the electromagnetic field can be classified into even and odd modes³ [122]

- **Even modes (TE):**

$$\mathbf{E}(x, y, 0) = (E_x(x, y, 0), E_y(x, y, 0), 0)$$

$$\mathbf{H}(x, y, 0) = (0, 0, H_z(x, y, 0))$$

- **Odd modes (TM):**

$$\mathbf{E}(x, y, 0) = (0, 0, E_z(x, y, 0))$$

$$\mathbf{H}(x, y, 0) = (H_x(x, y, 0), H_y(x, y, 0), 0).$$

Furthermore, as discussed in subsection 1.4.1, for a triangular lattice only TE modes have a photonic band gap, which implies we can restrict here to the determination of the TE mode field components to describe the modes localized inside the PhC cavity. These field components are obtained by solving the Maxwell eigenequation (see section 1.4)

$$\nabla \times \frac{1}{\epsilon_{eff}(\mathbf{r})} \nabla \times \mathbf{H} = \left(\frac{\omega}{c}\right)^2 \mathbf{H} \quad (2.9)$$

for the H_z component using a 2D finite-difference-frequency-domain (FDFD) solver. This implies that the unknown functions of the problem $f(x)$ are given by their values at discrete points on a cartesian grid $f_{n,m} = f(n\Delta x, m\Delta y)$ and the derivatives are approximated by $df_{n,m}/dx = (f_{n+1,m} - f_{n-1,m})/2\Delta x$. Equation (2.9) is written in the matrix form and solved using a numerical eigenvalue solver*, yielding the TE modes energies and $H_z(x, y)$ field distribution. The corresponding E_x and E_y field distributions are calculated using the Maxwell equations. The CM energies calculated with this 2D method depend on the approximated dielectric constant $\epsilon_{eff}(\mathbf{r})$. An exact determination of the CM energies and the field distributions away from the $z = 0$ plane requires a 3D model. Nevertheless, the 2D finite-difference method is faster than a 3D simulation and provides in a single run a good approximation of the mode dispersion and field distributions.

*The code used in this thesis to perform 2D FDFD simulations was implemented on the Matlab platform by Dr. K. F. Karlsson.

³Even modes satisfy $(E_x(x, y, z), E_y(x, y, z), E_z(x, y, z)) = (E_x(x, y, -z), E_y(x, y, -z), -E_z(x, y, -z))$, $(H_x(x, y, z), H_y(x, y, z), H_z(x, y, z)) = (-H_x(x, y, -z), -H_y(x, y, -z), H_z(x, y, -z))$ and odd modes satisfy $(E_x(x, y, z), E_y(x, y, z), E_z(x, y, z)) = (-E_x(x, y, -z), -E_y(x, y, -z), E_z(x, y, -z))$, $(H_x(x, y, z), H_y(x, y, z), H_z(x, y, z)) = (H_x(x, y, -z), H_y(x, y, -z), -H_z(x, y, -z))$. The difference in the signs between \mathbf{E} and \mathbf{H} comes from the fact that \mathbf{H} is a pseudovector[190].

2.2.2 3D finite-difference-time-domain method

The most common method used for solving time-domain problems is the finite-difference-time-domain (FDTD) method[122]. This method is used to compute the time dependent propagation of the electromagnetic field. This requires to divide space and time into a grid of discrete points. The Maxwell equations are then solved on this grid iteratively by approximating the spatial and temporal derivative using finite differences. A "leap frog" scheme is used for the propagation in time, in which the electric field \mathbf{E} at time t is calculated from its value at time $t - \Delta t$ and the value of the magnetic field \mathbf{H} at a time $t - \Delta t/2$ and vice-versa for the calculation of the \mathbf{H} field. The structure of the Maxwell equations also implies that the electric(magnetic) field components are calculated from magnetic(electric) field components on different grid points. The most common spatio-temporal grid used for the numerical implementation of this iterative calculation is the *Yee grid*[191].

In a 3D computation, the PhC slab cavity is defined by the dielectric function $\epsilon(\mathbf{r})$ associated with each grid point. In contrast to the 2D method described in subsection 2.2.1, the 3D grid allows to compute the field components at any point of the PhC slab and even above and under the slab. To avoid undesired reflexions at the grid boundaries, the computational domain has to be large enough, or appropriate boundary conditions implemented at the boundary. The simulation then consists in applying a short pulse inside the cavity using one or several grid points as a source of electromagnetic field, and iterating the Maxwell equation for a sufficient number of time steps n so that only confined modes remain in the simulation. The Fourier transform of a field component $f(\mathbf{r}, n\Delta t)$ then gives the frequency response $f(\mathbf{r}, \nu)$ of the system. Localized modes appear as strong peaks in the frequency spectrum. Their losses can be obtained by measuring the peaks full width at half maximum (FWHM) $\Delta\nu$, related to the quality factor by $Q = \nu/\Delta\nu$. This method also allows to observe the time evolution of a CM field pattern.

The code used in this thesis to perform 3D FDTD simulations was implemented on the Matlab platform by Dr. K. F. Karlsson, using MUR absorbing boundary conditions [192]. The source was either a grid point located near the center of the cavity and at the center of the slab with an H_z field amplitude following a Gaussian modulated sin function, or an ensemble of grid points with H_z amplitudes given by one of the CM H_z field distribution computed using the 2D finite difference method.

2.2.3 L_3 photonic crystal cavities

The simulation methods presented in subsections 2.2.1 and 2.2.2 were used to compute the mode energies and electric field pattern of L_3 PhC defect cavities. These cavities are formed by removing three holes in a triangular PhC pattern, creating a linear defect

2.2. Photonic crystal numerical simulations

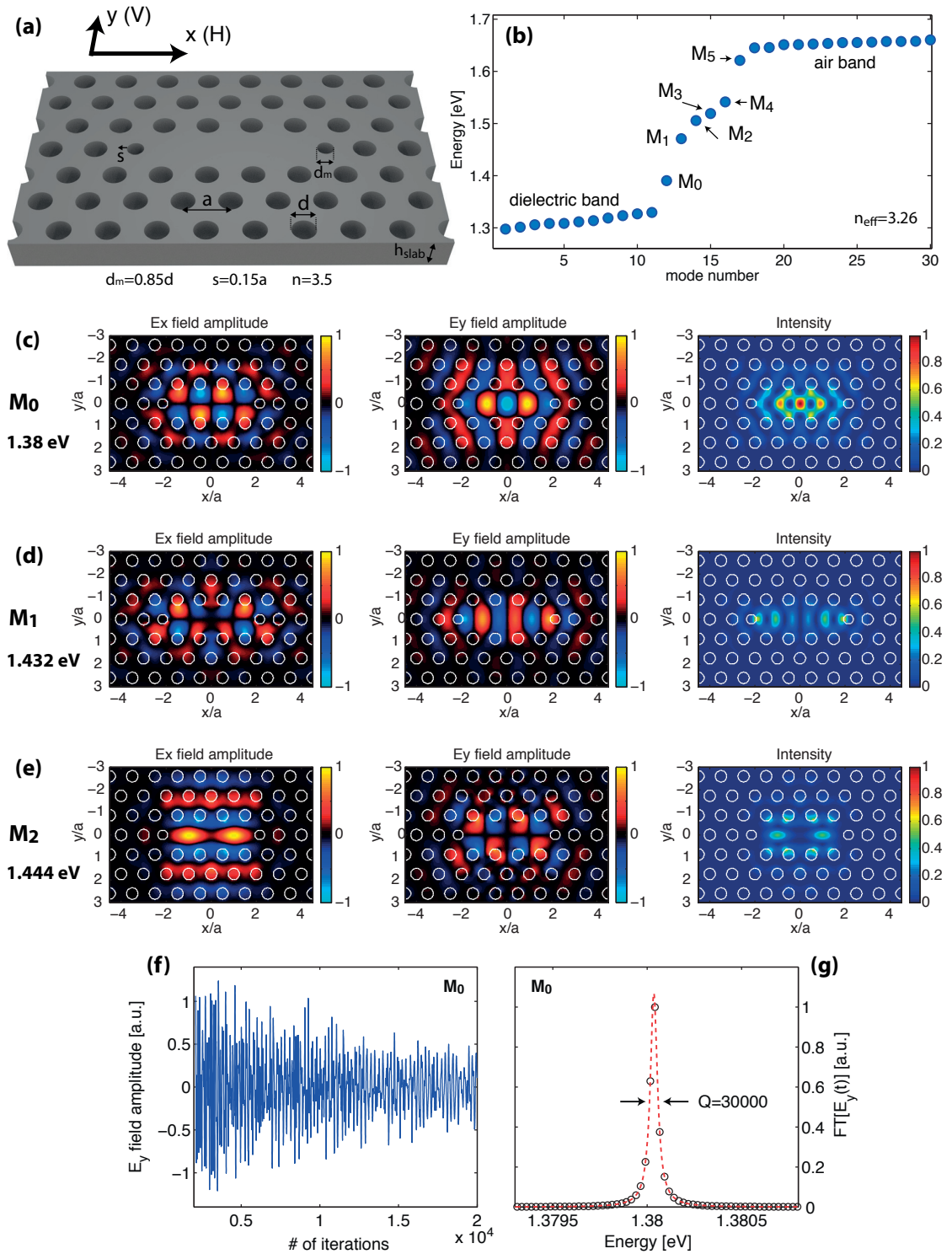


Figure 2.9: (a) Schematic of a modified L_3 PhC membrane cavity. (b) L_3 CM energies computed using a 2D finite-difference method. (c)-(e) Electric field and intensity spatial distributions of the three lowest energy CMs M_0 , M_1 and M_2 , calculated in the center of the slab using 3D FDTD. (f) E_y field amplitude of the M_0 as a function of the simulation iteration step in the center of the PhC slab cavity. (g) Simulated energy spectrum of the M_0 mode.

capable of confining light. In this work we use a modified cavity design in which the cavity side holes are shrunk and shifted as indicated in Fig. 2.9 (a) to increase the light confinement. The TE mode distribution of an L_3 cavity calculated using 2D finite-differences for a PhC pitch $a = 200 \text{ nm}$, hole diameter $r = 110 \text{ nm}$ and slab thickness $h_{slab} = 265 \text{ nm}$ is shown in Fig. 2.9 (b). The closely spaced modes correspond to delocalized modes belonging to the dielectric and air bands that define the limit of the PhC band gap. The modes localized inside the cavity lie within the PhC band gap. In this simulation, 5 CMs denoted M_0, M_1, \dots, M_5 were identified. Note that the number of confined mode can depend on the PhC parameters. The three lowest energy modes electric field and intensity spatial distributions, calculated using 3D FDTD (3000 iterations), are summarized in Fig. 2.9 (c)-(e). The E_x and E_y fields correspond to the projection of the electric field on the x and y directions. These field distributions are taken at the center of the PhC slab for which only the E_x and E_y components of the electric field are non-zero.

Fig. 2.9 (f) shows the evolution of the M_0, E_y field amplitude as a function of the number of 3D FDTD iteration steps. The losses of the cavity are responsible for the slow decrease of $|E_y|$ as the number of iteration steps increases. The Fourier transform (FT) of the field amplitude temporal evolution yields the energy spectrum of the M_0 mode shown in Fig. 2.9 (g). The theoretical Q factor, reflecting the radiation losses and extracted by fitting the peak associated to the M_0 resonant energy with a Lorentzian function, is $Q=30000$.

The out of plane emission of the M_0 CM is investigated in Fig. 2.10. Fig. 2.10 (a) and (b) show the absolute value of the E_x and E_y electric fields above the PhC slab. They correspond to the field profiles taken along the white dashed line indicated in the figures insets. Both fields display evanescent tail above the slab, but they are more pronounced for the E_y field. The far-field patterns of both components of the electric field are shown in Fig. 2.16 (c) and (d). They are obtained by calculating the Fourier transform (FT) of the fields near-field pattern several nanometers (15 nm) above the slab[193] (yellow line in Fig. 2.16 (a) and (b)). These far-field patterns show the distribution of reciprocal space wavevectors $k_{||} = (k_x, k_y)$ for the E_x and E_y fields. Large $k_{||}$ -vectors corresponds to propagation directions below the light cone (red circle) and lead to internal reflexions that confine the light inside the cavity. $k_{||}$ -vectors components inside the light cone, however lead to out of plane losses. Although Fig. 2.16 (c) and (d) indicate the losses are low for the M_0 modes, a finite amount of photons escape the cavity. Part of this emission, corresponding to reciprocal space components inside the white circle in Fig. 2.16 (c) and (d), is captured by the microscope objective used to collect the light emitted from the sample. The ratio of the E_y and E_x $k_{||}$ -vectors components captured by the microscope objective is 0.98, meaning that the far-off emission from the cavity is strongly polarized along the y direction. In PL measurements, the cavity emission will be registered as a narrow peak with a DOLP close to 1.

2.2. Photonic crystal numerical simulations

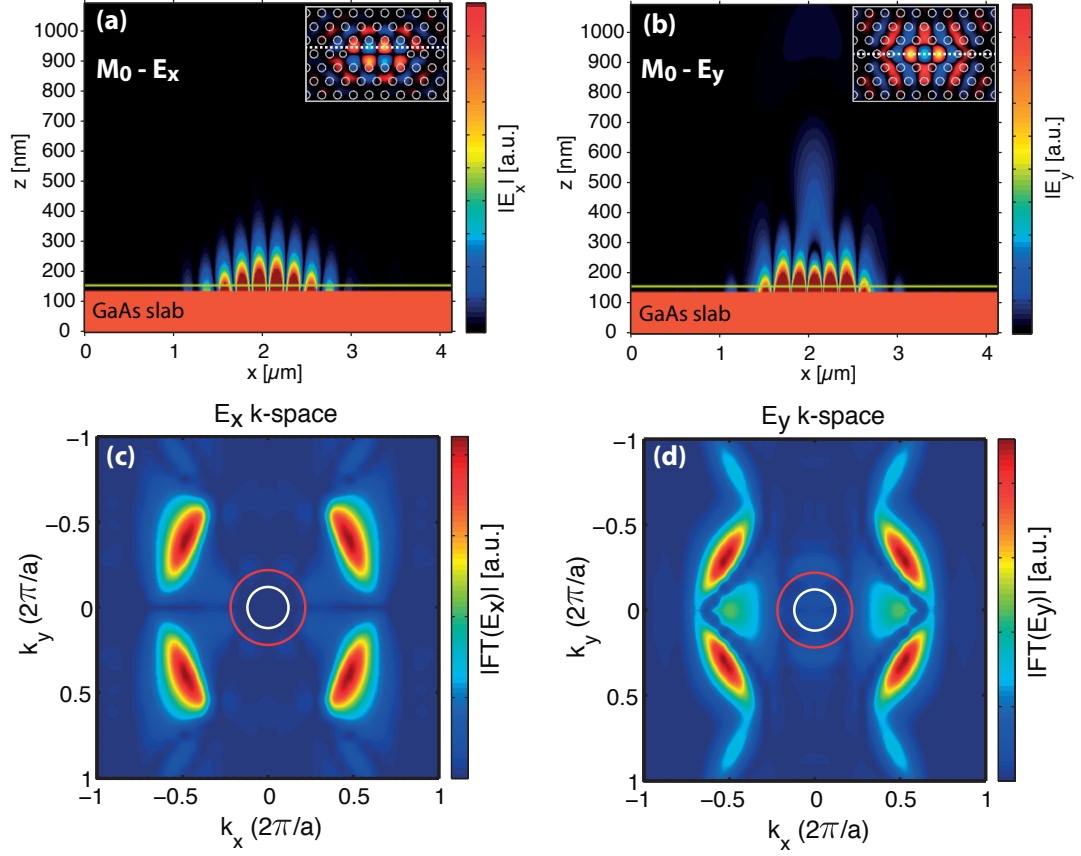


Figure 2.10: (a) and (b) M_0 E_x and E_y electric field spatial distributions calculated using 3D FDTD on the plane indicated by the white dashed line in the figure's inset. (c) and (d) k-space vector distribution for the E_x and E_y fields corresponding to the M_0 mode far-field distribution. The yellow line in (a) and (b) indicates the plane where the Fourier transform of the field was taken to obtain the far-field patterns. The red circle indicates the k-vector components satisfying $\sqrt{k_x^2 + k_y^2} = \omega/c$ (light cone), where ω is the mode frequency. The white circle indicates the k-vector components satisfying $\sqrt{k_x^2 + k_y^2} = \text{NA} \cdot \omega/c$ with $\text{NA} = 0.55$ the microscope objective numerical aperture.

2.3 Fabrication

The fabrication of site-controlled pyramidal QDs embedded in L_3 PhC cavities is a complex process that requires multiple fabrication steps and optimization runs described in the following sections.

2.3.1 Quantum dot fabrication process

The fabrication of InGaAs/GaAs pyramidal QDs consists of two main steps: fabrication of the patterned substrate and growth of the QD semiconductor layers.

Patterned substrate

To fabricate a regular, triangular array of inverted pyramids on the substrate, a 40 nm thick SiO₂ layer is deposited on a (111)B GaAs substrate by means of plasma-enhanced chemical vapor deposition (PECVD), followed by a spin-coated 200 nm thick poly(methyl methacrylate) (PMMA) layer. Arrays of equilateral triangles are then written with nanometer resolution on the PMMA layer using electron beam lithography (EBL). A methyl isobutyl ketone (MIBK) solution is used to develop the exposed parts of the PMMA and the triangular pattern is transferred onto the SiO₂ mask using reactive ion etching (RIE). Wet-chemical etching performed with a bromine-methanol solution defines inverted pyramidal recesses on the GaAs substrate due to the anisotropic removal of GaAs material through the SiO₂ openings. The inverted pyramidal pits consist of three {111}A gallium terminated planes. Using this process, homogeneous arrays (typically 300 μm × 300 μm square arrays) of pyramidal pits with pyramid size s_{pyr} (~ 10 nm accuracy) and pitch p were fabricated. This fabrication steps are illustrated in Fig. 2.11.

Quantum dot growth

QDs are grown inside the inverted pyramids by metalorganic chemical vapor deposition (MOCVD). This growth method relies on vaporized metalorganic precursors, for example trimethylgallium (TMGa) or trimethylindium (TMIn), to carry the desired semiconductor constituent to the substrate's surface. The heated surface of the substrate then induces a thermal decomposition of the precursor, realising the semiconductor adatoms and resulting in the epitaxial growth of crystalline semiconductor layers[173].

The growth sequence starts with 5 nm thick GaAs buffer layer, followed by an In_xGa_{1-x}As layer of thickness $h = 0.2 - 0.8$ nm. The QD is then capped with a 2 - 3 nm thick GaAs layer leading to the planarization of the pyramid. All thicknesses refer to equivalent growth on (100) unpatterned GaAs substrates and are considerably thicker for the

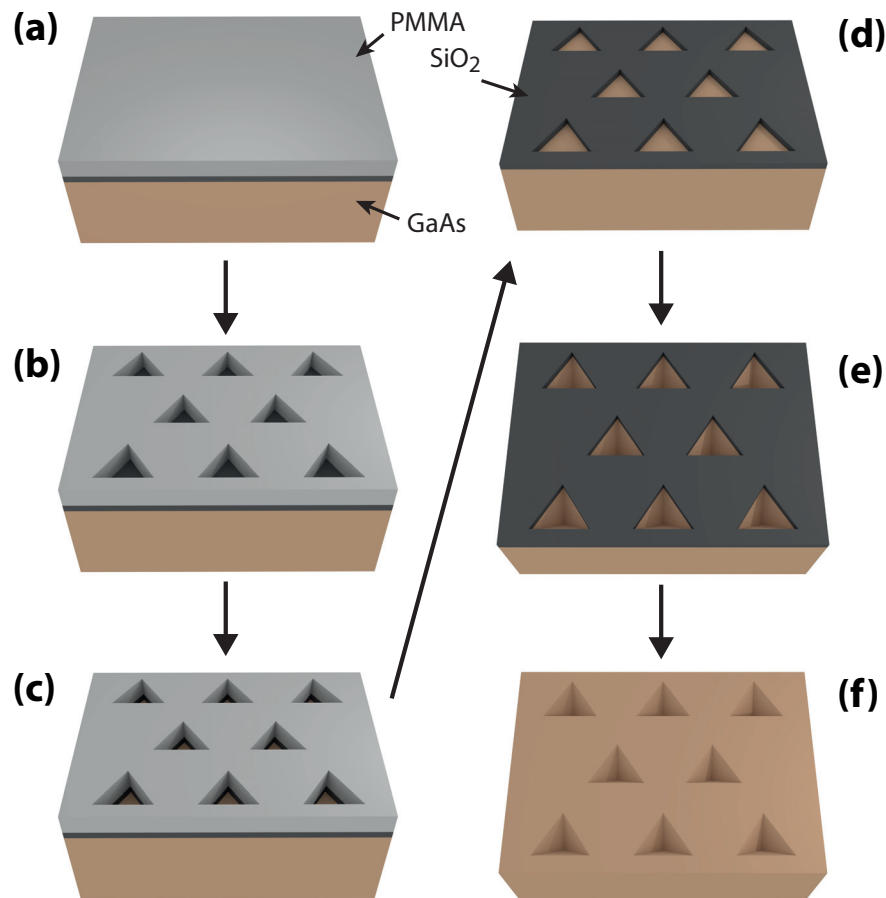


Figure 2.11: Illustration of the inverted pyramid arrays fabrication steps. (a) GaAs substrate coated with SiO₂ and PMMA. (b) Pattern inscription in PMMA using EBL and MIBK. (c) Pattern transfer in SiO₂ using RIE. (d) After removal of PMMA. (e) Wet-chemical etching of pyramid pits using bromine-methanol. (f) After removal of SiO₂.

actual structures. During the growth, either trimethylgallium or triethylgallium (TEGa) precursors were used for the buffer and QD layer while TMGa precursor were used for the cap layer[86]. The formation of the QD inside the pyramid is governed by several mechanisms[194]. First, the precursors decompose predominantly on the {111}A facets, limiting the growth on the (111)B surface. Secondly, the growth rate is more important on the {111}A orientation than the (111)B orientation, such that the growth occurs mostly inside the pyramid[195, 196]. Furthermore, the crystallographic plane are maintained during the growth, conserving the narrow tip and wedges of the pyramid[197]. Lastly, the adatoms, brought on the surface by the precursors, undergo a diffusion process that leads to a build up of adatoms on the concave apex and wedges of the pyramid caused by capillarity[198]. During the growth of the InGaAs layer, this results in the formation of a QD at the apex of the pyramid and three QWRs along the pyramid wedges[173]. Due to those growth mechanisms and the structural symmetry of the

Chapter 2. Experimental and modelling techniques

inverted pyramid the QD formed at the bottom of the pyramid is highly symmetric[199, 200]. The triangular symmetry in the growth plane translates in C_{3v} symmetry for the QD states[201], resulting in an isotropic polarization of the emission along the growth direction. This growth procedure is illustrated in Fig. 2.12.

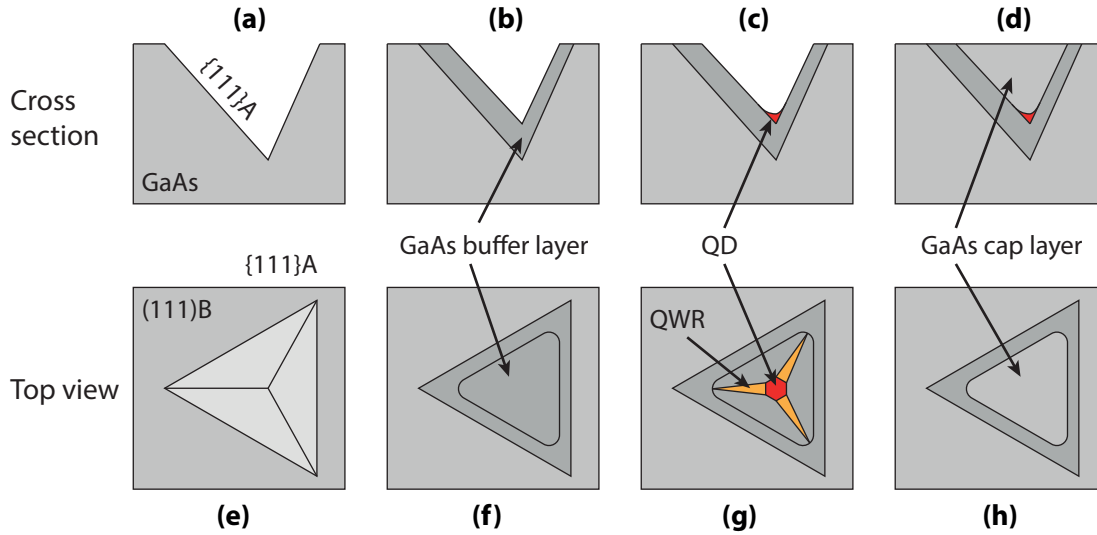


Figure 2.12: Illustration of the MOCVD QD growth steps in side view (a)-(d) and top view (e)-(h).

This QD fabrication method offers several advantages. The QD nucleation process is deterministic, ensuring that only one QD forms inside each pyramid. The QD nucleation site is fully determined by the position of the pyramid, which allows to control the QD location on the substrate with a 5 nm accuracy. The growth of QDs on regular, dense arrays of pyramids ensures a great reproducibility of MOCVD growth inside each pyramid, resulting in a high uniformity of the QD optical properties. This leads to a small inhomogeneous broadening of the QD array emission ranging from $6 - 20 \text{ meV}$. Furthermore, the QD emission energy can be tailored by changing the thickness h or indium composition x of the InGaAs layer. It is also important to note that the growth of pyramidal QDs does not generate a 2D wetting layer, as it is the case for self-assembled QDs, making it closer an ideal 0D system and removing spurious multi-excitonic effects which can be detrimental to cavity quantum electrodynamics (cavity-QED) experiments.

A more detailed description of the QD fabrication and growth can be found in reference [173].

PL characterization of QD arrays

The optimization of the QD fabrication process requires multiple iterations between growth and PL characterization to achieve the targeted QD wavelength, homogeneous

broadening and excitonic linewidth. Fig. 2.13 shows the photoluminescence of QD arrays after this optimization process. These measurements were performed using the μ -PL setup described in section 2.1.2. Given the $1\ \mu\text{m}$ diameter of the laser excitation spot, approximately 20 QDs of the array are probed in this experiment. Fig. 2.13 (a) shows the QD ensemble PL spectrum at low ($P = 10\ \mu\text{W}$) and high ($P = 500\ \mu\text{W}$) excitation powers. At low excitation powers, only the sum of the QDs s-state luminescence is visible ($1.4\ \text{eV}$). For higher excitation powers, additional features appear in the spectrum: the QD excited hole states emission at $1.41\ \text{eV}$, associated to an electron in the lowest energy state of the conduction band and a hole in the first excited state of the hole band[200, 201], the QDs p-state emission ($1.445\ \text{eV}$), the emission from the three wedge QWRs ($1.467\ \text{eV}$), the emission from the carbon impurity incorporated in the GaAs matrix ($1.496\ \text{eV}$) and the emission from the GaAs barriers ($1.515\ \text{eV}$). The emission spectrum of the QDs s-states for two different QD growth runs is shown in Fig. 2.13 (b) and (d). The ensemble emission is fitted by a Gaussian function to

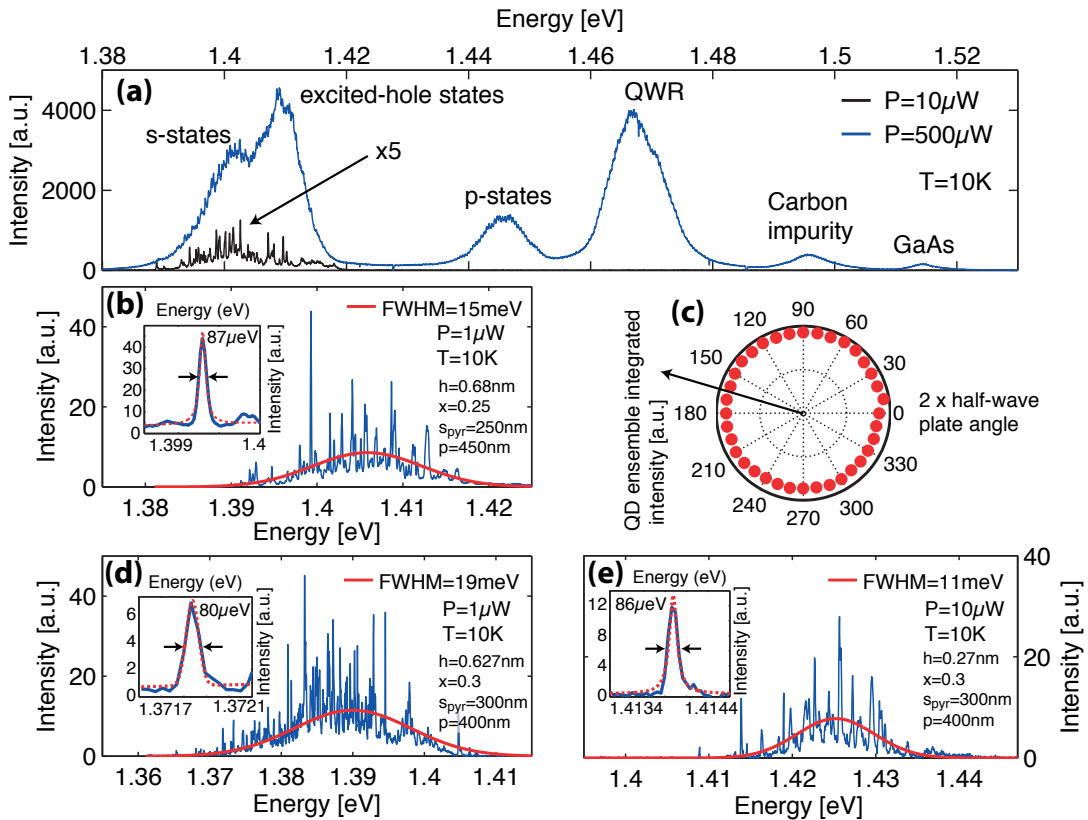


Figure 2.13: (a) PL spectra of a QD array for low ($P = 10\ \mu\text{W}$) and high ($P = 500\ \mu\text{W}$) excitation powers. (b) and (d) PL spectrum of the s-state emission of a QD array grown on a "dummy" GaAs substrate. Red line: Gaussian fit of the emission. Inset: Close-up of a single peak fitted by a Lorentzian function (red dashed line). (e) PL spectrum of the s-state emission of a QD array grown on a GaAs membrane substrate using the same growth parameters as in (d). (c) Polarization resolved top-view emission of a QD array. The QDs presented in this figure were grown with TMGa precursors.

retrieve the inhomogeneous broadening of the QD array. It is important to note that this inhomogeneous broadening of 15 and 19 meV is not related to the fluctuation of only the neutral exciton, but also reflect the emission and fluctuations of charged excitons and biexciton. The figures insets show a close up of one of the thin lines corresponding to the emission of a single QD. Polarization resolved PL measurements (Fig. 2.13 (c)), showing the QD ensemble integrated intensity versus the angle of the half-wave plate (see section 2.1.2), show the isotropy of the QDs top view emission, which is a result of the in-plane symmetry of the QDs.

Although the QD growth optimization is performed with GaAs "dummy" substrates, the final step requires to grow the QDs on a GaAs membrane wafer in view of their integration in PhC structures. These membrane wafers consist of a GaAs layer on top of an AlGaAs sacrificial layer. Fig. 2.13 (e) shows the PL spectrum of a QD array grown on a membrane substrate, with the same growth parameters used for the growth of the QD array probed in Fig. 2.13 (d), illustrating that QD fabrication procedure can be transferred to membrane substrates without any degradation of the QD emission. The QD ensemble mean emission energy, however, is shifted by 35 meV . This shift is the consequence of fluctuations from growth run to growth run in our system ($\sim 10 meV$) combined with the different precursor and adatom mobilities on dummy and membrane substrate surfaces which results in different effective growth rates. This shows the need to recalibrate some of the growth parameters when going from dummy to membrane GaAs substrates if controlling the absolute emission energy of the QDs is essential.

Fig. 2.14 summarizes characteristics of the QD ensembles gathered during the optimization process. Fig. 2.14 (a), (b) and (c) shows the QD ensemble center wavelength (s-state emission) as a function of pyramid size s_{pyr} , QD layer nominal thickness h and nominal indium mole fraction x . These results were gathered from 64 different growth runs performed during a one year time-span. Although the dispersion is important, due to long term variations of the MOCVD growth system, trends are visible, such as the decrease of the QD energy with the increase of the indium mole fraction and the increase of the QD layer thickness. Although these dependences are straightforward, the increase of the QD energy with increasing pyramid size is less trivial. Indeed the pyramid size influences the effective thickness of the QD in the growth direction. A smaller pyramid size will lead to a thicker QD because of the growth rate at the apex of the pyramid is influenced by the size of the $\{111\}A$ facets[81]. The QD emission energy also depends on the actual indium mole fraction in the InAs QD layer, which is subject to important In-As segregation effects[202]. These graphs illustrate how the QD energy can be tuned using these three parameters. Fig. 2.14 (d) shows the distribution of linewidth of single QD lines measured for different QD arrays. The distribution peaks at 80 μeV , which is the maximal resolution of our spectrometer, indicating a low defect density in the vicinity of the QDs. Linewidth values as low as 40 μeV were measured more recently using a higher resolution spectrometer. These numbers remain higher

however than those obtained for self-assembled QDs (linewidth $\sim 10 \mu\text{eV}$).

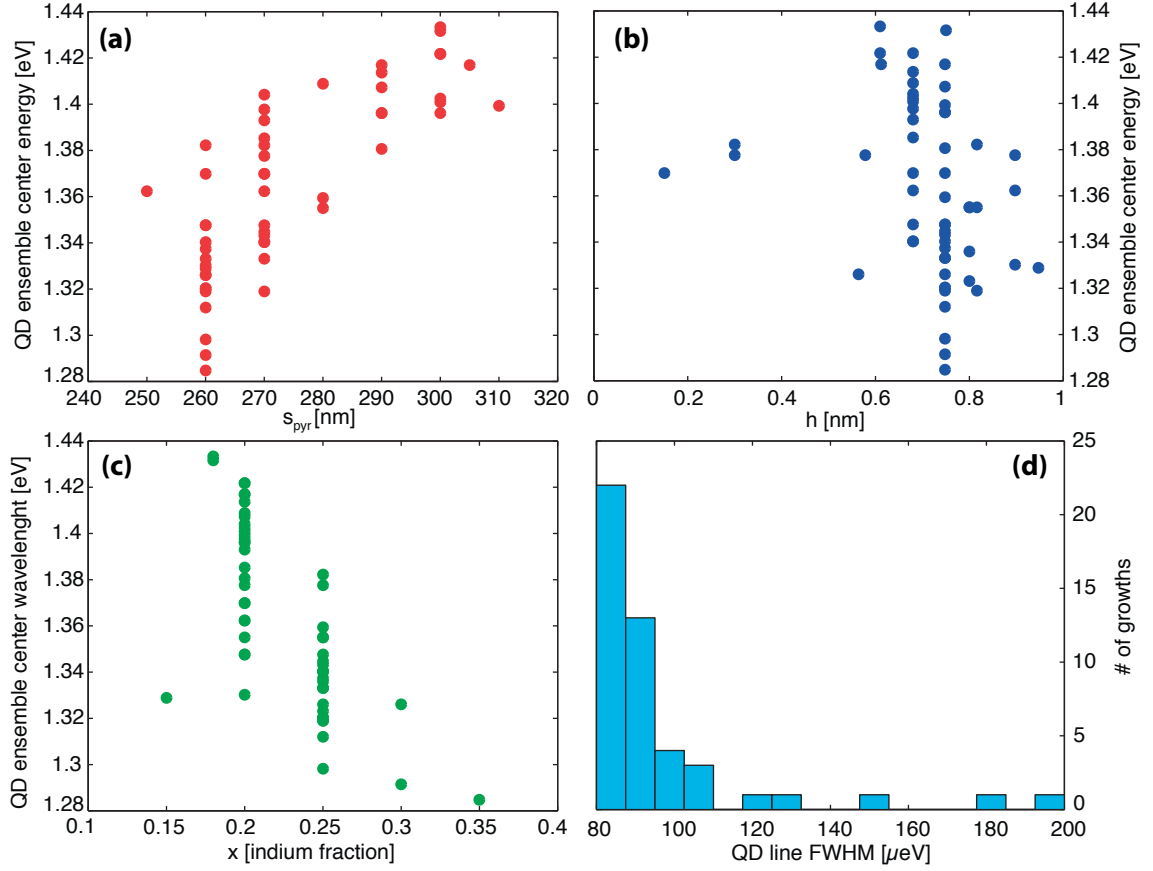


Figure 2.14: (a), (b) and (c) QD ensemble center energy as a function of pyramid size s_{pyr} , QD layer thickness h and indium mole fraction x , respectively. (d) Distribution of FWHM measured on single QD lines. Each point in (a)-(c) represents a different QD growth run. In total results from 64 different growth runs performed during a one year time-span are presented here. The QDs analysed here were grown with TEGa precursors.

2.3.2 QD integration in photonic crystal cavities

Cavity-QED experiment require to couple the emitter with the optical field of a cavity. In this study, pyramidal QDs are embedded inside modified L_3 PhC defect cavities. These cavities have been widely used in QD-cavity experiments due to their small mode volumes ($V \sim 0.1 \mu\text{m}^3$) which ensure a strong emitter-field interaction[44]. The high quality factors obtained experimentally with L_3 PhC cavities ($Q \sim 10000 - 30000$) were used to reach the strong coupling regime and obtain high Purcell factors in QD-cavity experiments[127, 140]. Self-assembled QDs are used in most QD-cavity coupling experiments reported in the literature. Due to the random positioning of these QDs, their alignment with the optical field of the cavity, which dictates the strength of the QD-cavity interaction, can be a challenging task (see subsection 1.3.4). The fabrication

method presented here ensures a near ideal positioning of the QD inside the cavity and offers a scalability only achievable with site-controlled QDs.

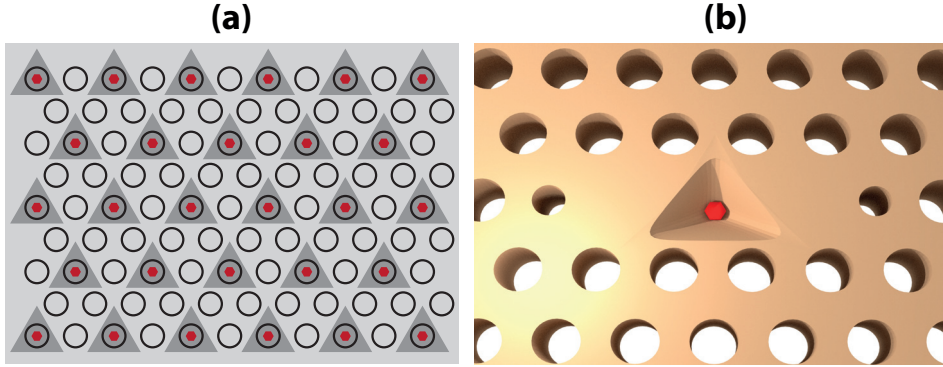


Figure 2.15: (a) Illustration of the alignment of the PhC array on the pyramid array. (b) Schematic of the pyramidal QD in the center of the PhC slab cavity.

The fabrication of the QD-cavity structures is done on a membrane substrate consisting of a 265 nm thick GaAs layer on top of a 1 μm thick sacrificial AlGaAs layer. Prior to the fabrication of the QDs, alignment marks are defined on the substrate using a combination of EBL and inductively-coupled-plasma (ICP) etching. The QD arrays are positioned on the sample using these alignment marks, with a 25 nm accuracy (relative to the position of the alignment marks). After the QD growth (see subsection 2.3.1) the GaAs substrate is coated with SiO₂ and PMMA resist. A triangular array of circles, indicating the location of the PhC holes, with pitch a equal to exactly half the pitch of the QD array ($a = p/2$) is written with EBL on the PMMA resist using the same alignment marks used to write the pyramid arrays (Fig. 2.15 (a)). The pattern is then transferred to the SiO₂ mask using RIE. ICP is used to etch the PhC holes into the GaAs layer before removing the AlGaAs sacrificial layer with a 4% HF : H₂O solution, releasing the GaAs PhC membrane.

Using the same alignment marks to write the QD and PhC pattern allows to position the PhC array such that every QD is removed from the substrate during the ICP etching of the PhC holes. By introducing a 3 hole defect in the PhC array, this procedure allows to position a single QD in the center of an L_3 cavity with an alignment accuracy better than 50 nm (Fig. 2.15 (b)). A more detailed description of the integration of QD in L_3 PhC cavities can be found in references [88, 173].

In these experiments, we are mainly interested in coupling the QD to the fundamental mode M_0 of the L_3 cavity. This requires to match the QD emission energy to the M_0 mode energy. Although in principle, a single PhC design with a target CM energy matching the energy of the QD emission could be implemented, uncertainties on the exact values of the system parameters after fabrication such as the hole diameter or slab thickness could lead to an offset of the mode energy rendering the sample obsolete. To avoid such a situation, series of PhC cavities with systematically-varied hole diameters

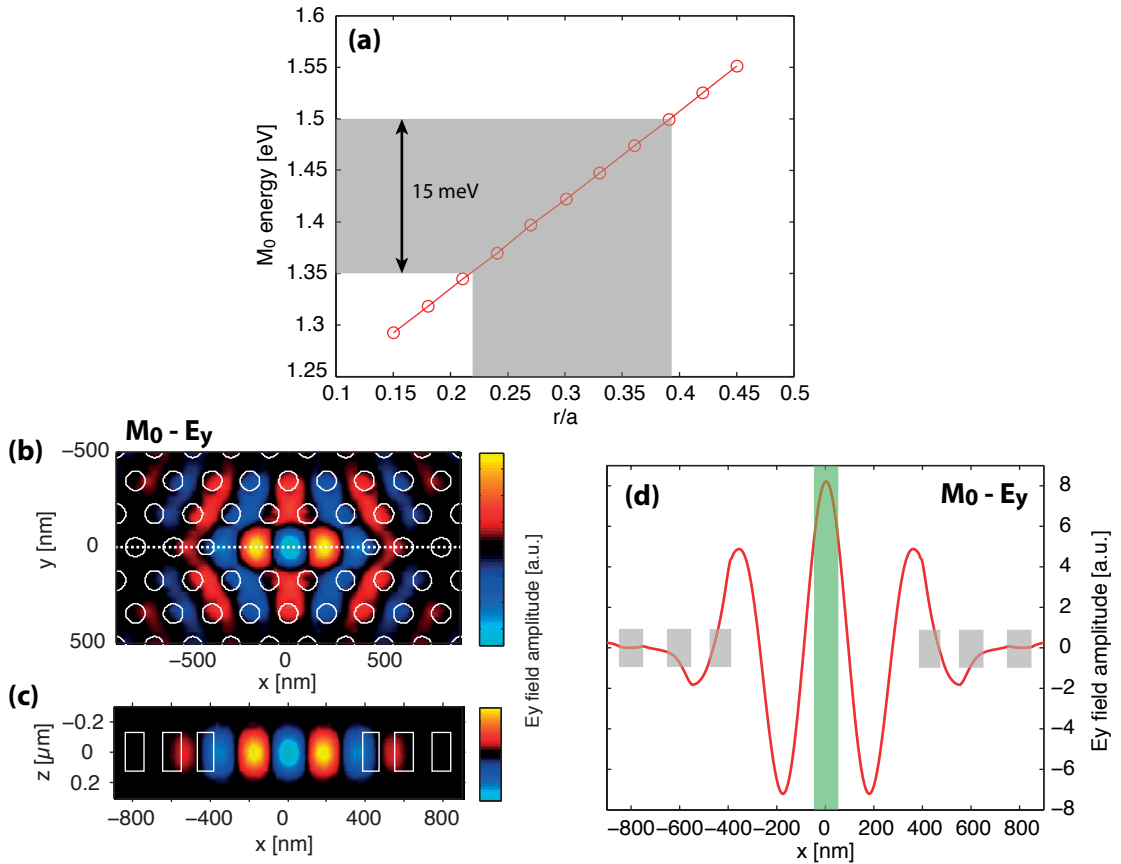


Figure 2.16: (a) M_0 mode energy calculated using 3D FDTD as a function r/a . The grey shaded region corresponds to the inhomogeneous broadening of QD arrays. (b) and (c) E_y electric field distribution along the $z = 0$ plane and $y = 0$ plane respectively. (d) E_y field amplitude along the white dashed line indicated in (b). The green shaded region spans the possible QD positions for a QD-cavity alignment accuracy of 50 nm .

are implemented on the sample. The expected dependence of the M_0 mode energy on the hole radius to pitch ratio (r/a) is shown in Fig. 2.16 (a). Furthermore, as mentioned in subsection 2.3.1, the QD energy also fluctuates around the mean energy of the QD array, characterized by a deviation of $\sim 15 \text{ meV}$ (indicated by the light grey region on Fig. 2.16 (a)). Implementing series of r/a ratios on the sample thus also allows to span the QD energy distribution.

Apart from spectral matching, spatial matching between the QD and CM field distribution is necessary to efficiently couple the QD to the CM. Moreover, the QD-cavity coupling strength is proportional to the scalar product between the QD dipole and cavity electric field (see section 3.1.3 of chapter 3). Inspecting the spatial distributions of the E_x and E_y component of the electric field (Fig. 2.9 (c)) shows that a QD located at the center of the cavity can couple only with the E_y component of the field. Indeed, the center of the cavity overlaps with a node of the E_x field distribution and a lobe

Chapter 2. Experimental and modelling techniques

of the E_y field distribution. Although the QD is nominally positioned in the center of the cavity, the finite alignment accuracy of the fabrication process ($< 50 \text{ nm}$) can reduce the overlap with the electric field. Fig. 2.16 (d) shows the profile of the E_y field along the white dashed line of Fig. 2.16 (b). The green shaded region indicates the possible locations of a misaligned QD, showing that the overlap with the field remains important. A QD with a 50 nm misalignment couples with 65% of the maximum field amplitude. The profile of the E_y field along the $y = 0$ plane is presented in Fig. 2.16 (c). The position of the QD along this direction depends on the growth parameters (mainly the GaAs buffer thickness and pyramid size) and can vary for different QD arrays. Given the rather smooth profile of the field along the growth direction, the uncertainty on the height of the QD should not strongly influence the coupling to the CM.

The QD-cavity structures studied in chapters 4 and 5 were fabricated using the procedure presented in this section. They belong to two different samples with parameters summarized in table 2.1. These samples were fabricated by M. Calic, A. Lyasota and co-workers.

Table 2.1: Summary of the fabrication parameters of the two samples studied in chapter 4 and 5. The thicknesses refer to equivalent growth on (100) unpatterned GaAs substrates.

	Sample A	Sample B
Pyramid size (s_{pyr}) [nm]	300	300
Pyramid pitch (p) [nm]	400	400
Growth parameters		
Buffer thickness [nm]	4.3	4.1
InGaAs layer thickness [nm]	0.2	0.268
Indium mole fraction (x)	0.2	0.2
Cap thickness [nm]	2.5	2.5
PhC parameters		
membrane thickness (h_{slab}) [nm]	265	265
PhC pitch (a) [nm]	200	200

In some experiments, probing the optical modes of a system of cavities can be achieved using light sources with broad spectral features. If the goal is not the study of the interaction between a QD and a CM, but simply probing the optical modes of the photonic structure, having a light source with a broader energy distribution relaxes the spectral matching condition. This is the case in chapter 6 that deals with optical modes of arrays of cavities. Site-controlled QWRs[203] are then embedded in the coupled cavity structure, providing a broader (FWHM $\sim 10 \text{ meV}$) light source capable of exciting multiple optical modes of the structure. The fabrication of these structures follows similar steps as those described here for QDs integrated in PhC cavities, and is presented in subsection 6.1.1.

Detuning dependent measurements

The PhC cavity structures fabricated on the samples are designed to obtain a spectral match between the QD and CM resonant energies. However, due to fabrication related fluctuations and uncertainties, this condition is often not met precisely in fabricated structures. There is thus a need to be able to control the energy difference between the QD and CM detuning. This would increase the number of useful structures on the sample and allow the study of their optical properties as a function of QD-cavity detuning.

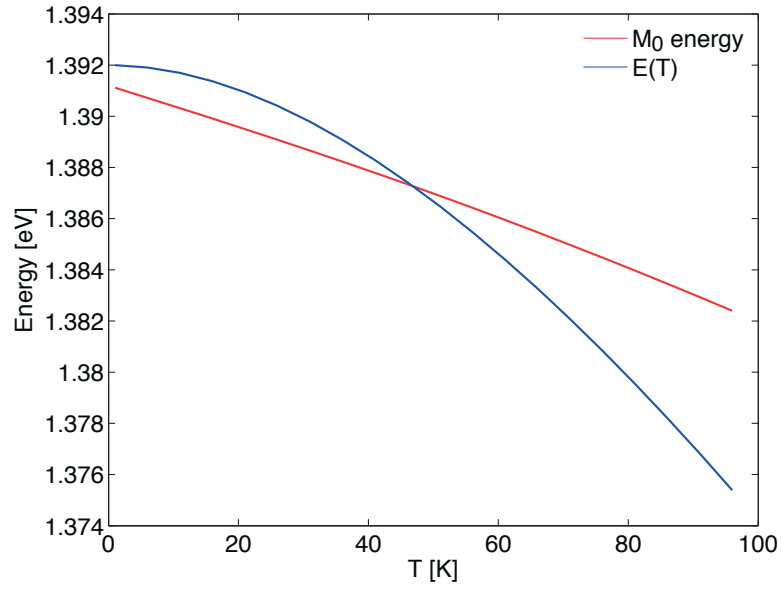


Figure 2.17: Calculated dependence of the CM and QD energy on the sample temperature.

The first method used to control the QD-cavity detuning relies on the different dependences on temperature of the QD and CM energies. The energy of the CM depends on the refractive index of the GaAs slab, which in turn is a function of the sample temperature. The energy of the M_0 mode is plotted as a function of temperature in Fig. 2.17. The energy was calculated using 2D finite differences for $a = 200 \text{ nm}$, $r = 110 \text{ nm}$ and $h_{slab} = 265 \text{ nm}$, and assuming the following dependence for the refractive index of GaAs[204]

$$n(T) = \sqrt{a_0 + a_1 T + a_2 T^2 + B} \quad (2.10)$$

with $a_0 = 5.96$, $a_1 = 7.2 \cdot 10^{-4} \cdot K^{-1}$, $a_2 = -0.95 \cdot 10^{-6} \cdot K^{-2}$ and $B = 6.3$. This dependence is to be compared with the variation of the QD energy with temperature. Assuming the QD transition energy $E(T)$ can be approximated by $E(T) = E_0 - \Delta E_g(T)$

with E_0 the low temperature QD energy and

$$\Delta E_g(T) = -5.408 \cdot 10^{-4} \frac{T^2}{T + 204} \quad (2.11)$$

the temperature dependent energy offset of the GaAs bandgap[205], the QD energy varies with temperature as shown in Fig. 2.17 for $E_0 = 1.394 \text{ eV}$. This shows that the CM and QD energies do not vary with the same rate as a function of temperature which allows to bring a red-shifted CM in resonance with a QD transition by increasing the sample temperature. Using this method, the QD-cavity energy detuning can be tuned by at most 5 meV (above 70 K , the QD emission degrades, limiting the available temperature range).

The second method relies on the condensation of water vapour on the sample's surface. Water deposited on the PhC slab and on the surface of the PhC holes reduces the confinement of the CM electric field which in turn reduces the mode energy. This condensation occurs during the cool-down of the sample prior to the PL experiment. Before cooling down the sample using liquid helium, the pressure inside the cryostat is 10^{-6} mbar . Once the the sample temperature reaches 10 K , the sample acts as a cryogenic pump that causes the residual gas molecules to condense on its surface, forming a thin dielectric layer, and the pressure inside the cryostat drops to 10^{-7} mbar . Similar techniques involving condensation of gases such as Xenon[206] have been used to tune the CM energy, achieving shifts up to 5 meV . Using water vapour condensation, we observed redshifts of the CM energy as large as 20 meV . The drawback of this method is the irreversibility of the energy shifts (the sample has to be heated up to remove the condensation) and, in our case, the lack of fine tuning.

2.3.3 QD isolation using mesas

We present here a fabrication method used for isolating a single pyramidal QD out of an array of QDs. This method does not rely on the implementation of PhC patterns, as it was the case in subsection 2.3.2, but instead makes use of mesa structures to isolate the QDs.

The fabrication process starts with a grown QD array (see section 2.3.1) coated with a Hydrogen silsesquioxane (HSQ) negative resist (thickness $\sim 120 \text{ nm}$). A circle is then written using EBL on top of a single QD. A Microposit MF-CD26 solution is used to develop the unexposed parts of the HSQ resist, leaving a hard mask layer on top of the designated QD. A 200 nm thick layer of the unprotected GaAs surface is then removed using ICP etching, leaving a single mesa with a diameter of approximately 500 nm incorporating the QD. The fabrication steps are illustrated in Fig. 2.3.3 (a)-(e). An SEM image of a fabricated mesa is shown in Fig. 2.18 (f).

These QDs, isolated using mesa structures, were used in PL experiments discussed in section 4.2.

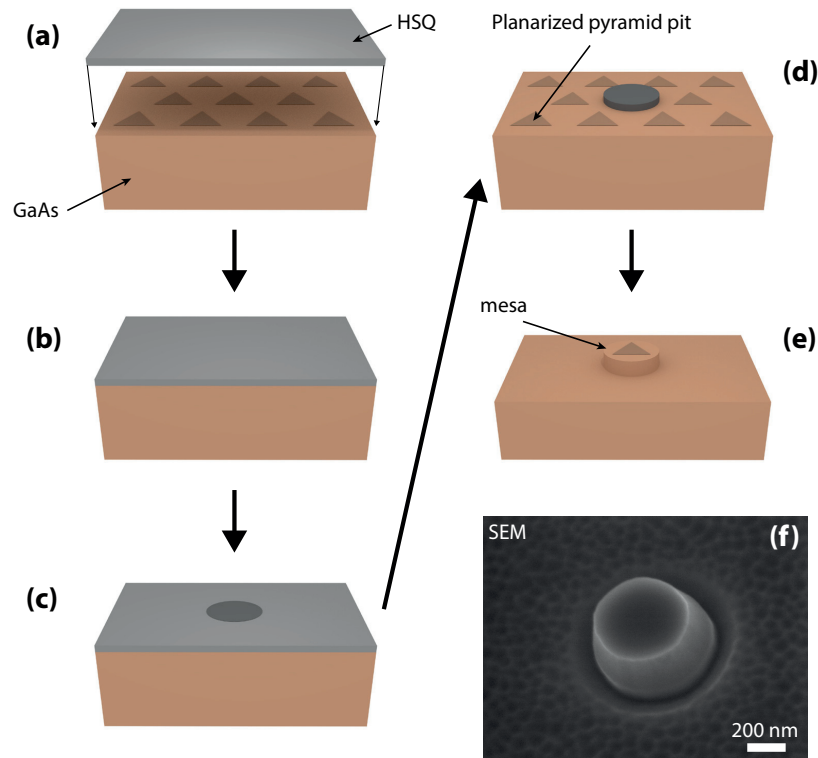


Figure 2.18: Illustration of fabrication process used to isolated pyramidal QDs using mesas. (a) and (b) GaAs substrate coated with HSQ. (c) EBL writing of the HSQ resist. (d) Development of the HSQ negative resist. (e) After ICP etching. (f) SEM image of mesa incorporating a single pyramidal QD. Courtesy of Dr. Kulkova.

2.4 Chapter summary

In this chapter we presented the basics of photoluminescence measurements and the optical setups that were used to perform μ -PL measurements, photon-correlation measurements and time-resolved PL measurements. The modeling tools used to calculate the electric field patterns and mode distributions of PhC structures were described. We explained the fabrication process of site-controlled pyramidal QDs and presented PL measurements of QD ensembles. Finally, we briefly presented the fabrication steps involved in the integration of pyramidal QDs in PhC cavities and mesa structures.

3 Cavity quantum electrodynamics with semiconductor quantum dots

Semiconductor quantum dots (QDs) coupled to nanocavities provide a promising platform to study cavity quantum electrodynamics (cavity-QED) in a solid-state environment. As already mentioned in chapter 1, experimental studies of QD-cavity coupling have brought to light new interesting phenomena not observed in atom-cavity systems. In particular the pronounced cavity mode (CM) emission persisting for large QD-cavity detunings was puzzling at first[148]. It soon became apparent that the simplistic picture of a QD behaving like a perfect two-level atomic transition was not sufficient to explain these observations. On the one hand, the QD is subject to decoherence induced by the solid-state environment. As explained in chapter 1, the main sources of decoherence come from the interaction of the QD with the crystal fluctuating electrostatic environment[74, 90] and phonon vibrations[102, 162]. On the other hand, the self-assembled QDs used in most QD-cavity experiments present complex electronic properties. The interaction of the QD localized states with delocalized 2D wetting layer states leads to a background emission[154, 155] that complicates the interpretation of cavity-QED experiments, leading for example to a far-off resonant cavity feeding[153]. This effect, intrinsic to self-assembled QDs, can overshadow the previously mentioned decoherence effects, preventing a quantitative analysis of their impact on QD-cavity coupling.

In this context, comparing experimental results to theoretical modeling of QD-cavity systems can be difficult. For pyramidal QDs, the absence of 2D wetting layer states simplifies the picture, bringing them closer to two-level system (TLS) like emitters. Modeling these QDs as two-level systems interacting with the semiconductor environment, as proposed in several theoretical studies[98, 100, 115, 164, 166], should then be sufficient to interpret the experimental measurements. In this chapter, we review in section 3.1 the well known Jaynes-Cummings model used to describe the interaction of a TLS with a CM. Section 3.2 presents the open Jaynes-Cummings model that was initially used to model the behavior of an atom with a leaky cavity. In section 3.3, we show how the open Jaynes-Cummings model is usually extended in the literature to

describe a realistic QD interacting with its environment. Finally, in section 3.4, we present the theoretical model used in this work to compute the photoluminescence spectra of pyramidal QDs coupled to L_3 PhC cavities in the presence of solid-state decoherence mechanisms.

3.1 Jaynes-Cummings model

The Jaynes-Cummings model was initially proposed by Jaynes and Cummings in 1963[207] to describe the interaction between a TLS and a quantized single mode radiation field. This model introduces three Hamiltonians that describe the TLS, the quantized electric field and the interaction between the TLS and the electric field. The TLS system Hamiltonian can be used to describe an atom inside an optical cavity when the quantized intra-cavity field is resonant with a single atomic transition. Hence, the Jaynes-Cummings model has been widely used as a tool to understand the physics behind atom-cavity experiments[20, 208]. Given the similar spectral characteristics of atoms and QDs, this model has also been used more recently, to understand cavity-QED experiments performed with semiconductor QDs[69, 160, 209].

Derivation of the Jaynes-Cummings model can be found in most quantum optics textbooks (see for example references [210, 211]).

3.1.1 Two-level system Hamiltonian

We consider a TLS with a ground state level $|g\rangle$ of energy E_g and a excited-state level $|e\rangle$ of energy E_e (see Fig. 3.1). In the context of QD cavity-QED the two-level system models a simplified QD, where the ground state represents an unoccupied QD and the excited state a QD populated with an exciton as illustrated in Fig. 3.1. The Hamiltonian of this TLS is

$$\hat{H}_0 = E_g|g\rangle\langle g| + E_e|e\rangle\langle e|. \quad (3.1)$$

Expressed as a function of Pauli matrices, the Hamiltonian becomes

$$\hat{H}_0 = E_g\hat{\sigma}_- \hat{\sigma}_+ + E_e\hat{\sigma}_+ \hat{\sigma}_- = E_g\hat{1} + (E_e - E_g)\hat{\sigma}_+ \hat{\sigma}_-. \quad (3.2)$$

where $\hat{\sigma}_+$ and $\hat{\sigma}_-$ are the *creation* and *annihilation* operators of the TLS system, with $\hat{\sigma}_+|g\rangle = |e\rangle$ and $\hat{\sigma}_-|e\rangle = |g\rangle$. The first term can be ignored because the choice of zero energy is arbitrary, giving

$$\hat{H}_0 = \hbar\omega_0\hat{\sigma}_+\hat{\sigma}_- \quad (3.3)$$

where $\hbar\omega_0 = E_e - E_g$ is the energy difference between the excited and ground state levels.

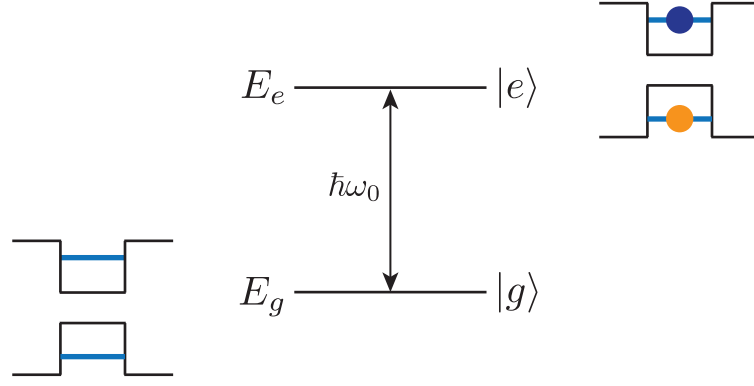


Figure 3.1: TLS with ground state level $|g\rangle$ of energy E_g and a excited-state level $|e\rangle$ of energy E_e ($\hbar\omega_0 = E_e - E_g$). Next to the ground and excited levels, the corresponding QD state is illustrated in a picture where the TLS represents a simplified QD.

3.1.2 Theoretical description of a cavity mode

A quantized electromagnetic field with a single mode is described by the harmonic oscillator Hamiltonian

$$\hat{H}_{rad} = \frac{1}{2}(\hat{p}^2 + \omega_c \hat{q}^2) \quad (3.4)$$

with ω_c the harmonic oscillator frequency. \hat{q} and \hat{p} are the coordinate and momentum operators respectively, obeying the canonical commutation $[\hat{q}, \hat{p}] = i\hbar\mathbb{1}$. After introducing the *creation* and *annihilation* operators for the cavity photons

$$\hat{a} = \frac{\omega_c \hat{q} + i\hat{p}}{\sqrt{2\hbar\omega_c}} \quad \text{and} \quad \hat{a}^\dagger = \frac{\omega_c \hat{q} - i\hat{p}}{\sqrt{2\hbar\omega_c}} \quad (3.5)$$

the Hamiltonian reads

$$\hat{H}_{rad} = \hbar\omega_c(\hat{a}^\dagger \hat{a} + \frac{1}{2}) = \hbar\omega_c(\hat{n} + \frac{1}{2}) \quad (3.6)$$

Chapter 3. Cavity quantum electrodynamics with semiconductor quantum dots

where \hat{n} is the number operator. When applied to the Fock state $|n\rangle$, the operators \hat{a}^\dagger and \hat{a} raise and lower the occupation number by 1

$$\hat{a}^\dagger |n\rangle = \sqrt{n+1} |n+1\rangle \quad (3.7)$$

$$\hat{a} |n\rangle = \sqrt{n} |n-1\rangle. \quad (3.8)$$

The term $\hbar\omega_c \frac{1}{2}$ in (3.6), associated with the vacuum state ($n = 0$) and often called "vacuum field energy", will be neglected in the rest of this chapter because the average of the electric field in this state is null. The variance of the field in the vacuum state however is finite and corresponds to vacuum field fluctuations which are responsible for the spontaneous emission of atoms.

The Hamiltonian $\hat{H}_{rad} = \hbar\omega_c \hat{a}^\dagger \hat{a}$ will be used to describe the single mode intra-cavity electric field with energy $\hbar\omega_c$ of a TLS-cavity system.

3.1.3 Hamiltonian of the coupled system

The Jaynes-Cummings model uses the particle-radiation interaction Hamiltonian under the dipole approximation which reads

$$\hat{H}_{int} = -\hat{\mathbf{d}} \cdot \hat{\mathbf{e}}(r) \quad (3.9)$$

with

$$\hat{\mathbf{d}} = \boldsymbol{\mu}(\hat{\sigma}_+ + \hat{\sigma}_-) \quad \text{and} \quad \hat{\mathbf{e}}(r) = -\epsilon \sqrt{\frac{\hbar\omega_c}{2V}} \boldsymbol{\psi}(\mathbf{r})(\hat{a}^\dagger + \hat{a}) \quad (3.10)$$

where $\hat{\mathbf{d}}$ is the TLS dipole operator and $\hat{\mathbf{e}}(r)$ is the electric field operator. $\boldsymbol{\mu} = q \langle e | \mathbf{r} | g \rangle$ is the dipole matrix element with $q = -e$ the charge of an electron and $\boldsymbol{\epsilon}$ is the field polarization vector at the location of the TLS. $\boldsymbol{\psi}(\mathbf{r})$ is the normalized electric field spatial function given by

$$\boldsymbol{\psi}(\mathbf{r}) = \frac{|E(\mathbf{r})|}{\sqrt{\epsilon(\mathbf{r}_m) |E(\mathbf{r}_m)|^2}} \quad (3.11)$$

with $E(r)$ the classical electric field at the position of the TLS, $\epsilon(\mathbf{r})$ the dielectric constant of the medium and \mathbf{r}_m the position of the maximum field intensity. The effective

mode volume V is defined as

$$V = \int \epsilon(\mathbf{r})\psi(\mathbf{r})^2 d^3\mathbf{r}, \quad (3.12)$$

with $\psi(\mathbf{r})$ the field spatial function. The dipole approximation is valid when the displacement of the charges interacting with the field is much smaller than the radiation wavelength. By substituting the expressions of $\hat{\mathbf{d}}$ and $\hat{\mathbf{e}}(r)$ in (3.9), we get

$$\hat{H}_{int} = \boldsymbol{\mu} \cdot \boldsymbol{\epsilon} \sqrt{\frac{\hbar\omega_c}{2V}} \psi(\mathbf{r})(\hat{a}^\dagger + \hat{a})(\hat{\sigma}_+ + \hat{\sigma}_-) \quad (3.13)$$

$$\Rightarrow \hat{H}_{int} = \hbar g(\hat{a}^\dagger \hat{\sigma}_- + \hat{a} \hat{\sigma}_+ + \hat{a}^\dagger \hat{\sigma}_+ + \hat{a} \hat{\sigma}_-) \quad (3.14)$$

with

$$g = \boldsymbol{\mu} \cdot \boldsymbol{\epsilon} \sqrt{\frac{\omega_c}{2\hbar V}} \psi(\mathbf{r}) \quad (3.15)$$

the TLS-field coupling strength. The coupling strength depends on the alignment of the TLS dipole and electric field polarization, the spatial positioning of the TLS with respect to the field spatial distribution and the field mode volume.

In a situation where the TLS and electric field mode energies are similar (near-resonance), the last two terms of (3.14) oscillate much faster than the first two terms. Neglecting these last two terms is called the *rotating wave approximation* (RWA) and is equivalent to keeping only the terms conserving the number excitations in the Hamiltonian. In the RWA, the Jaynes-Cummings interaction Hamiltonian reads

$$\hat{H}_{int} = \hbar g(\hat{a}^\dagger \hat{\sigma}_- + \hat{a} \hat{\sigma}_+). \quad (3.16)$$

The total Hamiltonian of the system is then

$$\hat{H}_{tot} = \hat{H}_0 + \hat{H}_{rad} + \hat{H}_{int} = \hbar\omega_0 \hat{\sigma}_+ \hat{\sigma}_- + \hbar\omega_c \hat{a}^\dagger \hat{a} + \hbar g(\hat{a}^\dagger \hat{\sigma}_- + \hat{a} \hat{\sigma}_+). \quad (3.17)$$

Uncoupled Hamiltonian

The eigenstates of the uncoupled Hamiltonian ($g=0$) are the *uncoupled* states $|i, n\rangle = |i\rangle \otimes |n\rangle$ with $i = e, g$ and $n = 0, 1, 2, \dots$. Their eigenenergies are

$$(\hat{H}_0 + \hat{H}_{rad}) |g, n\rangle = \hbar n \omega_c |g, n\rangle \quad (3.18)$$

$$(\hat{H}_0 + \hat{H}_{rad}) |e, n\rangle = \hbar(\omega_0 + n\omega_c) |e, n\rangle. \quad (3.19)$$

Since $\omega_0 \approx \omega_c$, the eigenenergies are arranged in closely spaced doublets $D_n : \{|g, n\rangle, |e, n-1\rangle\}$ separated by $\hbar\delta = \hbar(\omega_0 - \omega_c)$. Successive doublets are separated by $\hbar\omega_0$ as illustrated in Fig. 3.2 (a).

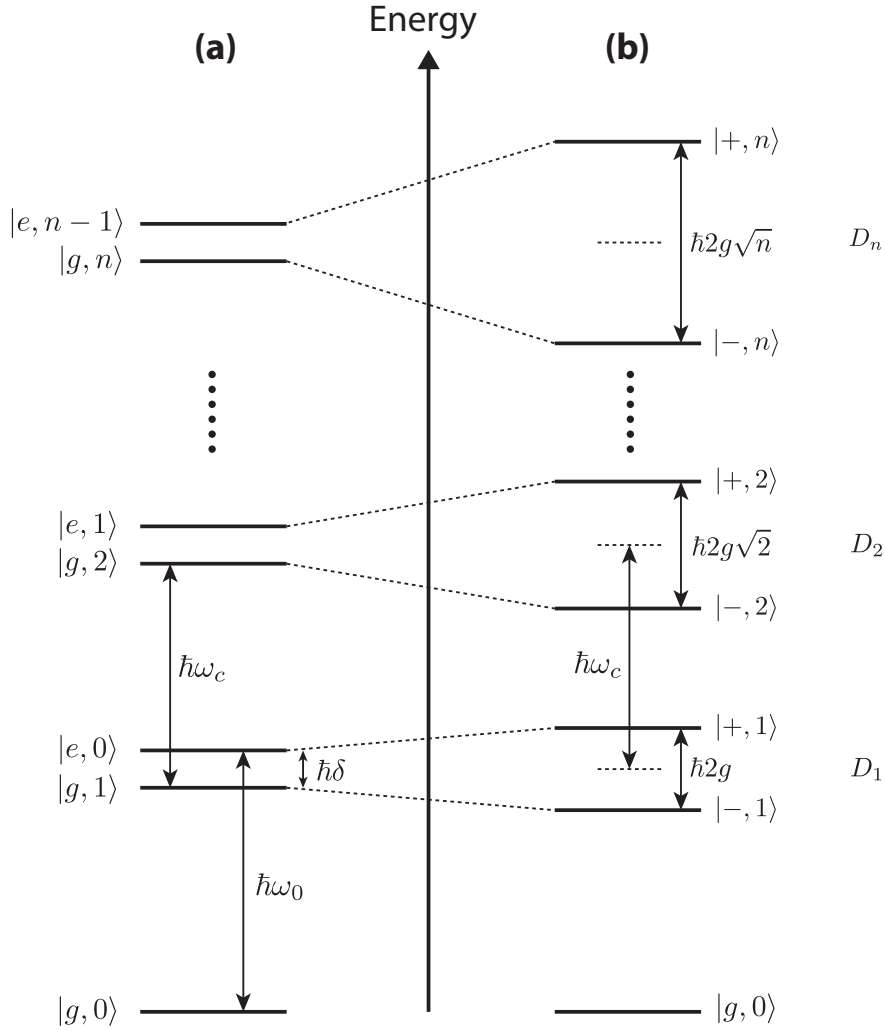


Figure 3.2: Energy levels for the uncoupled (a) and coupled Jaynes-Cummings Hamiltonian.

Coupled Hamiltonian

If we now consider the interaction Hamiltonian, we see that its matrix elements in the $|i, n\rangle = |i\rangle \otimes |n\rangle$ basis consist of

$$\langle i, n | \hat{H}_{in} | i', n' \rangle = \hbar g (\langle i, n | \hat{a}^\dagger \hat{\sigma}_- | i', n' \rangle + \langle i, n | \hat{a} \hat{\sigma}_+ | i', n' \rangle) \quad (3.20)$$

which only couples the states inside a subspace D_n , which tells us the total Hamiltonian can be diagonalised separately in each subspace D_n . In the subspace D_n , the Hamiltonian can be written in matrix form

$$\hat{H}_{tot} = \hbar \begin{bmatrix} n\omega_c & g\sqrt{n} \\ g\sqrt{n} & \delta + n\omega_c \end{bmatrix}. \quad (3.21)$$

The corresponding eigenvalues are

$$E_{\pm}^n = \hbar n\omega_c + \hbar \frac{\delta}{2} \pm \frac{\hbar}{2} R_n \quad (3.22)$$

with $R_n = \sqrt{\delta^2 + 4g^2n}$ the generalized Rabi frequency. The corresponding eigenstates are

$$|+, n\rangle = \cos(\theta_n) |g, n\rangle + \sin(\theta_n) |e, n-1\rangle \quad (3.23)$$

$$|-, n\rangle = -\sin(\theta_n) |g, n\rangle + \cos(\theta_n) |e, n-1\rangle \quad (3.24)$$

with $\tan(2\theta_n) = -\frac{2g\sqrt{n}}{\delta}$. These eigenstates are often called the *dressed states* of the system, while the eigenstates of the uncoupled system are called *bare states*. It is interesting to note that when $|\delta| \rightarrow \infty$, θ_n tends to 0 or $\frac{\pi}{2}$ and the two dressed eigenstates tend to the bare states $|g, n\rangle$ and $|e, n-1\rangle$. In the special case $\omega_0 = \omega_c$, the eigenstates become

$$|\pm, n; \delta = 0\rangle = \frac{1}{\sqrt{2}} (\pm |g, n\rangle + |e, n-1\rangle) \quad (3.25)$$

with eigenenergies $E_{\pm, \delta=0}^n = \hbar n\omega_c \pm \hbar g\sqrt{n}$. The dressed states are thus split by $\hbar 2g\sqrt{n}$ as depicted in Fig. 3.2 (b), which means the energy separation of the state doublets increases with \sqrt{n} . This nonlinear scaling of the energy separation is a quantum effect not observed for two classical coupled oscillators. When only one excitation is present in the system ($n = 1$), the eigenstates are split by $\hbar 2g$ which is called the *vacuum Rabi*

splitting.

3.2 Open-system Jaynes-Cummings model

Up to now we have considered a *closed* quantum TLS-cavity system that does not interact with the environment. A more realistic description of QD-cavity systems requires to take into account the spontaneous emission of the QD exciton and the radiation losses of the CM. These relaxation processes can be seen as an interaction between the TLS and cavity quantum systems with large reservoirs consisting of an ensemble of harmonic oscillators with which a continuum of Bohr frequencies is associated. This defines a new system comprised of *open* TLS and cavity quantum systems interacting with large reservoirs, governed by the Hamiltonian[212]

$$\hat{H}_{OS+R} = \hat{H}_{OS} + \hat{H}_R + \hat{H}_{OS,R} \quad (3.26)$$

with \hat{H}_{OS} the open system Hamiltonian, \hat{H}_R the Hamiltonian of the reservoir and $\hat{H}_{OS,R}$ the interaction Hamiltonian between the open system and the reservoir. In contrast to a closed system, this new system can only be described by a density matrix $\hat{\rho}$, for which the time evolution is described by the *von-Neumann* master equation[213]

$$\frac{d\hat{\rho}}{dt} = -\frac{i}{\hbar}[\hat{H}_{OS+R}, \hat{\rho}]. \quad (3.27)$$

This problem can be solved for the reduced density matrix $\hat{\rho}_r = \text{tr}_R\{\hat{\rho}\}$ with the following assumptions

- on a time scale Δt , the coupling between the open system and the reservoir is assumed small enough to comply with 2nd order perturbation theory (Born approximation).
- a coarse grain derivative for the density matrix $\frac{d\hat{\rho}}{dt} \approx \frac{\hat{\rho}(t) - \hat{\rho}(t_0)}{t - t_0}$ can be used, with $\Delta t = t - t_0$, because Δt is supposed to be long compared to the correlation variables of the phonon bath and the density matrix does not change significantly on that time scale because of the weak system-reservoir coupling hypothesis.
- the phonon bath is assumed to be Markovian on a time scale Δt (the memory effect of the reservoir are neglected).

These approximations give the master equation in the Lindblad form[214]

$$\dot{\hat{\rho}}_r = -\frac{i}{\hbar}[\hat{H}_{tot}, \hat{\rho}_r] - \frac{1}{2} \left\{ \sum_l \hat{L}_l^\dagger \hat{L}_l, \hat{\rho}_r \right\} + \sum_l \hat{L}_l \hat{\rho}_r \hat{L}_l^\dagger \quad (3.28)$$

where the first term describes the coherent part of the dynamic. The second and third terms account for the incoherent relaxation processes expressed by the Lindblad operators \hat{L}_l . The spontaneous emission of the TLS at rate γ is given by the operator

$$\hat{L}_\gamma = \sqrt{\gamma} \hat{\sigma}_- \quad (3.29)$$

and the cavity losses at rate κ are described by the operator

$$\hat{L}_\kappa = \sqrt{\kappa} \hat{a}. \quad (3.30)$$

By restricting ourselves to the subset $\{|g, 0\rangle, |e, 0\rangle, |e, 1\rangle\}$, which is valid in the limit of weak excitation of the system, it is possible to compute the eigenvalues of the system given by

$$\Omega_\pm = \omega_c - i\frac{1}{2} \frac{\kappa + \gamma}{2} \pm \sqrt{g^2 - \left(\frac{\kappa - \gamma}{4}\right)^2}. \quad (3.31)$$

with $\delta = 0$. Depending on the relative weight of the parameters g , κ and γ , the above expression leads to the definition of *strong* and *weak* coupling.

3.2.1 Strong coupling

The strong coupling regime is reached when the TLS-cavity coupling strength is greater than any losses of the system ($g \gg \kappa, \gamma$). This implies that the term under the square root of (3.31) is positive and the system spectrum consists of two peaks with frequencies

$$\text{Re}(\Omega_\pm) = \omega_c \pm \sqrt{g^2 - \left(\frac{\kappa - \gamma}{4}\right)^2} \quad (3.32)$$

split in frequency by $2\sqrt{g^2 - \left(\frac{\kappa - \gamma}{4}\right)^2}$ and broadened by $\frac{\kappa + \gamma}{2}$. This result is similar to what was obtained for a closed system: the two lines correspond to new states which are entangled states of the TLS and electric field. This situation is illustrated in Fig. 3.3 for the parameters $\hbar\gamma = 0.6 \mu\text{eV}$ (1 ns lifetime), $\hbar\kappa = 70 \mu\text{eV}$ and $\hbar g = 200 \mu\text{eV}$.

Fig. 3.3 (a) shows the computed power spectrum¹ of the TLS, consisting of two peaks separated by $2\hbar g = 400 \mu\text{eV}$. The FWHM of each peak is equal to the average of the TLS and cavity linewidths. Fig. 3.3 (b) shows the time evolution of the TLS and cavity occupation numbers when the system is initially in the state $|e, 0\rangle$. Since the losses are much weaker than the coupling strength, the excitation oscillates coherently between the TLS and the cavity field at a frequency given by the Rabi frequency R_n . These oscillations are called Rabi oscillations. The oscillations are damped due to the finite losses of the system.

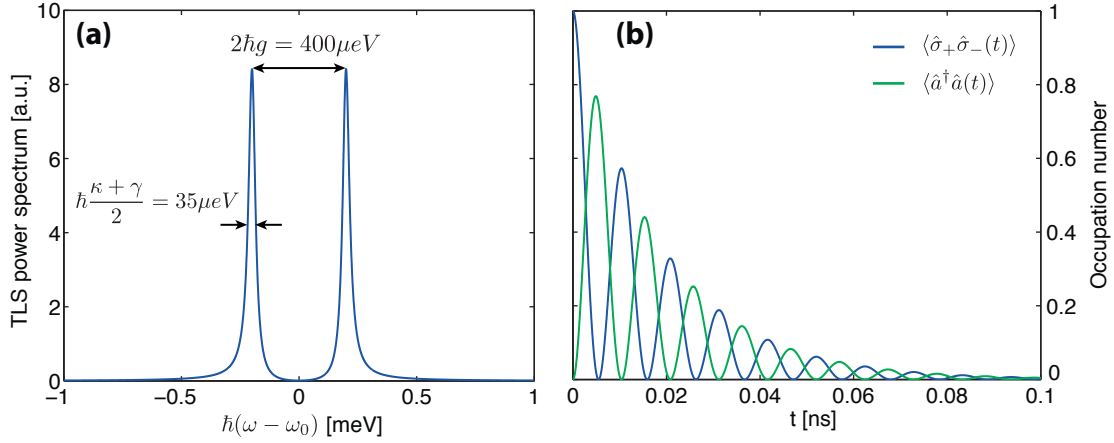


Figure 3.3: **Example of a strongly coupled TLS-cavity system** (a) TLS power spectrum. (b) Time evolution of the TLS (blue) and cavity (green) occupation numbers with the system is initially in the state $|e, 0\rangle$. *Parameters:* $\hbar\gamma = 0.6 \mu\text{eV}$ (1ns), $\hbar\kappa = 70 \mu\text{eV}$ and $\hbar g = 200 \mu\text{eV}$.

3.2.2 Weak coupling

When the losses are much greater than the TLS-cavity coupling strength ($\kappa \gg g$), the system is in the weak coupling regime. In that case, the term under the square root of (3.31) is negative, which implies the two peaks of the spectrum have the same frequency ω_c , but a damping (imaginary part of the frequency) given by

$$D_{\pm} = \frac{1}{2} \left(\frac{\kappa + \gamma}{2} \mp \sqrt{\frac{(\kappa + \gamma)^2}{4} - 4g^2} \right) = \frac{\Gamma_{\pm}}{2}. \quad (3.33)$$

In this regime the spectrum consists of the superposition of two peaks broadened by Γ_{\pm} . In the special case ($\kappa \gg \gamma$) which constitutes the "bad cavity" regime, the new

¹The power spectrum and occupation number shown in Fig. 3.3 are obtained by solving the master equation using a numerical solver[215]. The TLS power spectrum is defined as the Fourier transform of the correlation function $\langle \hat{\sigma}_+(t)\sigma(0) \rangle$. The simulation of the power spectrum required to add a small incoherent pumping of the TLS with the Lindblad operator $\hat{L}_P = \sqrt{P}\hat{\sigma}_+$ ($P \ll \kappa, \gamma$).

3.2. Open-system Jaynes-Cummings model

decay rates associated with the damping simplify to

$$\Gamma_{cav} \equiv \Gamma_+ = \kappa \quad (3.34)$$

$$\Gamma_{TLS} \equiv \Gamma_- = \frac{4g^2}{\kappa}. \quad (3.35)$$

The peak associated with the cavity retains the decay rate of the cavity, while the second peak, associated with the TLS has a modified decay rate. This modified decay rate can be compared to the spontaneous emission rate of the same emitter placed in an homogeneous medium without the effect of the cavity given by

$$\Gamma_0 = \frac{n\mu^2\omega_0^3}{3\pi\hbar\epsilon_0c^3}. \quad (3.36)$$

The ratio Γ_{TLS}/Γ_0 gives the Purcell factor, using the value of g given by (3.15)

$$F_P \equiv \frac{\Gamma_{TLS}}{\Gamma_0} = \frac{3}{4\pi^2} \left(\frac{\lambda}{n} \right)^3 \frac{Q}{V} \quad (3.37)$$

with $Q = \omega_c/\kappa$ the cavity quality factor and λ the wavelength associated with the TLS transition. For most systems, $F_P > 1$ and the Purcell factor quantifies the increase of the TLS emission rate under the influence of the interacting cavity field. This translates the fact that the spontaneous emission of an emitter is proportional to the density of electromagnetic states of its environment, which is modified here by placing the emitter inside a cavity. This situation is illustrated in Fig. 3.4 for the parameters $\hbar\gamma = 0.6 \mu eV$ (1 ns lifetime), $\hbar\kappa = 700 \mu eV$ ($Q = 2000$) and $\hbar g = 50 \mu eV$. The modified decay rate of the TLS emission reflects in the simulated power spectrum shown in Fig. 3.4 (a) which has a FWHM of $\hbar\frac{4g^2}{\kappa} = 14 \mu eV$, different from the linewidth $\hbar\gamma$ expected for $g = 0$. Fig. 3.4 (b) shows the time evolution of the TLS and CM occupation numbers. In contrast to the strong coupling regime (Fig. 3.3 (b)), no Rabi oscillations are visible. The weak coupling regime corresponds to an overdamping of the Rabi oscillations caused by the important losses of the cavity. The TLS population decays exponentially with characteristic decay time of 46 ps. The decay time is drastically reduced when compared to the $2\pi/\gamma = 1$ ns decay time of the TLS for $g = 0$. The ratio of the decay time corresponds to the Purcell factor $F_P = \frac{4g^2}{\kappa\gamma} = 24$ for these parameters.

Note that the Purcell factor was calculated for a TLS positioned at the maximum of the field ($\mathbf{r} = \mathbf{r}_m$), with a dipole moment collinear with the field polarization vector ($\boldsymbol{\mu} \cdot \boldsymbol{\epsilon} = 1$) and in resonance with the CM ($\delta = 0$). The general Purcell factor expressed

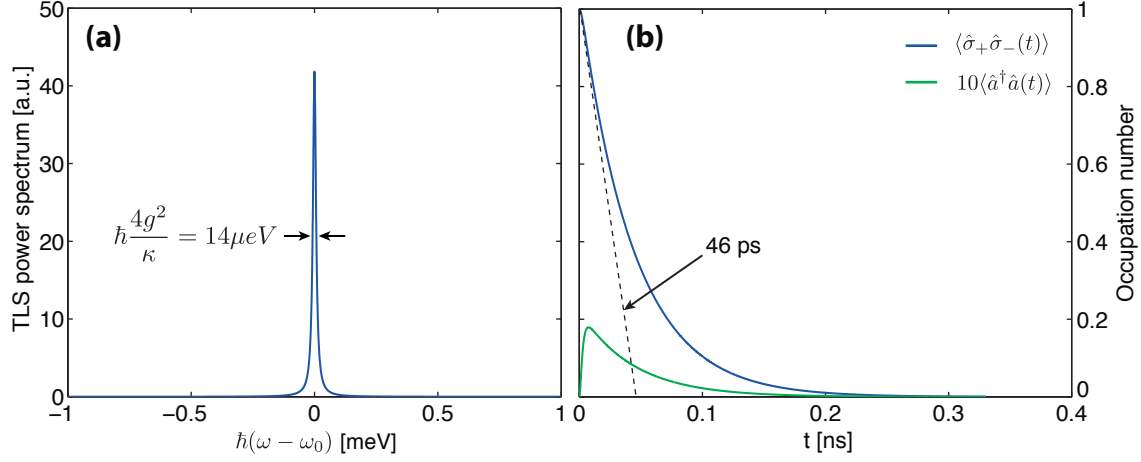


Figure 3.4: **Example of a weakly coupled TLS-cavity system** (a) TLS power spectrum. (b) Time evolution of the TLS (blue) and cavity (green) occupation numbers with the system is initially in the state $|e, 0\rangle$. Parameters: $\hbar\gamma = 0.6 \mu\text{eV}$ (1ns), $\hbar\kappa = 700 \mu\text{eV}$ ($Q = 2000$) and $\hbar g = 50 \mu\text{eV}$.

as a function of detuning is[181]

$$F_P(\delta) = \frac{3}{4\pi^2} \left(\frac{\lambda}{n} \right)^3 \frac{Q}{V} \psi(\mathbf{r})^2 \frac{(\boldsymbol{\mu} \cdot \boldsymbol{\epsilon})^2}{|\boldsymbol{\mu}|^2} \frac{\kappa^2}{4\delta^2 + \kappa^2}. \quad (3.38)$$

The Purcell factor is thus expected to be smaller if the QD is not positioned at the maximum of the electric field or if its dipole moment is not collinear with the field polarization vector. As a function of detuning, the Purcell factor follows a Lorentzian function with a FWHM given by $\kappa/2$.

3.3 Modeling semiconductor dephasing effects

In the previous section, relaxation processes were added to the description of the TLS-cavity system to account for the losses experienced by a "real" emitter-cavity system, i.e., spontaneous emission of the emitter and radiation losses of the CM. This model would be sufficient to describe the dynamics and spectral features of an isolated atom coupled to an optical cavity. When the emitter is a semiconductor QD exciton, however, additional interaction processes with the environment have to be taken into account. As explained in chapter 1, semiconductor QD excitons interact with the surrounding crystal lattice leading to additional incoherent processes: spectral diffusion of the QD which leads to pure dephasing and the interaction of the QD excitons with crystal lattice vibration leading to phonon-assisted mechanisms.

3.3.1 Pure dephasing

The interaction of the QD exciton with the fluctuating electric field generated by randomly trapped charges in defects located in the vicinity of the QD leads to energy shifts of the exciton transition[93]. When the energy shifts are weak and occur at a rate slower than the exciton emission rate, they lead to spectral diffusion which is manifested by spectral jumps of the emission peak following a Gaussian distribution. However when the exciton energy shifts occur at a faster rate than the exciton emission rate, spectral jumps are inhibited and the broadening become homogeneous, following a Lorentzian distribution[90, 216]. This last process is indicated to be predominant for InGaAs QDs[93, 217] and can be effectively modeled by adding a pure dephasing Lindblad term to the master equation of the TLS-cavity system[99]

$$\hat{L}_d = \sqrt{\frac{\gamma_d}{4}} \hat{\sigma}_z \quad (3.39)$$

with γ_d the pure dephasing rate and $\hat{\sigma}_z = 2\hat{\sigma}_+\hat{\sigma}_- - 1$. In contrast to relaxation terms, this dephasing term does not modify the population of the TLS but provides time-dependent perturbations to the eigenstates of the system, causing the phase relation of the two-level system states to become uncorrelated[218]. This additional Lindblad term causes a broadening of the TLS spectral feature by γ_d .

3.3.2 Phonon cavity feeding

The QD exciton also interacts with phonon lattice vibrations. This interaction has been shown to introduce phonon sidebands such that the emission features of QDs deviate from a Lorentzian shaped peak[102, 107]. The sidebands originate from QD dephasing induced by the interaction of the exciton electrons and holes with phonons. These phonon sidebands, unique to semiconductor QDs, were shown to increase the detuning range for which coupling occurs between QDs and CM: the energy mismatch between the exciton and the CM can be compensated by the absorption or emission of a phonon, resulting in a transfer of excitation from the exciton to the cavity mode field[115, 165]. This process is known as off-resonant phonon cavity feeding and can be included in the TLS-cavity model by adding another Lindblad term[219]

$$\hat{L}_{ph} = \sqrt{\Gamma_{ph}} \hat{\sigma}_- \hat{a}^\dagger \quad (3.40)$$

with Γ_{ph} the phonon-scattering rate. This expression neglects back-scattering (the absorption of a cavity photon by the TLS mediated by the phonons) which is valid in the bad cavity regime. The physics of the exciton-phonon interaction is then included

Chapter 3. Cavity quantum electrodynamics with semiconductor quantum dots

in the phonon scattering rate which is a function of the detuning δ and the temperature T . It can be expressed using Fermi's Golden rule[164] as

$$\Gamma_{ph}(\delta) = \frac{2\pi}{\hbar^2} \left(\frac{g}{\delta} \right)^2 D(\delta) \quad (3.41)$$

with $D(\Omega)$ the effective phonon density of states that includes the information of about the phonon modes interacting with the TLS. We assume the QD interacts only with longitude acoustic (LA) phonons and we neglect the contribution of longitude optical (LO) phonons because of their large energies ($\sim 37 \text{ meV}$)[166]. The effective phonon density of states[166] is given by

$$D(\Omega) = \pi \sum_{\mathbf{k}} |M_{\mathbf{k}}|^2 [n(\omega_{\mathbf{k}})\delta(\Omega + \omega_{\mathbf{k}}) + (n(\omega_{\mathbf{k}}) + 1)\delta(\Omega - \omega_{\mathbf{k}})] \quad (3.42)$$

where the TLS is assumed to interact with a continuum of phonon modes, \mathbf{k} denoting the k^{th} phonon mode. $n(\omega_{\mathbf{k}}) = [\exp(\hbar\omega_{\mathbf{k}}/k_B T) - 1]^{-1}$ is the Bose-Einstein distribution and $M_{\mathbf{k}}$ is the electron-phonon interaction matrix element[166] written

$$M_{\mathbf{k}} = \sqrt{\frac{\hbar k}{2\rho c_s V}} D \int d^3\mathbf{r} |\phi(\mathbf{r})|^2 e^{-i\mathbf{k}\cdot\mathbf{r}}. \quad (3.43)$$

Here $D = D_e - D_g$ is the difference of the TLS excited and ground state deformation potentials, V is the phonon quantization volume, c_s is the speed of sound in the material and ρ is the mass density. We assume here the same Gaussian wave function for the ground and excited states, i.e., for a confined electron in the valance and conduction bands, given by

$$\phi(\mathbf{r}) = \frac{1}{\sqrt{\pi^{\frac{3}{2}} l^2 l_z}} e^{-(x^2+y^2)/2l^2} e^{-z^2/2l_z^2}. \quad (3.44)$$

with l the confinement length of the electrons in the (x, y) plane and l_z their confinement length in the z direction. This anisotropic confinement is consistent with site-controlled pyramidal QDs that exhibit a stronger confinement in the growth direction (z direction). By combining expressions (3.42), (3.43) and (3.44) we computed the following expression for the effective phonon density of states (see appendix A.1 for

3.3. Modeling semiconductor dephasing effects

details)

$$D(\Omega) = \frac{\hbar D^2}{16\rho c_s^4 \sqrt{\pi}} \Omega^2 [n(\Omega) - n(-\Omega) + 1] e^{-\Omega^2 l^2 / 2c_s^2} \frac{\text{erf}\left[\frac{\Omega}{c_s} \sqrt{\frac{l_z^2 - l^2}{2}}\right]}{\sqrt{\frac{l_z^2 - l^2}{2}}} \quad (3.45)$$

which finally gives for the phonon scattering rate

$$\Gamma_{ph} = \frac{2\pi}{\hbar^2} A g^2 [n(\delta) - n(-\delta) + 1] e^{-\delta^2 l^2 / 2c_s^2} \frac{\text{erf}\left[\frac{\delta}{c_s} \sqrt{\frac{l_z^2 - l^2}{2}}\right]}{\sqrt{\frac{l_z^2 - l^2}{2}}} \quad (3.46)$$

with $A = \frac{\hbar D^2}{16\rho c_s^4 \sqrt{\pi}}$.

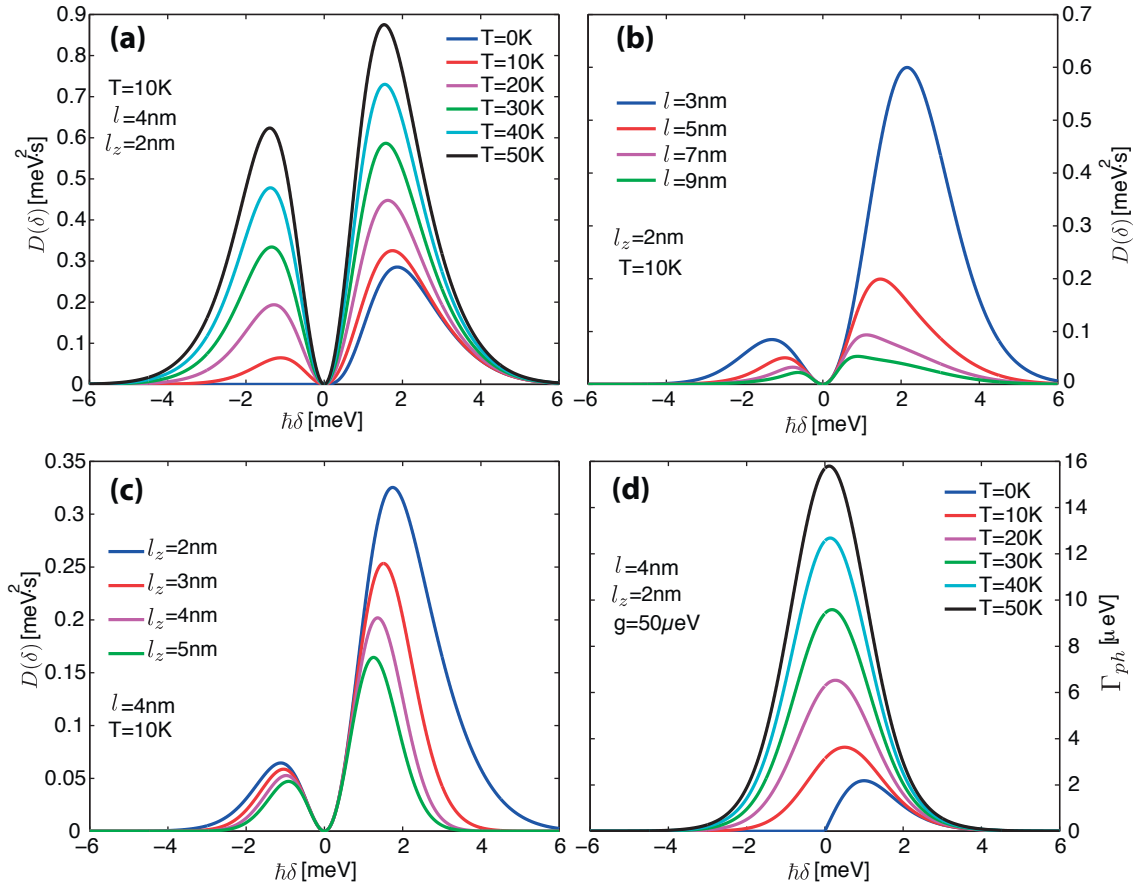


Figure 3.5: Effective phonon density of states for different temperatures (a), in-plane (b) and out-of-plane (c) confinement lengths. (d) Phonon scattering rate calculated for different temperatures. Parameters: $c_s = 5110\text{ m/s}$, $D = -10\text{ eV}$ and $\rho = 5370\text{ Kg/m}^3$.

Chapter 3. Cavity quantum electrodynamics with semiconductor quantum dots

The behaviour of the phonon density of states and phonon scattering rate with detuning is illustrated in Fig. 3.5 using realistic parameters for InAs/GaAs QDs[220]: $c_s = 5110 \text{ m/s}$, $D = -10 \text{ eV}$ and $\rho = 5370 \text{ Kg/m}^3$. Fig. 3.5 shows the effective phonon density dependence on detuning for different temperatures and confinement lengths. The asymmetry of the phonon scattering process, with respect to detuning, is visible and more pronounced for low temperatures. For low temperatures, the phonon bath is less populated, which renders the emission of a phonon ($\delta = \omega_0 - \omega_c > 0$) during the interaction process more efficient than the absorption of a phonon ($\delta < 0$). The phonon density of state is null for $\delta < 0$ at $T = 0 \text{ K}$ because the phonon bath is not populated. When the temperature is increased, this asymmetry is quenched due to the thermal excitation of phonons. The effective density exhibits two peaks centered on $\sim \pm 2 \text{ meV}$, indicating that phonons with an energy around 2 meV interact more significantly with the QD exciton. The effective phonon density of state was measured in a recent experimental and theoretical study[131]. Fig. 3.5 (b) and (c) show that the energy associated with the peaks of $D(\delta)$ is inversely proportional to the exciton confinement length. In fact it can be estimated by $2\hbar c_s/l \sim 1.7$ for $l = 4 \text{ nm}$ [102]. The phonon scattering rate Γ_{ph} is displayed in Fig. 3.5 (d) for different temperatures.

3.4 Simulating photoluminescence spectra

Now that we have a master equation in the Lindblad form describing the dynamics of a cavity coupled to a TLS undergoing pure dephasing and phonon scattering, we apply it to our system comprising of a single pyramidal QDs coupled to the fundamental mode of an L_3 photonic crystal cavity illustrated in Fig. 3.6 (the fabrication of these QD-cavity structures is detailed in chapter 2 and the photoluminescence experiments presented in chapter 5). This requires several assumptions listed below

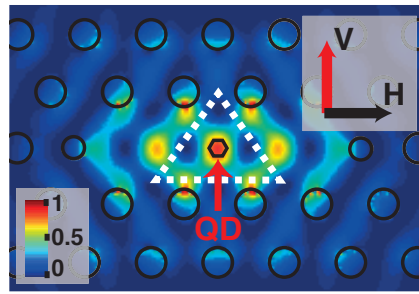


Figure 3.6: Schematic of the experimental QD-cavity system.

- Since the higher order mode of the L_3 cavity are separated by more than 80 meV , when $\delta \sim 1 - 3 \text{ meV}$, we can approximate the L_3 cavity by a single mode cavity described by the Hamiltonian given by H_{rad} .

3.4. Simulating photoluminescence spectra

- We assume the site-controlled pyramidal QD to be perfectly aligned with the PhC pattern, such that the QD exciton is located at the center of the cavity: $E(\mathbf{r}) = E(\mathbf{r}_m)$ and ϵ collinear with the V direction.
- Given the high in-plane symmetry of pyramidal QDs[221], the two QD exciton bright eigenstate are degenerate leading to a superposition of right and left circular polarization[222, 223]. This leads to a random orientation of the exciton dipole which gives

$$g_\theta \equiv g = \cos(\theta)\mu\sqrt{\frac{\omega_c}{2\hbar\epsilon(\mathbf{r}_m)V}} = \cos(\theta)g_0 \quad (3.47)$$

where θ is the angle between the V direction, with $\theta \in [0, 2\pi]$. This random dipole approximation was shown to be in good agreement with experiments[47].

- In the experiments the QD is excited by a cw-laser pump with an energy greater than the GaAs bandgap. This incoherent pumping is described by the Lindblad term

$$\hat{L}_P = \sqrt{P}\hat{\sigma}_+ \quad (3.48)$$

with P the incoherent pumping rate.

We summarize below the master equation of the system:

$$\dot{\hat{\rho}}_r = -\frac{i}{\hbar}[\hat{H}_{tot}^\theta, \hat{\rho}_r] - \frac{1}{2}\left\{\sum_l \hat{L}_l^\dagger \hat{L}_l, \hat{\rho}_r\right\} + \sum_l \hat{L}_l \hat{\rho}_r \hat{L}_l^\dagger \quad (3.49)$$

with

$$\hat{H}_{tot}^\theta = \hbar\omega_0\hat{\sigma}_+\hat{\sigma}_- + \hbar\omega_c\hat{a}^\dagger\hat{a} + \hbar\cos(\theta)g_0(\hat{a}^\dagger\hat{\sigma}_- + \hat{a}\hat{\sigma}_+) \quad (3.50)$$

and the Lindblad operators \hat{L}_γ , \hat{L}_κ , \hat{L}_d , \hat{L}_{ph} and \hat{L}_P given by (3.29), (3.30), (3.39), (3.40) and (3.48) respectively. A schematic of the model is given in Fig. 3.7 (a).

The master equation is solved numerically, through the Wiener-Khintchine theorem[215], yielding the steady-state power spectra for the TLS (S_{TLS}^θ) and cavity mode

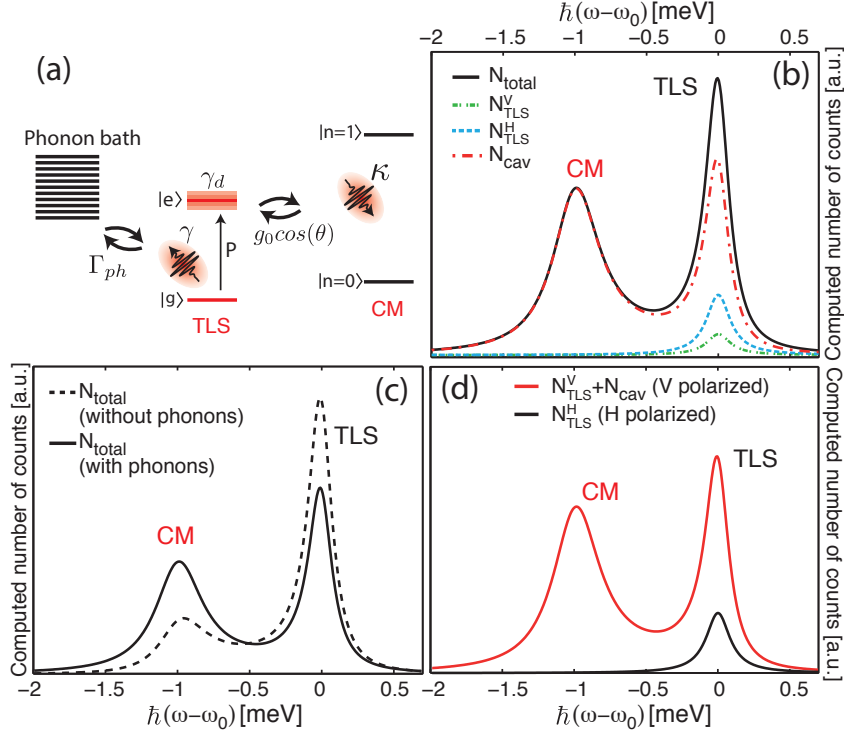


Figure 3.7: **Model of QD-cavity interactions:** (a) Schematic of the model describing the TS-cavity system. The decay rates of the two TLS and the cavity mode are γ and κ respectively. The coupling strength between the TLS and the CM is g_0 . The TLS pure dephasing rate is γ_d and the phonon scattering rate Γ_{ph} . (b) Computed PL spectrum N_{total} , N_{TLS}^V , N_{TLS}^H and N_{cav} (see text for parameter values). (c) PL spectra with the same simulation parameters as in (b), with (solid line) and without (dashed line) TLS-phonon interaction. (d) Computed PL spectrum linearly resolved in polarization along the directions indicated in Fig. 3.6 (same simulation parameters as in (b)).

(S_{cav}^θ) emissions:

$$S_{TLS}^\theta(\omega) = \int_{-\infty}^{\infty} \lim_{t \rightarrow \infty} \langle \hat{\sigma}_+(t+\tau) \hat{\sigma}_-(t) \rangle e^{-i\omega t} d\tau \quad (3.51)$$

$$S_{cav}^\theta(\omega) = \int_{-\infty}^{\infty} \lim_{t \rightarrow \infty} \langle \hat{a}^\dagger(t+\tau) \hat{a}(t) \rangle e^{-i\omega t} d\tau. \quad (3.52)$$

Following Auffèves et al. [224], we computed the following quantities

$$N_{TLS}^\theta(\omega) = |F_{at}|^2 \gamma S_{TLS}^\theta(\omega) \quad (3.53)$$

and

$$N_{cav}^\theta(\omega) = |F_{cav}|^2 \kappa S_{cav}^\theta(\omega). \quad (3.54)$$

3.4. Simulating photoluminescence spectra

that correspond to the QD exciton and CM spectra. The geometry of PhC systems prevents the straight-forward separation of the QD and cavity contributions in the PL spectrum since the sum of the QD and CM emission is collected by the microscope objective placed above the PhC. Furthermore, it is interesting to compare the simulations to spectra resolved in linear polarization along the V and H directions, which leads to the following definition of the V and H components of the simulated spectra

$$N_{total}^V(\omega) = \sum_{\theta} [N_{cav}^{\theta}(\omega) + \cos(\theta)^2 N_{TLS}^{\theta}(\omega) + \cos(\theta) F_{cav}^* F_{TLS} \sqrt{\kappa\gamma} S_{cav;TLS}^{\theta}(\omega) + \cos(\theta) F_{TLS}^* F_{cav} \sqrt{\gamma\kappa} S_{TLS;cav}^{\theta}(\omega)] \quad (3.55)$$

and

$$N_{total}^H(\omega) = \sum_{\theta} \sin(\theta)^2 N_{TLS}^{\theta}(\omega) \quad (3.56)$$

where the coefficients F_{at} and F_{cav} describe coupling efficiencies to the photon detector and relative phases of the TLS and cavity mode decay channels, respectively, and the last two terms of the sum in (3.55) account for the interferences between the TLS and cavity decay channels[143, 161] with

$$S_{cav;TLS}^{\theta}(\omega) = \int_{-\infty}^{\infty} \lim_{t \rightarrow \infty} \langle \hat{a}^{\dagger}(t + \tau) \hat{\sigma}_{-}(t) \rangle e^{-i\omega t} d\tau \quad (3.57)$$

$$S_{TLS;cav}^{\theta}(\omega) = \int_{-\infty}^{\infty} \lim_{t \rightarrow \infty} \langle \hat{\sigma}_{+}(t + \tau) \hat{a}(t) \rangle e^{-i\omega t} d\tau. \quad (3.58)$$

We find that these interference terms do not modify the qualitative conclusions of our study and thus neglect them in the rest of this report. F_{at} and F_{cav} describe coupling efficiencies to the photon detector and relative phases of the TLS and cavity mode decay channels, respectively. We take the sum over all values of theta to account for all possible QD exciton dipole orientations, since the PL integration time is much larger than the TLS radiative lifetime. The total spectrum is then given by

$$N_{total} = N_{total}^V(\omega) + N_{total}^H(\omega). \quad (3.59)$$

Fig. 3.7 (b) shows the computed spectra $N_{total}(\omega)$, $N_{cav}(\omega)$, $N_{TLS}^V(\omega) = \sum_{\theta} \cos(\theta)^2 N_{TLS}^{\theta}(\omega)$ and $N_{TLS}^H(\omega) = \sum_{\theta} \sin(\theta)^2 N_{TLS}^{\theta}(\omega)$ for the following realistic simulation parameters: $\hbar\delta = 1 \text{ meV}$, $\hbar\kappa = 400 \text{ } \mu\text{eV}$, $\hbar\gamma = 0.2 \text{ } \mu\text{eV}$, $\hbar\gamma_d = 200 \text{ } \mu\text{eV}$, $\hbar g_0 = 50 \text{ } \mu\text{eV}$, $\frac{2\pi}{\hbar} A = 0.8 \text{ nm/meV}$, $T = 10 \text{ K}$, $\hbar P = 0.1 \text{ } \mu\text{eV}$, $\ell = 4 \text{ nm}$, $\ell_z = 2 \text{ nm}$, $F_{cav} = 0.4$ and $F_{at} = 0.3$. Fig. 3.7 (c) shows $N_{total}(\omega)$ without ($A = 0$) and with ($\frac{2\pi}{\hbar} A = 0.8 \text{ nm/meV}$) phonon assisted cavity feeding (other parameters are as in Fig. 3.7 (b)). Resolution of the

Chapter 3. Cavity quantum electrodynamics with semiconductor quantum dots

simulated emission spectra into V and H components is shown in Fig. 3.7 (d).

3.4.1 Photoluminescence spectra for N quantum dots

Small modifications to the master equation allow to compute the spectrum of N QDs coupled to the same CM. For N QDs, the master equation reads

$$\dot{\hat{\rho}}_r = -\frac{i}{\hbar}[\hat{H}_{tot}^{\theta,N}, \hat{\rho}_r] - \sum_N \left(\frac{1}{2} \left\{ \sum_l \hat{L}_l^{N\dagger} \hat{L}_l^N, \hat{\rho}_r \right\} - \sum_l \hat{L}_l^N \hat{\rho}_r \hat{L}_l^{N\dagger} \right) \quad (3.60)$$

with

$$\hat{H}_{tot}^{\theta,N} = \sum_N \hbar\omega_0 \hat{\sigma}_+^N \hat{\sigma}_-^N + \hbar\omega_c \hat{a}^\dagger \hat{a} + \sum_N \hbar \cos(\theta) g_0^N (\hat{a}^\dagger \hat{\sigma}_-^N + \hat{a} \hat{\sigma}_+^N) \quad (3.61)$$

which is essentially the Tavis-Cummings Hamiltonian[225]. The N^{th} QD power spectra becomes

$$S_{\text{TLS}}^{\theta,N}(\omega) = \int_{-\infty}^{\infty} \lim_{t \rightarrow \infty} \langle \hat{\sigma}_+^N(t + \tau) \hat{\sigma}_-^N(t) \rangle e^{-i\omega t} d\tau \quad (3.62)$$

The V and H components of the total simulated spectra are then

$$N_{total}^V(\omega) = \sum_N \sum_{\theta} [N_{\text{cav}}^{\theta}(\omega) + \cos(\theta)^2 N_{\text{TLS}}^{\theta,N}(\omega)] \quad (3.63)$$

and

$$N_{total}^H(\omega) = \sum_N \sum_{\theta} \sin(\theta)^2 N_{\text{TLS}}^{\theta,N}(\omega) \quad (3.64)$$

with

$$N_{\text{TLS}}^{\theta,N}(\omega) = |F_{at}|^2 \gamma^N S_{\text{TLS}}^{\theta,N}(\omega). \quad (3.65)$$

The Tavis-Cummings Hamiltonian describe the interaction of N TLSs with a single mode of a radiation field. Although the N TLSs are not interacting with each other (no dipole-dipole interactions), their mutual coupling to the same optical mode can lead to cooperative behavior[226]. In particular, under certain conditions, the collective coupling of the TLSs to the radiation field can lead to an increase of the decay rate. This collective spontaneous emission, referred to as super-radiance, has been the

subject of many theoretical and experimental studies[227] since the pioneering article of Dicke[228]. Recently, the progress of solid-state cavity-QED system, in which several emitters can be coupled to the same optical mode, renewed the interest for the Tavis-Cummings Hamiltonian. Recent experimental studies of multiple solid-state emitters coupled to nanocavities are reviewed in chapter 5.

One striking feature of the Tavis-Cummings Hamiltonian is the non-linear scaling of the vacuum Rabi splitting with the number of emitters. In the strong coupling regime, when the N TLSs are resonant with the CM, the cavity absorption spectrum consists of two peaks separated by $2\hbar\sqrt{N}g$ [229]. When $N = 1$ this corresponds to the result found in subsection 3.1.3 for a single TLS interacting with a CM.

This situation is illustrated in Fig. 3.8 (a) that shows the CM spectrum $N_{cav}^{\theta}(\omega)$ calculated with the model presented above for $N = 1$ and $\theta = 0$. The CM spectrum for $N = 2$ is also shown in Fig. 3.8 (a) and exhibits a larger splitting given by approximately $2\hbar\sqrt{2}g$. The vacuum Rabi splitting extracted from the simulations for $N = 1 - 5$ is compared to the theoretical Rabi splitting $2\hbar\sqrt{N}g$ in Fig. 3.8 (b), showing a good agreement between the simulations and the exact solution. A similar situation in the weak coupling regime is illustrated in Fig. 3.8 (c) for $N = 2$. Here the high losses of the cavity damp the vacuum Rabi oscillations and the total spectrum of the TLS-cavity system consists of a single peak. The spectrum for $N = 2$ is compared to the sum of the spectrum of two independent TLS-cavity systems. Interestingly, the peak intensity is larger for $N = 2$, indicating the TLSs are collectively coupled to CM, resulting in an increase of the emission rate. This effect is even more pronounced for 3 TLSs as shown in Fig. 3.8 (d). This increase of the emission intensity when the TLSs are collectively coupled to the CM is a sign of super-radiant emission. For N TLS initially inverted, the super-radiant emission translates in a peak intensity and decay rate N times larger than the emission of N independent TLSs[230]. In Fig. 3.8 (c) and (d) this ratio is not respected, probably because the pumping rate is not high enough to fully invert the TLSs and introduces decoherence detrimental to the super-radiant behavior. The simulations in Fig. 3.8 (a)-(d) were performed without pure dephasing and phonon scattering.

Fig. 3.8 (e) shows the spectra of 2 TLSs detuned by $\pm 0.5 meV$ from the CM transition in the presence of pure dephasing and phonon cavity feeding. The off-resonant CM emission is fed by both QDs. However, due to the asymmetry of phonon cavity feeding, the contribution from the blue-shifted TLS is more important, as shown by the spectrum of each TLS, individually coupled to the CM (blue and green lines). The sum of the individual TLS spectra (dark line) reproduces the spectrum of the 2 TLS coupled to the CM, indicating the absence of super-radiant emission. The decoherence induced by the dephasing processes and the finite TLS-CM detunings destroy the coherent interaction of the TLSs with the optical field.

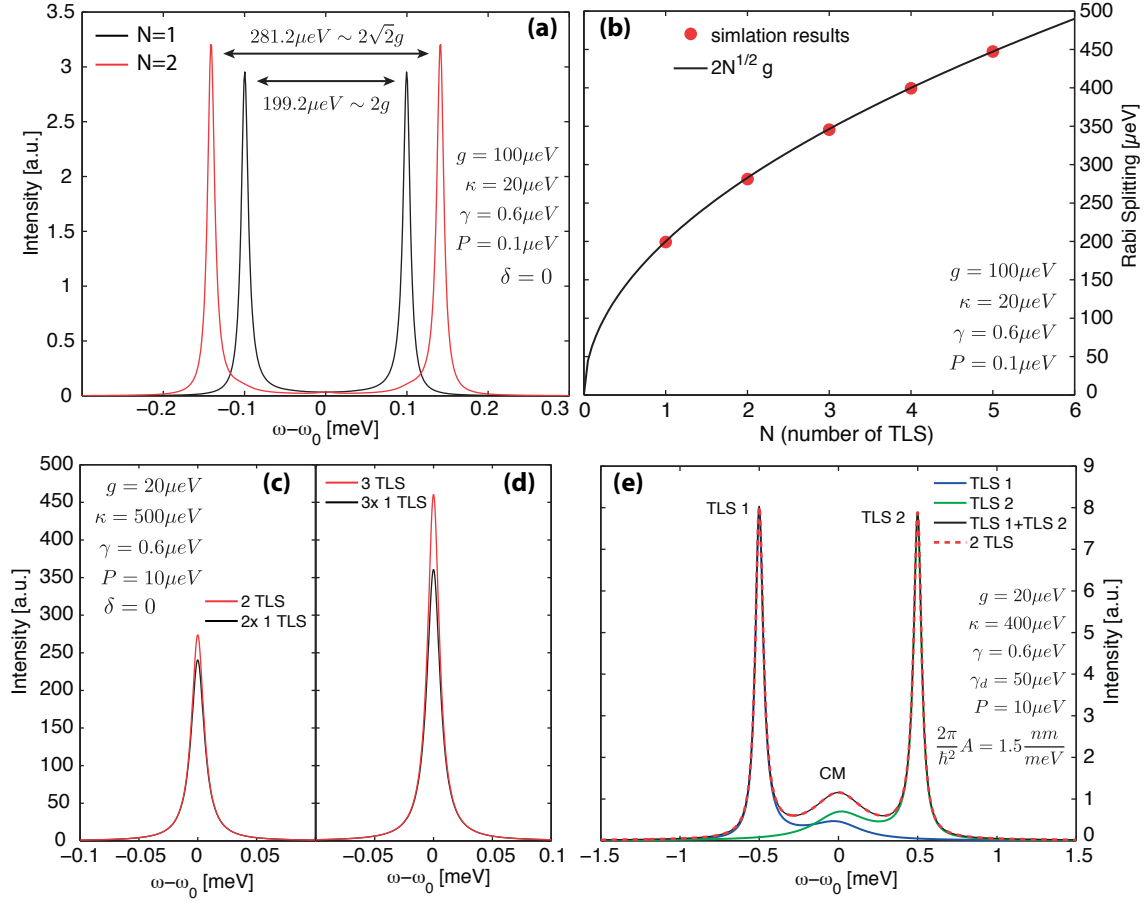


Figure 3.8: (a) Simulated CM spectrum $N_{cav}^\theta(\omega)$ for $N = 1$ and 2 TLSs resonant with the CM transition in the strong coupling regime ($\gamma_d = 0$ and $A = 0$). (b) Vacuum Rabi splitting extracted from the simulations as a function of the number of TLSs, compared to the analytic expression $2\sqrt{N}g$. (c) Calculated total spectrum of the TLS-CM system for $N = 2$ (red line) in the weak coupling regime, compared to the sum of spectra of 2 TLSs individually coupled to the CM (dark line). (d) Same as (c) with $N = 3$. (e) Spectrum of 2 TLSs detuned by $\pm 0.5 \text{ meV}$ from the CM transition compared to the spectra of 2 TLSs sequentially coupled to the CM (blue and green lines), including pure dephasing and phonon scattering. (a)-(e) Simulation performed for $\theta = 0$. To simplify the notation, the factor \hbar was omitted in this figure. For each simulation, the TLSs are assumed identical and coupled to the CM with the same coupling strength g .

3.5 Chapter summary

In this chapter we reviewed the theoretical formalism describing the quantum interaction of a TLS and the confined electric field of a cavity. The dynamics of the open-system Jaynes-Cummings model in the Lindblad form was presented, leading to the definition of the strong and weak coupling regimes. Motivated by the possibility to model a QD excitonic transition by a TLS transition, the interaction of the QD with the solid-state environment was included in the open-system Jaynes-Cummings model by adding appropriate Lindblad terms. The interaction of the QD with the fluctuating electrostatic environment was modeled by a pure dephasing Lindblad term. The interactions of the QD exciton with acoustic phonons were taken into account by an effective cavity feeding Lindblad term, with a characteristic phonon scattering rate calculated for pyramidal QDs using a microscopic description of the QD-phonon interaction. Finally, the procedure used to calculate the spectrum of site-controlled pyramidal QDs coupled to the fundamental mode of an L_3 photonic crystal cavity was explicated, and extended to general case of N QDs coupled to the same CM. In chapter 5, this QD-cavity model is used to fit the spectrum of one and two pyramidal QDs embedded in an L_3 PhC cavity.

4 Exciton complexes in site-controlled pyramidal quantum dots

Interpreting the photoluminescence (PL) spectrum of quantum dots (QDs) coupled to nanocavities can be a challenging task given the complex electronic properties of semiconductor QDs. In chapter 1 we saw that QD s-states can be populated by several excitonic species with different transition energies, that can all potentially interact with the cavity mode (CM). Comparing a QD-cavity system to a single two-level system (TLS) interacting with a CM, as presented in chapter 3, thus requires a detailed knowledge of the QDs electronic properties. In particular, knowing which excitonic species populate the QD and what are their spectral and dynamical characteristics is essential for interpreting properly the luminescent features of a QD-cavity system.

Apart from these practical considerations, the study of excitonic complexes in semiconductor QDs revealed fascinating physics and opened the way to many potential applications in quantum information processing and quantum communication protocols. Several schemes relying on spins of excitons (X) and biexcitons (2X) confined in QDs, called forth the need to control the biexciton binding energy. In particular, large binding energies are desired for realizing quantum logic gates[231] and vanishing binding energy is of particular relevance for producing entangled pairs of photons through time reordering of 2X-X radiative cascaded emission[232]. The 2X binding energy is determined by the interplay of quantum confinement, Coulomb correlations and exchange interactions[233], and therefore strongly depends on the QD geometry, composition and environment. Since the conjecture of their existence by Lampert[234] and their observation by Haynes[235], extensive work has been performed on these excitonic molecules. After establishing the existence of 2X states in QDs [236], efforts were made to control their binding energy, in particular with an external electric field[237]. However, application of an electric field is detrimental to spin relaxation, which is enhanced through the Rashba effect [238, 239]. Dependence on QD size[240–244] or piezoelectric fields [245] were exploited in the same perspective, but these studies were performed on a limited number of QDs, forbidding to realize statistical studies.

In this chapter, we present a detailed study of excitonic complexes formed in single, site-controlled pyramidal InGaAs/GaAs QDs integrated into non-resonant photonic crystal (PhC) slab cavities. Their fabrication procedure is explained in chapter 2. This chapter is divided into two sections. In section 4.1 we start by presenting the general spectral properties of single site-controlled pyramidal QDs. We then investigate more complex features of the QD luminescence by performing power dependent (subsection 4.1.1) and photon correlation (subsection 4.1.2) measurements, which also provide a rigorous identification of the QD's s-state excitonic features. Subsection 4.1.3 presents a statistical study of the excitonic binding energies, followed in subsection 4.1.4 by an investigation of QDs exhibiting a null 2X binding energy. Finally, time-resolved PL measurements of single pyramidal QDs are studied in section 4.2.

Some of the results presented in this chapter were published in reference [246].

4.1 Pyramidal quantum dots spectral properties

This section presents PL measurements performed on single pyramidal QDs embedded inside an L_3 PhC cavity, using the fabrication method presented in chapter 2. This chapter focuses on QDs with a transition energy inside the PhC band gap, but far detuned from the CM. An example of high excitation power, single QD spectrum is shown in Fig. 4.1. Compared to the QD ensemble spectra discussed in subsection 2.3.1, the single QD emission consists of fewer peaks. For this QD, the s-state emission is centered on 1.42 eV and consists of thin lines that will be discussed below. Due to the high excitation power ($1000\ \mu\text{W}$), the QD excited hole states, associated to an electron in the lowest energy state of the conduction band and a hole in the first excited state of the hole band, are populated and emit at 1.43 eV . At higher energies, the emission from the InGaAs quantum wires (QWRs) and carbon impurity of the GaAs material is visible, as was the case for QD ensemble spectra.

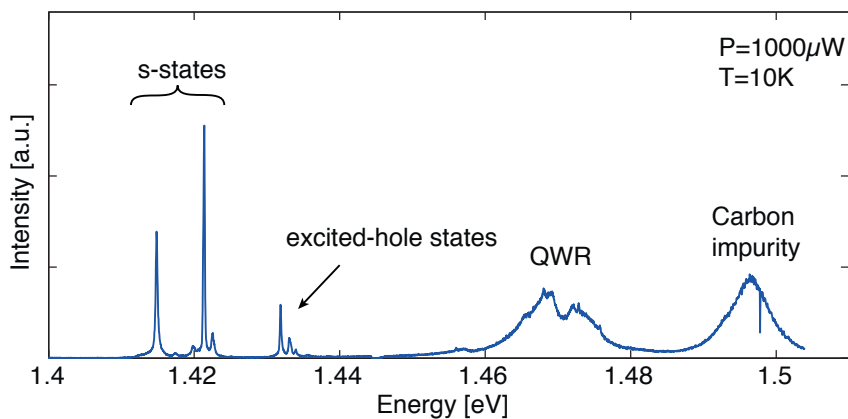


Figure 4.1: Spectrum of an isolated site-controlled pyramidal QD, embedded in an L_3 PhC cavity. The CM is far-off resonant from the QD emission and not visible in the spectrum.

4.1. Pyramidal quantum dots spectral properties

Systematic polarisation resolved PL measurements were performed on a large number of similar structures. A few typical spectra are presented in Fig. 4.2. The upper panel of each spectra shows the DOLP of the emission. No polarized emission is visible in the DOLP, indicating that no CM is present in the vicinity of the QD transitions and that the QD emission is unpolarized. This absence of linear polarization in the QD s-state emission is a consequence of the high structural symmetry of pyramidal QDs (see subsection 2.3.1) which results in a random in-plane statistical orientation of the exciton dipole moment. The absence of a 2D wetting layer in pyramidal QDs also ensures that no far-off resonant coupling with a far-detuned CM can occur.

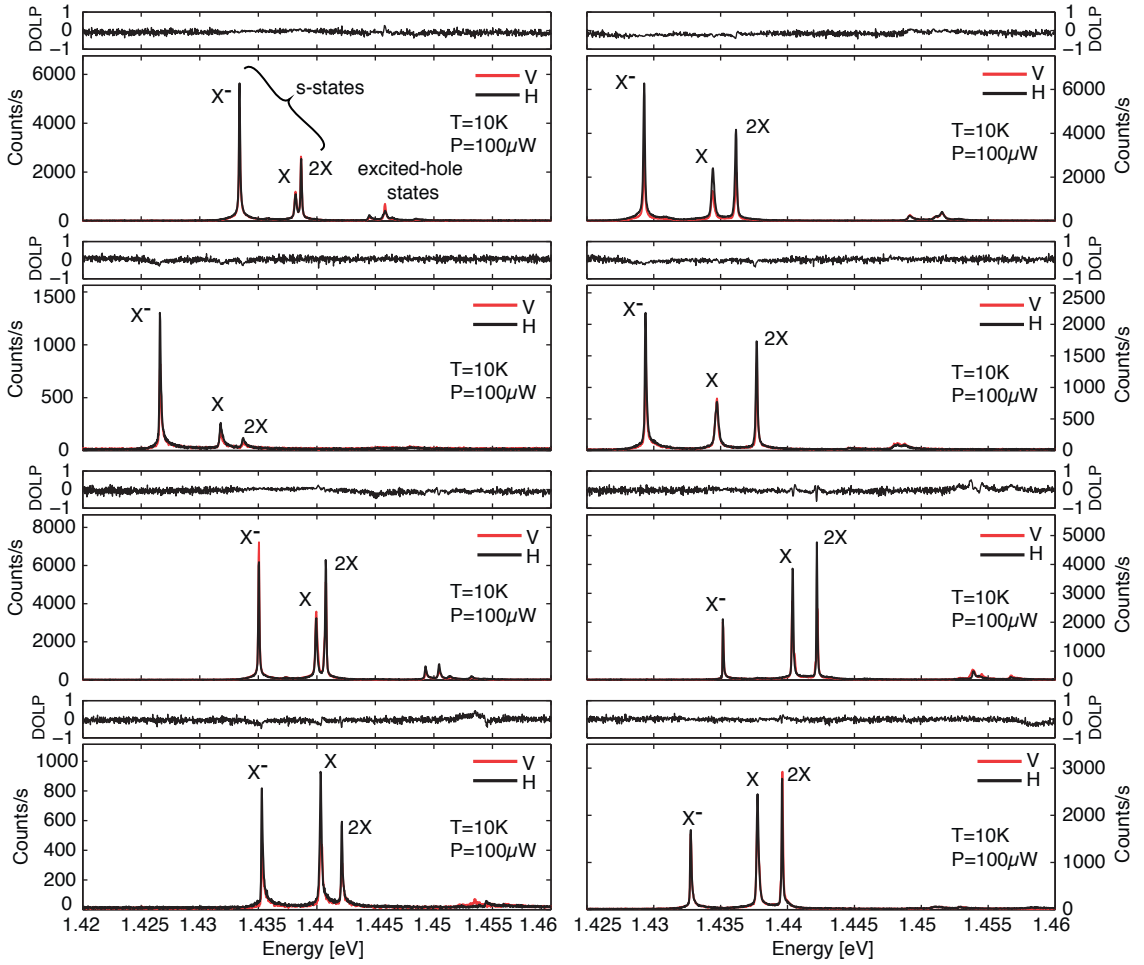


Figure 4.2: PL spectra of single pyramidal QDs in non-resonant L_3 PhC cavities. The spectra are resolved in linear polarisation along the axis perpendicular (V) and collinear (H) with the cavity elongation. The upper panel displays the corresponding DOLP.

The s-state emission of these QDs consists of only three peaks. As will be evidenced below, these three transitions correspond to the neutral exciton X , the biexciton $2X$ and the negatively charged exciton X^- . The excited-hole state emission is blue shifted from the s-state emission by 10 – 15 meV. For this low excitation power of 100 μW , the

QD spectrum is dominated by the s-state emission. The reproducibility of pyramidal QDs is already visible in Fig. 4.2, but becomes even more apparent in Fig. 4.3 (a) which displays the spectrum of 15 QDs. Three s-state transitions are systematically present in the s-state emission. The QDs transitions can be fitted by Lorentzian functions to retrieve their full width at half maximum (FWHM) as illustrated in Fig. 4.3 (b). This procedure was repeated for 30 QDs grown with TMGa precursors. The distribution of linewidth for the X , $2X$ and X^- transitions is summarized in Fig. 4.3 (c). The FWHM distribution is centered on $150 \mu\text{eV}$ for the X^- and $2X$ transitions, while the FWHM distribution of the neutral exciton is centered on $225 \mu\text{eV}$. These values are much larger than the lifetime limited linewidth (see chapter 1). Indeed, the transitions are broadened due to dephasing induced by carbon-related impurities incorporated in the bulk material during the growth process or by PhC hole surface states. The smaller linewidth observed for the $2X$ may be explained by its smaller lifetime with respect the neutral exciton[247, 248], which minimizes its interactions with the fluctuating electric field induced by fluctuating charges trapped in nearby defects or impurities.

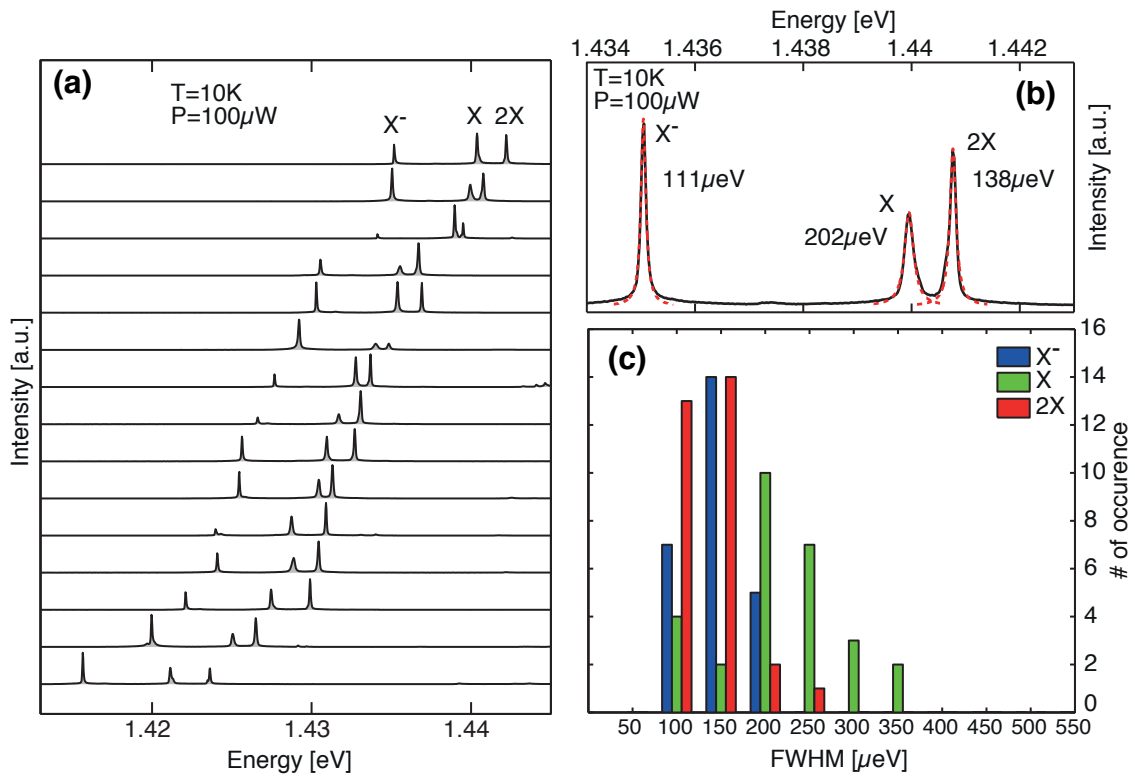


Figure 4.3: (a) PL spectra of QD s-state transitions. (b) Close-up on the s-state feature of a single QD. Lorentzian fits of the QD transitions (red dashed lines) were used to retrieve the peaks FWHM. (c) Distribution of the X , $2X$ and X^- FWHMs measured on 30 QDs.

4.1.1 Power dependent measurements

The excitonic species were identified by means of power dependent measurements[241, 242]. Such measurements performed on two pyramidal QD structures are summarized in Fig. 4.4. The PL spectra of the s-state emission is shown as a function of excitation power in Fig. 4.4 (a) and (b). For both QDs, the X and X^- transitions appear first for low excitation powers. Their intensity increases with increasing excitation power. When the pump power is further increased, the $2X$ transition appears and dominates the spectra for large excitation powers. The peaks integrated intensities are displayed as a function of pump power in Fig. 4.4 (c) and (d). The peaks integrated intensities increase linearly in loglog scale with increasing excitation power. For both QDs, the X

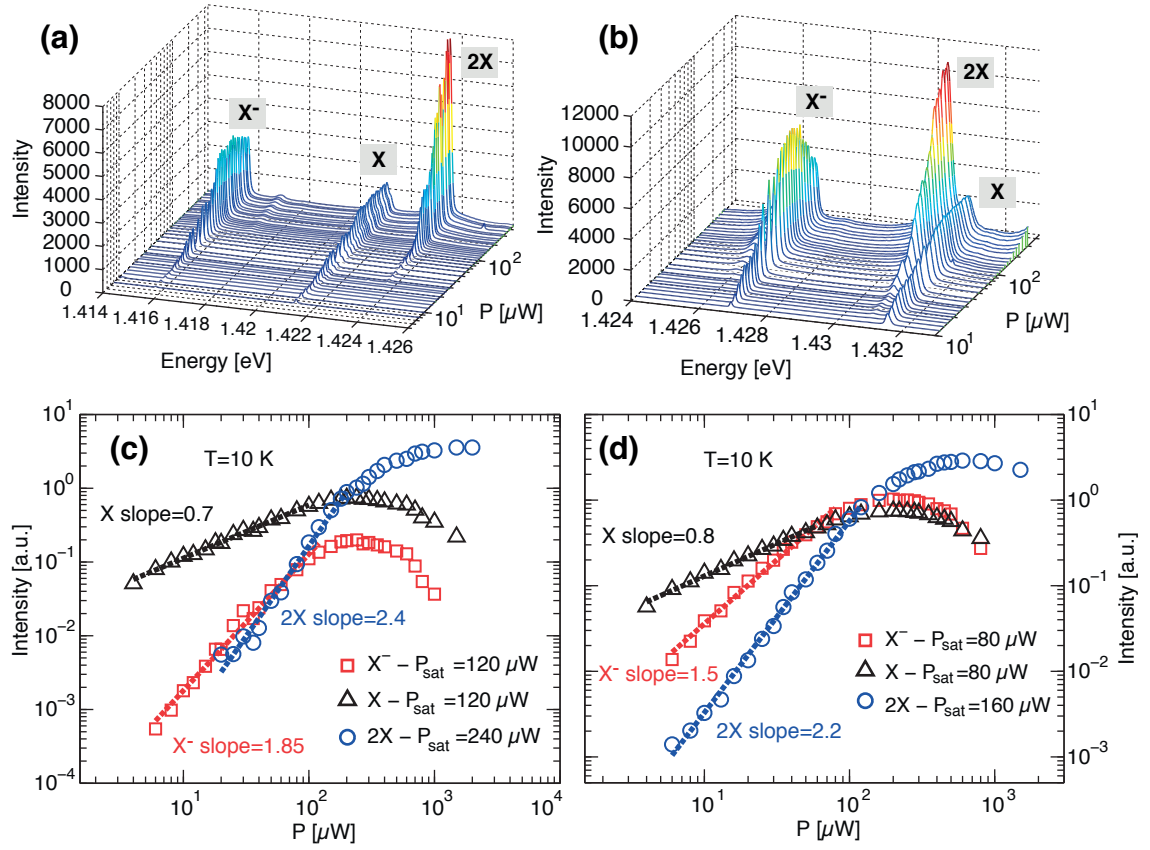


Figure 4.4: (a) and (b) Spectra displayed as a function of excitation power for two QDs. (c) and (d) Integrated intensities of s-state features of QDs (a) and (b) as a function of excitation power in loglog scale. Linear fits (dashed line) give the slopes indicated on the figure. Saturation powers P_{sat} are indicated in the figure's legend.

feature integrated intensity grows linearly with increasing excitation power as expected, while the $2X$ feature is characterized by a steeper slope[242, 249] and a saturation excitation power which is about twice that of the X . The third feature also shows a superlinear pump power dependence (slope of 1.85 and 1.5 for the QDs of Fig. 4.4 (c)

and (d) respectively), indicating that it belongs to a charged excitonic species, and saturates with the X line. Given the residual n-type background doping of our sample, its emission energy lower than the neutral exciton and the previous identifications made on similar pyramidal QDs[250–253], we attribute this third line to the X^- .

4.1.2 Photon correlation spectroscopy

The nature of the excitonic species is further investigated using photon correlation spectroscopy[186]. As explained in subsection 2.1.3, correlation measurements give access to the second order photon correlation function $g^2(\tau)$. Fig. 4.5 shows the measured second order correlation histograms acquired for the QD shown in Fig. 4.4 (a). For this QD, the complete correlation picture of the s-state emission requires 6 photon correlation measurements: the auto-correlation of the $2X$, X and X^- (Fig. 4.5 (a), (b) and (d) respectively) as well as their cross-correlations $2X - X$, $2X - X^-$ and $X - X^-$ (Fig. 4.5 (c), (e) and (f) respectively).

The corresponding g^2 functions can be calculated using the following three-level rate equation model

$$\begin{aligned}
 \frac{dp_0(t)}{dt} &= \frac{p_1(t)}{t_X} - \frac{p_0(t)}{t_{eh}} \\
 \frac{dp_1(t)}{dt} &= \frac{p_2(t)}{t_{2X}} + \frac{p_0(t)}{t_{eh}} - p_1(t) \left(\frac{1}{t_X} + \frac{1}{t_{eh}} \right) \\
 \frac{dp_2(t)}{dt} &= \frac{p_1(t)}{t_{eh}} - \frac{p_2(t)}{t_{2X}} \\
 p_0(t) + p_1(t) + p_2(t) &= 1.
 \end{aligned} \tag{4.1}$$

were $p_n(t)$ is the time dependent probability of the QD being occupied with $n = 0, 1$ and 2 e-h pairs. t_{2X} and t_X are the $2X$ and X decay rates respectively and t_{eh} is the e-h pair capture time. The solution to those three coupled differential equations are linked to the second order correlation function as follows:

$$\begin{aligned}
 \bullet \tau \geq 0: \quad g_{X,X}^2(\tau) &= \frac{p_1(\tau)}{p_1(\infty)} \\
 \tau < 0: \quad g_{X,X}^2(\tau) &= g_{X,X}^2(-\tau)
 \end{aligned}$$

4.1. Pyramidal quantum dots spectral properties

with initial conditions $p_0(0) = 1$, $p_1(0) = 0$ and $p_2(0) = 0$, for which:

$$p_1(t) = \frac{t_{eh}e^{-\frac{1}{2}t(\sqrt{4t_{eh}t_X+(t_X-t_{2X})^2+2t_{eh}+t_X+t_{2X}})}}{2(t_{eh}^2+t_{2X}(t_{eh}+t_X))} \left[\frac{((2t_{eh}^2+t_{2X}(t_X-t_{2X}))(e^{t\sqrt{4t_{eh}t_X+(t_X-t_{2X})^2}}-1))}{2\sqrt{4t_{eh}t_X+(t_X-t_{2X})^2}} \right. \\ \left. -t_{2X}e^{t\sqrt{4t_{eh}t_X+(t_X-t_{2X})^2}}+t_{2X}(2e^{\frac{1}{2}t(\sqrt{4t_{eh}t_X+(t_X-t_{2X})^2+2t_{eh}+t_X+t_{2X}})}-1) \right]. \quad (4.2)$$

$$\begin{aligned} \bullet \tau \geq 0: \quad g_{2X,2X}^2(\tau) &= \frac{p_2(\tau)}{p_2(\infty)} \\ \tau < 0: \quad g_{2X,2X}^2(\tau) &= g_{2X,2X}^2(-\tau) \end{aligned}$$

with initial conditions $p_0(0) = 0$, $p_1(0) = 1$ and $p_2(0) = 0$, for which:

$$p_2(t) = \frac{t_{eh}e^{-\frac{1}{2}t(\sqrt{4t_{eh}t_X+(t_X-t_{2X})^2+2t_{eh}+t_X+t_{2X}})}}{2(t_{eh}^2+t_{2X}(t_{eh}+t_X))} \left[-t_{eh}(1+e^{t\sqrt{4t_{eh}t_X+(t_X-t_{2X})^2}}) \right. \\ \left. +2t_{eh}e^{\frac{1}{2}t(\sqrt{4t_{eh}t_X+(t_X-t_{2X})^2+2t_{eh}+t_X+t_{2X}})} - \frac{(t_{eh}t_X-t_{2X}(t_{eh}+2t_X))(e^{t\sqrt{4t_{eh}t_X+(t_X-t_{2X})^2}}-1)}{\sqrt{4t_{eh}t_X+(t_X-t_{2X})^2}} \right]. \quad (4.3)$$

$$\begin{aligned} \bullet \tau \geq 0: \quad g_{2X,X}^2(\tau) &= \frac{p_1(\tau)}{p_1(\infty)}, \quad \text{with } p_0(0) = 0, p_1(0) = 1 \text{ and } p_2(0) = 0 \\ \tau < 0: \quad g_{2X,X}^2(\tau) &= \frac{p_2(-\tau)}{p_2(\infty)}, \quad \text{with } p_0(0) = 1, p_1(0) = 0 \text{ and } p_2(0) = 0. \end{aligned}$$

These initial conditions give the probability functions:

$$p_1(t) = \frac{e^{-\frac{1}{2}t(\sqrt{4t_{eh}t_X+(t_X-t_{2X})^2+2t_{eh}+t_X+t_{2X}})}}{2(t_{eh}^2+t_{2X}(t_{eh}+t_X))} \left[\frac{(-t_{eh}^2t_X+t_{2X}(t_{eh}+t_X)^2-t_Xt_{2X}^2)(e^{t\sqrt{4t_{eh}t_X+(t_X-t_{2X})^2}}-1)}{\sqrt{4t_{eh}t_X+(t_X-t_{2X})^2}} \right. \\ \left. +(t_{eh}^2+t_Xt_{2X})e^{t\sqrt{4t_{eh}t_X+(t_X-t_{2X})^2}} +2t_{eh}t_{2X}e^{\frac{1}{2}t(\sqrt{4t_{eh}t_X+(t_X-t_{2X})^2+2t_{eh}+t_X+t_{2X}})}+t_{eh}^2+t_Xt_{2X} \right] \quad (4.4)$$

$$p_2(t) = \frac{t_{eh}^2 e^{-\frac{1}{2}t(\sqrt{4t_{eh}t_X+(t_X-t_{2X})^2}+2t_{eh}+t_X+t_{2X})}}{2(t_{eh}^2 + t_{2X}(t_{eh} + t_X))} \left[\frac{((2t_{eh} + t_X + t_{2X})(-e^{t\sqrt{4t_{eh}t_X+(t_X-t_{2X})^2}} - 1))}{\sqrt{4t_{eh}t_X + (t_X - t_{2X})^2}} - e^{t\sqrt{4t_{eh}t_X+(t_X-t_{2X})^2}} + 2e^{\frac{1}{2}t(\sqrt{4t_{eh}t_X+(t_X-t_{2X})^2}+2t_{eh}+t_X+t_{2X})} - 1 \right]. \quad (4.5)$$

Background photon detection is taken into account following reference [254] by considering the noise influenced correlation function:

$$g_{A,B}^{2,N}(\tau) = \rho^2 g_{A,B}^2(\tau) + (1 - \rho^2), \quad (4.6)$$

with $A = X, 2X$, $B = X, 2X$ and $\rho = \frac{S}{S+N}$, with S the X or $2X$ photon detection rate and N the uncorrelated background photon detection rate. The finite response time of the HBT setup is taken into account by convoluting this function with a gaussian of FWHM equal to $t_{res}=700$ ps, giving:

$$g_{A,B}^{2,conv}(\tau) = \int_{-\infty}^{\infty} g_{A,B}^{2,N}(t) \frac{e^{-\frac{(\tau-t)^2}{2\sigma^2}}}{\sigma\sqrt{2\pi}} dt \quad (4.7)$$

with $\sigma = \frac{t_{res}}{2\sqrt{2\ln 2}}$.

These correlation functions were used to fit the correlations histograms of Fig. 4.5 and Fig. 4.6 (red dashed lines). Anti-bunching is observed in the $2X$ - $2X$, X - X and X^- - X^- autocorrelations, indicating that these QDs are single-photon sources. Indeed, after deconvolution of the HBT setup response time (700 ps) on the fits of Fig. 4.5 (b) and (d), we obtain $g_{X,X}^{2,N}(0) = 0.22$ and $g_{X^-,X^-}^{2,N}(0) = 0.01$. A high value of $\rho > 0.9$ was obtained for all the fits. The auto-correlation of the $2X$ feature shows antibunching for $\tau = 0$, followed by bunching shoulders for delay times of $\tau \approx \pm 2$ ns. Since we are not in a regime of high carrier density for which such a behavior can be expected for neutral excitons[255], this bunching is specific to the $2X$ - X radiative cascade. Indeed, when the probability of the QD being occupied by 1 e-h pair is lower than unity, the QD is more likely to be occupied by an exciton after the detection of the $2X$ emission, which increases the reexcitation probability of the $2X$ state[184]. This bunching behavior, specific to the $2X$ - X radiative cascade, is reproduced by the second order correlation function $g_{X,X}^2(t)$ obtained by solving the rate equation model described previously. The cross-correlation of the $2X$ and X features (Fig. 4.5 (c)) shows antibunching for negative delay time, and bunching for positive delay times, which is expected for the $2X - X$ radiative cascade. The fitting procedure gives e-h pair capture times varying between 2 and 4.8 ns. This variation can be due to the uncertainty on the exact position of the laser excitation spot during the measurement, which results in an uncertainty on the exact excitation power. The ratio of ~ 2 between the $2X$ and X decay times

4.1. Pyramidal quantum dots spectral properties

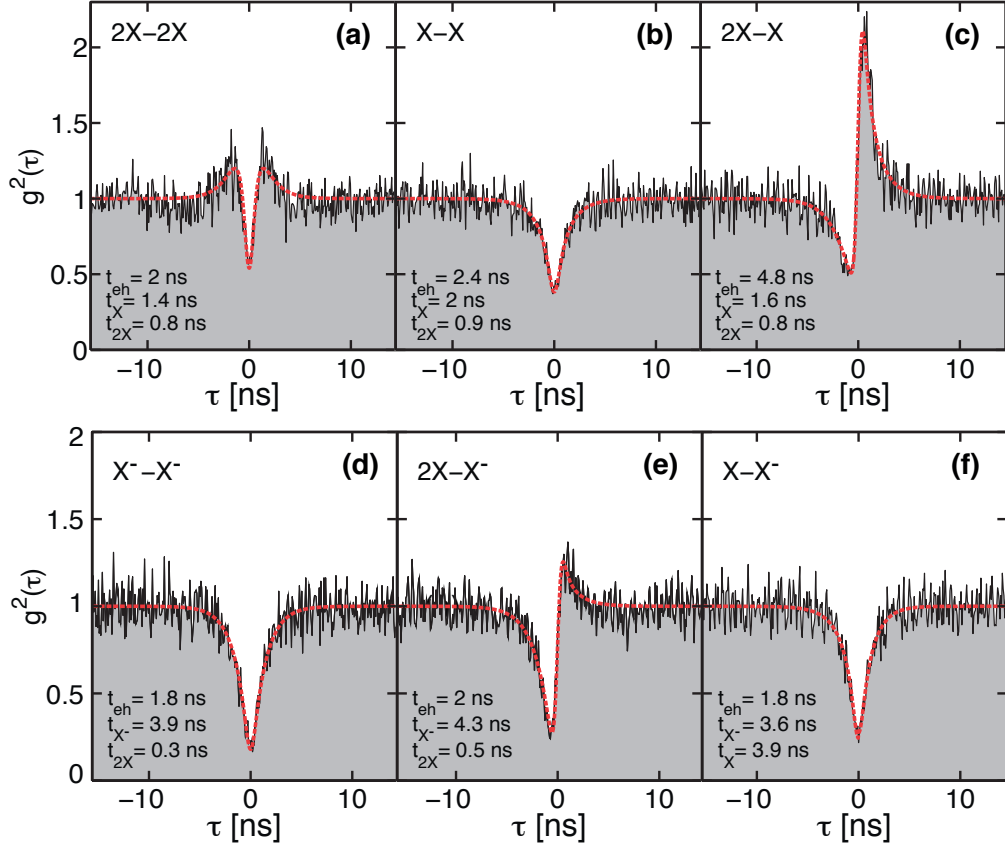


Figure 4.5: Second order correlation histograms for the QD of Fig. 4.4 (a) and (c) measured for an excitation power of $100 \mu W$. Autocorrelation histograms of the $2X$ (a), the X (b) and the X^- (d) spectral features. Cross-correlation histograms of (c) the $2X$ and X features, (e) the $2X$ and X^- features and (f) the X and X^- features. The histograms are normalized so as to correspond to the second order correlation function $g^2(\tau)$. A rate equation model describing the population dynamics of the QD was used to fit the data (red lines). After deconvolution of the HBT setup response time, the fits of (b) and (d) give $g_{X^-,X}^{2,N}(0) = 0.22$ and $g_{X^-,X^-}^{2,N}(0) = 0.01$.

obtained from the fits is in agreement with calculated values[256]. The correlation histograms featuring the X^- transition are shown in Fig. 4.5 (d)-(f). They were fitted using the same second order correlation functions used for the X and $2X$ correlations. Although a more complete system of rate equations would be preferable to fit the exact dynamic of the X^- transition, the simpler rate equation model used here is sufficient to understand the important features of the correlations. For example, the cross-correlation between the $2X$ and X^- lines show a less pronounced bunching for positive delay times than for the $2X - X$ cross-correlation. A possible explanation is the additional electron that has to be captured after the emission of the $2X$ photon, which reduces the probability of having subsequent X^- emission. This also explains the longer X^- decay times obtained from the fits, which include here the capture time of this additional electron. These measurements and fits were repeated for the QD of

Fig. 4.4 (b) and present a similar behaviour.

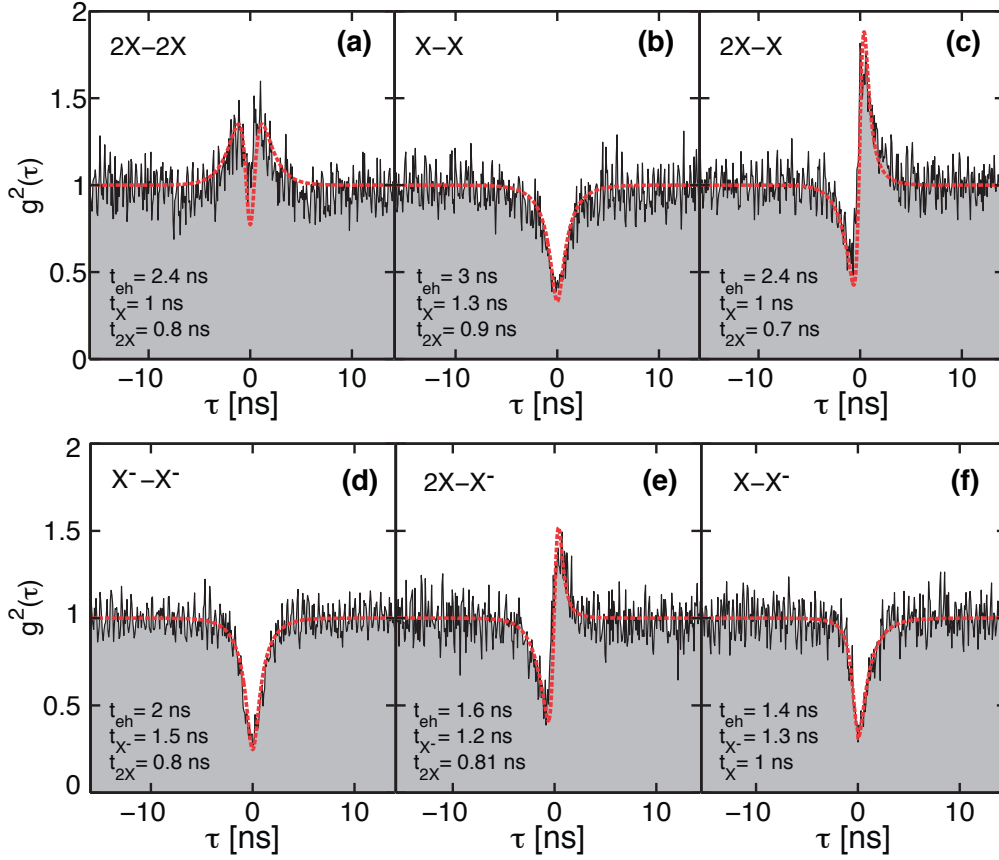


Figure 4.6: Second order correlation histograms for the QD of Fig. 4.4 (b) and (d) measured for an excitation power of $50 \mu W$. Autocorrelation histograms of the $2X$ (a), the X (b) and the X^- (d) spectral features. Cross-correlation histograms of (c) the $2X$ and X features, (e) the $2X$ and X^- features and (f) the X and X^- features. The histograms are normalized so as to correspond to the second order correlation function $g^2(\tau)$. A rate equation model describing the population dynamics of the QD was used to fit the data (red lines). After deconvolution of the HBT setup response time, the fits of (b) and (d) give $g_{X,X}^{2,N}(0) = 0.15$ and $g_{X^-,X^-}^{2,N}(0) = 0.01$.

4.1.3 Exciton binding energies

The X^- , X and $2X$ features were identified on the PL spectrum of 83 site-controlled pyramidal QDs using the power dependent and photon correlation measurements presented in sections 4.1.1 and 4.1.2. This allowed to measure for these QDs the binding energies of the $2X$ and the X^- excitonic species defined as $E_{2X}^B = E_X^{photon} - E_{2X}^{photon}$ and $E_{X^-}^B = E_X^{photon} - E_{X^-}^{photon}$ respectively, where E_X^{photon} , E_{2X}^{photon} and $E_{X^-}^{photon}$ stand for the X , $2X$ and X^- transition energies (see subsection 1.3.3). These binding energies are reported in Fig. 4.7 as a function of the energy of the X excitonic transition. The X^- binding energy shows very little dispersion with a mean value of 4.9 meV and

4.1. Pyramidal quantum dots spectral properties

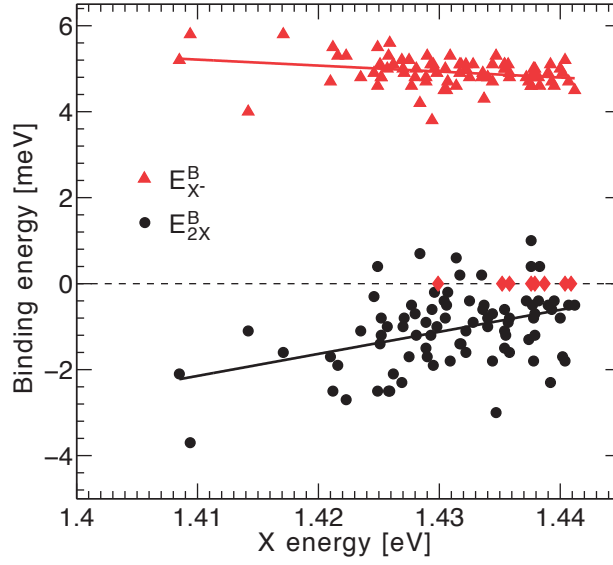


Figure 4.7: $2X$ binding energy (E_{2X}^B) and X^- binding energy ($E_{X^-}^B$) as a function of the energy of the X feature. The linear fits (black and red line) serve as guides to the eye. The red diamonds correspond to QDs assumed to have zero $2X$ binding energy. Reprinted with permission from [246]. Copyright 2012, AIP Publishing LLC.

remarkably small standard deviation of 0.33 meV. Most of the QDs studied exhibit negative $2X$ binding energy, including the QD of Fig. 4.4 (a). However, the dispersion of the $2X$ binding energy makes it possible to select dots with positive $2X$ binding energies in our sample (an example is given by the QD of Fig. 4.4 (b)). Moreover, the $2X$ binding energy increases slightly as the X emission energy increases. The variation in emission energy of the neutral exciton is attributed to fluctuations of the QD size, which impact the confinement of electrons and holes. An increase of the emission energy reflects a reduction of the QD size. It has been established previously from spectra of pyramidal QD ensembles that the QD emission yields a standard deviation of ~ 6 meV[81], which indicates a very good homogeneity of the QDs size. However, here, we rely on long range fluctuations of QD thickness due to long scale diffusion of the precursor during metalorganic chemical vapor deposition (MOCVD) growth, to achieve a more important variation of their emission energy (~ 30 meV). This made possible the observation of a reduction of E_{2X}^B , from 1 meV to -4 meV, as the QD size increases. Furthermore, we observe remarkably small binding energies of $\pm 200 \mu\text{eV}$ for some of the QDs. For 10% of the QDs, we observed only two s -state features in their PL spectra instead of the three usual ones (X , X^- and $2X$). We attribute the peak at lower energy to the X^- and the other at higher energy to the overlapping X and $2X$ transitions (denoted hereafter $X/2X$ transition). This attribution will be justified in the following section. The absolute emission energy of those dots is in the range corresponding to zero $2X$ binding energy. They are indicated by red diamonds in Fig. 4.7.

Chapter 4. Exciton complexes in site-controlled pyramidal quantum dots

A simple expression for the $2X$ binding energy is $E_{2X}^B = 2V_{Coul}^{e,h} - V_{Coul}^{e,e} - V_{Coul}^{h,h}$, where $V_{Coul}^{e,e}$, $V_{Coul}^{h,h}$ and $V_{Coul}^{e,h}$ are respectively the energies associated with electron-electron, hole-hole, and electron-hole Coulomb interactions (see subsection 1.3.3). The relative weight of these attractive and repulsive contributions is strongly dependent on the distribution of the electron and hole wave functions within the QD. The decrease of E_{2X}^B for larger QDs is believed to be caused by charge separation within the QD induced by increasing piezoelectric fields. Strain is more important in large QDs and is responsible for the presence of piezoelectric fields that affect the charge distribution. Separation of the electron and hole wave functions results in a reduction of $V_{Coul}^{e,h}$ and can also lead to an increase of $V_{Coul}^{e,e}$ and $V_{Coul}^{h,h}$. The $2X$ binding energy is thus reduced as the QD size, along with strain, is increased. This trend was also observed with site-selected InAs/InP QDs and was also attributed to the increase of piezoelectric fields with increasing QD size[240]. The opposite trend was observed with self-assembled InAs/GaAs QDs, where the decrease of the $2X$ binding energy with decreasing QD size was attributed to a quenching of particle correlation and exchange interactions[243]. In a different study relying on InGaAs/AlGaAs pyramidal QDs, no significant dependence of the $2X$ binding energy on the QD emission energy was observed[257]. This shows that the binding energy, which depends on few particle interaction effects, is strongly dependent on the QD geometry and chemical composition[258].

Effect of strain on the binding energies of excitonic complexes has been recently established[245]. In this simple model, the attractive and repulsive contributions can eventually compensate, giving rise to vanishing binding energies, which is consistent with the observation of zero $2X$ binding energy for 10 QDs of our sample (within the resolution of our PL setup, i.e., $80 \mu\text{eV}$). In a recent article, the effect of strain and electric fields on the X and $2X$ energies was combined to tune the $2X$ binding energy from binding to anti-binding while maintaining a constant X emission energy[259].

4.1.4 Null binding energy biexciton

We used power dependent measurements to clearly identify the zero $2X$ binding energy QDs and evidence the spectral overlap of the X and $2X$ features. If indeed the X line is spectrally superposed with the $2X$ transition, we expect their luminescence contributions to sum up in the power dependence of the $X/2X$ transition. Fig. 4.8 (a) shows the spectra of one of these QDs as a function of excitation power. Two main peaks are visible in the spectra. The lowest energy peak belongs to the X^- transition. The second peak, labelled $X/2X$, appears before the X^- , for low excitation powers, which would indicate it belongs to the X transition. However, this peak does not saturate with

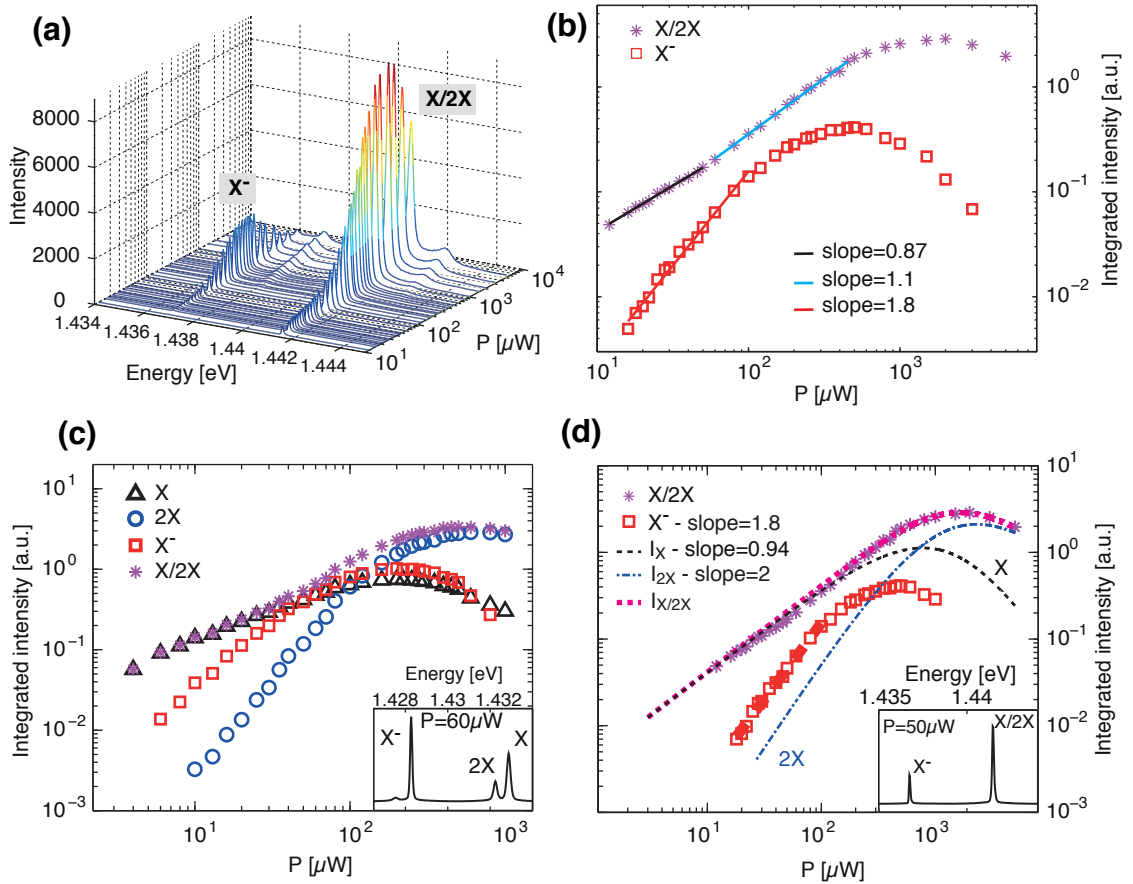


Figure 4.8: PL spectra (a) and peak integrated intensities (b) of a QD with null biexciton binding energy displayed as a function of excitation power. (c) QD of Fig. 4.4 (b) peaks integrated intensities versus pump power. The curve corresponding to the feature $X/2X$ (stars) is simply the sum of the X and $2X$ curves. Inset figure: PL spectrum of the corresponding QD. (d) QD with null $2X$ binding energy: the dotted lines X and $2X$ were retrieved from the fit of the $X/2X$ data (stars) with a rate equation model. Linear fits of the X , $2X$ and X^- curves before saturation were performed to retrieve the slopes indicated in the figure's legend. Inset figure: PL spectrum of corresponding QD where $X/2X$ denotes the spectrally overlapping X and $2X$ lines.

the X^- transition and behaves at high excitation powers like a $2X$ transition. Fig. 4.8 (b) shows the peaks integrated intensities as a function of pump power. In logarithmic scale, the integrated intensity of the X^- transition has a linear slope similar to what we observed for the QDs of Fig. 4.4 (a) and (b). The behaviour of the integrated intensity of the second peak is more peculiar. Indeed, although the integrated intensity increases with a slope of 0.87, above $P = 80 \mu W$, the slope increases to 1.1. Furthermore, this line saturates for $P = 300 \mu W$, which is approximately twice the saturation power of the X^- transition ($P_{sat} = 140 \mu W$). This behaviour is identical to what is observed for the sum of the X and $2X$ integrated intensities of a QD with finite $2X$ binding energy (Fig. 4.8 (c)). This indicates that the peak blue-shifted by $5 meV$ from the X^- in Fig. 4.8 (a) is very likely to be the superposition of the X and $2X$ features.

To confirm this assumption, we used the following four level rate equation model[133] to compute two analytical expressions giving the emission intensities of the X and $2X$ transitions as a function of pump power,

$$\frac{dp_0}{dt} = \frac{p_1}{t_X} - \frac{p_0}{t_{eh}} \quad (4.8)$$

$$\frac{dp_1}{dt} = \frac{p_0}{t_{eh}} + \frac{p_2}{t_{2X}} - p_1 \left(\frac{1}{t_X} + \frac{1}{t_{eh}} \right) \quad (4.9)$$

$$\frac{dp_2}{dt} = \frac{p_1}{t_{eh}} + \frac{p_3}{t_{ex}} - p_2 \left(\frac{1}{t_{2X}} + \frac{1}{t_{eh}} \right) \quad (4.10)$$

$$\frac{dp_3}{dt} = \frac{p_2}{t_{eh}} - \frac{p_3}{t_{ex}} \quad (4.11)$$

$$1 = p_0(t) + p_1(t) + p_2(t) + p_3(t) \quad (4.12)$$

where p_n , $n = 0, 1, 2$ are the time dependent probabilities for the QD to be occupied by 0, 1 and 2 e-h hole pairs. p_3 is the probability for the QD to be in an excited state of higher energy. t_X and t_{2X} are the decay rates of the X and $2X$ levels respectively, while t_{ex} is the decay rate associated with the excited state. The e-h pair capture time is given by t_{eh} . Since the QD is pumped in cw mode, we can simplify this set of equations by taking the stationary limit. Assuming the pumping rate to be proportional to the inverse

4.1. Pyramidal quantum dots spectral properties

of the e-h pair capture time $\frac{1}{t_{eh}} = \alpha P$, the rate equations simplify to

$$0 = \frac{p_1}{t_X} - p_0 \alpha P \quad (4.13)$$

$$0 = p_0 \alpha P + \frac{p_2}{t_{2X}} - p_1 \left(\frac{1}{t_X} + \alpha P \right) \quad (4.14)$$

$$0 = p_1 \alpha P + \frac{p_3}{t_{ex}} - p_2 \left(\frac{1}{t_{2X}} + \alpha P \right) \quad (4.15)$$

$$0 = p_2 \alpha P - \frac{p_3}{t_{ex}} \quad (4.16)$$

$$1 = p_0 + p_1 + p_2 + p_3. \quad (4.17)$$

By solving this set of equations, we get the power dependent probabilities for the QD to be occupied by 1 and 2 e-h pairs

$$p_1(P) = \frac{\alpha P}{1/t_X + \alpha P + t_{2X}(\alpha P)^2 + t_{2X}t_{ex}(\alpha P)^3} \quad (4.18)$$

$$p_2(P) = \frac{t_{2X}(\alpha P)^2}{1/t_X + \alpha P + t_{2X}(\alpha P)^2 + t_{2X}t_{ex}(\alpha P)^3}. \quad (4.19)$$

These probabilities can be used to express the X and $2X$ emission intensities I_X and I_{2X} , respectively, as

$$I_X = \beta \frac{1}{t_X} p_1(P) \quad (4.20)$$

$$I_{2X} = \beta \frac{1}{t_{2X}} p_2(P) \quad (4.21)$$

with β a proportionality constant. We used the sum of these two analytical expressions, $I_{X/2X} = I_X + I_{2X}$, to fit the power dependence of the $X/2X$ feature shown in Fig. 4.8 (d). Using the knowledge acquired from the correlation measurements, the X and $2X$ decay times were fixed to $t_X = 1.6 \text{ ns}$ and $t_{2X} = 0.8 \text{ ns}$. The result of the fit gave $t_{ex} = 0.5 \text{ ns}$, $\alpha = 8.7 \cdot 10^{-4} (\text{s} \cdot \mu\text{W})^{-1}$ and $\beta = 4.7$. This fitting procedure allowed us to recover the individual X and $2X$ integrated intensities which are indicated by dotted lines in Fig. 4.8 (d). Their behavior as a function of power is consistent with what we observed on non-zero $2X$ binding energy QDs: the X transition follows a linear slope and saturates together with the X^- line while the $2X$ feature follows a super linear dependence in logarithmic scale and dominates the spectrum for higher excitation powers. This brings further proof that this QD has a null biexciton binding energy, within the $80 \mu\text{eV}$ resolution of our setup. These QDs with zero $2X$ binding energy represent 10% of the QDs investigated in this study, and could be useful for several

applications, such as the emission of entangled pairs of photons using time reordering as was proposed by Avron et al.[232].

4.2 Exciton dynamics

In this last section, we present time-resolved PL measurements of isolated site-controlled pyramidal QDs. Unlike the QDs presented in the previous sections, the QDs investigated here were isolated using mesa etching (see subsection 2.3.3 for details on fabrication process). This makes them more similar to QDs placed in a bulk matrix, which allows to investigate their dynamics when they are not affected by the presence of the PhC band gap.

PL spectra from the QDs s-state emission is shown in Fig. 4.9 (a). The X , $2X$ and X^- transitions are once again present in the s-state luminescence. Both binding and anti-binding $2X$ QDs were found on the sample. Fig. 4.9 (b) shows a close up of the s-state transitions. The transitions were fitted with lorentzian functions to retrieve the lines FWHMs, which are similar to those observed for the QDs investigated in the previous sections. The power dependence of the transitions integrated intensities is shown in Fig. 4.9 (c). The increase of the peaks integrated intensity with increasing pump power is consistent with what was observed in section 4.1.1. Some important fine-structure splitting (FSS) of the X and $2X$ lines is visible for some of the QDs. For QD4 the FSS is as large as 200 eV . Due to high symmetry of pyramidal QDs, the FSS is, on average, $20\text{ }\mu\text{eV}$ when they are placed in the bulk GaAs matrix, and is not resolved in the PL spectrum. Here, important electric fields generated by surface states of the mesa structure is most probably responsible for this increase of the FSS[260].

We performed time-resolved PL measurements on these QDs to investigate the dynamics of the s-state transitions. The QDs were excited with 3 ps width laser pulses at a 80 MHz repetition rate. More details on the measurement setup can be found in subsection 2.1.4. The time-resolved PL traces of the s-state transitions for QD1 and QD3 are shown in Fig. 4.10 (c) and (d) respectively. The energy resolution of the time-resolved setup is $300\text{ }\mu\text{eV}$, which means that for the X and $2X$ of QD3, the FSS split lines both contribute to the PL traces shown in Fig. 4.10 (d). We observe a sharp increase of the emission intensity following the excitation of the QDs by the laser pulse at $t = 1\text{ ns}$. This increase of the emission is followed by a clamping at maximum intensity, which is caused by the relatively high power levels that had to be used for this experiment due to low intensity of the QDs, and for which the $2X$ state is already populated. A bi-exponential decay of the emission is then registered. The fast component constitutes the QD transition radiative decay (yellow dashed line in Fig. 4.10 (c) and (d)), while the slow component could arise either from spin-flipped dark excitons[261] or from a refilling process from neighbouring defect states[247]. We observe a ratio of ~ 2 between the X and $2X$ decay times for both QDs, consistent with what was

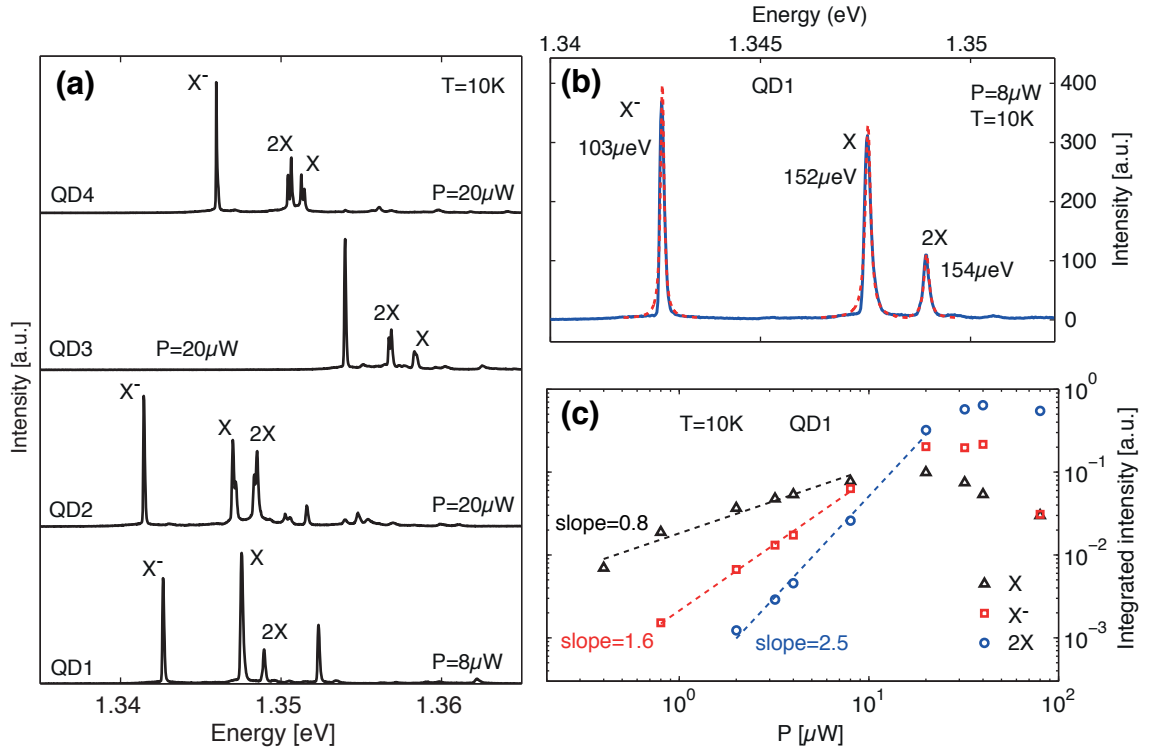


Figure 4.9: (a) PL spectra of 4 QDs isolated using mesas. (b) Close-up of the s-state emission of QD1. Lorentzian fits of the transitions (red dashed lines) were used to retrieve the peaks FWHM. (c) Integrated intensities of QD1 X , $2X$ and X^- transitions as a function of the laser pump excitation power.

obtained in section 4.1.2. The X^- decay time is similar to that of the neutral exciton. Surprisingly, the decay times of QD1 are about twice as long as those of QD3. This difference in lifetime could result from different non-radiative decay rates. Indeed, the decay times of semiconductor QDs is the sum of radiative and non-radiative lifetimes, the latter being related to the rate at which carriers escape the QD non-radiatively. In particular, non-radiative centers in the vicinity of the QD can cause this carrier escape, and their density may vary from QD to QD, explaining the difference in decay times observed for QD1 and QD3. Furthermore, the decay times measured here are similar to the ones estimated from the photon correlation measurements presented in section 4.1.2. In section 4.1.2, the QDs were embedded in a PhC, so one would expect their radiative lifetimes to be longer due to the inhibition of the emission by the PhC band gap. However, since the quantity we measure is the decay time, inhibition of the QD emission, which increases the radiative lifetime, may not reflect in PL measurements if the non-radiative lifetimes are comparable to the bulk radiative lifetimes. The fact we measure similar decay times for QDs in the bulk and QDs embedded in a PhC indicates it is the case.

4.3 Chapter summary

In this chapter we investigated the spectral and temporal characteristics of the photoluminescence of single site-controlled pyramidal QDs. The QD s-state emission spectrum was found to be very reproducible from QD to QD, exhibiting three excitonic transitions at low excitation powers. The three excitonic complexes populating the QD were identified as the X , X^- and $2X$ by performing excitation power dependent measurements. Their emission was analysed by means of photon correlation measurements, showing in particular pronounced single photon emission for the X and X^- transitions. Particular attention was paid to the exciton binding energies which were measured on 83 different QDs. Although the binding energies were reproducible from QD to QD, an increase of the $2X$ binding energy was observed with increasing QD absolute emission energy, and explained by the dependence of the electron and hole Coulomb interaction on the QD size and strain induced piezoelectric fields. About 10% of the QDs have vanishing $2X$ binding energies, leading to a superposition of the X and $2X$ spectral features. Finally, the dynamics of QDs isolated using mesa etching was investigated using time-resolved PL measurements, giving a good estimation of the decay rates of pyramidal QDs placed in a bulk GaAs matrix. This study showed that site-controlled pyramidal QDs present good optical properties nearly matching those of self-assembled QDs, and provide a control and reproducibility promising

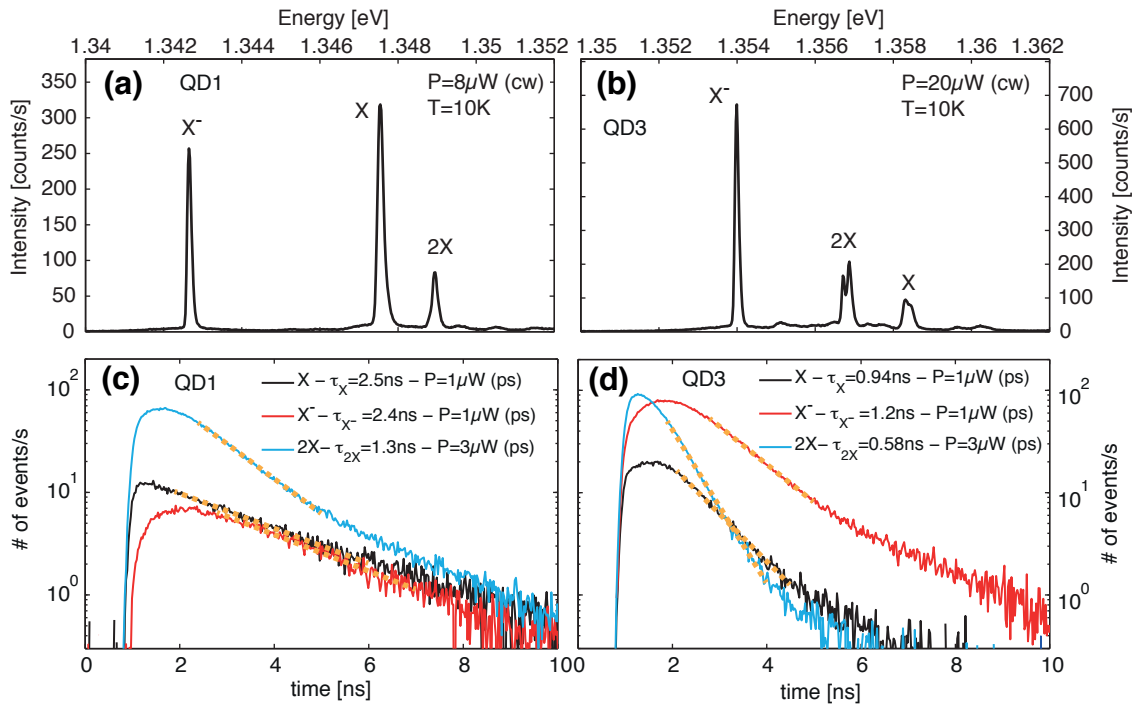


Figure 4.10: (a) and (b) s-state PL spectra of QDs isolated using mesas. (c) and (d) Time-resolved PL traces of the X , $2X$ and X^- excitonic transitions, measured for QD1 (a) and QD3 (b) respectively.

4.3. Chapter summary

for quantum information applications. Informations such as typical linewidths and decay rates provided by this study are important to analyse the QD-cavity coupling experiments presented in chapter 5.

5 Site-controlled quantum dots in L_n photonic crystal cavities

Atom-cavity systems are an excellent platform to study light-matter interactions at a fundamental level. However, in the past decades, researchers have been seeking to reproduce, with semiconductor quantum dots (QDs), cavity quantum electrodynamic (cavity-QED) experiments originally performed with atoms. Indeed, working with solid-state systems offers control and scalability that atomic systems cannot provide. The electrical properties of quantum dots can be tailored by altering their fabrication process and they are suitable for on-chip integration. There is however a fundamental difference between atoms and QDs. As explained in chapter 1, unlike their atomic counterparts, semiconductor QDs interact with the surrounding crystal matrix, which ultimately leads to decoherence and linewidth broadening. Interactions with crystal lattice vibrations, known as phonon scattering, and pure dephasing induced by the fluctuating electrostatic environment are among the mechanisms responsible for decoherence (Fig. 5.1). These decoherence processes drastically alter the physics of QD-cavity coupling[69, 97, 98, 100, 143]. Either strong or weak coupling can be obtained depending on the magnitude of pure dephasing, and phonon scattering has been shown to be responsible for off-resonant cavity emission[113–115]. Although dephasing processes can be detrimental to the observation of QD photon indistinguishability[16], the observation of the strong coupling regime or the implementation of quantum gates[231], they can also be used as a tool to enhance QD-cavity coupling[99], cavity feeding effects[100] or resonant single QD spectroscopy[150]. In both cases, it is crucial to get a better understanding of how dephasing processes affect the coupling between a QD and a nano-cavity.

Exploring the details of the impact of solid-state decoherence mechanisms on the photoluminescence (PL) of QD-cavity systems requires a full control of the QD-cavity coupling. This involves positioning a single QD in a specific location of the semiconductor nanocavity, and ensuring that the QD behaves as much as possible like a single atomic transition. These prerequisites are essential to compare the experiment with the two-level system (TLS)-cavity model presented in chapter 3. In most previous QD-

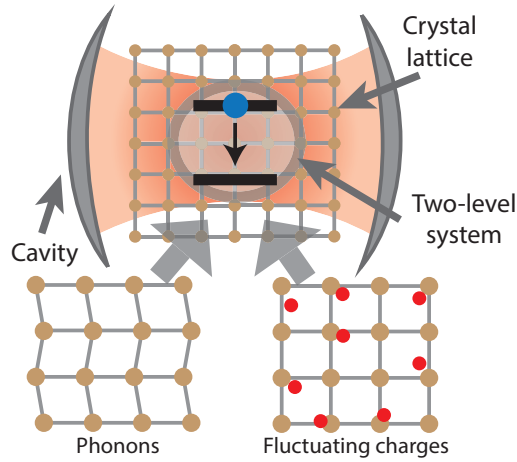


Figure 5.1: Schematic of a two-level system in an optical cavity embedded in a crystal lattice.

cavity experiments relying on self-assembled QDs, these conditions are not met. The random nucleation of self-assembled QDs prevents a straight forward deterministic positioning of the QD in the cavity. Furthermore, it is difficult to rule out the possibility that more than one QD interacts with the cavity mode (CM), especially when photonic crystal (PhC) cavity are involved. Deterministic positioning of single self-assembled QDs inside micropillar cavities was demonstrated relying on the pre-characterisation of the QD emission to locate its position[70]. However, the nucleation position of the QDs is still governed by a random process, preventing the scaling up of the study to the coupling of multiple QDs with multiple cavities, which is required to realize distributed quantum computation schemes. Furthermore, self-assembled QDs electronic states were shown to deviate from fully confined atomic-like electronic states[154]. The interaction of the QD confined excitonic states with delocalized 2D wetting layer states leads to the formation of a quasi-continuum of states[148, 153, 155] (see section 1.5). This results in a broadband emission that can interfere with the observation of off-resonant CM emission induced by QD pure dephasing and phonon scattering.

Motivated by these observations, we rely here on site-controlled pyramidal QDs embedded in PhC cavities to deterministically couple one and two QDs to a single mode of the cavity. The full control of the QD-cavity coupling and the absence of wetting layer states in pyramidal QDs, making them closer to ideal atomic-like emitters, enables the comparison of the system optical features with simulated spectra obtained by modeling the QD by a TLS coupled to a CM in the presence of solid state decoherence mechanisms. This allows a quantitative analysis of the impact of pure dephasing and phonon mediated cavity feeding on the spectral features of the weakly coupled QD-cavity system.

In this chapter the coupling of a single pyramidal QD to an L_3 PhC cavity is studied

in section 5.1. Temperature dependent experimental PL spectra are presented in subsection 5.1.1 and compared to simulations in subsection 5.1.2. The detuning dependent QD-cavity dynamics are analysed in subsection 5.1.3. In section 5.2, the coupling of two pyramidal QDs to the same CM of an L_3 PhC cavity is investigated.

5.1 One quantum dot coupled to an L_3 photonic crystal cavity

In this section, we study the luminescence of site-controlled pyramidal QDs coupled to the fundamental mode of a modified L_3 PhC cavity to elucidate the role of quantum decoherence on CM feeding[149] and exciton emission co-polarization[113, 262] at finite CM-QD energy detuning. Relying on the theoretical modeling of polarization-resolved PL spectra presented in chapter 3, we provide a comprehensive analysis of the impact of pure dephasing and phonon scattering on cavity feeding and the co-polarization effect in these systems, yielding insight crucial for QD-based integrated quantum photonics applications.

The QD-cavity system under investigation is schematized in Fig. 5.2 (a). It consists of a single InGaAs/GaAs pyramidal QD aligned (within ~ 50 nm) with the maximum of the field intensity distribution of the fundamental mode of an L_3 PhC cavity (Fig. 5.2 (b)). Details of the fabrication process can be found in chapter 2. The measured spectra of two different QD-cavity structures QD A and QD B, coming from samples A and B respectively (see table 2.1 of chapter 2 for the sample parameters) are shown in Fig. 5.2 (c) and (d). For both QDs, the ground state transitions consist of the X , $2X$ and X^- excitonic species. The upper panels of Fig. 5.2 (c) and (d), show, for the two selected structures, the luminescence of the X^- and the red shifted CM. For these measurements, the samples temperature was adjusted to get a QD-cavity detuning $\delta \sim 1$ meV. Since the binding energies (with respect to X) of X^- and $2X$ in these dots are ~ 5 meV and < 1 meV[246], respectively, this system well represents an isolated QD transition coupled to a CM. The absence of fine structure splitting (FSS) for the X^- transition[263, 264] further facilitates interpretation of the observations. The QD and CM peaks are fitted with Lorentzian functions, giving the full width at half maximum (FWHM) of the CM line ($\kappa_A = 590$ μ eV and $\kappa_B = 440$ μ eV) and the exciton line ($\Gamma_A = 450$ μ eV and $\Gamma_B = 450$ μ eV). Differences in CM and exciton linewidth stem from variations in cavity Q-factor and exciton dephasing from sample to sample. The lower panels show the emission spectra resolved in linear polarization along the V and H directions indicated in Fig. 5.2 (b). Both structures show signatures of QD-cavity coupling. Indeed, QDs A and B have a finite V polarization, quantified by the degree of linear polarization (DOLP) spectra displayed in the center panels. Although initially unpolarized, the presence of the CM transition forces the excitonic line to acquire the CM polarization, i.e., become co-polarized. Furthermore, a pronounced emission at the CM energy is observed for the detuned QD-cavity systems. This off-resonant CM emission is referred to as cavity feeding and is a signature of coupling specific to

solid-state systems undergoing dephasing.

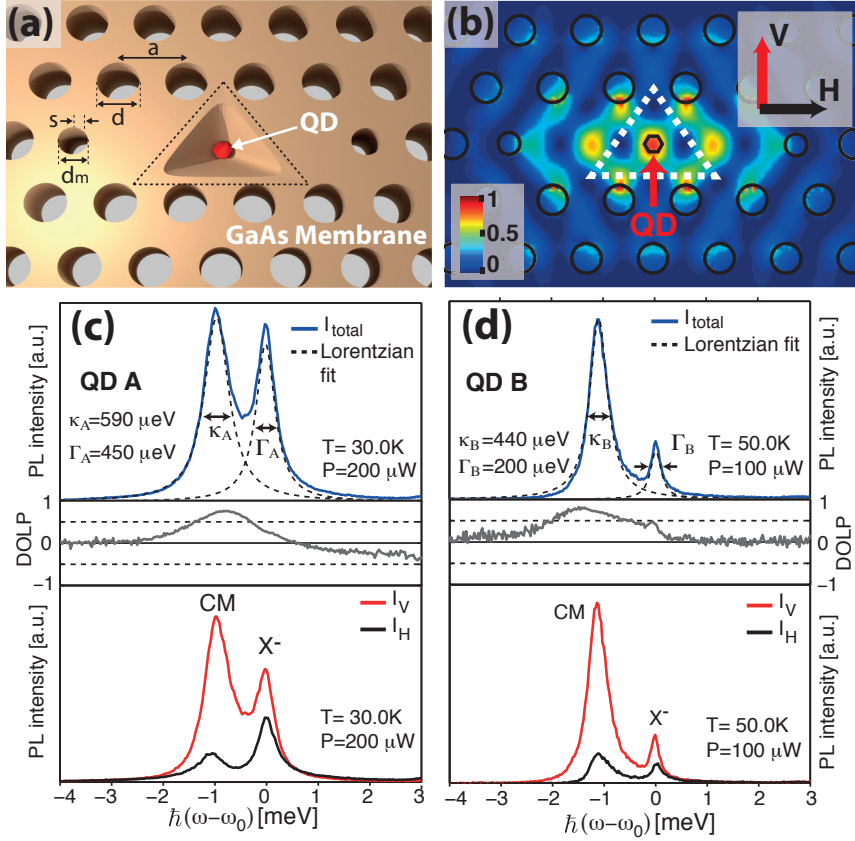


Figure 5.2: **(a)** Schematic of the QD positioned at the center of a modified L_3 PhC cavity: $a=200$ nm, $d=130$ nm, $d_m=110$ nm and $s=30$ nm. **(b)** Computed field intensity distribution of the fundamental mode of the L_3 cavity. The nominal position of the QD is indicated by a red dot. **(c)** **(d)** Top: PL spectrum of QD A [QD B] coupled to the fundamental mode of an L_3 cavity. Lorentzian fits (dashed lines) yield the linewidths κ and Γ of, respectively, the CM and X^- transitions. Bottom: PL spectrum resolved in linear polarization along the vertical (V) and horizontal (H) directions indicated in **(b)**. Center: Degree of linear polarization of the PL.

5.1.1 Detuning dependent photoluminescence

Off-resonant CM emission and QD co-polarization are studied in this section with the help of detuning dependent PL spectra. Observing how these effects vary over a large detuning range is necessary to understand how they are related to dephasing mechanisms.

Figure 5.3 displays temperature dependent PL spectra obtained for QDs A and B. Changing the sample temperatures allows to vary the energy detuning between the QD and CM lines. Indeed, the QD energy follows the (In)GaAs bandgap variation with temperature, while the CM transition energy changes due to the temperature depen-

5.1. One quantum dot coupled to an L_3 photonic crystal cavity

dence of the refractive index. This results in a redshift of the QD and CM transition with increasing temperature, but occurring at a faster rate for the QD than for the CM, giving the opportunity to tune a red-shifted CM into resonance with an excitonic line. A change in temperature from 10 K to 70 K corresponds to a shift of the detuning by approximately 3.5 meV. The spectra of QDs A and B as a function of temperature

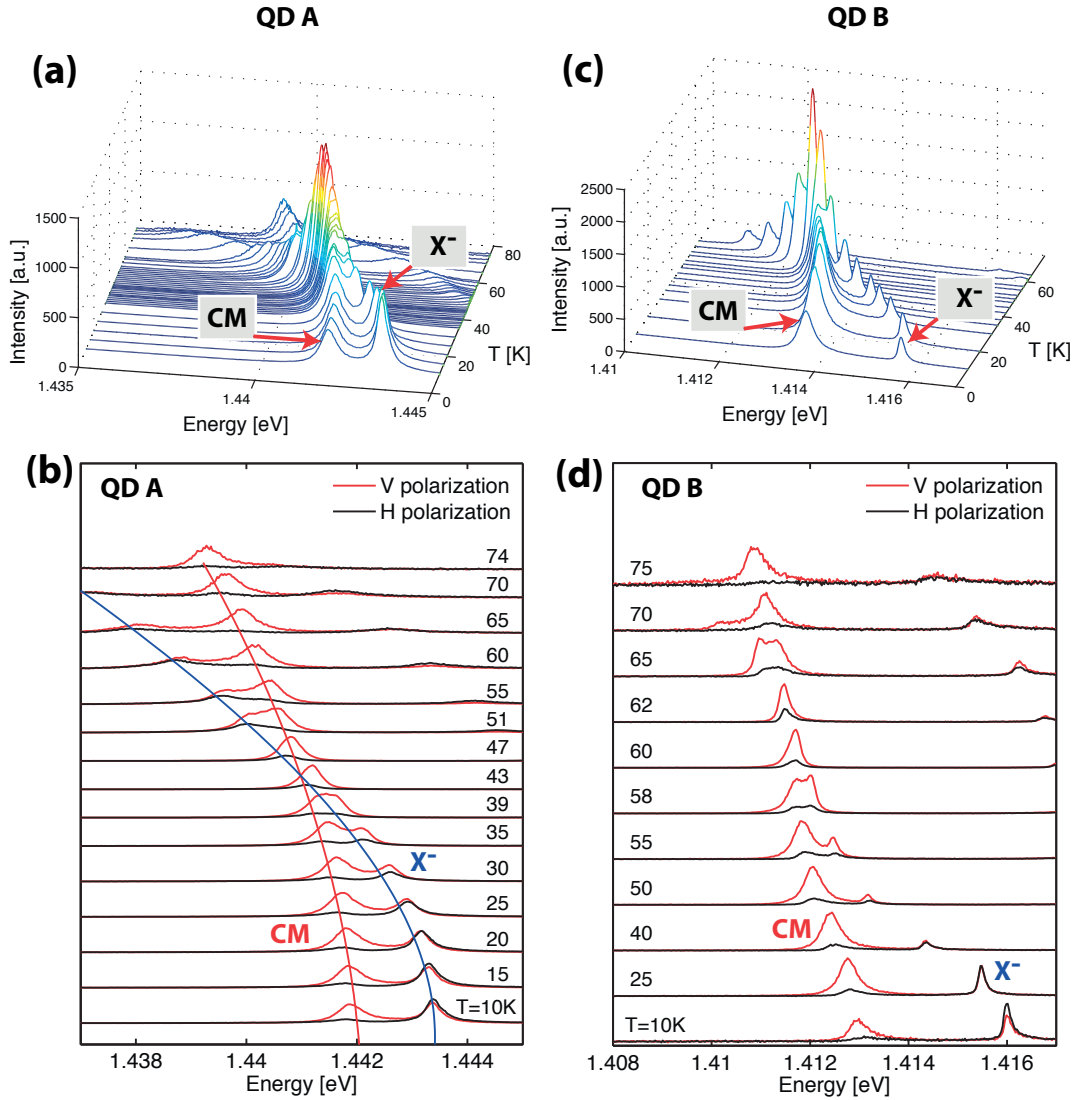


Figure 5.3: (a) [(c)] PL spectra of QD A [B] displayed as a function of the sample temperature. (b) [(d)] Polarization resolved spectra of QD A [B] for different sample temperatures. For each temperature, the spectra are normalized by their maximum intensity.

are shown in Fig. 5.3 (a) and (c). The spectra are normalized by the total recorded intensity to remove the drop in emission intensity of the structure with increasing temperature due to the onset of non-radiative recombination processes. As the temperature increases, the CM and X^- peaks are brought into resonance, eventually merging into a single peak at 45 K for QD A and 60 K for QD B. For both structures, the QD

and CM lines cross (rather than anti-cross), indicating that both systems are in the weak coupling regime. When approaching resonance, the CM and X^- peaks increase in intensity, a consequence of the Purcell reduction of the QD exciton lifetime. The maximum intensity output is reached for zero detuning. Fig. 5.3 (b) and (d) show the corresponding polarization resolved spectra. They are also displayed as a function of the sample temperature, but each spectrum is now normalized by its maximum intensity. The evolution of the X^- and CM transition energy with temperature is highlighted in Fig. 5.3 (b). These detuning dependent polarization resolved measurements bring to light two important behaviors, present for both QDs. First, the co-polarization of the X^- transition varies with detuning. As the QD-cavity detuning is reduced, the QD transition gradually acquires the CM polarization, until it becomes fully co-polarized for zero detuning. Second, the cavity feeding effect also appears to be dependent on the magnitude of the detuning. Indeed, a close inspection of Fig. 5.3 (d), reveals that the relative CM peak intensity first increases and then decreases as the detuning is reduced.

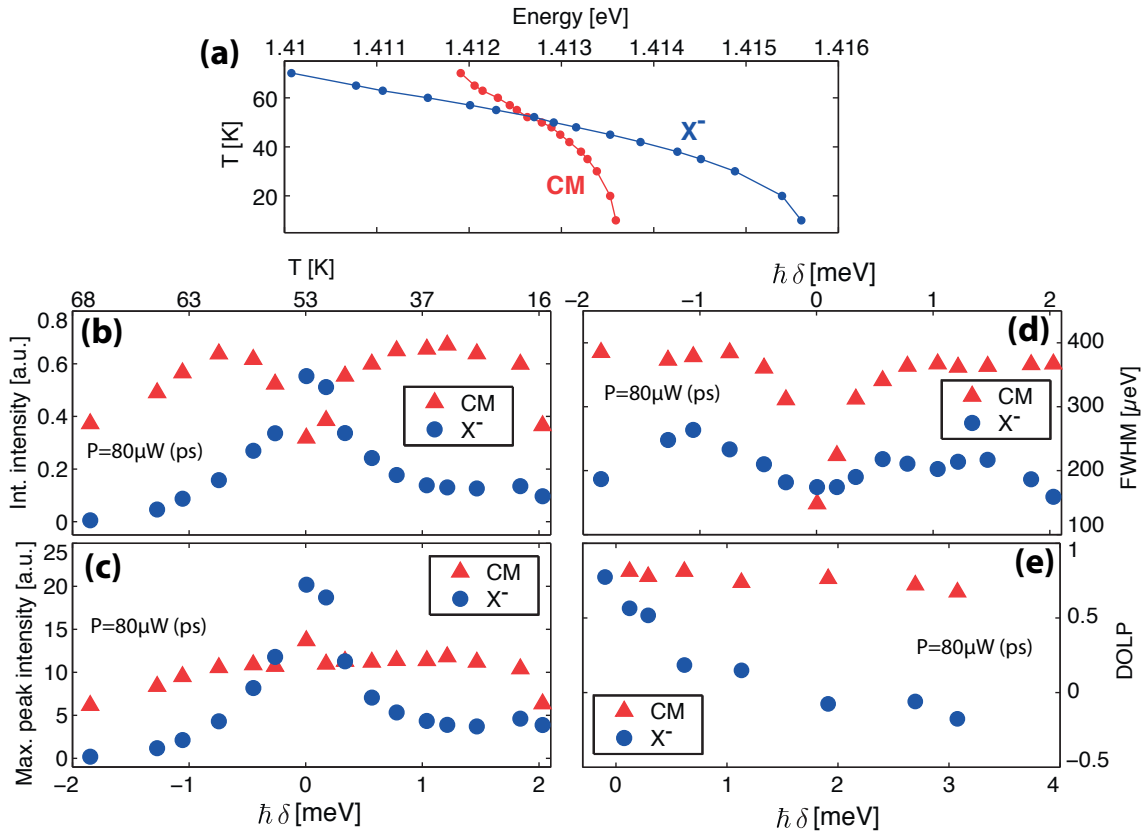


Figure 5.4: QD B: (a) Transition energies of the X^- and CM as a function of temperature. X^- and CM integrated intensities (b), maximum peak intensities (c), FWHM (d), and DOLP (e) as a function of detuning.

5.1. One quantum dot coupled to an L_3 photonic crystal cavity

A quantitative analysis of these behaviors for QD B is summarized in Fig. 5.4. The spectra were fitted with the sum of two Lorentzian functions. The transition energies of the CM and X^- transitions as a function of temperature (Fig.5.4 (a)) show a clear crossing, a signature of the weak coupling regime. Fig 5.4 (b) and (c) show respectively the integrated and maximum peak intensities as a function of detuning. A clear increase of the X^- emission intensity is visible. The X^- integrated and maximum peak intensities undergo a tenfold enhancement at resonance. The behavior of the CM intensity is more complex. The CM peak intensity does not vary significantly with detuning, whereas the CM peak integrated intensity reaches a maximum for $\delta = \pm 0.7 \text{ meV}$, and decreases near resonance. A similar behavior was recently observed in a similar experiment performed with micro pillars[171]. This reduction of the CM integrated intensity can be understood by considering the results of Fig. 5.4 (d) that displays the peak FWHMs as a function of detuning. A clear decrease of the CM FWHM is observed for small detunings, which is a consequence of the interaction between the CM and the QD phonon sidebands[171]. Given the nearly constant CM peak intensity, this reduction of the FWHM induces a decrease of the CM integrated intensity. Fig. 5.4 (e) shows the DOLP of the X^- and CM peak as a function of detuning. As expected the CM polarization is not affected by changes in the detuning. The X^- , however, becomes co-polarized with the CM as both transitions are brought into resonance. At zero detuning, both peaks have a DOLP of 0.8. Whereas off-resonant CM emission is observed for detuning as large as $\pm 3 \text{ meV}$, co-polarization of the X^- transition is visible only for detuning as large as $\pm 1 \text{ meV}$, in agreement with previous reports[113].

5.1.2 Modeling of photoluminescence

To get a better understanding of the co-polarization and cavity feeding effects with QD-CM detuning, we now compare the temperature dependent experimental spectra discussed in the previous section to simulations performed with the theoretical model presented in chapter 3. The parameters used in the simulations are summarized in table 5.1. γ_d and κ were retrieved from the fits of Fig. 5.2 (c) and (d). γ , the intrinsic QD linewidth in the PhC band-gap, was obtained from time-resolved measurements performed on nominally identical pyramidal QDs inside the PhC band gap and corresponds to a lifetime of 3 ns. F_{cav} and F_{at} were computed using 3D FDTD simulations. The values used for ℓ and ℓ_z are suitable for InGaAs QDs with confinement dimensions of 10 nm in plane and 5 nm in the growth direction. The remaining three parameters (g , A and P) were adjusted to fit the experimental data.

Table 5.1: Table of parameters used for the simulations of Figs. 5.5 (b) and (d). The fitting parameters are indicated in blue. The other parameters were retrieved from independent measurements or estimated from typical pyramidal QD characteristics.

Parameter	Symbol [unit]	QD A	QD B
TLS loss rate	$\hbar\gamma$ [μeV]	0.2	
CM loss rate	$\hbar\kappa$ [μeV]	590	440
Pure dephasing rate	$\hbar\gamma_d$ [μeV]	450	200
TLS-CM coupling strength	$\hbar g_0$ [μeV]	20	50
Phonon density of state constant	$\frac{2\pi}{\hbar^2} A$ [nm/meV]	1.3	1.4
Incoherent pumping rate	$\hbar P$ [neV]	10	5
Wave function standard deviation (in plane)	ℓ [nm]	4	
Wave function standard deviation (vertical)	ℓ_z [nm]	2	
CM coupling efficiency to detector	F_{cav}	0.4	
TLS coupling efficiency to detector	F_{at}	0.3	

The comparison between the experimental and simulated spectra is displayed in Fig. 5.5. The results of the modeling reproduce remarkably well the spectral features of QD A and B over a large detuning and temperature range. Discrepancies between experiment and simulation appear above 65 K. They are attributed to non-radiative recombination, such as thermally activated non-radiative recombination in barriers[265] and thermally induced escape of carriers[266], that were not accounted for in the model. For lower temperatures, the CM off-resonant emission is reproduced by the simulations, as well as the co-polarization of the QD line close to resonance.

5.1. One quantum dot coupled to an L_3 photonic crystal cavity

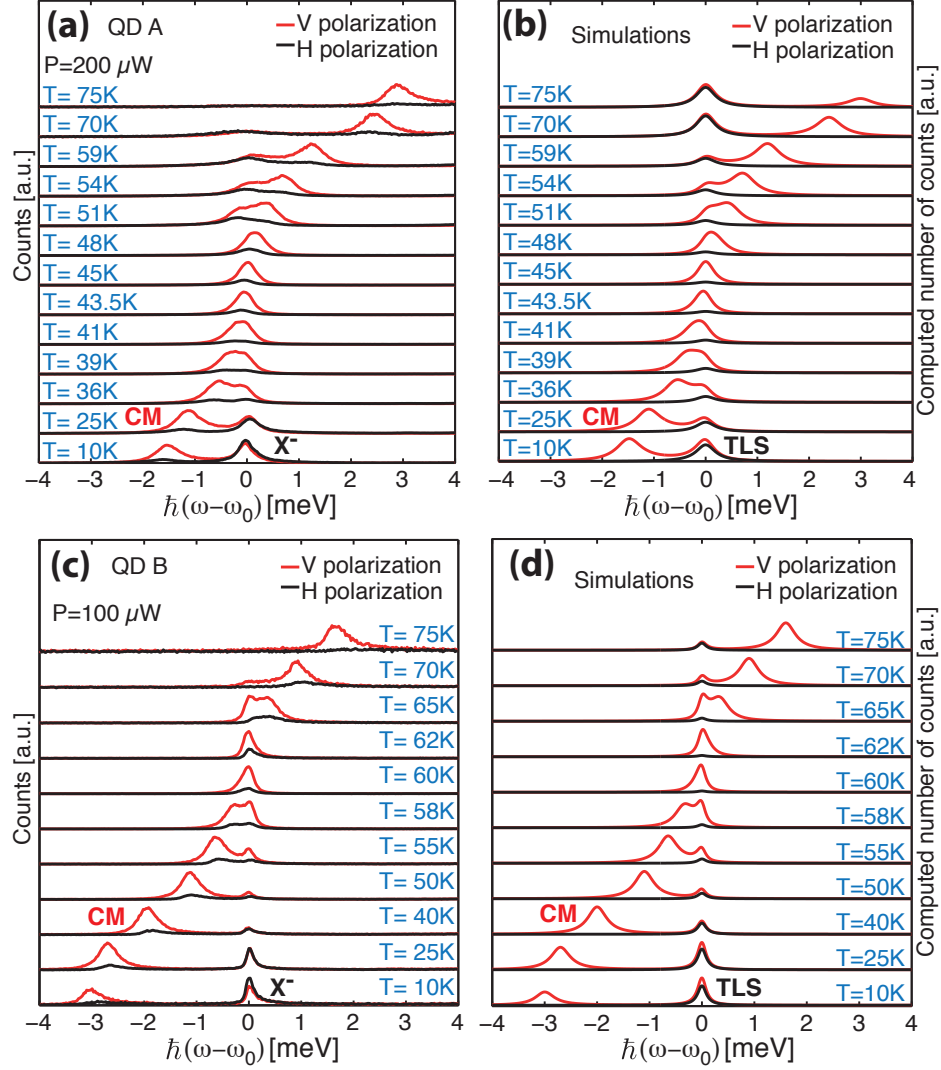


Figure 5.5: Experimental (a) and simulated (b) temperature dependent PL spectra of the cavity-QD systems, resolved in linear polarization along the directions indicated in Fig. 5.2 (b) for QD A. (c) and (d): same for QD B.

Fig. 5.6 displays a more quantitative comparison between the simulations and the experiment for QD B. The simulated spectra were fitted with two Lorentzian functions, following the same procedure used to fit the experimental data. Fig. 5.6 (a) shows the evolution of the peaks integrated intensities as a function of detuning retrieved from the experiment and the simulation. The experimental and simulated integrated intensities are normalized by the CM peak maximum integrated intensity, to allow a comparison. The increase of the X^- intensity at resonance is reproduced by the simulation as well as the decrease of the CM emission for zero detuning. Fig. 5.6 (b) compares the experimental and simulated FWHM of the CM and QD peaks. Again the reduction in the CM FWHM at resonance is accounted for by the simulation.

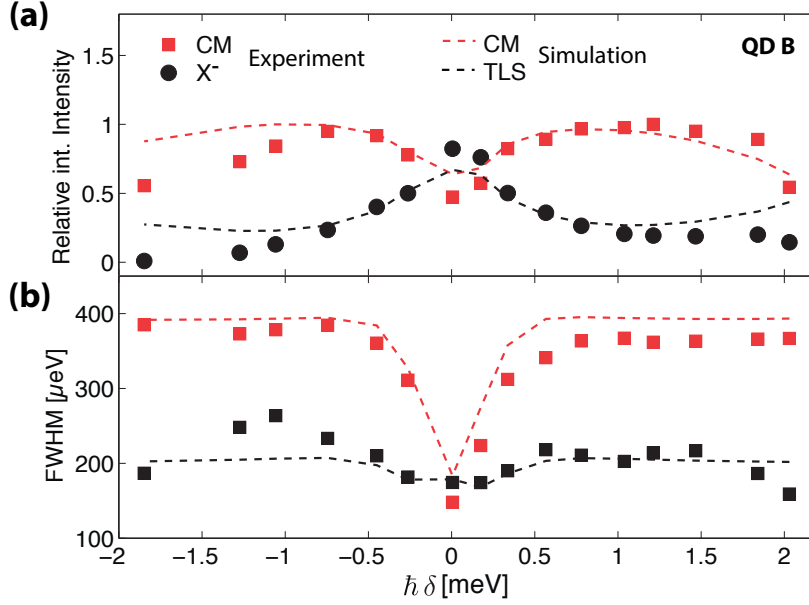


Figure 5.6: (a) CM and X^- experimental integrated intensities compared to the peak integrated intensities extracted from the simulations. The experimental and simulated datasets are normalized by the maximum CM integrated intensity. (b) Comparison between the peaks FWHM obtained from the experiment and the simulation by fitting the spectra with two Lorentzian functions.

Given the good fit between the model and the experiment, we can extract from the simulations information hidden in the experimental spectra. Figure 5.7 (a) shows the simulated spectra obtained with the simulation parameters of QD B, including QD-phonon interactions ($\frac{2\pi}{\hbar}A = 1.4 \text{ nm}/\text{eV}$) and neglecting phonon scattering ($A = 0$). It becomes apparent that phonon scattering is responsible for most of the CM off-resonant emission. Indeed, as it can clearly be seen for $T = 55 \text{ K}$, phonon scattering causes a redistribution of the emission probability from the QD transition to the off-resonant CM transition, resulting in an increase of the CM intensity, but also an inhibition of the QD emission. Without phonon scattering ($A = 0$), there is nevertheless a finite emission of photons at the CM energy. Indeed, the QD is subject to pure dephasing, which acts as a cavity feeding mechanism[100]. Pure dephasing combined with QD-phonon coupling are thus the mechanisms responsible for off-resonant CM emission. Fig. 5.7 (b) shows how pure dephasing and phonon scattering contribute to the CM peak intensity as a function of detuning. The quantity displayed as a function of detuning is the ratio between the CM peak integrated intensity when $A = 0$ and $\frac{2\pi}{\hbar}A = 1.4 \text{ nm}/\text{eV}$. This reveals that the contribution of pure dephasing to the CM off-resonant emission approaches 50% at resonance. In contrast, it reaches a minimum for $\pm 2 \text{ meV}$ detuning, leaving phonon scattering as the main mechanism responsible for off-resonant cavity feeding. This is consistent with the phonon scattering rate calculated in chapter 3 which showed that transfers of excitation from the QD to the CM via phonons was important within the $\pm 2 \text{ meV}$ detuning range. Although the contribution

5.1. One quantum dot coupled to an L_3 photonic crystal cavity

of phonon scattering remains important at resonance ($> 50\%$), it is reduced compared to detunings of ± 2 meV because it is in competition with pure dephasing.

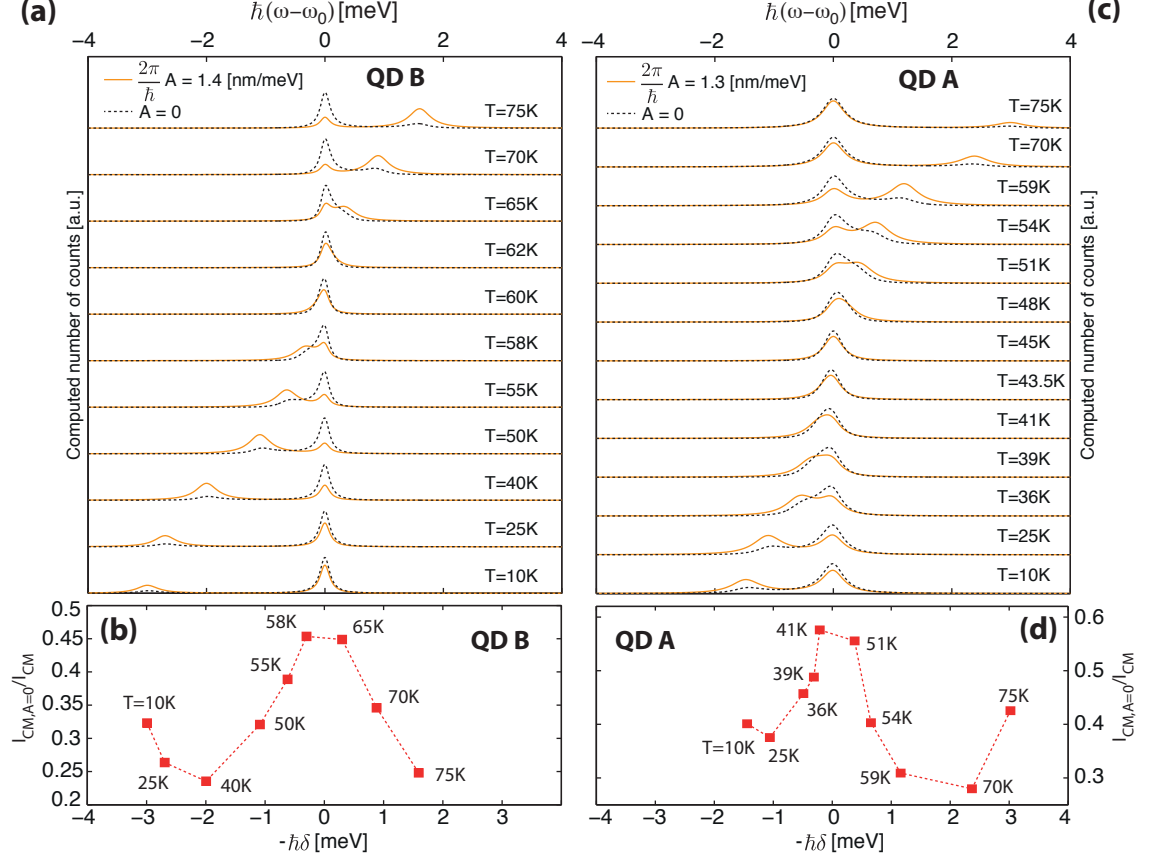


Figure 5.7: (a) [(c)] Simulated spectra obtained with the simulation parameters of QD B[QD A], including QD-phonon interactions ($\frac{2\pi}{\hbar} A = 1.4$ nm/eV) and neglecting phonon scattering ($A = 0$). (b)[(d)] Ratio between the CM simulated peak integrated intensity when $A = 0$ and $\frac{2\pi}{\hbar} A = 1.4$ nm/eV as a function of detuning for QD B[QD A].

A similar overall behavior is observed for the spectra obtained with the simulation parameters of QD A shown in Fig. 5.7 (c). However, the pure dephasing rate used to model QD A is higher than for QD B ($\hbar\gamma_d^A = 450$ μ eV and $\hbar\gamma_d^B = 200$ μ eV). Indeed, the linewidth of the X^- is twice larger for QD A than for QD B. This translates in the simulations into a more important contribution of pure dephasing to the CM off-resonant emission. This is clearly visible in Fig. 5.7 (d) that shows the ratio between the CM peak integrated intensity when $A = 0$ and $\frac{2\pi}{\hbar} A = 1.3$ nm/eV. This ratio is higher than for QD B, and indicates a contribution of pure dephasing to the CM off-resonant emission above 50% near resonance. This observation shows that both phonon scattering and pure dephasing contribute to the CM off-resonant emission. However the contributions of each dephasing mechanism varies with detuning. Phonon scattering is predominant in the $\pm(1 - 3)$ meV detuning range and pure dephasing can overcome

phonon scattering for a sufficiently high γ_p close to resonance.

The simulations also give access to the individual contributions of the CM and TLS decay channels to the total photolumuminescence. As explained in chapter 3, the total simulated emission spectrum corresponds to the sum of the CM spectrum N_{cav} , the projection of the TLS spectrum on the V axis N_{TLS}^V and the projection of the TLS spectrum on the H axis N_{TLS}^H . The simulated emission spectra of the CM and TLS decay channels are shown in Fig. 5.8 for QD A and B. For each QD, the simulations were performed with the simulation parameters of table 5.1 and are shown for three different CM-TLS detunings. For a positive detuning (Fig. 5.8 (a) and (d)), the interaction of the TLS with the CM has two interesting effects. On the first hand, it inhibits the TLS V polarized emission. This is caused by the transfer of excitation from the TLS to the CM, preferentially occurring for TLSs with dipoles collinear to the V direction, ensuring a high coupling with the V polarized near field at the center of the L_3 PhC cavity. On the other hand, a second peak appears in the CM spectrum, centered on the TLS transition energy. This means the TLS peak is the sum of the luminescence originating from the

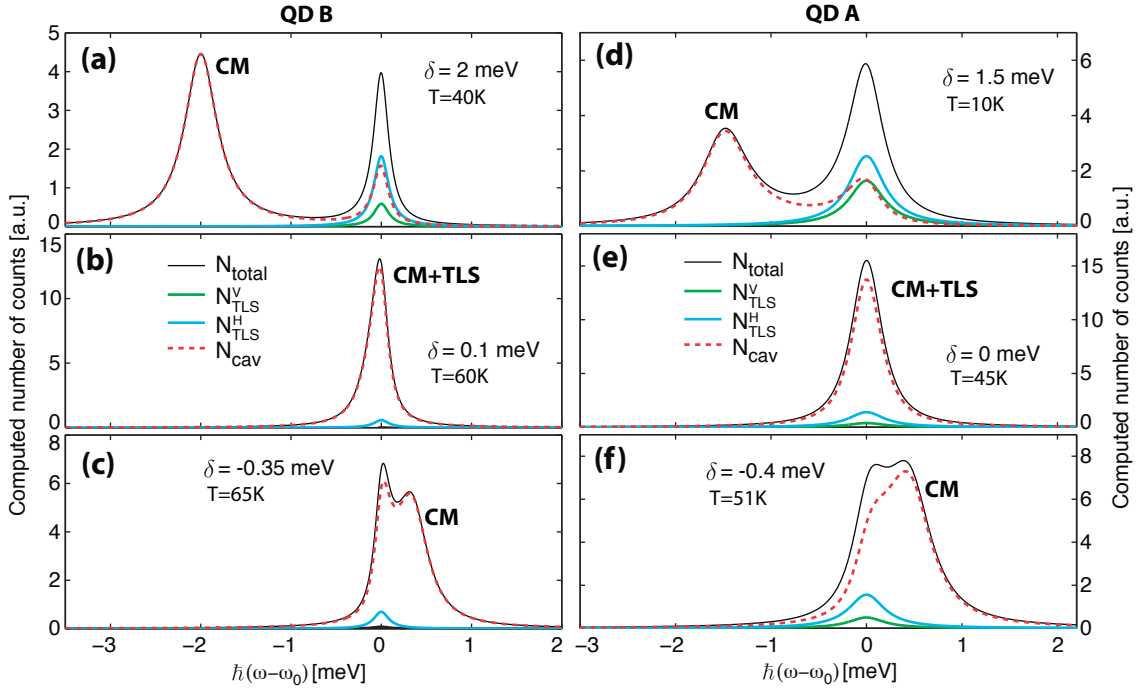


Figure 5.8: Calculated spectrum for different TLS-CM detunings using the simulation parameters of QD B (a)-(c) and QD A (d)-(f). The total spectrum is shown, as well as the contribution from the cavity N_{cav} and the projections of the TLS spectrum on the V and H axes (N_{TLS}^V and N_{TLS}^H respectively.)

TLS as well as the cavity decay channel. The additional peak centered on the energy of the TLS in the CM spectrum can be understood by considering the definition of the power spectrum. As explained in chapter 3, the power spectrum is the Fourier transform of the field first order correlation function. In the weak coupling regime,

5.1. One quantum dot coupled to an L_3 photonic crystal cavity

when the TLS is initially inverted, the TLS-cavity coupling leads to a transfer of the excitation from the TLS to the CM which is rapidly lost by the cavity due to its important decay rate. This means the dynamics of the cavity population is closely related to the TLS population. Consequently, the cavity first order correlation function will be similar to the TLS system first order correlation function, leading to a Lorentzian feature centered on the TLS energy in the CM power spectrum. The contribution from the cavity decay channel is important due to the high decay rate of the cavity. Since it is V polarized, this additional contribution of the cavity decay channel to the QD emission is responsible for the co-polarization of the coupled QD line. The intensity of the CM peak centered at the TLS transition energy increases near resonance, resulting in the increase of the QD line co-polarization observed in Fig. 5.4 (e). At resonance, when the CM and TLS peaks merge into a single line (Fig. 5.8 (b) and (e)), the CM spectrum dominates and the TLS emission is almost completely inhibited. At resonance, the coupling strength between the CM and the TLS is maximum, and the transfer of excitations from the TLS to the CM becomes very efficient. In the "bad cavity" regime ($\kappa \gg \gamma$), nearly all these excitations are lost through the CM decay channel, resulting in an almost completely V-polarized emission. For a small negative detuning (Fig. 5.8 (c) and (f)), the CM spectrum still dominates the emission. However, two peaks can be identified in the total emission spectrum, although the higher pure dephasing rate of QD A makes the distinction between the CM and TLS peak more difficult.

Since in the weak coupling regime no anti-crossing of the QD and CM emission is observed, a direct measurement of the QD-cavity coupling strength is not possible. However from this fitting procedure, we were able to extract coupling strengths of $\hbar g_0 = 20 \mu eV$ for QD A and $\hbar g_0 = 50 \mu eV$ for QD B (see Table 5.1). These values are in line with those reported in the literature for InGaAs/GaAs QDs[39, 69, 145]. Note that these values of the coupling strength correspond to a QD dipole moment collinear to the electric field polarization vector, the actual coupling strength entering in the simulation being $g_0 \cos(\theta)$, where θ is the angle between the dipole moment and the electric field vector. Furthermore, the deterministic positioning of the QD ensures an overlap with at least 60% of the electric field maximum amplitude. This tends to show that the small QD-cavity coupling strengths measured for InAs/GaAs QDs is not necessarily the result of a misalignment between the dipole and field or poor spatial overlap between the QD and field distribution, as often expressed in the literature[125], but might stem from small dipole moments of InGaAs QDs[51, 267]. Another possible explanations for the relatively small g_0 values reported here may come from the assumption that the QD dipole moment lies in-plane. Taking into account in the simulations a finite out-of-plane component of the dipole moment would result in larger g_0 values extracted from the fitting procedure.

The phonon density of states constant A extracted from the fit (see Table 5.1) is related to the deformation potential D by $A = \frac{\hbar D^2}{16\rho c_s^4 \sqrt{\pi}}$. This allows us to get an estimate of the deformation potential felt by both QD, $D = -7.6 eV$ for QD A and $D = -7.9 eV$ for QD

B, which are consistent with values of the deformation potential for GaAs[164].

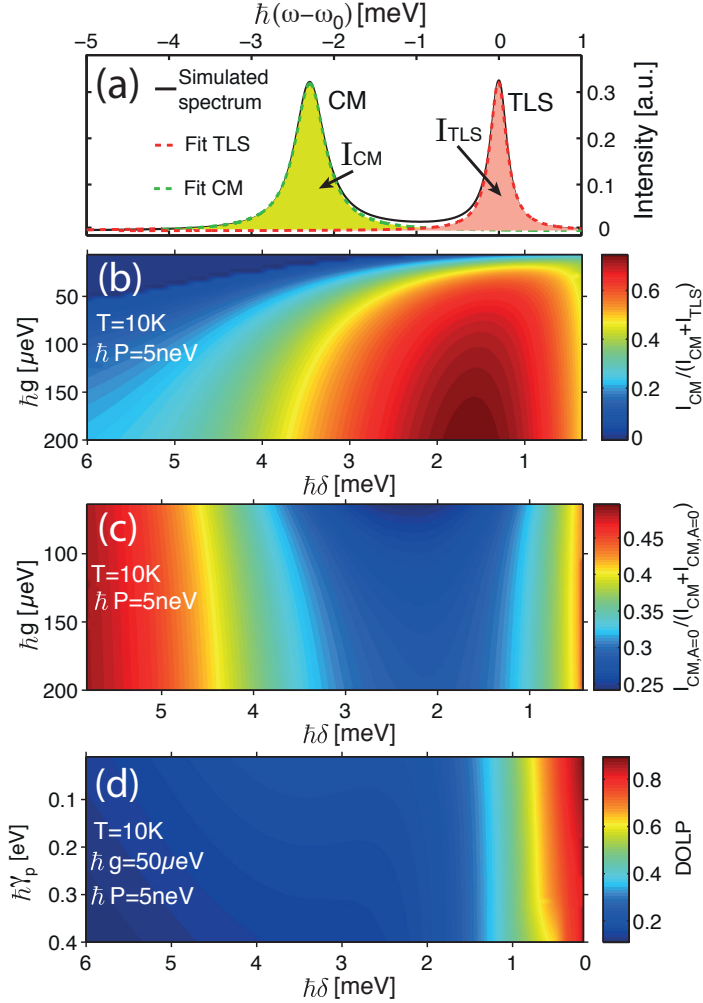


Figure 5.9: (a) Simulated spectrum with simulation parameters as in Fig. 5.5 for QD B, except that $\hbar g = 105\mu eV$. Peak integrated intensities evaluated using Lorentzian lineshapes I_{CM} and I_{TLS} . (b) Relative CM peak intensity for various coupling strengths g and TLS-CM detunings. (c) Intensity of the CM peak without phonon scattering $I_{CM,A=0}$ relative to I_{CM} including phonon scattering. (d) TLS peak DOLP for various pure dephasing rates γ_d and TLS-CM detunings.

The more general trends of the evolutions of the cavity feeding and CM-exciton co-polarization versus phonon scattering and pure dephasing are presented in the maps of Fig. 5.9. Fig. 5.9 (b) shows the calculated relative intensity of the CM peak $I_{CM}/(I_{CM} + I_{TLS})$ as a function of detuning and QD-cavity coupling strength. The relative CM peak intensity reaches a maximum for detunings of $1.7 meV$ and increases with g . The decrease in relative CM emission for detunings smaller than $1.7 meV$ is in agreement with our measurements and experimental observations reported in the literature[150]. Fig. 5.9 (c) presents the intensity of the CM peak without phonon scattering $I_{CM,A=0}$, where the only decoherence mechanism is pure dephasing, relative to I_{CM} , which includes phonon scattering. The relative contribution of pure

5.1. One quantum dot coupled to an L_3 photonic crystal cavity

dephasing is small in the range of detunings of $1 - 3 \text{ meV}$, for which phonon-scattering is most efficient. However, the contribution of pure dephasing to the off-resonant CM emission becomes comparable to that of phonon scattering for detunings greater than 5 meV . The behavior of the co-polarization effect is summarized in Fig. 5.9 (d), where the calculated DOLP is plotted versus detuning and pure dephasing rates. The DOLP is larger than 0.5 for detunings in the range $0 - 1 \text{ meV}$.

In conclusion, using a TLS-like QD system embedded in a solid-state environment coupled to a single mode photonic cavity we elucidated the roles of phonons and pure dephasing on exciton-cavity interaction in the weak coupling regime. Besides providing insight into weak-coupling mechanisms in solid-state cavity-QED phenomena, the results yield useful information for designing integrated quantum photonic systems for quantum information technology.

5.1.3 Detuning dependent QD-cavity dynamics

QD-cavity systems are of interest for their applications in quantum information technologies, e.g., as sources of single, indistinguishable photons[16, 96, 268]. In this context, understanding their dynamics, including the Purcell effect[17] and the dynamics of CM feeding at finite cavity-QD energy detuning[149, 269] is important for realizing efficient sources of quantum light. Most studies of cavity-QD coupling involved Stranski-Krastanov QDs, in which parasitic wetting layer states hybridizing with QD multi-excitonic complexes were shown to promote cavity feeding not related to the intrinsic QD single exciton dynamics[152, 156]. Similar studies demonstrated the reduction of the QD lifetime at resonance but did not clarify its behavior as a function of QD-cavity detuning, nor investigated the dynamics of the CM emission[69, 126, 138]. Most studies of the dynamics of the QD and CM lines as a function of detuning were performed with micropillar cavities[133, 134] for which the cavity mode volume is large compared to PhC membrane cavities. A study of the exciton-CM dynamics was performed with PhC cavities as well[111], but effects of temperature and non-radiative recombination channels were not included. Hence, there is a need for elucidating exciton dynamics in cavity-QD model systems that closely resemble two-level systems embedded in a solid-state matrix and unveiling the impact of dephasing and non-radiative processes on the Purcell effect and CM dynamics.

Some of the results presented in this section were published in reference [157].

Here, we study the exciton and CM dynamics of QD B. The PL spectrum of QD B for $\delta = 2 \text{ meV}$ is shown in Fig. 5.10 (a). Fig. 5.10 (b) shows the dynamics of the X^- and CM emissions corresponding to the detuning situation of Fig. 5.10 (a). The time-resolved

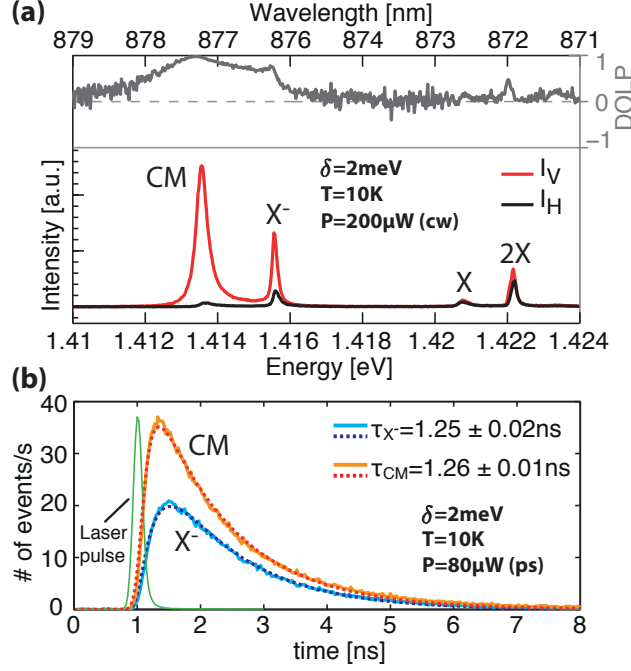


Figure 5.10: (a) QD spectrum with the X^- near resonant with the CM, resolved in linear polarization along the directions indicated in Fig. 1 (a). Top panel: Corresponding degree of linear polarization. (b) Time-resolved PL of the X^- and CM lines: measured - solid lines; fitted (see text) - dashed lines. Reprinted with permission from [157]. Copyright 2015, AIP Publishing LLC

PL traces were fitted with the following 3-level system rate equation model:

$$\frac{dp_e}{dt} = -\frac{p_e}{\tau_e}, \quad \frac{dp_X}{dt} = -\frac{p_X}{\tau_X} + \frac{p_e}{\tau_e}, \quad \frac{dp_g}{dt} = \frac{p_X}{\tau_X} \quad (5.1)$$

where p_e , p_X and p_g are the occupation probabilities of the excited states level, excitonic level and ground state level respectively (see Fig. 5.11). p_X is given by

$$p_X(t) = \frac{1}{\tau_e} \frac{e^{-(\frac{1}{\tau_X} - \frac{1}{\tau_e})(e^{\frac{t}{\tau_X}} - e^{\frac{t}{\tau_e}})}}{\frac{1}{\tau_e} - \frac{1}{\tau_X}}. \quad (5.2)$$

By fitting (5.2) to the time-resolved data, accounting for the finite response of our detectors (175 ps), we obtain a decay time of $\tau_{X^-} = 1.25$ ns for the X^- emission and $\tau_{CM} = 1.26$ ns for the CM peak emission. We use the same expression to fit the X^- and CM time-resolved emission because they are expected to have the same behavior in the weak coupling regime[149], since in the absence of parasitic background emission,

5.1. One quantum dot coupled to an L_3 photonic crystal cavity

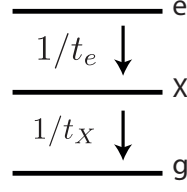


Figure 5.11: Schematic of the 3-level system used to fit the time-resolved PL traces. It consists of an excited state level (e), an excitonic state level (X) and a ground state level representing an empty QD (g).

the CM is fed only by the QD. We repeated this measurement for different sample temperatures to investigate the dependence on detuning.

Figure 5.12 (a)-(d) shows the time-resolved PL traces of the X^- and CM peaks for different detunings. The decay times τ_{X^-} and τ_{CM} as a function of detuning, and hence temperature, are summarized in Fig. 5.12 (e). These measurements were performed for excitation powers bellow the QD saturation regime ($P_{sat} \sim 400 \mu W$), for which only ground state emission was observed in the spectra. A clear decrease of τ_{X^-} and τ_{CM} is observed near resonance. The two decay times follow the same trend, indicating that the CM is fed solely by the QD transition (for small detunings, the X^- and CM emission could not be spectrally resolved in the measurements, so a single decay time value was measured and attributed to the X^- emission in Fig. 5.12 (e)). Furthermore, we observe a global decrease of the decay times with increasing temperature, which we attribute to a reduction of the lifetime due to the onset of non-radiative recombination channels[265, 266].

The decay time of a spectrally broadened QD exciton coupled to a CM as a function of detuning can be written, according to [47, 138], as follows

$$\frac{\tau_0}{\tau_X(\delta)} = \frac{F_P(1 + 2Q\gamma_d)}{8\frac{\delta^2}{\Delta\omega_c^2} + 2(1 + 2Q\gamma_d)^2} f^2 + \frac{\tau_0}{\tau_{leak}} + \tau_0\Gamma_{nr}(T) \quad (5.3)$$

where F_P is the Pucell factor, Q the cavity quality factor, $\Delta\omega_c$ the cavity linewidth, γ_d the inverse exciton quality factor, proportional to the emitter linewidth, broadened by dephasing, τ_0 the bulk exciton lifetime and τ_{leak} the exciton lifetime when off-resonant with the CM (inhibited by the photonic bandgap), and f a dimensionless constant describing the field intensity at the position of the QD. This expression assumes a random in-plane QD dipole orientation. The last term of the equation $\Gamma_{nr}(T)$ is the QD non-radiative decay rate, and was added to account for the decrease of the decay time with temperature[127]. The non-radiative decay rate was assumed to increase linearly with temperature as $\Gamma_{nr} = \alpha T + \beta$. This dependence is an approximation and does not describe the physical processes responsible for the decrease of the decay time with temperature. The solid line in Fig. 5.12 (e) shows the fit of $\tau_X(\delta)$ for fixed parameters

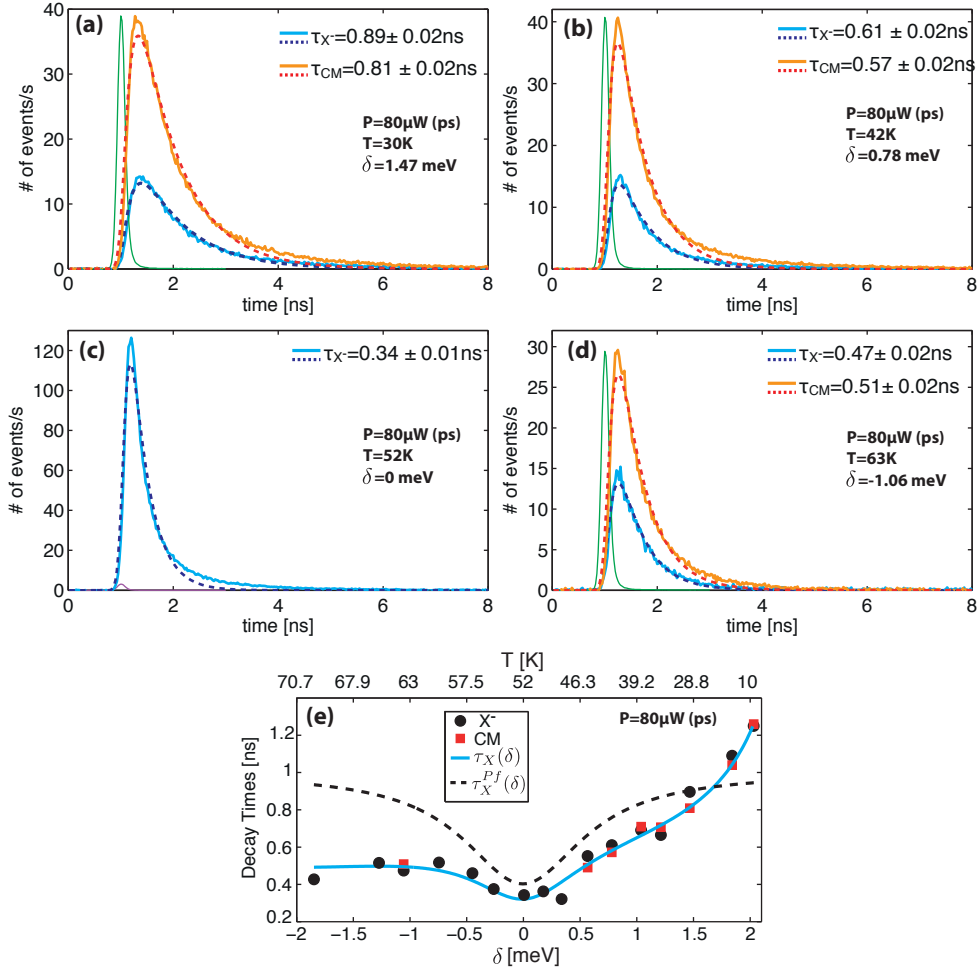


Figure 5.12: X^- and CM time-resolved PL traces for energy detuning $\delta = 1.47 \text{ meV}$ (a), $\delta = 1.47 \text{ meV}$ (b), $\delta = 1.47 \text{ meV}$ (c), $\delta = 1.47 \text{ meV}$ (d): measured - solid lines; fitted (see text) dashed lines. For $\delta = 0$, only a single peak is visible in the spectrum resulting in a single time-resolved PL trace shown in (c). (e) X^- and CM lines decay times as a function of X^- -CM detuning δ . (e) Reprinted with permission from [157]. Copyright 2015, AIP Publishing LLC

$Q = 3500$, $\Delta\omega_c = 400 \mu\text{eV}$, $\gamma_d = 1.5 \times 10^{-4}$, $\tau_0 = 1 \text{ ns}$, $f = 0.6$ and fit parameters $1/\tau_{\text{leak}} + \beta = 0.5 \pm 0.06 \text{ ns}^{-1}$, $F_P = 17 \pm 5$ and $\alpha = 0.02 \pm 0.003 \text{ (ns} \cdot \text{K)}^{-1}$ and is in very good agreement with the experimental data. The fixed parameters were obtained from the spectral characteristics of the CM and X^- peaks in Fig. 5.10 (a), except for the bulk radiative lifetime $\tau_0 = 1 \text{ ns}$ which is a typical value obtained from independent measurements on similar isolated QDs in bulk GaAs, and $f = 0.6$ which corresponds to the QD being coupled to 60% of the maximum field intensity. We extract from the fit a Purcell factor of $F_P = 17 \pm 5$, in line with values reported in the literature[69, 127]. However it is far from the theoretical maximal value of 220 for this structure, probably due to the misalignment between the exciton dipole and the cavity electric

5.1. One quantum dot coupled to an L_3 photonic crystal cavity

field. From the fit, we also obtain the following relation between the non-radiative lifetime $\tau_{nr} = 1/\Gamma_{nr}$ and τ_{leak}

$$\tau_{nr} = \frac{1}{0.02T + 0.5 - \frac{1}{\tau_{leak}}} \quad (5.4)$$

Estimating τ_{leak} is not trivial without a direct measurement of the non-radiative decay rates. If we assume $\tau_{leak} = 3 \text{ ns}$ we can compute using (5.4) non-radiative lifetimes of $\tau_{nr} = 2.7 \text{ ns}$ at 10 K and $\tau_{nr} = 0.6 \text{ ns}$ at 70 K . This important decrease of the non-radiative lifetime with temperature reduces the visibility of the Purcell effect in temperature scanning experiments, as opposed to gas condensation detuning scan experiments[111]. To highlight the impact of non-radiative effects, $\tau_X(\delta)$ can be compared to $\tau_X^{Pf}(\delta)$ (dark dashed line in Fig. 5.12 (e)), given by

$$\frac{\tau_0}{\tau_X^{Pf}(\delta)} = \frac{F_P}{2} \frac{1 + 2Q\gamma_d}{4\frac{\delta^2}{\Delta\omega_c^2} + (1 + 2Q\gamma_d)^2} f^2 + 1 \quad (5.5)$$

which corresponds to the case $\tau_{leak} = \tau_0$ and $\Gamma_{nr} = 0$, and gives access to the isolated contribution of the Purcell effect on the lifetime reduction at resonance, showing explicitly the impact of non-radiative effects on the visibility of lifetime reduction at resonance. Furthermore, this effect is not present in similar experiments performed with micropillar cavities[133, 134] suggesting it is specific to PhC structures. This might be explained by the larger surface to volume ratio of PhC structures, exposing the QD to more pronounced surface effects that can induce non-radiative recombinations.

Above the saturation power of the QD ground state transitions, we observe qualitatively different dynamics. Figure 5.13 (a) displays the panoramic PL spectrum of the structure at such high pump level, revealing transitions related to the QD as well as the quantum wire (QWR) barrier states. Figure 5.13 (b) shows the X^- dynamics measured for different excitation powers and a detuning $\delta = 16 \text{ meV}$ (obtained with water vapor condensation). Under these conditions no QD polarization was observed indicating that the QD was not coupled to the CM. For $P = 100 \text{ } \mu\text{W}$ ($< P_{sat}$), the X^- emission exhibits a fast rise time, limited by the carrier capture and relaxation dynamics. For $P = 500 \text{ } \mu\text{W}$ ($P > P_{sat}$), the rise time increases due to the finite p-state occupation. The maximum emission intensity is delayed by as much as 3.5 ns at $P = 2000 \text{ } \mu\text{W}$. The recombination lifetime of the X^- inside the PhC band gap ($\tau \sim 1.6 \text{ ns}$), on the other hand, is not affected by changes in P up to $5000 \text{ } \mu\text{W}$. When compared to $\tau_0 = 1 \text{ ns}$, this corresponds to an apparent increase of the spontaneous emission lifetime by a factor 1.6. However, without a better knowledge of the non-radiative decay rate, it is not possible to conclude on the actual inhibition of the spontaneous emission by the PhC band gap. Above $P = 2000 \text{ } \mu\text{W}$, an additional peak appears at short delay times with a small decay time of $\sim 270 \text{ ps}$. Similar effects have been reported in self-assembled QD systems and attributed to wetting layer state continuum[156] or

multiexcitonic background emission[270]. To investigate the origin of this additional

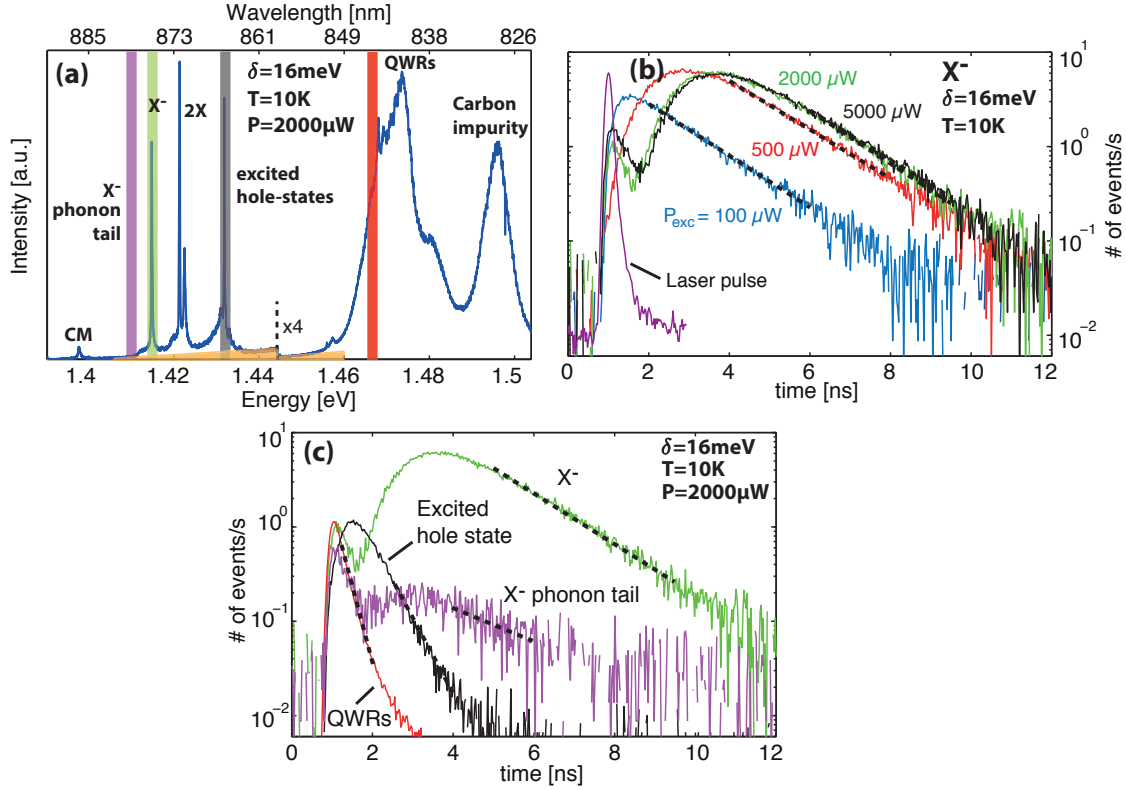


Figure 5.13: (a) Spectrum of QD B at high excitation power. Low energy tail of QWRs emission is highlighted in yellow. (b) Time-resolved PL of the X^- transition of QD1 for different laser excitation powers and far-detuned from the CM. The decay times corresponding to each powers are $\tau_{100} = 1.58 \pm 0.04 \text{ ns}$, $\tau_{500} = 1.68 \pm 0.03 \text{ ns}$, $\tau_{2000} = 1.55 \pm 0.05 \text{ ns}$, $\tau_{5000} = 1.65 \pm 0.05 \text{ ns}$. (c) Time-resolved PL of different features highlighted in (a). Lifetimes: $\tau_{X^-} = 1.61 \pm 0.04 \text{ ns}$, $\tau_{X^-, \text{phonon tail}} = 2.47 \pm 1 \text{ ns}$, $\tau_{\text{excited hole}} = 0.54 \pm 0.04 \text{ ns}$, $\tau_{\text{QWRs}} = 0.268 \pm 0.008 \text{ ns}$. Reprinted with permission from [157]. Copyright 2015, AIP Publishing LLC

peak in our system, we measured the dynamics of several key features of the spectrum in Fig. 5.13(a). For high excitation powers (above $2000 \mu\text{W}$), additional features are observed in the QD spectrum beside its ground state emission. Emission from the excited hole states is observed at 1.432 eV , and bright emission from the three wedge QWRs is observed centered at 1.47 eV . Figure 5.13 (c) shows the dynamics of the different transitions observed at high P . Three subsequent emissions are observed: first the emission of the QWRs delayed by 0.5 ns (decay time $\tau = 0.268 \text{ ns}$), then the emission of the p-states delayed by 0.9 ns ($\tau = 0.54 \text{ ns}$) and finally the emission of the ground state delayed by 3.5 ns ($\tau = 1.61 \text{ ns}$). By comparing the emission from the QWRs with the fast dynamics feature observed at high power in the X^- emission, we conclude that the latter represents emission from the low energy tail of the QWRs (see Fig. 5.13 (b)). Apart from the QWR tails at high excitation powers, no additional parasitic emission is observed at the energy of the QD ground states at high P . Indeed,

5.1. One quantum dot coupled to an L_3 photonic crystal cavity

we do not see evidence of background emission related to the hybridization of excited state manifolds with delocalized barrier state, as observed for self-assembled QDs[152, 153]. No emission correlated with the population of excited states is observed either in the dynamics of the X^- emission.

Finally, we investigated the dynamics of the X^- and CM for a detuning of $\delta = 2.5 \text{ meV}$ under low ($40 \mu\text{W}$) and high ($2000 \mu\text{W}$) excitation powers (see PL spectra in Fig. 5.14 (a) and dynamics of the X^- and CM transitions in Fig. 5(b)). For $P = 40 \mu\text{W}$, the X^- and CM lines exhibit similar decay times of $1.56 \pm 0.09 \text{ ns}$ and $1.63 \pm 0.09 \text{ ns}$ respectively, consistent with a detuning of $\delta = 2.5 \text{ meV}$. A single exponential decay is visible in the dynamics of both transitions. For an excitation power of 2 mW , above the QD saturation, the X^- emission is delayed due to the finite p-state occupation, and the emission of the QWR background appears at short delay times. The CM line exhibits once again a dynamic similar to the X^- transition to which it is coupled. The delayed emission of the X^- is visible at the CM frequency. The same holds for the QWR background emission that is now the dominant contribution to the CM emission.

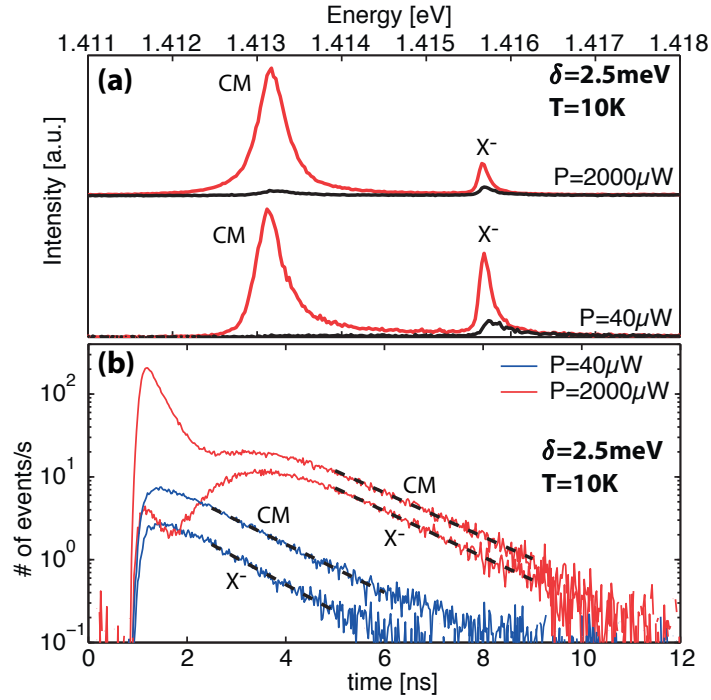


Figure 5.14: (a) Spectra of QD B at low ($40 \mu\text{W}$) and high (2 mW) excitation powers. (b) Time-resolved PL of the X^- and CM emission for low and high excitation powers. The decay times at low excitation powers are $\tau_{CM} = 1.63 \pm 0.09 \text{ ns}$ and $\tau_{X^-} = 1.56 \pm 0.09 \text{ ns}$. At high excitation powers the decay time are $\tau_{CM} = 1.49 \pm 0.08 \text{ ns}$ and $\tau_{X^-} = 1.35 \pm 0.12 \text{ ns}$. Reprinted with permission from [157]. Copyright 2015, AIP Publishing LLC

5.2 Two quantum dots coupled to an L_3 photonic crystal cavity

Up to now, most solid-state QED studies have been performed with single emitters, whether it be superconducting qubits or semiconductor QDs. Recently, two research groups investigated a system made of two emitters, atoms in one case[271] and ions in the other[272], interacting with a single cavity. For the first time, they observed subradiant and superradiant behaviour for exactly two emitters coupled to a cavity. In the past decade, scientists have been trying to achieve similar results in solid-state systems. The study of systems comprising of two or more solid-state emitters coupled to single optical cavity has been motivated by various quantum information applications. Systems comprising of two qubits embedded in a microcavity have been proposed for realizing long distance interaction between spin qubits[273] and multi particle entanglement[274, 275]. Quantum computing schemes requiring multiple emitters communicating through their interaction with a confined optical field have also been proposed[276, 277] to carry out parallel quantum logic operations. Such systems are also of interest to study collective behavior[230] and are promising candidates to realize low threshold nanolasers[278].

Superconducting qubits coupled to microwave cavities are promising candidates to investigate collective interactions of few emitters embedded in a cavity. The deterministic nature of superconducting qubits as well as the high quality factors of microwave cavities facilitate the investigation of collective states in such systems. In 2009, J.M. Fink et al. demonstrated the coupling of $N = 1, 2$ and 3 superconducting qubits with a microwave cavity, evidencing the presence of bright and dark Tavis-Cummings collective multiqubit states[279] along with the \sqrt{N} scaling of the collective dipole coupling strength. More recently, they achieved with the same system W-type entanglement of Dicke states[280].

Semiconductor QDs coupled to PhC or micropillar cavities offer an interesting alternative due to their higher operating temperature ($10 - 80 K$) and larger dipole-cavity coupling strength originating in part from smaller cavity mode volumes ($1 - 6 (\lambda/n)^3$). The first report of cavity mediated coupling of two emitters was published in 2006 by Reitzenstein et al. They demonstrate the coherent coupling of two energy separated self-assembled QDs by the optical mode of a micropillar cavity[281]. Soon after, the coupling of two QDs to the same CM of a micropillar cavity was demonstrated using a deterministic far-field optical lithography technique[70]. In 2010, cavity-mediated coupling was reported in a weakly coupled system comprising of two self-assembled QDs coupled to a PhC cavity[282]. Soon after, the collective behavior of two self-assembled QDs strongly coupled to a PhC cavity by tuning two exciton spin states into resonance using an electric field[283] and a magnetic field[147] was evidenced. In 2012, Majumdar et al. observed up- and down-frequency conversion of light via phonons

5.2. Two quantum dots coupled to an L_3 photonic crystal cavity

in a system made of two self-assembled QDs coupled to a PhC cavity[219]. Finally, intertalk between two remote self-assembled QDs coupled to the same PhC cavity was demonstrated in 2013[284]. All these studies were performed with self-assembled QDs randomly distributed in position inside the cavity. As a consequence, the exact position of the QDs was not known and parasitic emission from additional QDs cannot be neglected. Controlling the position of the QDs within the cavity is essential to achieve radiative coupling between distant emitters[285]. As for the case of one QD coupled to a cavity, the presence of delocalized 2D wetting layer states in the vicinity of self-assembled QDs influences QD-cavity coupling mechanisms, adding complexity to the interpretation of coupling experiments. Furthermore, systems using randomly located emitters are not suitable for the realization of on-chip scalable quantum information networks[286].

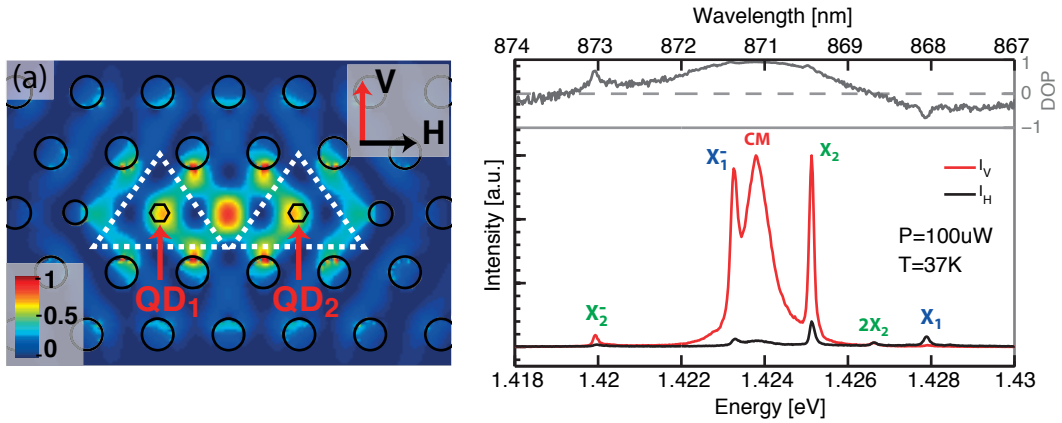


Figure 5.15: (a) Illustration of the two pyramidal QDs positioned on the secondary antinodes of the CM spatial intensity distribution. (b) Spectrum of the two QD-cavity structure resolved in linear polarization along the V and H directions indicated in (a).

The structures studied in this section consists of two site-controlled QDs embedded in an L_3 PhC cavity. The two QDs, labeled QD1 and QD2, are positioned on the two secondary antinodes of the fundamental CM (Fig. 5.15 (a)). They are separated by subwavelength distance of $\sim 350 \text{ nm}$. A full description of the fabrication method of these structures as well a systematic investigation of their PL characteristics can be found in reference [173]. This section focuses on one structure for which the CM transition is coupled to the X^- transition of QD1 and the X transition of QD2 (Fig. 5.15 (b)). A previous study demonstrated the simultaneous coupling of those two QDs to the same CM[173]. Here we apply the theoretical formalism presented in chapter 3 to the case of two QDs coupled to a CM and compare the PL properties of these two QD structures to simulations.

5.2.1 Detuning dependent photoluminescence

Fig. 5.16 (a) and (b) shows the temperature dependent PL measurement of the structure presented in Fig. 5.15. In Fig. 5.16 (b), the spectra are normalized by their maximum intensity for each temperature. At $T = 10 K$, the CM transition is near-resonant with the X_1^- transition of QD1. As the temperature is increased, the CM transition blueshifts with respect to X_1^- and at $40 K$ is located in between X_1^- and the neutral exciton X_2 of QD2. At $55 K$, the CM is brought in resonance with X_2 . Fig. 5.16 (c) shows the peaks transition energies as a function of temperature. No anti-crossing is visible between either of the QD line and the CM. However, Purcell enhancement of the emission at resonance is clearly visible in Fig. 5.16 (d) that displays the integrated intensity of X_1^- and X_2 as a function of detuning. Furthermore, a strong co-polarization of the emission is visible in Fig. 5.16 (e) that summarizes the transitions DOLP as a function of detuning. Both QDs are thus weakly coupled to the CM. In the $35 - 40 K$ temperature range, when the CM transition is in between the two QD lines, both X_1^- and X_2 are strongly co-polarized, indicating that both QDs are simultaneously coupled to the CM.

5.2.2 Modeling of photoluminescence

The theoretical model presented in chapter 3 and used to reproduce the PL emission of a single QD-cavity system is applied here to the case of two QDs coupled to the same CM. As detailed in chapter 3, the model can easily be extended to describe a system with more than one QD. Simulations were performed using the list of parameters summarized in Table 5.2. As for the 1 QD simulations, the only fitting parameters are the TLS-CM coupling strength g , the phonon density of state constant A and the incoherent pumping rate P . Two TLS-CM coupling constants are however required to account for the coupling of each QD to the CM. The results of the simulation are shown and compared to the experimental temperature dependent measurement in Fig. 5.17. The experimental and simulated spectra are normalized by their maximum intensity for each temperature. The simulations are in good agreement with the experimental measurements over a large detuning range. The off-resonant feeding of the CM by the two QD lines and strong co-polarization of their emission are well accounted for by the simulations.

The un-normalized simulated spectra are displayed as a function of temperature in Fig. 5.18 (a), revealing the increased emission of the TLSs when resonant with the CM. The evolution of the TLS's maximum intensity with detuning is compared to the experimental data in Fig. 5.18 (b). The profiles of the maximum intensities are remarkably well reproduced by the simulations for both QD lines. The Purcell enhancement of the emission at resonance is well accounted for by the model. Fig. 5.18 (c) shows the evolution of the peak integrated intensities as a function of detuning.

5.2. Two quantum dots coupled to an L_3 photonic crystal cavity

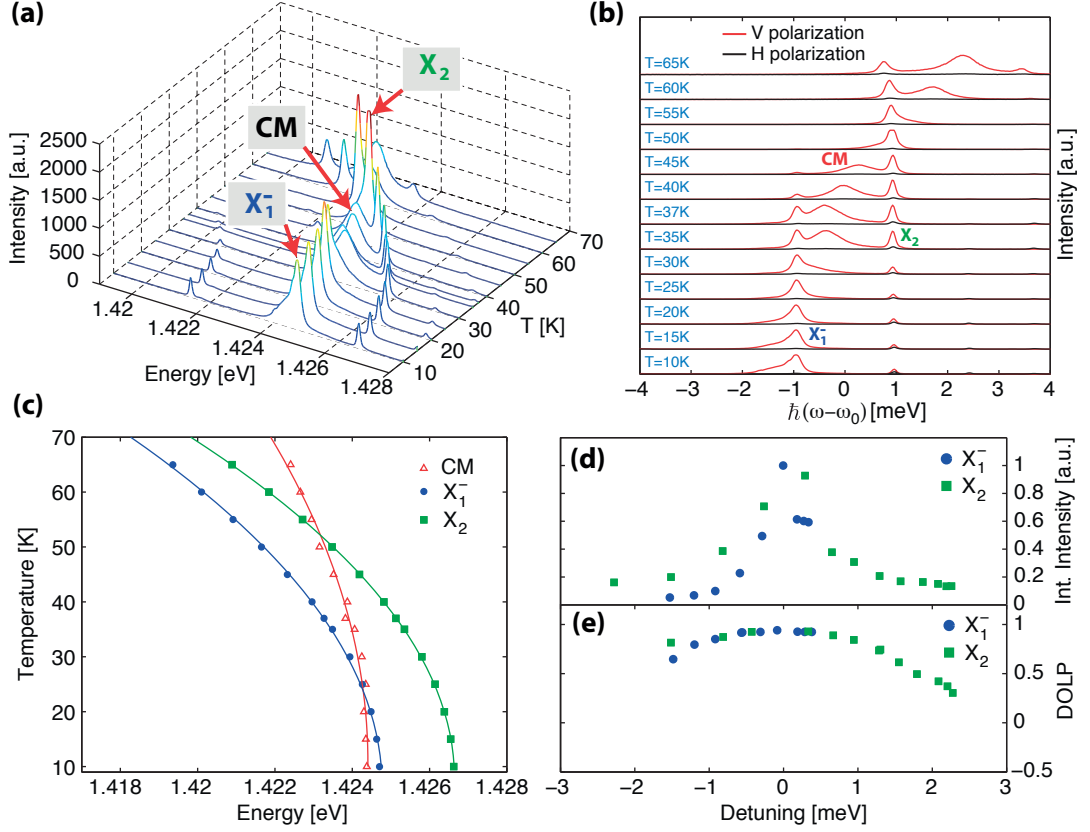


Figure 5.16: (a) PL spectra of the two QDs coupled to the CM displayed as a function of temperature. (b) PL spectra centered on the QD energies displayed as a function of the temperature. Each spectra is normalized by its maximum intensity. (c) Transition energies of the CM, X_1^- and X_2 as a function of temperature. Integrated intensity (d) and DOLP (e) of the X_1^- and X_2 lines as a function of detuning.

The profile is once again well reproduced by the simulation of the X_1^- of QD1. For QD2, however, the increase of the integrated intensity at resonance is underestimated by the simulation. This might be explained by the high sample temperature for which the resonance occurs. Indeed, above 50 K, the linewidth of the QD lines start to increase due to thermally induced dephasing[102]. This phenomenon is not included in the model and the deviation from the simulation observed in Fig. 5.18 (c) may result from an underestimation of the X_2 linewidth at higher temperatures. The DOLP of the QD lines and TLSs extracted from the experiment and simulation, respectively, is shown in Fig. 5.17 (d). The simulations reproduce the general trend of the DOLP. Both TLSs reach a DOLP of 0.9 at resonance, as do the X_1^- and X_2 QD transitions.

The best simulation results were obtained using the same TLS-CM coupling strength $\hbar g_0 = 50 \mu eV$ for both QDs. This is consistent with the position of the QDs on the two secondary antinodes of the fundamental CM, which ensures that both QD couple

Chapter 5. Site-controlled quantum dots in L_n photonic crystal cavities

Table 5.2: Table of parameters used for the simulation of Fig. 5.17. The fitting parameters are indicated in blue. The other parameters were retrieved from independent measurements or estimated from typical pyramidal QD characteristics.

Parameter	Symbol [unit]	QD1	QD2
TLS loss rate	$\hbar\gamma$ [μeV]	0.2	
CM loss rate	$\hbar\kappa$ [μeV]	650	
Pure dephasing rate	$\hbar\gamma_d$ [μeV]	230	104
<i>TLS-CM coupling strength</i>	$\hbar g_0$ [μeV]	50	50
Phonon density of state constant	$\frac{2\pi}{\hbar^2} A$ [nm/meV]	1.4	
Incoherent pumping rate	$\hbar P$ [μeV]	1	
Wave function standard deviation (in plane)	ℓ [nm]	4	
Wave function standard deviation (vertical)	ℓ_z [nm]	2	
CM coupling efficiency to detector	F_{cav}	0.4	
TLS coupling efficiency to detector	F_{at}	0.3	

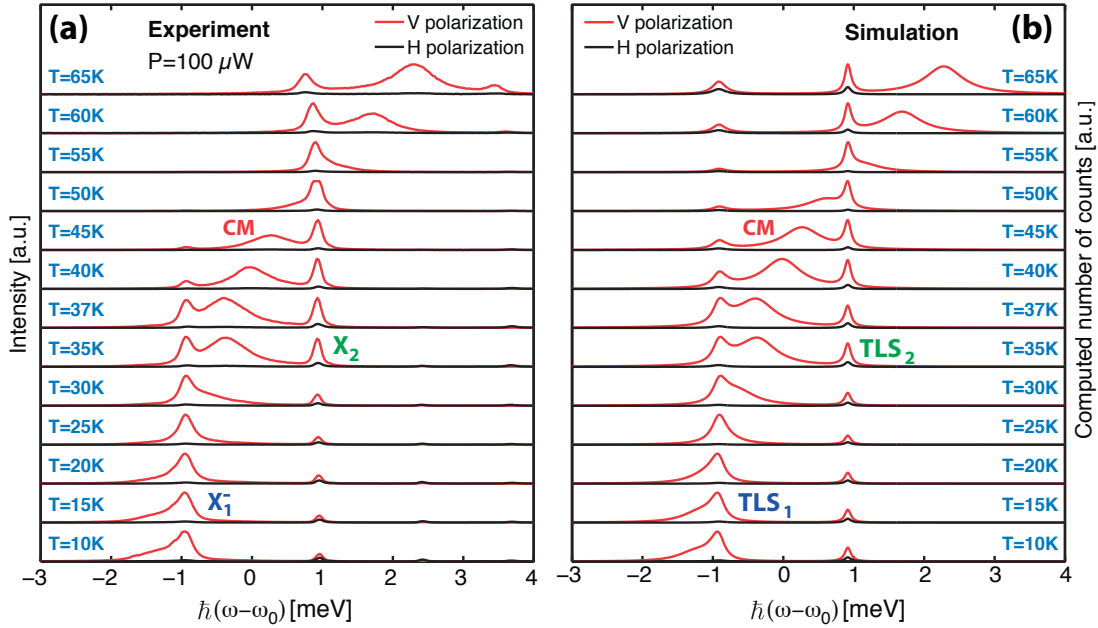


Figure 5.17: Experimental (a) and simulated (b) temperature dependent PL spectra of the two QDs coupled to the CM, resolved in linear polarization along the directions indicated in Fig. 5.15 (a). The spectra are normalized by their maximum intensity.

5.2. Two quantum dots coupled to an L_3 photonic crystal cavity

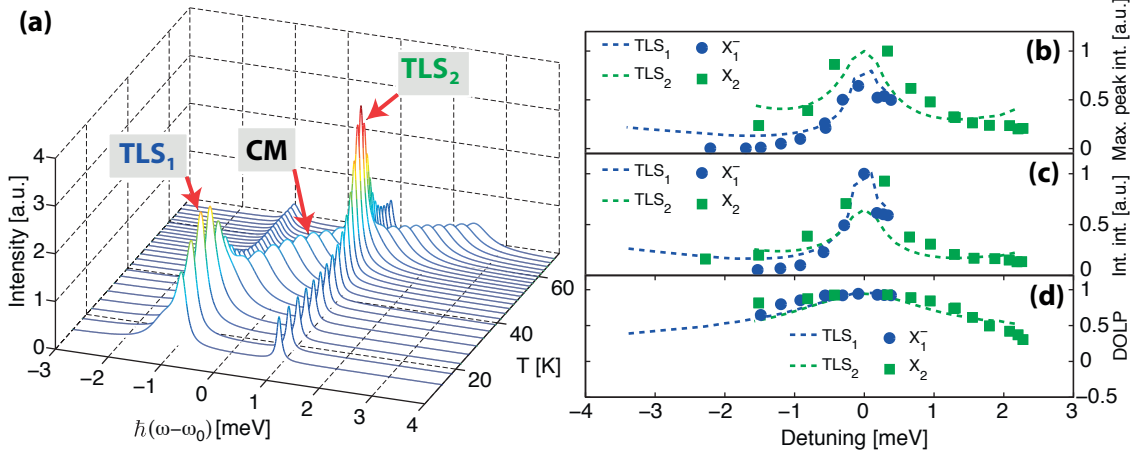


Figure 5.18: (a) Simulated spectrum of the two TLSs coupled to the same CM as a function of temperature shown in Fig. 5.17 without normalization. (b) Comparison of the maximum peak intensities (b), integrated intensities (c) and DOLP (d) of the X_1^- and X_2 transitions with the simulations (dashed lines).

equally with the mode electric field (Fig. 5.15 (a)). A phonon coupling constant $\frac{2\pi}{\hbar^2}A = 1.4 \text{ nm/meV}$ was obtained from the fit, identical to the one obtained for QD B (see subsection 5.1.2). The fact that the spectra of single and double QD-cavity structures are fitted using nearly identical simulation parameters indicates the good control of the QD-cavity coupling in these experiments and consolidates the TLS-cavity model presented in chapter 3.

These results clearly demonstrate that both QDs are coupled to the same CM. However, a point that needs to be clarified is whether or not collective coupling of the QDs occurs via the CM. In the case of weak QD-cavity coupling, the PL spectrum does not give sufficient information to answer this question. The results of the simulations however can give some insight as to whether or not collective effects are hidden in the experimental spectra. Indeed, the simulations give access to the individual TLS contributions of the total PL spectrum. Fig. 5.19 (a)[(b)] shows detuning dependent simulations including only TLS_1 [TLS_2] performed with the parameters of table 6.5. These results show the behaviour of each TLS when coupled independently to the CM, which can be compared to the two TLS system simulations of Fig. 5.17. As can be seen from Fig. 5.19 (a) and (b), each TLS contributes to the off-resonant CM emission. These contributions are labeled CM_1 and CM_2 .

In the presence of collective coupling, one would expect the CM off-resonant emission to differ from the case of sequential coupling of two QDs. For example, under superradiant conditions, more light should be collected at the energy of the CM. In our system this can be investigated by comparing the integrated intensity of the CM peak when both QDs are coupled to the CM, the sum of integrated intensities of CM_1

and CM_2 . This is summarized in Fig. 5.19 (c) that shows the evolution of the CM peak integrated intensity of the different systems as a function of detuning. The CM intensity when both QDs are simultaneously coupled to the CM (red dots) presents two dips corresponding to temperatures of $T = 22 K$ and $T = 33 K$, corresponding to the resonances with TLS_1 and TLS_2 respectively. The individual contributions to the CM off-resonant emission of TLS_1 and TLS_2 correspond to the blue and green line respectively. The sum of these contributions (dashed line) matches perfectly the CM intensity of the 2 QD system in the temperature range for which the CM stands in between both QDs ($T = 30 - 40 K$), corresponding to an equal coupling of the CM to both QDs. This shows that for this structure, both QDs are sequentially coupled to the CM, and no collective coupling of the QDs occurs.

5.3 Chapter summary

In this chapter we investigated the coupling of pyramidal QDs to the CM of an L_3 PhC cavity. The polarization resolved spectra of a single QD interacting with a single CM were compared to simulations of a single TLS couple to a CM in the presence of pure dephasing and phonon scattering. The off-resonant CM emission and QD co-polarization induced by the QD-cavity coupling were reproduced by the model over a large detuning and temperature range. By fitting the experimental spectra of two different QDs, we extracted coupling strengths of $\hbar g_0 = 20 \mu eV$ and $\hbar g_0 = 50 \mu eV$, corresponding to a weak QD-cavity coupling. We also obtained detuning dependent values of the phonon cavity feeding rate which allowed a quantitative analysis of the impact of phonon scattering and pure dephasing on the CM off-resonant emission. This showed that although exciton-phonon interactions are mainly responsible for off-resonant CM emission, both decoherence mechanisms contribute to the CM emission, but with efficiencies that strongly depend on QD-cavity detuning. The study of the dynamics of the excitonic and CM transitions revealed that the CM is fed only by the coupled QD for weak above band gap excitation. The QD decay rate was measured on a large detuning range showing an increase of the decay rate at resonance corresponding to a Purcell factor of 17. This enhancement of the QD spontaneous emission was partially masked by a decrease of the QD decay rate with temperature, attributed to thermally activated non-radiative recombination channels. Measurements of the time-resolved QD emission for high pump powers revealed a non negligible contribution of the low energy tail emission of QWRs located in the vicinity of the QD. This fast dynamics emission occurs before the pyramidal QD emission and strongly contributes to the off-resonant CM emission. No other parasitic emission was observed even for high excitation powers, confirming the absence of the broadband emission observed for self-assembled QDs due to the presence of the 2D wetting layer.

This study was extended to a more complex structure comprising two QDs coupled to the same CM. Polarization resolved spectra acquired for different sample temperatures

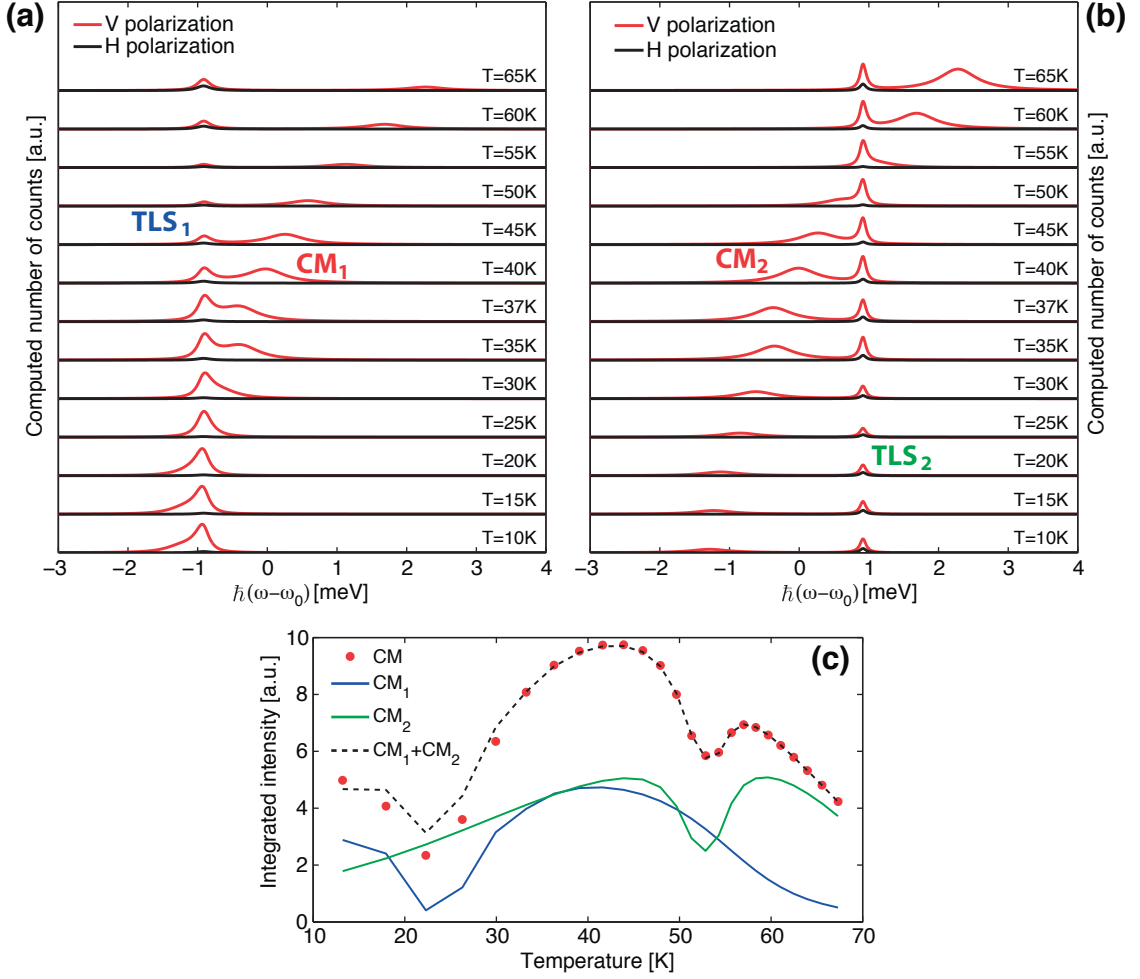


Figure 5.19: Spectrum of TLS₁ (a) and TLS₂ (b) individually coupled to the CM. The simulation of both TLSs simultaneously coupled to the CM is shown in Fig. 5.17. (c) CM peak integrated intensity when only coupled to TLS₁ (blue line) and only coupled to TLS₂ (green line). The dashed line corresponds to the sum of these two integrated intensities. The red dots show the CM peak integrated intensity when both TLSs are simultaneously coupled to the CM.

evidenced that both QDs were coupled to the CM. By comparing the simulations to a model describing the interaction of two TLSs with the same CM, we showed that the coupling was sequential, i.e., no collective coupling occurs. This absence of collective emission is understandable given the energy difference of 2 meV between the two coupled QDs and important dephasing effects that inhibit superradiant emission. Observing collective coupling could be achieved by increasing the number of QDs as shown in Fig. 5.20. Coupling of up to four pyramidal QDs to the same CM of an L7 cavity was reported [175]. Although the magnitude of the QD-cavity coupling is reduced in these structures due to the larger cavity mode volume, increasing the number of QDs could facilitate the observation of collective effects as the intensity of superradiant

emission scales with N^2 for N emitters initially inverted (see chapter 3). However, achieving collective emission with multiple pyramidal QDs embedded in L_n cavities remains challenging and has yet to be reported.

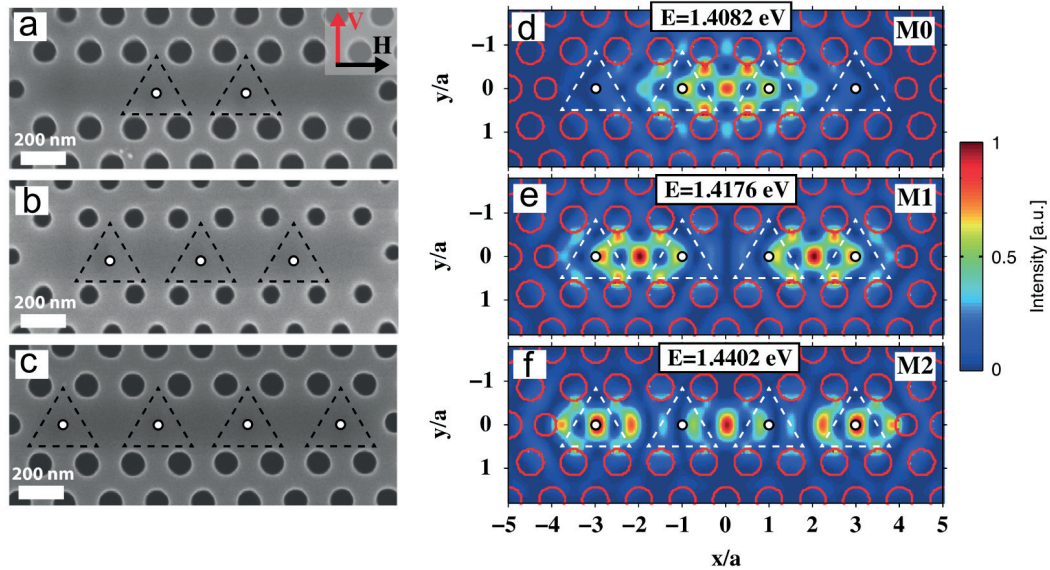


Figure 5.20: ((a)–(c)) Scanning electron microscope images of the L7 PhC cavities incorporating different numbers of pyramidal QDs. ((d)–(f)) calculated near field patterns of the first confined modes of the PhC cavities (pitch $a = 200$ nm and hole radius $r = 60$ nm). The resonance energies are indicated. Reprinted from Publication [175], Copyright (2014), with permission from Elsevier.

6 Supermodes in 1D and 2D coupled cavity arrays

The study of cavity quantum electrodynamics (cavity-QED) using solid-state implementations has been motivated by potential applications in quantum information processing[287] and quantum computing[288]. In this context, the coupling of semiconductor quantum emitters to nanocavities has been studied extensively, leading to the realization of quantum information circuits building blocks such as all-optical switching gates[289] or single quanta selection devices[290]. These systems exploit the interaction between a quantum emitter and a single optical cavity. However, the need for scalability in quantum circuits has motivated the extension of this study to multiple cavities. Coupled cavity arrays (CCAs) are promising candidates for realizing quantum networks[291, 292], enabling the transfer of information between spatially separated quantum objects via transmission of confined photons. They are also an ideal platform to pursue the implementation of quantum simulators[293, 294], motivated by the observation of quantum phase transitions with ultra-cold atoms in optical lattices[295].

The simplest CCA system comprising two nominally identical cavities, has been demonstrated with micropillars[296–298], microdisks[299] and photonic crystal (PhC) structures[300–305]. The two cavities interact via their overlapping evanescent localized electro-magnetic fields. The interaction is characterized by a coupling strength, which if sufficient, leads to the formation of new non-degenerate delocalized supermodes. Optical coupling in larger scale CCAs is more difficult to realize since fabrication-induced optical disorder prevents the realization of identical cavities. This, in turn, results in mode localization, which effectively prevents optical coupling between sufficiently remote cavities. To counteract disorder effects, cavity configurations with large enough optical coupling are necessary. Nevertheless, ultra slow light pulse propagation has been achieved in large scale linear CCAs coupled to waveguides[306, 307], and more recently, 2D arrays of coupled cavities have also been investigated[308]. However, these experiments employed either passive optical excitation or randomly positioned emitters to probe the optical modes. While the first approach is less suited

for the realization of on-chip devices, the second one renders the identification of delocalized coupled modes difficult. Indeed, if light emitters are inserted in all the cavities of the CCA, frequency shifts of individual cavities caused by disorder[309] rather than cavity coupling can explain the observation of multiple optical modes in the spectrum of the array. A more direct method of identifying mode delocalization consists in observing the field distribution by performing optical near-field measurements[310].

In this chapter, we investigated experimentally 1D and 2D arrays of coupled L_3 photonic crystal cavities. In section 6.1, the optical modes of the coupled cavity arrays are fed by a site-controlled quantum wire (QWR) light source. By performing photoluminescence measurements and relying on near-field calculation of the cavity modes, we evidence optical coupling between the cavities as well as supermode delocalization. In particular, for small cavity separations, fabrication induced disorder effects are shown to be negligible compared to optical coupling between cavities. In section 6.2, we demonstrate the coupling of two site-controlled pyramidal quantum dots (QDs) to the delocalized optical mode of two coupled L_3 PhC cavities.

6.1 1D and 2D arrays of coupled cavities with site-controlled quantum wire light sources

We present in this section the first demonstration of coupling between a localized QWR emitter and arrays of three and five coupled PhC membrane cavities. By performing photoluminescence (PL) spectral measurements, we show that short site-controlled QWRs[15], located in one cavity of the coupled array, are sufficient to excite all the supermodes of the CCA. This renders the identification of delocalized optical modes straightforward, removing the need to rely on statistical arguments or near field measurements. Furthermore, the study of the optical modes is made easier by using QWRs rather than QDs. The broader emission spectrum of the QWRs facilitates spectral matching with the supermodes of the arrays, thus requiring less control over their spectral characteristics.

Some of the results presented in this section were published in reference [311].

6.1.1 Fabrication of photonic crystal cavity arrays with integrated quantum wire light sources

The structures investigated in this chapter consist of V-groove quantum wires coupled to arrays of L_3 PhC cavities. First, a (100)-oriented 200 nm thick GaAs membrane on top of a $1\mu\text{m}$ $\text{Al}_{0.7}\text{Ga}_{0.3}\text{As}$ was patterned with a $10\mu\text{m}$ pitch V-groove grating using e-beam lithography as depicted in Fig. 6.1 (a). Vertical stacks of five $\text{In}_{0.15}\text{Ga}_{0.85}\text{As}/\text{GaAs}$ QWRs were then grown on the patterned substrate (Fig. 6.1 (b)). After the QWR growth, the planarized sample had a total membrane thickness of 260 – 265 nm. Using

6.1. 1D and 2D arrays of coupled cavities with site-controlled quantum wire light sources

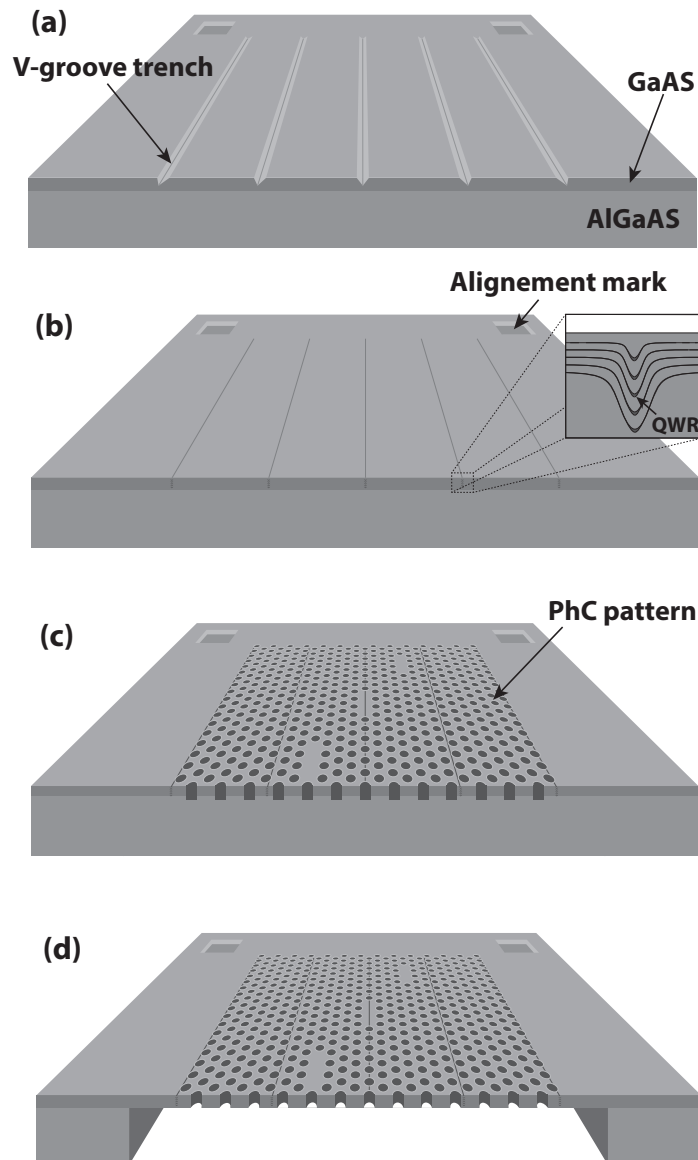


Figure 6.1: Schematics of the fabricated structure after (a) V-groove patterning, (b) growth of the five $\text{In}_{0.15}\text{Ga}_{0.85}\text{As}/\text{GaAs}$ QWRs (inset: cross-section of the stacked QWRs), (c) PhC patterning using e-beam lithography and (d) PhC membrane release.

high-precision alignment (~ 40 nm accuracy), PhC cavity patterns were produced in a polymethyl methacrylate layer (PMMA), transferred into a SiO_2 hard mask and then etched into the GaAs layer using an optimized BCl_3/N_2 ICP recipe[312] to produce straight cylindrical PhC holes (Fig. 6.1 (c)). The GaAs membrane was released by etching the sacrificial $\text{Al}_{0.7}\text{Ga}_{0.3}\text{As}$ layer using a 4% $\text{HF}:\text{H}_2\text{O}$ solution at slightly elevated temperature ($\sim 30^\circ\text{C}$) in order to exclude the formation of cracks (Fig. 6.1 (d)). Before characterization, the samples were etched by a 1 mol citric acid solution[313] in order to remove GaAs oxide and residues of SiO_2 . The sample investigated in this section

Chapter 6. Supermodes in 1D and 2D coupled cavity arrays

was fabricated by K. A. Atlasov and co-workers. Schematics of the final structures are shown in Fig. 6.2 (a) and (b). They consist of a fully suspended PhC GaAs slab with L_3 defect cavities. The alignment of the cavity pattern with the V-groove grating allows for the QWR stacks to be inserted only in the central cavity of the CCA.

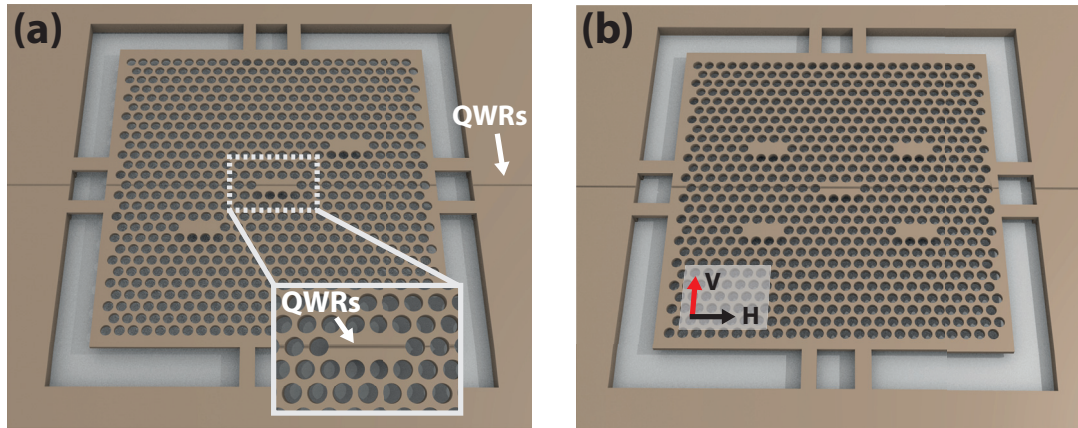


Figure 6.2: Schematics of PhC coupled cavity array with integrated QWR light sources made of three (a) and five (b) cavities. The inset of (a) shows the position of the QWRs.

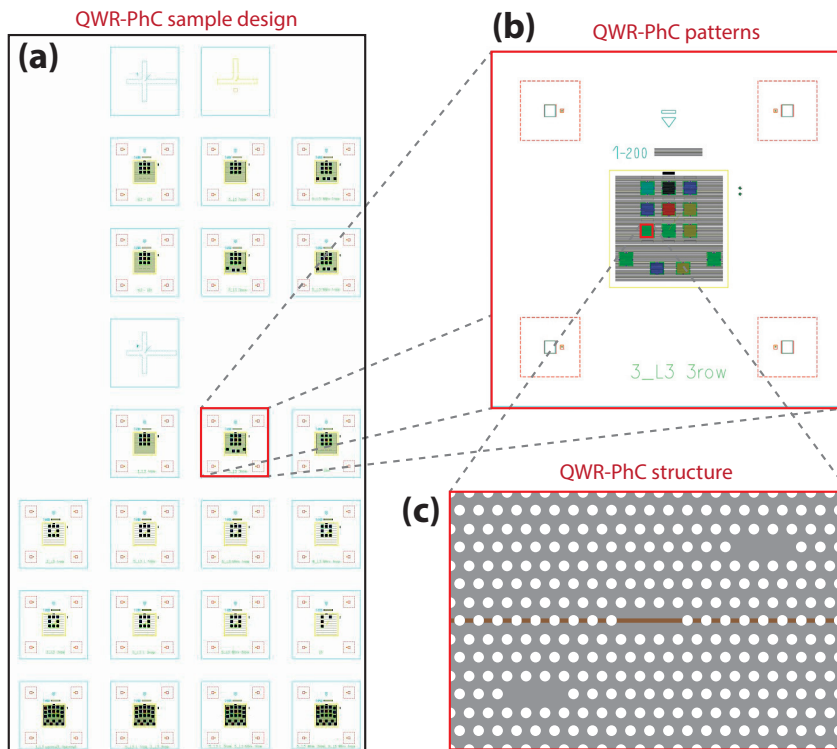


Figure 6.3: Design of the investigated sample. (a) Map of the sample containing 21 QWR-PhC patterns. (b) Close up of one pattern containing 13 QWR-PhC structures. (c) Close up on one structure comprising three PhC L_3 cavities with an integrated QWR light source.

6.1. 1D and 2D arrays of coupled cavities with site-controlled quantum wire light sources

The structure of the sample is shown in Fig. 6.3 (a). It contains 21 patterns, each consisting of up to 22 QWR-PhC structures with different r/a ratio. This was obtained by keeping the PhC pitch constant ($a=200\text{nm}$) and by varying the hole radius from 43.5 nm to 52.5 nm in steps of 1.8 nm . Examples of a QWR-PhC pattern and structure are given in Fig. 6.3 (b) and (c) respectively. Schematics of the coupled cavity structures studied in this chapter are given in Fig. 6.4. The cavities are diagonally positioned to increase the overlap between the evanescent tails of their localized optical field. This configuration optimizes their optical coupling[314] and helps counteract the impact of optical disorder on mode localization. Fig. 6.4 (a) and (b) correspond to 1D CCAs with inter-cavity separations (distance between the centers of two adjacent cavities) of $0.8\mu\text{m}$ and $1.4\mu\text{m}$ which is equivalent to the cavities being separated by 1 row and 3 rows of PhC holes along the y direction. Fig. 6.4 (c) corresponds to a 1D CCA comprising of 5 cavities with $1.4\mu\text{m}$ inter-cavity separation. Fig. 6.4 (d) corresponds to a 2D CCA with $1.4\mu\text{m}$ inter-cavity separation.

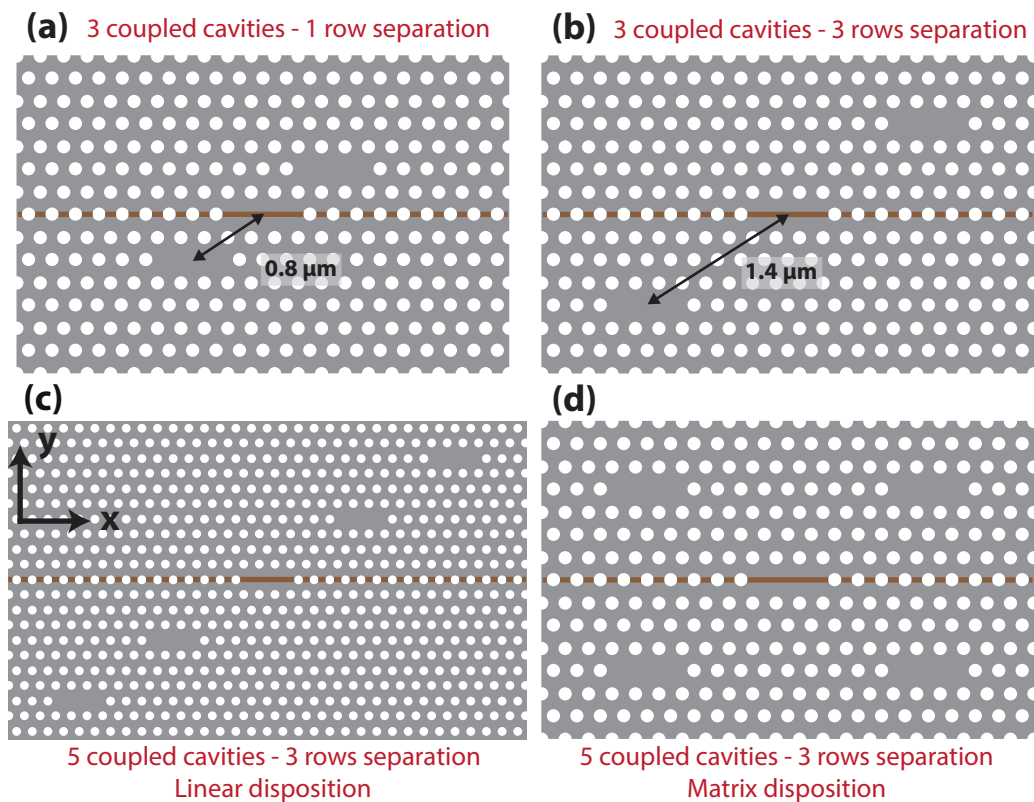


Figure 6.4: Designs of the structures present on the sample: Three linearly coupled cavities with QWRs integrated in the central cavity of the array with 1 (a) and 3 (b) row separation (Refers to the number of rows of PhC holes in between the cavities along the y direction). (c) Five linearly coupled cavities with 3 rows separation and a QWR light source in the central cavity of the array. (d) 2D array comprising of five cavities with QWRs integrated in the central cavity of the array.

6.1.2 Supermode finite difference simulations

The notion of supermode mentioned in the previous section can be better understood by calculating the electric field distributions of CCAs. They can be obtained by performing 2D finite difference simulation for the different CCA designs of Fig. 6.4 and Fig. 6.13 (b). Our 2D simulation relies on an effective index method which allows to compute with great efficiency the electric field distribution at the symmetry plane of the PhC slab (see section 2.2). This method also allows us to obtain an estimation of the energy distribution of the optical mode, which will help interpret the CCA emission spectra.

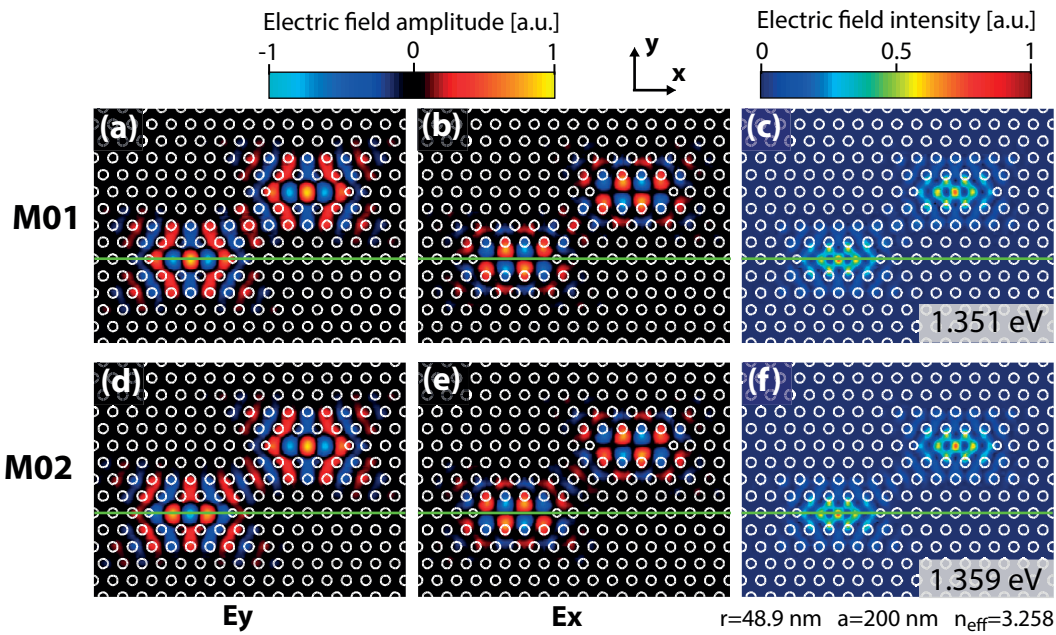


Figure 6.5: Computed near-field distributions for the modes of two coupled cavities. (a) and (b) y and x component of the electric field for M_{01} . (c) Electric field intensity distribution for M_{01} . (d) and (e) y and x component of the electric field for M_{02} . (f) Electric field intensity distribution for M_{02} . The green horizontal line indicates the position of the QWR light source.

The result of these simulations for two coupled cavities is shown in Fig. 6.5. The simulations shown in this section focus on the fundamental TE modes of the CCAs. For the particular case of two coupled cavities, only two fundamental modes, M_{01} and M_{02} , are predicted by the simulations and were observed in the experimental spectrum (Fig. 6.13 (b)). Both modes have a similar electric field intensity distribution (Fig. 6.5 (c) and (d)) and are delocalized over the two cavities forming the array. However, the supermodes M_{01} and M_{02} are not completely identical as revealed by closely inspecting the electric field amplitude distribution. Indeed, for M_{01} the sign of the electric field amplitude taken at the center of the cavities is identical, while for M_{02} it is opposite. For this reason, the M_{01} mode is often referred to as the *even mode*, and the M_{02} mode as the *odd mode*. The difference in parity between the two modes can be understood

6.1. 1D and 2D arrays of coupled cavities with site-controlled quantum wire light sources

and generalized to larger arrays of cavity with coupled mode theory.

Coupled mode theory

We consider the system illustrated in Fig. 6.6, consisting of a chain of N cavities separated by a distance R . In the spirit of Tight Binding theory, we write the electric field of this coupled cavity system, following coupled mode theory[315, 316], as

$$\mathbf{E}_\nu(\mathbf{r}) = \sum_{n=1}^N A_n \mathbf{E}_\omega(\mathbf{r} - nR\mathbf{e}_z) \quad (6.1)$$

where \mathbf{E}_ω is the electric field of an individual cavity and A_n is the amplitude and phase of the n^{th} cavity. The coefficients A_n can be calculated by imposing that \mathbf{E}_ν satisfies Maxwell's equations and using the boundary conditions $A_0 = A_{N+1} = 0$, giving for the q^{th} supermode[317]

$$A_n^q = \sqrt{\frac{2}{N+1}} \sin\left(\frac{\pi q}{N+1}n\right) \quad (6.2)$$

where only nearest neighbour interactions are considered. In this case, the frequency of the q^{th} supermode is[317]

$$\nu^q = \Omega \sqrt{\frac{C^q - \beta}{C^q - \alpha + C^q \Delta\alpha}} \quad (6.3)$$

with

$$\beta = \int d\mathbf{r} \epsilon^0(\mathbf{r} - (m \pm 1)R\mathbf{e}_z) \mathbf{E}_\omega(\mathbf{r} - mR\mathbf{e}_z) \cdot \mathbf{E}_\omega(\mathbf{r} - (m \pm 1)R\mathbf{e}_z) \quad (6.4)$$

$$\alpha = \int d\mathbf{r} \epsilon(\mathbf{r}) \mathbf{E}_\omega(\mathbf{r} - mR\mathbf{e}_z) \cdot \mathbf{E}_\omega(\mathbf{r} - (m \pm 1)R\mathbf{e}_z) \quad (6.5)$$

$$\Delta\alpha = \int d\mathbf{r} [\epsilon(\mathbf{r}) - \epsilon^0(\mathbf{r} - mR\mathbf{e}_z)] \mathbf{E}_\omega(\mathbf{r} - mR\mathbf{e}_z) \cdot \mathbf{E}_\omega(\mathbf{r} - mR\mathbf{e}_z) \quad (6.6)$$

where $\epsilon^0(\mathbf{r})$ and $\epsilon(\mathbf{r})$ are the dielectric function distributions of an individual cavity and the coupled cavity system respectively.

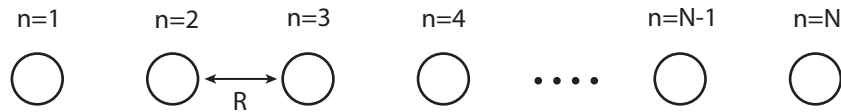


Figure 6.6: Schematics of chain of N cavities separated by a distance R .

Chapter 6. Supermodes in 1D and 2D coupled cavity arrays

For $N = 2$, the corresponding superposition coefficients are summarized in table 6.1. For the first supermode ($q = 1$), the superposition coefficients are identical, while for the second supermode ($q = 2$), they have an opposite sign. This result can be seen in the field patterns of Fig. 6.5 (a) and (d). The supermode field pattern in each cavity is very similar to the field pattern of the M_0 mode of an individual L_3 cavity. This is a necessary condition to apply coupled mode theory which is valid only for weak inter-cavity coupling.

Table 6.1: Coupled mode theory superposition coefficients calculated for $N=2$.

$n =$	1	2
A_n^1	$\frac{1}{\sqrt{2}}$	$\frac{1}{\sqrt{2}}$
A_n^2	$\frac{1}{\sqrt{2}}$	$-\frac{1}{\sqrt{2}}$

This simple analysis can help understand what to expect for three linearly coupled cavities with $1.4\mu m$ inter-cavity separation. In this case we expect three supermodes, with superposition coefficients summarized in table 6.2. Once again the sign of the superposition coefficients correspond to the sign of the y- component of the electric field at the center of cavity of the array (Fig. 6.7 (a)-(c)). Furthermore, in contrast to the case of two coupled cavities, the amplitude of the coefficients varies from cavity to cavity. For M_{01} , the electric field is more intense in the center cavity of the array (Fig. 6.7 (g)). For M_{02} , the electric field intensity is equal to zero in the center cavity (Fig. 6.7 (h)).

Table 6.2: Coupled mode theory superposition coefficients calculated for $N=3$.

$n =$	1	2	3
A_n^1	$\frac{1}{2}$	$\frac{1}{\sqrt{2}}$	$\frac{1}{2}$
A_n^2	$\frac{1}{\sqrt{2}}$	0	$-\frac{1}{\sqrt{2}}$
A_n^3	$\frac{1}{2}$	$-\frac{1}{\sqrt{2}}$	$\frac{1}{2}$

Although the same general trends are reproduced for three linear cavities with $0.8\mu m$ inter-cavity separation, the electric field patterns are different. This inter cavity separation does not correspond to weak inter-cavity coupling and coupled mode theory starts to break down. Indeed, for the M_{02} supermode, the field intensity in the center cavity deviates from zero.

6.1. 1D and 2D arrays of coupled cavities with site-controlled quantum wire light sources

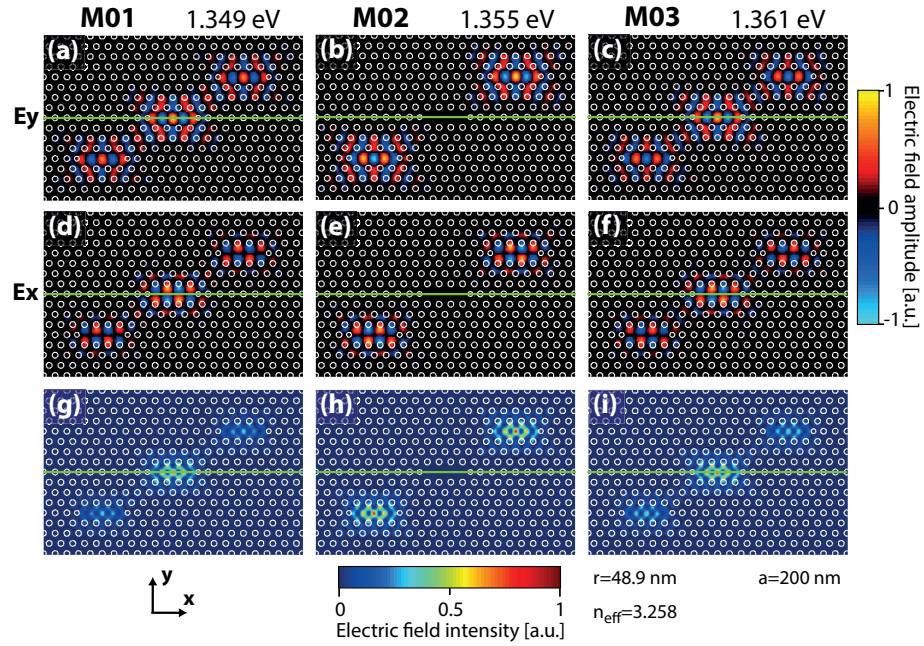


Figure 6.7: Computed near-field distributions for the modes of three coupled cavities with 3 rows separation. (a)-(c) y component of the electric field for M_{01} , M_{02} and M_{03} . (d)-(f) x component of the electric field for M_{01} , M_{02} and M_{03} . (g)-(i) Electric field intensity distribution for M_{01} , M_{02} and M_{03} . The green horizontal line indicates the position of the QWR light source.

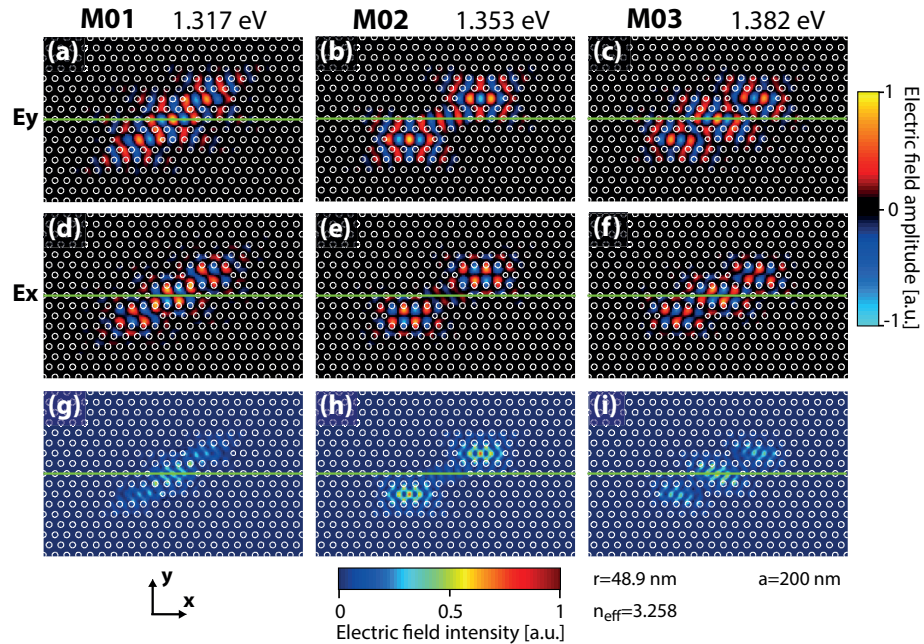


Figure 6.8: Computed near-field distributions for the modes of three coupled cavities with 1 row separation. (a)-(c) y component of the electric field for M_{01} , M_{02} and M_{03} . (d)-(f) x component of the electric field for M_{01} , M_{02} and M_{03} . (g)-(i) Electric field intensity distribution for M_{01} , M_{02} and M_{03} . The green horizontal line indicates the position of the QWR light source.

Chapter 6. Supermodes in 1D and 2D coupled cavity arrays

The case of 5 linearly coupled cavities with $1.4\mu m$ inter-cavity separation follows the same logic as for 3 cavities. The superposition coefficients calculated using coupled mode theory are summarized in table 6.3. The electric field patterns of the five supermodes computed using 2D finite differences are shown in Fig. 6.9. For this longer chain of coupled cavities it becomes apparent that the field intensity in each cavity is modulated by a sine function, which is consistent with equation (6.2).

Table 6.3: Coupled mode theory superposition coefficients calculated for N=5.

$n =$	1	2	3	4	5
A_n^1	$\frac{1}{2\sqrt{3}}$	$\frac{1}{2}$	$\frac{1}{\sqrt{3}}$	$\frac{1}{2}$	$\frac{1}{2\sqrt{3}}$
A_n^2	$\frac{1}{2}$	$\frac{1}{2}$	0	$-\frac{1}{2}$	$-\frac{1}{2}$
A_n^3	$\frac{1}{\sqrt{3}}$	0	$-\frac{1}{\sqrt{3}}$	0	$\frac{1}{\sqrt{3}}$
A_n^4	$\frac{1}{2}$	$-\frac{1}{2}$	0	$\frac{1}{2}$	$-\frac{1}{2}$
A_n^5	$\frac{1}{2\sqrt{3}}$	$-\frac{1}{2}$	$\frac{1}{\sqrt{3}}$	$-\frac{1}{2}$	$\frac{1}{2\sqrt{3}}$

With five cavities, it is also possible to form a 2D CCA, while maintaining an optimal inter-cavity coupling (Fig. 6.4 (d)). The calculated electric field patterns for this structure are summarized in Fig. 6.10. The superposition coefficients calculated using coupled mode theory for a linear chain of cavity do not apply here. However, a similar calculation for 2D arrays of cavities[318] can explain the mode patterns observed here.

6.1. 1D and 2D arrays of coupled cavities with site-controlled quantum wire light sources

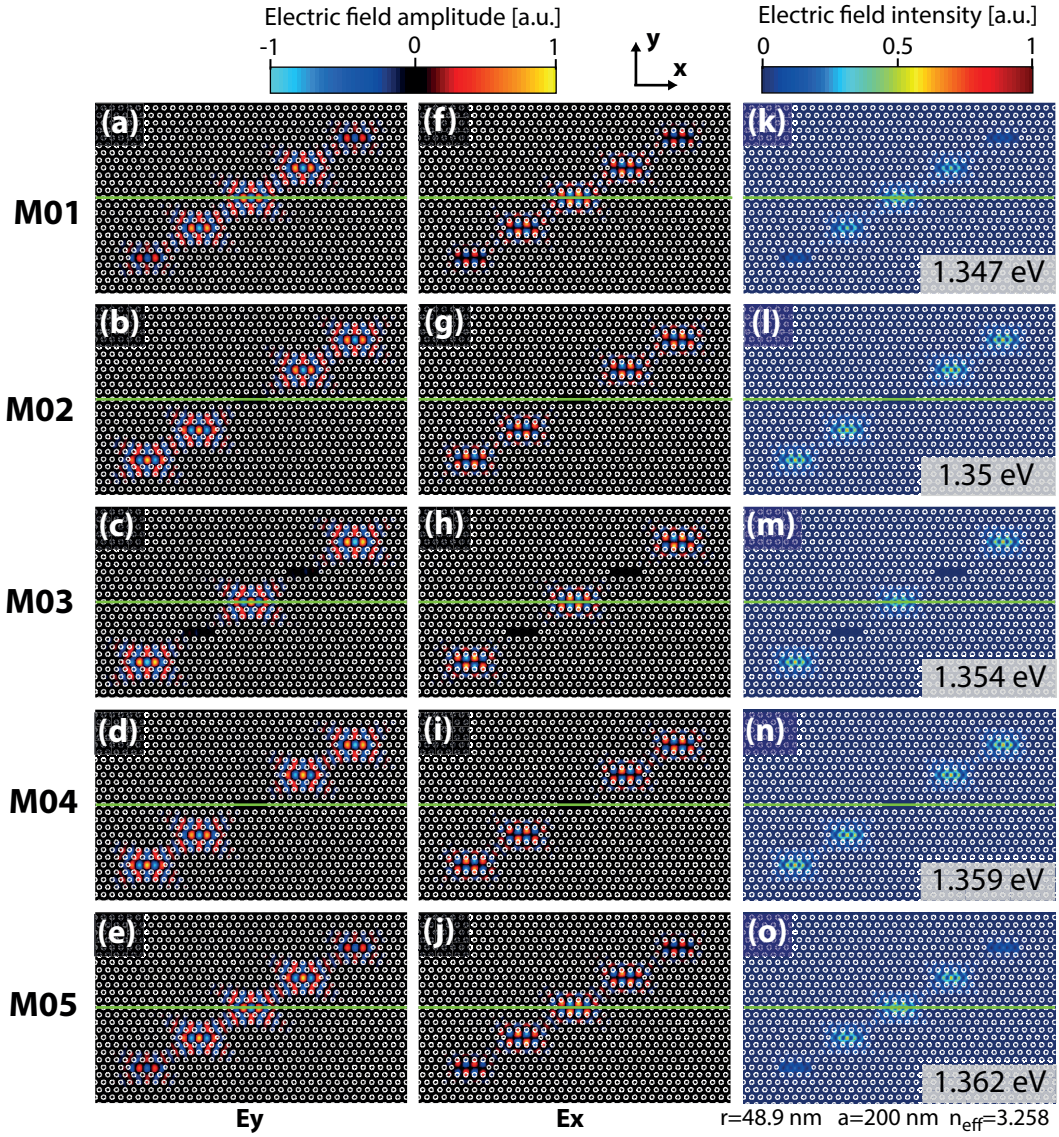


Figure 6.9: Computed near-field distributions for the modes of five linearly coupled cavities with 3 rows separation. (a)-(e) y component of the electric field for M_{01} , M_{02} , M_{03} , M_{04} and M_{05} . (f)-(j) x component of the electric field for M_{01} , M_{02} , M_{03} , M_{04} and M_{05} . (k)-(o) Electric field intensity distribution for M_{01} , M_{02} , M_{03} , M_{04} and M_{05} . The green horizontal line indicates the position of the QWR light source.

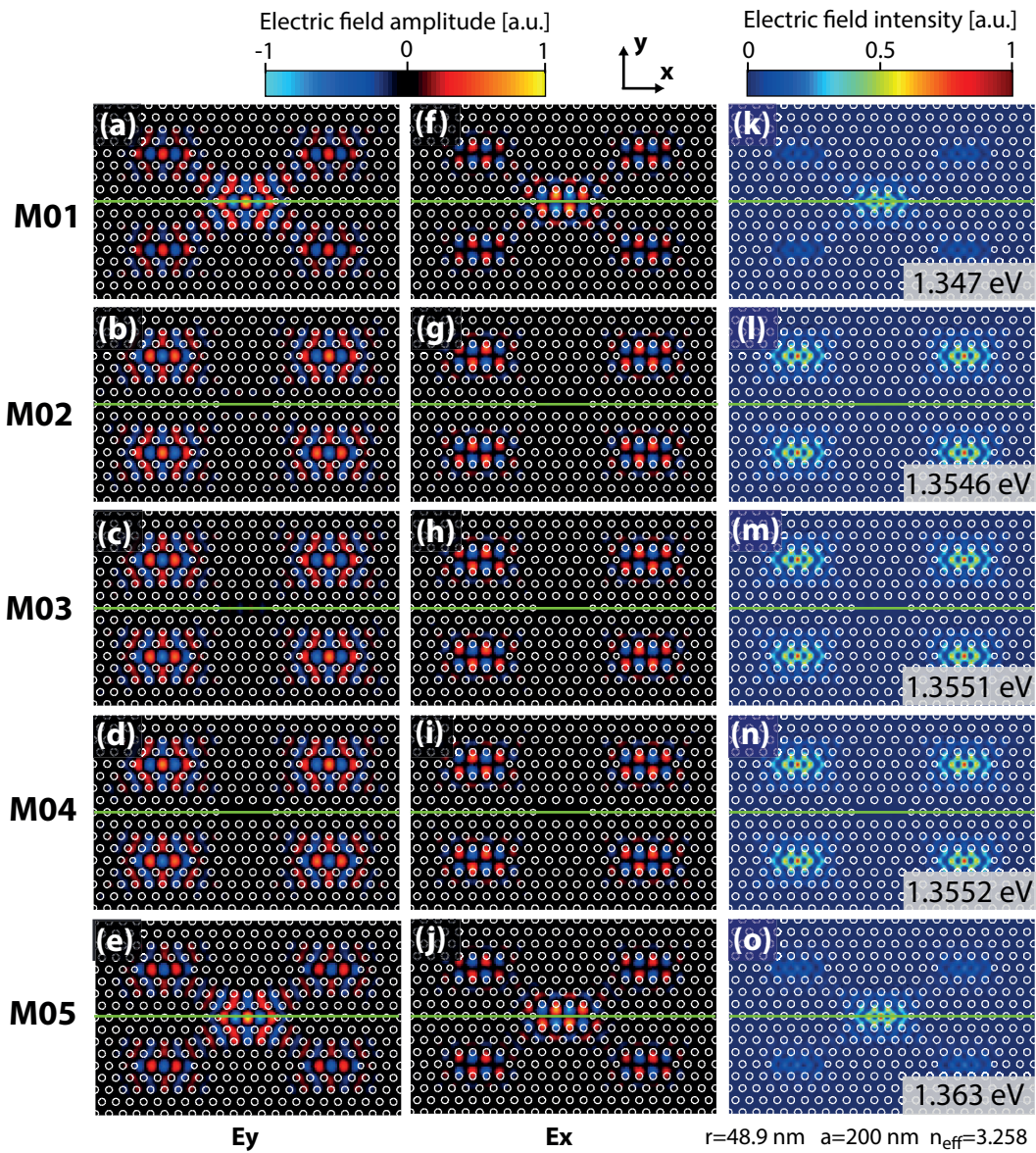


Figure 6.10: Computed near-field distributions for the modes of 2D array made of five coupled cavities with 3 rows separation. (a)-(e) y component of the electric field for M_{01} , M_{02} , M_{03} , M_{04} and M_{05} . (f)-(j) x component of the electric field for M_{01} , M_{02} , M_{03} , M_{04} and M_{05} . (k)-(o) Electric field intensity distribution for M_{01} , M_{02} , M_{03} , M_{04} and M_{05} . The green horizontal line indicates the position of the QWR light source.

6.1. 1D and 2D arrays of coupled cavities with site-controlled quantum wire light sources

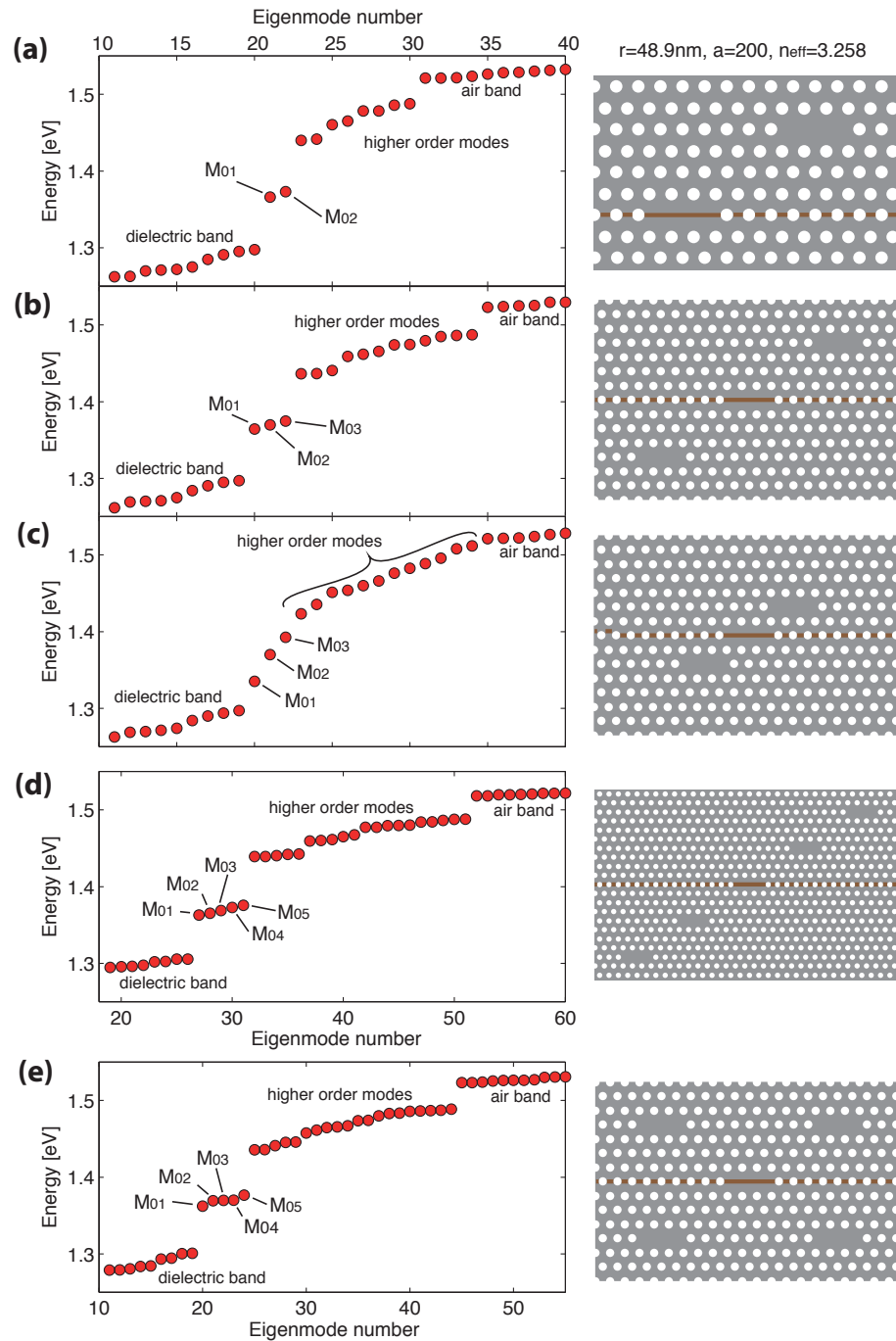


Figure 6.11: TE modes of coupled cavity arrays calculated with 2D finite difference for (a) two coupled cavities, (b) three coupled cavities with 3 rows separation, (c) three coupled cavities with 1 row separation, (d) five linearly coupled cavities and (e) a 2D array of five coupled cavities.

The mode energy distribution of the five CCA presented in this section are shown in Fig. 6.11. The localized supermodes lie within the PhC band gap, between the dielectric and air bands (see subsection 1.4.1). The fundamental supermodes (labelled

M_{01} , M_{02} , etc.), stemming from the interaction of the M_0 modes of the individual L_3 cavities are located right above the dielectric band. Their field pattern distributions are shown in Figs. 6.5 and 6.7-6.10. Higher order localized modes were also predicted by the simulations. These higher energy modes result from interaction of the higher order modes (M_1 , M_2 , etc.) of the individual L_3 cavities of the array. However, the QWR growth and PhC design were optimized to match the QWR emission with the fundamental mode energies. We also see from Fig. 6.11 that for a given design, the fundamental modes are not at the same energy. In particular, for two cavities (Fig. 6.11 (a)), the modes M_{01} and M_{02} are split in energy. Indeed this system is analog to two coupled oscillators of frequency ω_1 and ω_2 , interacting with a coupling strength G . The Hamiltonian for this system in matrix form is

$$H = \begin{bmatrix} a^\dagger & b^\dagger \end{bmatrix} \begin{bmatrix} \omega_1 & G \\ G & \omega_2 \end{bmatrix} \begin{bmatrix} a \\ b \end{bmatrix}. \quad (6.7)$$

The eigenvalues of this system are

$$\Omega_{\pm} = \frac{\omega_1 + \omega_2}{2} \pm \frac{1}{2} \sqrt{(\omega_1 - \omega_2)^2 + 4G^2}. \quad (6.8)$$

For two identical cavities ($\omega_1 = \omega_2$) we get $\Omega_{\pm} = \omega \pm G$, which corresponds to an energy splitting $\Delta = 2G$ between the two modes. For PhC CCAs, the mode energy separation is dependent on the inter-cavity coupling strength G , which is related to the overlap between the evanescent fields of each cavity, and thus the inter-cavity separation. Indeed, as can be seen in Fig. 6.11 (b) and (c), the three coupled cavities with a smaller inter-cavity separation of $0.8\mu\text{m}$ have a greater mode energy splitting (Fig. 6.11 (c)).

6.1.3 Photoluminescence measurements

Optical characterization of the CCA arrays was conducted using a standard micro-PL setup (see subsection 2.1.2 for details). The samples were placed inside a He-flow cryostat and excited optically with a Ti:sapphire laser at 700 nm wavelength under continuous wave operation. A single microscope objective was used to focus the laser beam on the sample surface (spot diameter of $1\mu\text{m}$) and collect the luminescence. A half-wave plate and a linear polarizer were placed in the detection path for polarization-resolved measurements.

Fig. 6.12 (b) shows the PL of bare QWRs, resolved in polarization along the V and H directions indicated in Fig. 6.12 (a). The energy width of the QWR emission spectrum is approximately 10 meV . A few sharp features can be seen in the luminescence of the wires. They correspond to the luminescence of localized excitons, trapped in disorder induced potential traps along the QWR[319, 320]. Fig. 6.12 (b) also displays the DOLP of the luminescence. The QWR emission is H-polarized, reaching a maximum of -0.5 at

6.1. 1D and 2D arrays of coupled cavities with site-controlled quantum wire light sources

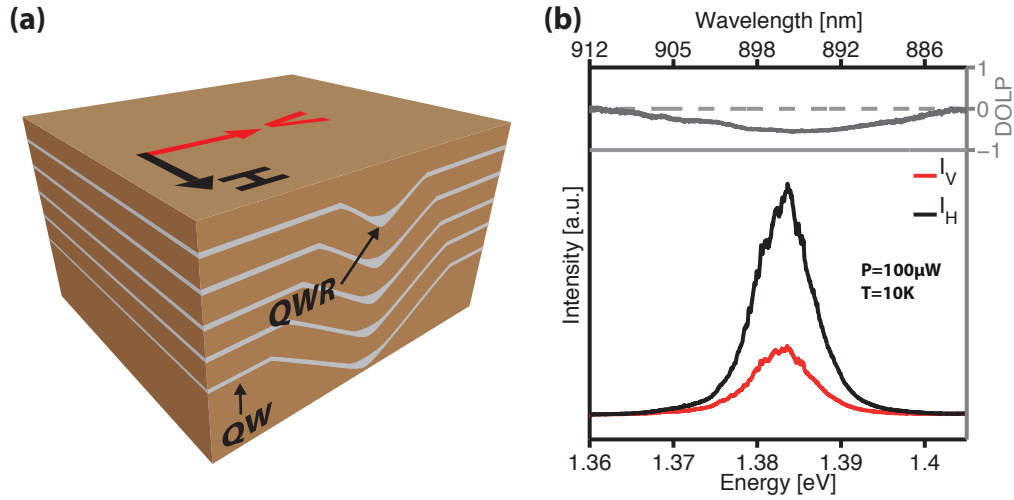


Figure 6.12: (a) Schematics of the cross-sectional view of the stacked QWRs light sources integrated in the cavities. (b) Photoluminescence measurement of isolated QWRs linearly resolved in polarization along the V and H directions indicated in (a). Upper panel: Corresponding degree of linear polarization shown in grey.

the center of the QWR emission. This polarization anisotropy is consistent with mixing between heavy-hole and light-hole bands induced by the two-dimensional quantum confinement[321].

The PL of typical structures consisting of a stack of 5 QWRs integrated in the center of an L_3 PhC cavity is shown in Fig. 6.13 (a). The photoluminescence is resolved in linear polarization and displayed in semilogarithmic scale. The enhancement of the QWR emission by the fundamental mode of the cavity can be clearly seen in the luminescence. This is a consequence of the Purcell effect, and a signature of QWR-cavity coupling. At the emission energy of the CM, the polarization anisotropy has been reversed, and the emission is now V-polarized. Indeed, QWR excitations spectrally and spatially overlapping with the CM are more efficiently channeled into the microscope objective by the fast decaying and V-polarized CM, than non coupled QWR excitations. Fig. 6.13 (b) shows similar results for a structure with two L_3 cavities. The QWRs are integrated only in the bottom cavity. The two fundamental modes of the cavities denoted M_{01} and M_{02} are clearly visible in the spectra. The fact that two CM are excited by the QWRs is already an indication that the two cavities are coupled, hosting two fundamental supermodes delocalized over both cavities. Indeed, in the case of uncoupled cavities, only the fundamental mode of the bottom cavity would be coupled to the QWRs and thus visible in the spectra. This CCA made of two cavities is often referred to as a *photonic molecule*.

Fig. 6.14 (a) and (b) show typical PL spectra of CCAs comprising of three cavities, corresponding to the designs of Fig. 6.4 (a) and (b). Here, three optical modes (M_{01} , M_{02} and M_{03}) are visible in the spectra. The QWRs are integrated only in the center

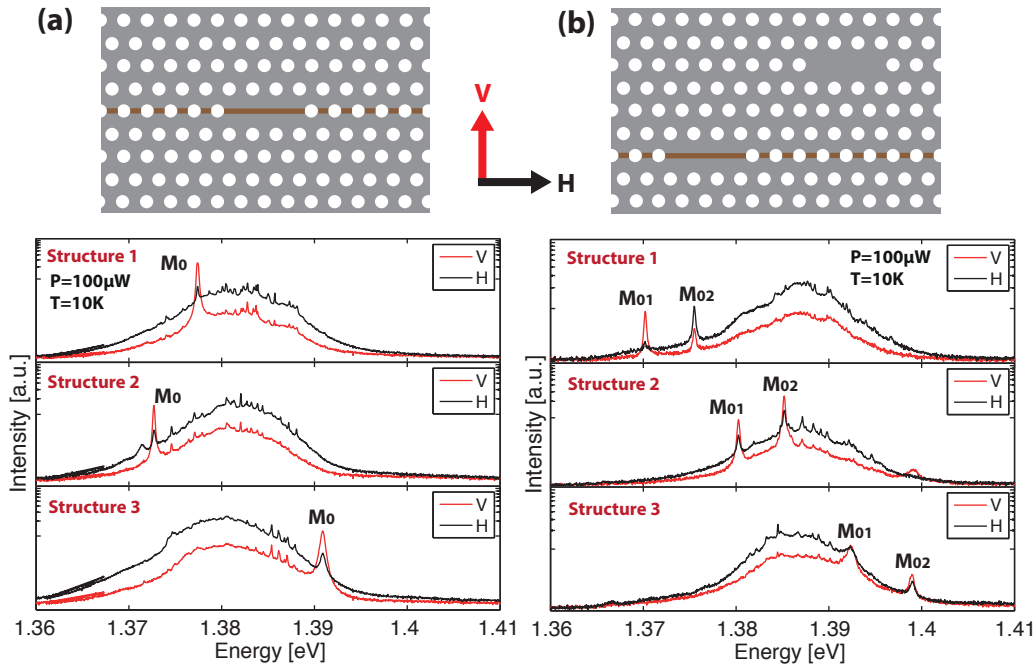


Figure 6.13: (a) Measured spectra of QWRs integrated in an L_3 PhC cavity, linearly resolved along the V and H directions. (b) Measured spectra of two coupled cavities with 3 rows separation and QWRs integrated in the bottom cavity only (cf. schematic). The spectra are resolved in linear polarization along the V and H directions.

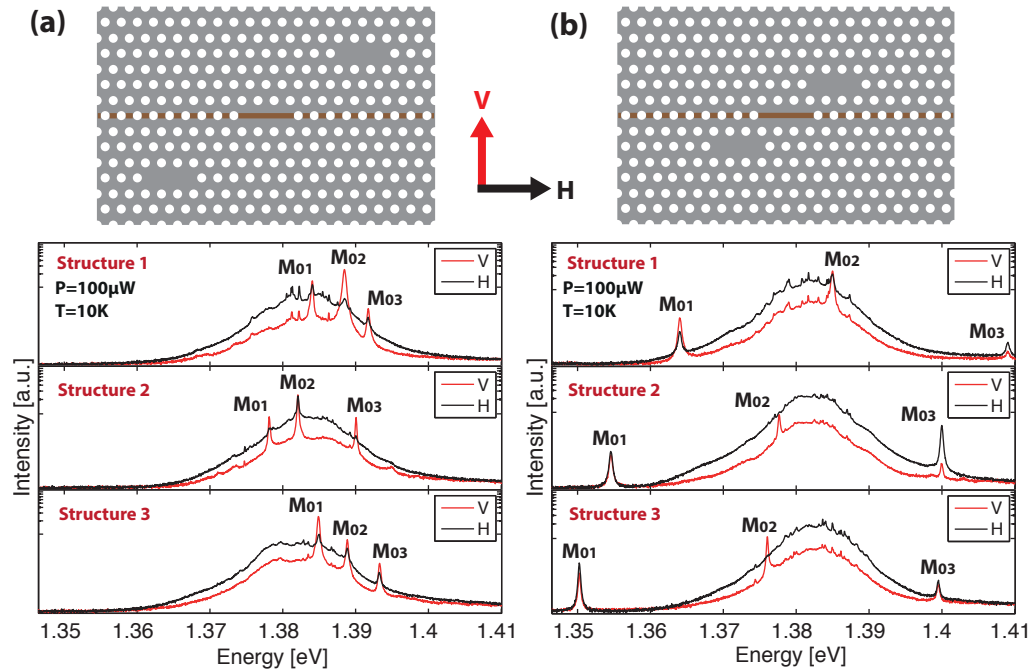


Figure 6.14: Measured spectra of three coupled cavities with 3 rows (a) and 1 row (b) separation. The QWR light source is integrated in the central cavity of the array (cf. schematics). The spectra are resolved in linear polarization along the V and H directions.

6.1. 1D and 2D arrays of coupled cavities with site-controlled quantum wire light sources

cavity. Once again, the presence of three CM in the spectra is an indication of inter-cavity coupling and optical mode delocalization. A striking difference between the spectra of Fig. 6.4 (a) and (b) is the much larger CM energy separation observed for Fig. 6.4 (b), which is in qualitative agreement with the finite difference calculations (Fig. 6.11 (b) and (c)). For Fig. 6.4 (b), the larger mode separation is a consequence of larger inter-cavity coupling, which is consistent with the smaller inter-cavity separation ($0.8\mu m$ as opposed to $1.4\mu m$). A more detailed analysis of mode energy separation will be given in section 6.1.4.

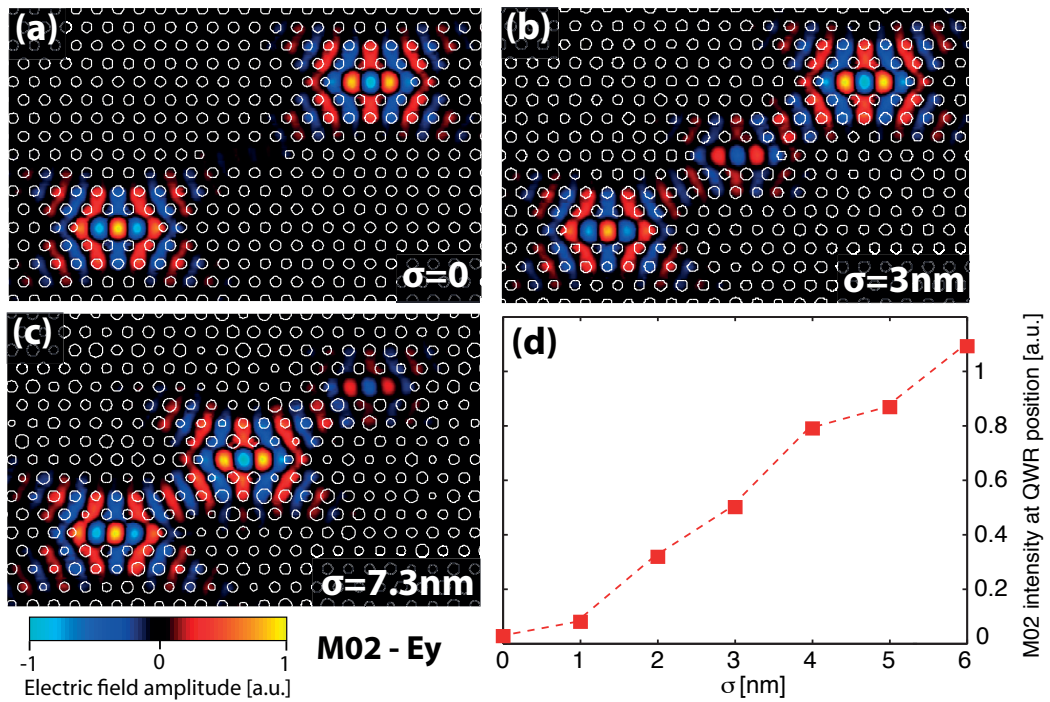


Figure 6.15: (a)-(c) M_{02} y component of the electric field with hole radius disorder characterized by a standard deviation $\sigma = 0$, $\sigma = 3 \text{ nm}$ and $\sigma = 7.3 \text{ nm}$, for $r = 48.9 \text{ nm}$ and $a = 200 \text{ nm}$. (d) Integrated intensity of the M_{02} mode along the QWRs position within the central cavity as a function of σ .

It might seem surprising that we observe coupling between the QWRs and the super-mode M_{02} in the spectra of Fig. 6.4 (a), which, for an ideal structure, has a vanishing field intensity at the central cavity (Fig. 6.7 (h)). This observation is explained by the effect of fabrication-induced structural disorder. Indeed, structural disorder is expected to alter the envelope function shapes, causing increasing localization at either one of the cavities with increasing disorder and/or increasing distance between the cavities (lower coupling). To get a qualitative picture of this effect on the mode distributions, we artificially introduced disorder in our numerical simulation by changing randomly the PhC hole sizes, following a normal distribution characterized by an average radius $r = 48.9 \text{ nm}$ and a standard deviation σ . Fig.6.15 (c) displays the calculated y-component of the M_{02} field distribution for $\sigma = 3 \text{ nm}$. Compared to the

case of vanishing disorder (Fig.5.2 (b)), it is apparent that the disorder significantly increases the electric field amplitude in the central cavity. In addition, we calculated the integrated intensity of the M_{02} mode along the QWRs position within the central cavity as a function of σ (Fig.6.15 (d)). For each σ , this value was averaged over 150 repetitions of the simulation. We observe a clear enhancement of the central cavity near-field intensity as σ is increased. In our structures, hole size variations of a few nanometers are expected, explaining the observation of mode M_{02} in the PL measurements.

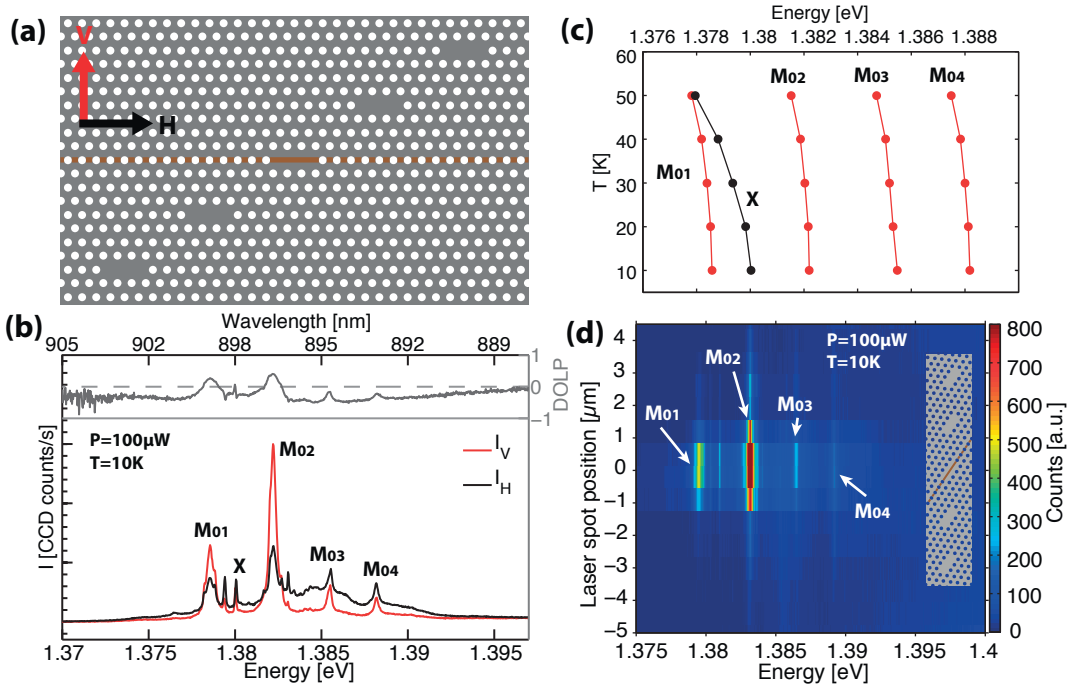


Figure 6.16: Schematics of five linearly coupled cavities with 3 rows separation. (b) Measured spectrum linearly resolved in polarization along the V and H directions indicated in (a). Upper panel: corresponding DOLP showed in grey. (c) CCA supermodes and localized QWR exciton X energies as a function of sample temperature. (d) Measured spectra showing the supermode intensities as a function of excitation laser spot position.

Fig. 6.16 shows results of PL measurements for a larger linear CCA made out of five L_3 PhC cavities (Fig. 6.16 (a)). The polarization resolved PL spectra of the structure are shown in Fig. 6.16 (b). Four CMs, labelled M_{01} , M_{02} , M_{03} and M_{04} , can be identified by their different polarization, with respect to the background QWR emission. They can be more clearly identified by examining the DOLP of the luminescence in the top panel of Fig. 6.16 (b). Here only four modes were identified instead of the five fundamental supermodes expected for such a structure. This can happen if one of the mode field pattern does not have a significant overlap with the QWRs located in the central cavity. By examining the field patterns of this structure (Fig. 6.9), we can see that two of the five supermodes do not overlap with the QWRs. However, as for the case of three linearly coupled cavities (see Fig. 6.15), we expect the structural disorder to alter the field distribution and induce a finite coupling between these two modes and the QWRs.

6.1. 1D and 2D arrays of coupled cavities with site-controlled quantum wire light sources

For this particular structure, the modification of the field pattern by the fabrication induced disorder may be insufficient for one of these modes, which would explain its absence in the PL spectrum. To confirm the mode identification, the energy of the modes was monitored while the temperature of the sample was scanned from 10 K to 50 K as shown in Fig. 6.16 (c). As expected the mode energies shift with temperature, but at a different rate than the localized QWR excitons. To prove that all CMs are indeed fed by the QWRs in the central cavity of the CCA, we scanned the laser excitation spot across the CCA. The spectra are shown as a function of the laser spot position in Fig. 6.16 (d). The maximum CM intensities are registered when the laser spot is centered on the cavity incorporating the QWRs, corresponding to a spot position of 0 μm . The CM intensities rapidly decrease when the laser spot is moved away from the central cavity, and become negligible for a distance greater than 1 μm corresponding to the laser spot diameter. When the laser spot is directly above the other cavities of the array, no emission from either the QWRs or the modes is registered as expected. This gives further evidence that the QWRs in the central cavity of the array couples to, in this case, four CMs of the array.

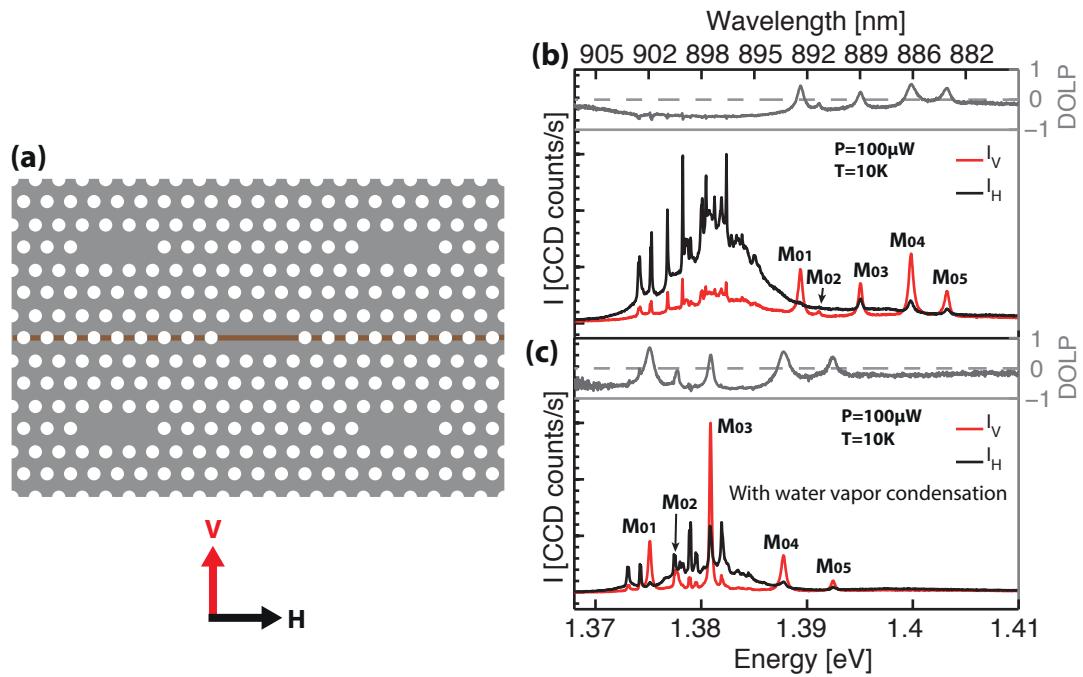


Figure 6.17: (a) Schematics of a 2D array of cavities with 3 row separation. (b) [(c)] Measured low temperature spectrum resolved in linear polarization along the V and H directions with [without] water vapor condensation. Upper panel: corresponding DOLP shown in grey.

Finally, PL measurements performed on a 2D CCA, comprising of five cavities are shown in Fig. 6.17. The cavities are arranged in a matrix form, maximizing the inter-cavity coupling (Fig. 6.16 (a)). Fig. 6.16 (b) shows the polarization resolved PL of the

structure. Five modes are clearly visible in the DOLP of the luminescence (upper panel). The CMs are not centered on the QWR emission but have a sufficient spectral overlap to allow coupling. Fig. 6.16 (c) shows the spectrum of the same structure after water vapor condensation (see subsection 2.3.2 for details on water vapor condensation technique). The condensation results in a 15 meV redshift of the modes, bringing them in resonance with the QWR emission.

6.1.4 Coupled cavity mode delocalization

Incorporating a site-controlled light source in a CCA allows to unambiguously determine via PL spectral measurements whether or not the cavities are coupled and if the supermodes are delocalized. Fig.6.18 (a) and (b) display the low temperature (10K) PL spectra for the three-cavity CCAs with 3 rows (see Fig.6.3 (b)) and 1 row (see Fig.6.3 (a)) cavity separations, respectively. In Fig.6.18 (a), Purcell enhancement of the QWRs emission[15] is clearly observed in the form of three thin peaks (quality factor ~ 3800) at distinct energies, suggesting that the QWRs in the central cavity emit into three confined optical modes. Note that the DOLP of these mode peaks is opposite in sign to that of the QWR background emission, including the sharp PL lines of the QWR that

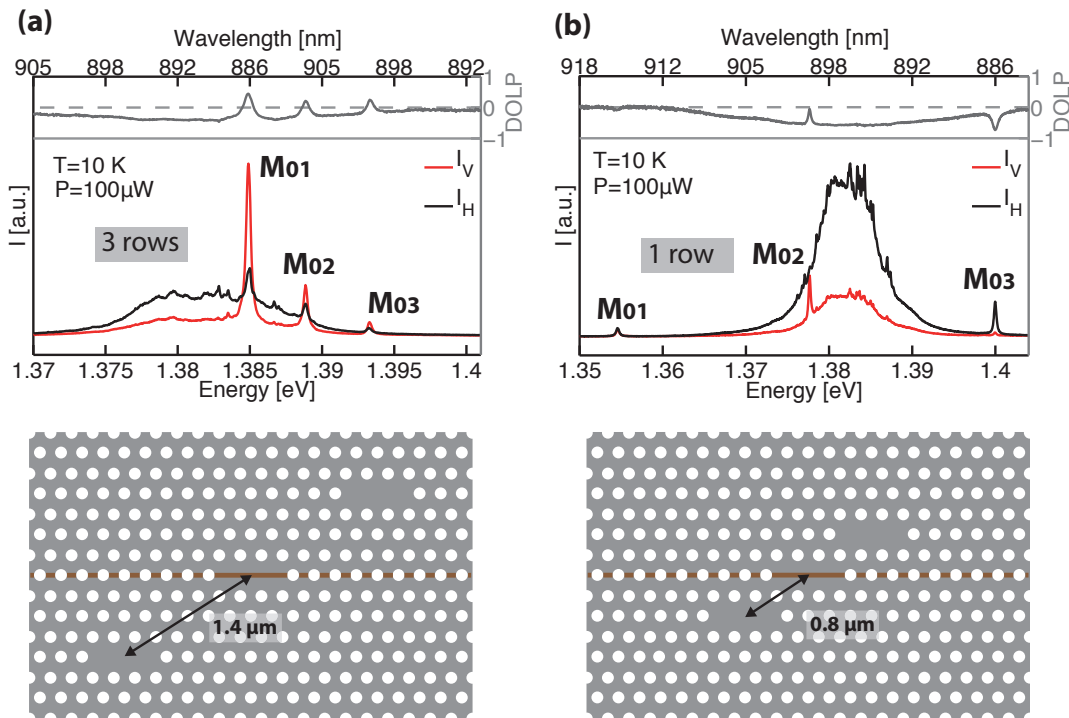


Figure 6.18: Measured PL spectra of three diagonally coupled L_3 cavities, resolved in linear polarization along the directions V and H; QWR light source inserted in center cavity only: (a) spectra for 3 rows separation, (b) spectra for 1 row separation. The DOLP is indicated for both spectra.

6.1. 1D and 2D arrays of coupled cavities with site-controlled quantum wire light sources

arise from localized exciton recombination. These cavity modes correspond to the three supermodes of the array M_{01} , M_{02} and M_{03} , as will be shown more quantitatively below. In case of complete localization of the modes at different cavities, only the mode localized in the center cavity, incorporating the localized QWR light source, would have a signature in the PL. The observation of more than one cavity peak in the PL spectrum is a proof that mode delocalization and thus optical coupling among cavities occurs.

Table 6.4: Calculated mode energies associated to the modes of Fig.5.2 for three coupled cavities separated by 3 rows (top) and 1 row (bottom). The energy separations Δ_{12} and Δ_{32} are the energy differences between the modes M_{02} and M_{01} , and M_{03} and M_{02} .

3 row	M_{01}	M_{02}	M_{03}
Energy [eV]	1.3688	1.3722	1.3754
Energy separation [meV]	$\Delta_{12} = 3.4$	$\Delta_{32} = 3.2$	
1 row	M_{01}	M_{02}	M_{03}
Energy [eV]	1.3444	1.3708	1.3917
Energy separation [meV]	$\Delta_{12} = 26.3$	$\Delta_{32} = 20.9$	

Fig.6.18 (b) shows the PL spectra of a CCA with 1 row separation, where the inter-cavity coupling is expected to be larger than for 3 rows separation. The three delocalized supermodes can be clearly identified here as well, and their spectral separation is much greater than for the 3 rows separation. This is in qualitative agreement with the calculations of the mode splitting in a three-element coupled system which scales with the coupling strength as $\Delta = \sqrt{2}G$, as well as the 3D FDTD mode energy computations summarized in table 6.4. Note the different polarization of mode M_{03} , believed to occur due to the stronger optical coupling in this case.

Further evidence for the occurrence of delocalized modes in the three-element CCAs was obtained by observing similar PL spectra for 17 other nominally identical structures on the same sample. For each of these structures, we recorded the mode energies $E_{M_{01}}$, $E_{M_{02}}$, $E_{M_{03}}$ which are displayed as a function of the mean energy $(E_{M_{01}} + E_{M_{03}})/2$ in Fig. 6.19 (a) and (b). From these measurements, we computed the mode separations $\Delta_{12} = E_{M_{02}} - E_{M_{01}}$ and $\Delta_{23} = E_{M_{03}} - E_{M_{02}}$. The fabrication-induced disorder present in real CCAs prevents a straightforward estimation of the coupling strength G from mode splitting measurements. Indeed, in the case of two coupled cavities, the mode separation can be expressed as

$$\Delta = \sqrt{\Delta_0^2 + 4G^2} \quad (6.9)$$

where Δ_0 is the energy difference between the two cavities induced by disorder[308].

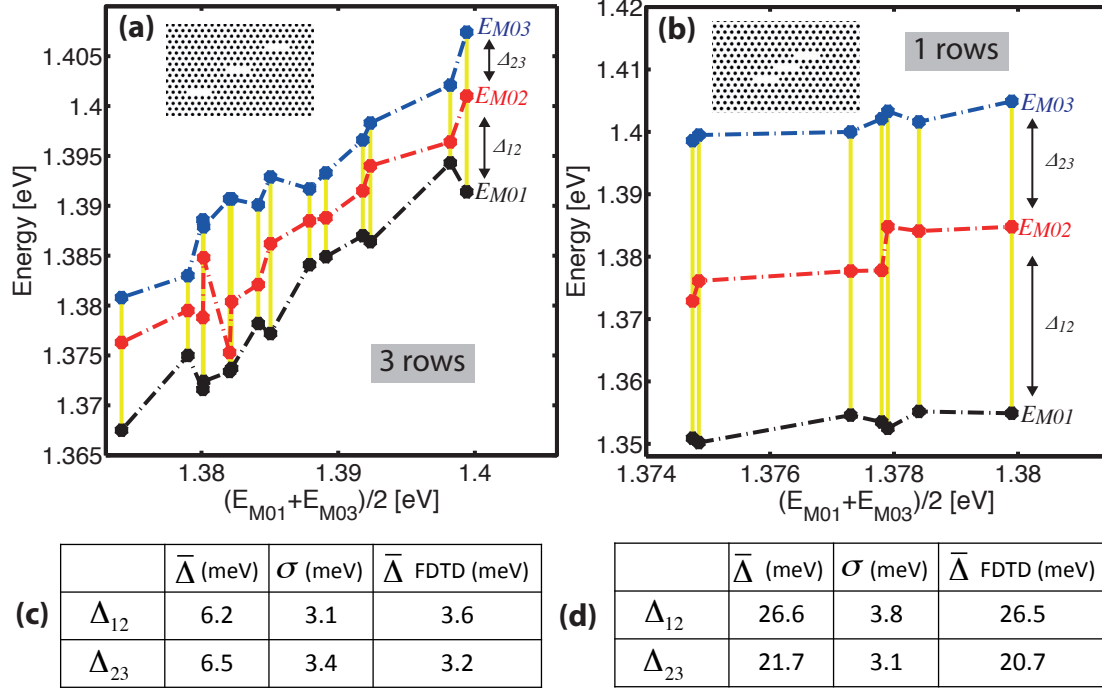


Figure 6.19: Measured energies of the M_{01} , M_{02} and M_{03} supermodes as a function of their mean energy value (dotted lines) for three cavity CCAs with a cavity separation of 3 rows (a) and 1 row (b). The vertical yellow lines indicate the set of points belonging to the same structure. The mean value of the supermodes energy separation $\bar{\Delta}$ as well as its standard deviation σ are indicated in (c) and (d) for respectively the 3 rows and 1 row separations. $\bar{\Delta}$ is compared to the values computed using 3D FDTD.

Although Δ_0 is difficult to estimate, the relative weight between the contributions of the disorder and the coupling strength to the total mode splitting can be derived from a statistical analysis. Indeed, as explained in Ref [308], these contributions can be estimated by considering the ratio between the mean mode separation $\bar{\Delta}$ of nominally identical CCAs and its corresponding standard deviation σ . In particular, a ratio $\sigma/\bar{\Delta} \ll 1$ indicates a dominant contribution of the coupling strength to the mode separation.

Fig.6.19 (c) and (d) list the average mode separations and corresponding standard deviations as well as the mode splittings computed with 3D FDTD simulations for the 3 rows separation and 1 row separation configurations. For the smaller inter-cavity separation, we get a ratio $\sigma/\bar{\Delta} \sim 0.1$ which indicates a strong inter-cavity coupling and a relatively negligible disorder effect. This is confirmed by comparing the average mode separations to the mode splitting of the system without disorder calculated with 3D FDTD simulations. As expected, the FDTD simulations reproduce the measured mode splitting since the disorder effect in that case is negligible. For the 3 rows configuration, the CCA no longer satisfies the condition $\sigma/\bar{\Delta} \ll 1$, meaning that the contribution of

6.1. 1D and 2D arrays of coupled cavities with site-controlled quantum wire light sources

the coupling strength is now comparable to the contribution of the disorder to the total mode splitting. As a result, the measured average mode separation is now more important than the value obtained from the FDTD simulation of the system without disorder. As explained in the previous section, this disorder modifies the modes field distribution and explains why the M_{02} supermode is excited by the QWRs located in the central cavity. However, we show here that even when the fabrication-induced disorder is comparable to the inter-cavity coupling strength, mode delocalization still occurs, as evidenced by the observation of the three supermodes in the spectrum. In other words, the formation of supermodes in a CCA is surprisingly robust to disorder.

One-dimensional CCAs are useful because of their relative simplicity and use in applications such as slow light propagation. However, to achieve the necessary scalability required to implement quantum networks, CCAs of higher dimensionality have to be fabricated. We investigated also the five-cavity 2D cross-shaped CCAs (Fig. 6.3 (d)), with the QWRs inserted at the center cavity alone, by performing PL-measurements.

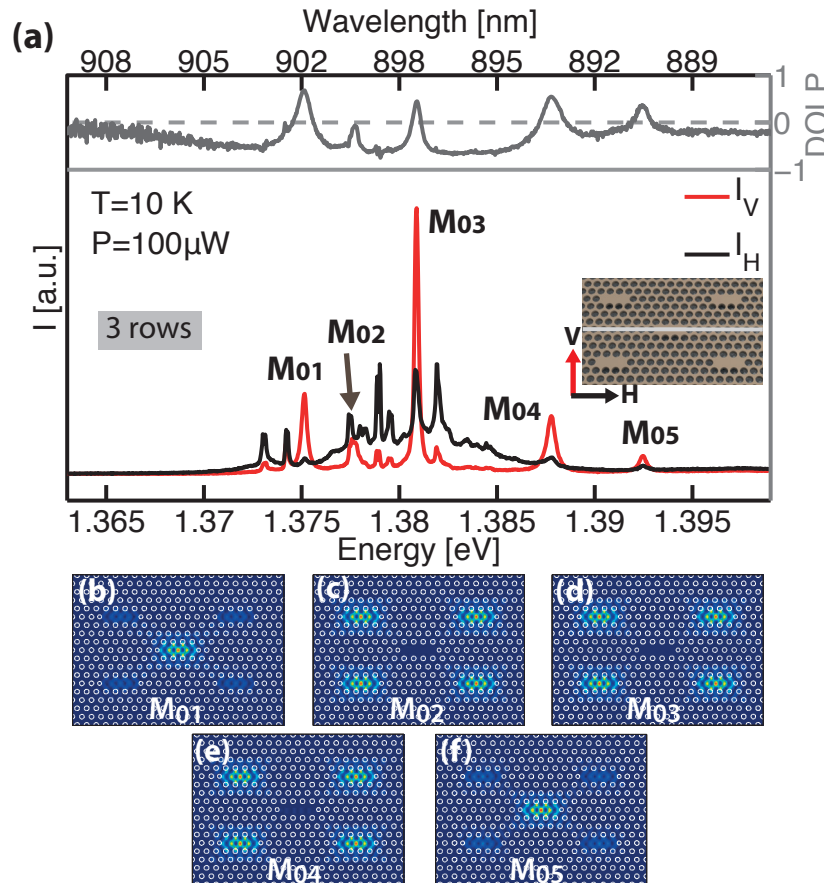


Figure 6.20: (a) PL spectra linearly resolved in linear polarization along the directions defined in figure 1 for a structure consisting of 5 coupled cavities (refer to inset for design). (b)-(f) Calculated intensity distributions for the M_{01} , M_{02} , M_{03} , M_{04} and M_{05} supermodes.

Chapter 6. Supermodes in 1D and 2D coupled cavity arrays

Fig.6.20 (a) shows the PL spectra of a structure for which we could identify 5 modes fed by the QWR emission. We observe the Purcell enhancement of the QWR emission for 5 distinct energies, together with a change in the far-field polarization of the luminescence clearly visible in the DOLP (see top panel of Fig.6.20 (a)). Polarized mode emission, a consequence of the Purcell effect, has been observed previously in QD-cavity systems[113, 262]. The QWR emission that is resonant with the cavity modes acquires their polarization properties, explaining the difference in polarization between the coupled and uncoupled QWR emission. This adds further proof that the QWR light source feeds the first 5 delocalized modes of the 2D CCA: M_{01} , M_{02} , M_{03} , M_{04} and M_{05} . Their calculated near-field distributions are shown in Fig.5 (b)-(f). In Table 6.5, the energy spacing between the modes is reported and compared with the calculated mode spacing. The difference between the calculated and experimental mode separations is explained by the finite amount of structural disorder present in the fabricated CCA. The average difference between the calculated and experimental values amounts to 3.08 meV and is comparable to the difference obtained for the 3 coupled cavities with 3 rows separation (Fig.6.20 (c)). Indeed, the optical inter-cavity coupling and fabrication-induced disorder are nominally the same for these two designs, thus we expect similar contributions of the coupling strength and disorder to the total mode splitting. However, despite this fabrication-induced disorder, the QWR light source of the central cavity feeds the 5 CCA modes, indicating that cavity modes are delocalized. The coupling of QWRs to the M_{02} , M_{03} and M_{04} is also explained by an increase of the near-field intensity in the central cavity of the array caused by structural disorder. The experimental demonstration of coupling between a single site-controlled light source and the supermodes of a 2D CCA is an important step towards the realization of larger scale cavity arrays incorporating site-controlled emitters such as QDs in each cavity.

Table 6.5: Calculated and experimental mode splitting for the five-cavity 2D CCA.

Mode splitting	Δ_{12}	Δ_{23}	Δ_{34}	Δ_{45}
Calculated	4.83	0.25	0.02	4.40
Experimental	2.57	3.19	6.86	4.66

In summary, we reported the fabrication of 1D and 2D CCAs with an embedded site-controlled QWR light source. The QWR light source was placed only in one of the cavities of the CCA structure. This design allowed us to distinguish between structures for which optical coupling was sufficient to allow for mode delocalization from structures for which fabrication-induced disorder dominated over the optical coupling, using simple PL characterization. We studied photonic crystal CCAs with different cavity separation and showed that mode delocalization persists even when the disorder

6.2. Site-controlled quantum dots coupled to photonic crystal molecules

is comparable to the optical coupling strength. Mode delocalization was observed for 2D PhC cavity arrays. Such advanced emitter-cavity configurations could enable solid-state quantum simulators in the future[322]. Incorporating site-controlled QWR light sources in CCA structures is a first step towards the integration of site-controlled QDs in multiple cavity systems, which will provide the optical nonlinearities[323] required for quantum simulations.

6.2 Site-controlled quantum dots coupled to photonic crystal molecules

In this section, we present the optical study of two coupled L_3 PhC cavities incorporating site-controlled pyramidal QDs. This study was conducted jointly with B. Rigal and published in reference [86]. In the previous section we evidenced supermode delocalization in CCAs using QWR light sources. Using QWR light sources facilitated the spectral matching of the emitter emission with the CM transitions, due the QWR broad emission (~ 10 meV). However, the realization of quantum networks with coupled cavity arrays requires large intra-cavity nonlinearity only achievable with two-level system like emitters strongly coupled to the cavities[308]. In addition, transfer and storage of information between distant sites of a quantum network, which can be achieved by coupling distant cavities, also requires two-level system like emitters with well defined electronic and optical properties[291, 292]. This shows that, ultimately, QDs have to be integrated in coupled cavity arrays to provide the solid-state structures most suited for solid-state quantum information applications. Coupling QD emitters to arrays of cavities is a challenging task since it requires positioning the QDs inside the cavities of the array, while spectrally matching the QD narrow spectral features with the CM transitions. This has been achieved with randomly positioned self-assembled QDs, demonstrating the coupling of single QD to the optical modes of a photonic molecule consisting of two coupled L_3 PhC cavities[303]. However, it is evident that scaling this system to multiple QDs deterministically coupled to multiple cavities can only be achieved using site-controlled emitters.

We present here the coupling of two site-controlled pyramidal QDs, deterministically positioned in the center of two coupled L_3 PhC cavities, to the delocalized optical mode of the coupled cavity structure. These structures were fabricated on sample A (see table 2.1).

6.2.1 Structure design and photonic molecule properties

The coupled cavity structure consisting of two diagonally coupled L_3 PhC cavity with an inter-cavity separation of $0.8 \mu m$ is illustrated in Fig. 6.21 (a). A single pyramidal QD is located in the center of each cavity with an alignment accuracy better than $50 nm$. More details of the fabrication these QD-cavity structures can be found in chapter

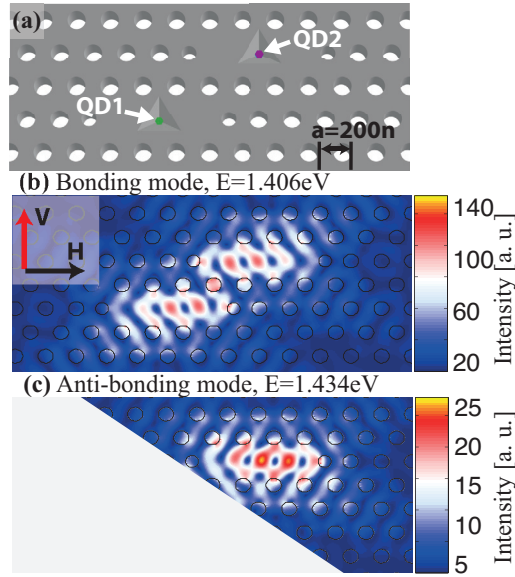


Figure 6.21: Two pyramidal QDs integrated in a photonic molecule. (a) Sketch of the structure. In the real structure, the pyramidal recesses are fully planarized. (b) Bonding (even mode) and (c) anti-bonding (odd mode) electric field intensity spatial distributions computed with 3D FDTD (refractive of the GaAs membrane is 3.52, slab thickness is 265 nm , PhC pitch is $a = 200 \text{ nm}$ and PhC hole radius is $r = 57 \text{ nm}$). Black and red arrows indicate, respectively, the horizontal and vertical polarization directions. Reprinted with permission from [86]. Copyright 2015, AIP Publishing LLC.

2. These structures were fabricated on sample A (see table 2.1 for fabrication and growth parameters). Fig. 6.22 (a) displays the spectra resolved in linear polarization of a structure with PhC hole radius $r = 61 \text{ nm}$. For this high excitation power conditions ($P=5 \text{ mW}$), the QDs s-state and excited states are visible in the spectrum. Furthermore, the broadband emission of the low energy tail of the three wedge QWRs (see subsection 5.1.3) reveals the CMs of the photonic molecule. Two CM modes, labelled M_{0b} and M_{0a} , were identified by means of temperature dependent measurements and from their pronounced linear polarization visible in the top panel of Fig. 6.22 (a) showing the DOLP of the emission spectrum. These CMs are the fundamental even and odd modes of the photonic molecule and originate from the interaction of the M_0 modes of the individual L_3 cavities. Their electric field intensity spatial distributions are shown in Fig. 6.21 (b) and (c). The transition energies of M_{0b} and M_{0a} were measured on 60 different structures and are displayed in Fig. 6.22 (b) as a function of the PhC hole radius. The measured transition energies are in good agreement with the energies calculated using 3D FDTD simulations for a disorder free PhC molecule. The mean energy separation between the even and odd modes is $\bar{\Delta} = 32.6 \text{ meV}$, corresponding to a strong inter-cavity coupling consistent with the small inter-cavity separation ($0.8 \mu\text{m}$). The standard deviation σ of the mean energy separation is $\sigma = 1.07 \text{ meV}$, which result in a standard deviation to mean value ratio of $\sigma/\bar{\Delta} = 0.033 \ll 1$. As explained in subsection 6.1.4, $\sigma/\bar{\Delta} \ll 1$ indicates a weak impact of the fabrication-induced

6.2. Site-controlled quantum dots coupled to photonic crystal molecules

disorder on the inter-cavity coupling and is characteristic of a system for which mode delocalization occurs. The coupled PhC L_3 cavities studied here are thus strongly coupled, with CMs delocalized over both cavities of the array. This is a necessary condition to couple either of these two CMs to both site-controlled QDs.

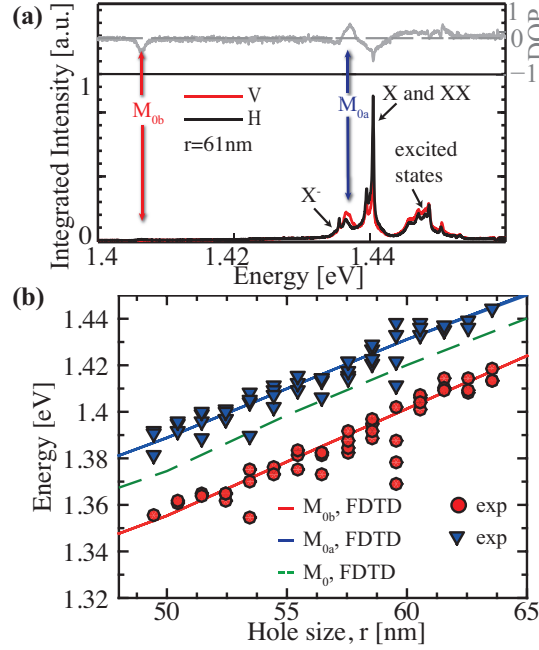


Figure 6.22: (a) Polarization spectrum resolved in linear polarization of a structure with $r = 61 \text{ nm}$ (see Fig. 6.21 for H and V definition) at high optical excitation level ($P = 5 \text{ mW}$, $T = 10 \text{ K}$), DOLP in grey is defined as $\text{DOP} = (I_V - I_H)/(I_V + I_H)$. (b) Energies of the even M_{0b} (red) and odd M_{0a} (blue) modes of a photonic molecule computed with 3D FDTD (slab width = 265 nm ; $a = 200 \text{ nm}$, and $n = 3.52$) as a function of r , compared to the mode energies measured on samples with different PhC hole radius values. The calculated energies of L_3 cavities (M_0) are also given (dashed line). Reprinted with permission from [86]. Copyright 2015, AIP Publishing LLC.

6.2.2 Optical signatures of coupling between two quantum dots and the supermode of a photonic molecule.

One QD-cavity structure with a PhC hole radius $r = 61 \text{ nm}$ was selected for further investigation. The two QDs are separated by a distance of $0.69 \mu\text{m}$ allowing a preferential excitation of each QD by properly positioning the excitation laser spot. The QDs s-state emission spectra are shown in Fig. 6.23 (a), with the laser spot position indicated in the figure's inset. The QDs spectrum consists of X , $2X$ and X^- excitonic transitions, which is characteristic of these pyramidal QDs (see chapter 4). This selective excitation method allows to clearly identify the excitonic transitions of each QD, which is clearly visible here for the QDs X^- transitions. The spectra presented in Fig.

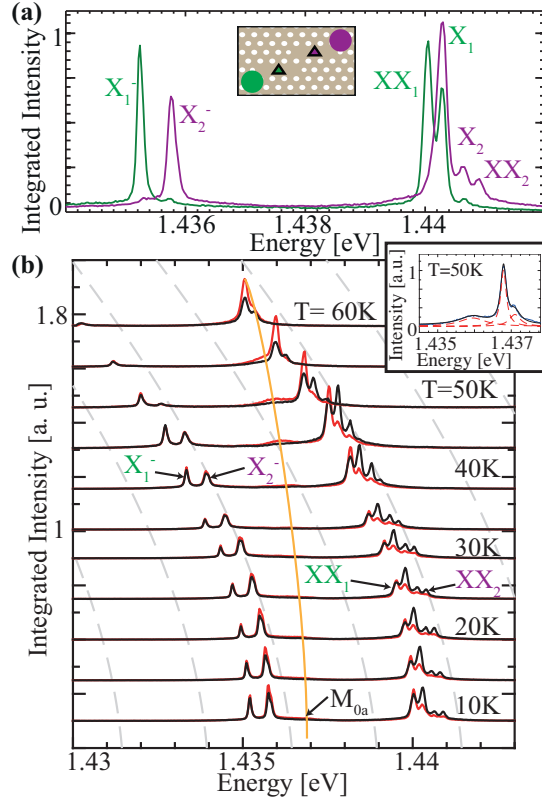


Figure 6.23: (a) Selective excitation of QD1 (green) and QD2 (violet); the green and violet disks in the inset indicate the excitation spot position ($P = 100 \mu\text{W}$; $T = 10\text{K}$). (b) H and V polarized spectra of the photonic molecule recorded at different temperatures ($P = 250 \mu\text{W}$); $r = 61\text{nm}$. Dashed lines show the calculated band gap variation of $\text{In}_{0.2}\text{Ga}_{0.8}\text{As}$ with temperature. Orange line serves as guide to the eye for following the M_{0a} mode energy ($Q = 1600$). A fit of the cavity and excitonic lines for $T = 50\text{K}$ and V polarization is shown in the inset. Reprinted with permission from [86]. Copyright 2015, AIP Publishing LLC.

6.23 (a) provide a good example of the uniformity of pyramidal QDs. As emphasized in chapter 2, pyramidal QDs have a small energy distribution which is characterized for this sample by a QD ensemble emission with a FWHM of $\sim 10\text{meV}$. This value is actually an upper bound for the energy distribution of single excitonic transitions since it includes the energy distribution and fluctuations of multiple s-state transitions. When studying structures with multiple QDs, having a small energy distribution and reproducible spectral features increases the probability to find structures with closely spaced excitonic transitions originating from different QDs. Here for example, the X^- features of the QDs (X_1^- and X_2^-) are separated in energy by $600\mu\text{eV}$, giving the opportunity to couple both transition to the same CM.

The structure's polarization resolved spectra is displayed in Fig. 6.23 (b) for different sample temperatures. For $T = 10\text{K}$ the odd mode M_{0a} is blue shifted by 1meV from the X^- transitions of the QDs. The CM quality factor is $Q = 1600$ resulting

6.2. Site-controlled quantum dots coupled to photonic crystal molecules

in a weak QD-cavity interaction. Nevertheless, the transitions X_1^- and X_2^- have a slightly more pronounced V-polarized emission than H-polarized emission, indicating a co-polarization behavior induced by the coupling with the delocalized CM. As the temperature is increased, the CM is moved further away in energy from the X^- transitions, and the co-polarization behavior is reduced. The CM then enters in resonance with the X and $2X$ transitions, which in turn acquire a linear vertical polarization.

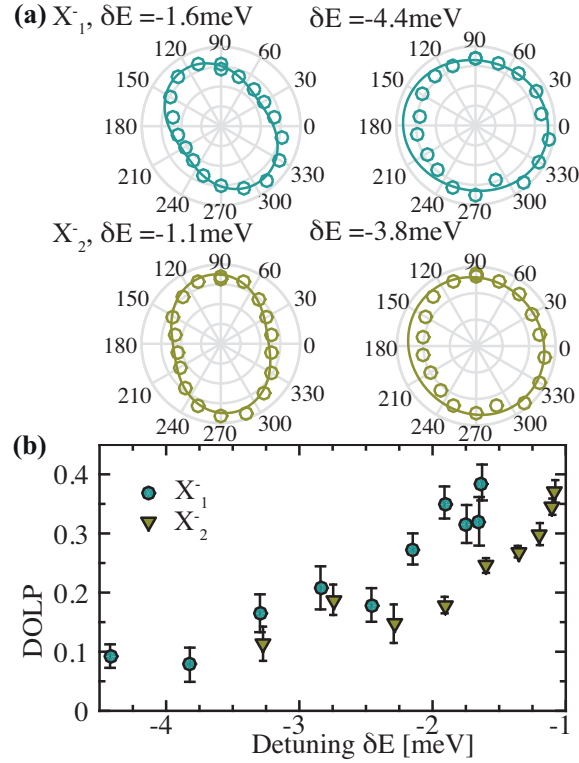


Figure 6.24: (a) Polar plots of the polarization for the two X^- lines at small ($T = 10 \text{ K}$) and large ($T = 55 \text{ K}$) cavity detuning. (b) Degree of linear polarization versus detuning for the two X^- lines, extracted from polar diagrams as in (a). $P = 200 \mu\text{W}$. Reprinted with permission from [86]. Copyright 2015, AIP Publishing LLC.

The polarization behavior of the X_1^- and X_2^- transitions with QD-cavity detuning is investigated in more details in Fig. 6.24. The polarization resolved spectra are acquired by placing a half-wave plate followed by a polarizer in the detection path (see subsection 2.1.2 for details). The intensity of the X^- emission as a function of the angle between the half-wave plate fast axis and polarizer axis is shown in polar plots in Fig. 6.24 (a). For large detunings δE , no significant linear polarization is visible in the X^- emission of both QDs, which translates in an isotropic out of plane emission expected for QDs presenting a high in-plane symmetry[199, 200]. For smaller detunings, the emission presents a more pronounced linear component corresponding to an elliptic shaped polar plot with a major axis oriented along the 90° direction (V

direction). This asymmetric out-of plane emission is induced by the coupling with the linearly polarized CM. The DOLP defined here as $\sqrt{S_1^2 + S_2^2}/S_0$, where S_i are the Stokes parameters, is shown as a function of detuning for the X_1^- and X_2^- transitions in Fig. 6.24 (b). When the detuning is reduced, the DOLP of both excitonic transitions increases. For detunings $|\delta E| < 2 \text{ meV}$, both QD lines exhibit a DOLP above 0.3 indicating that both QDs are simultaneously coupled to the same supermode of the PhC molecule.

6.3 Chapter summary

In this chapter, we studied arrays of coupled cavities, which are known to host optical modes delocalized over the entire structure. These extended optical modes have brought up a lot of interest in the past decades as they provide the means to transfer information between distant quantum objects and realize quantum simulators. Large arrays of coupled cavities remain however difficult to realize because they are sensible to fabrication-induced disorder, that can prevent mode delocalization. Although the progress in fabrication techniques recently enabled the realization of large scale arrays of PhC cavities[308], probing mode delocalization can prove challenging.

We presented here a method relying on site-controlled QWRs emitters that allows for a straightforward assessment of mode delocalization. The site-controlled emitters were integrated in a single cavity of the array and positioned to have a significant spatial overlap with several delocalized optical modes. We performed polarization resolved PL measurements to obtain the spectral signatures of the CCA excited by a deterministically positioned light source. Although a single cavity of the array was excited by the QWR emitter, we observed the optical signatures of multiple modes, providing a direct proof of mode delocalization. The measurements were repeated on a large number of structures, which allowed to perform a statistical study of the supermode energy separation, giving an estimation of the impact of fabrication-induced disorder on inter-cavity coupling. In particular, we observed that mode delocalization was still occurring when the influence of disorder on the supermode energy separation was comparable to the inter-cavity coupling strength. The finite disorder present in these structures allowed the coupling of a supermode with the QWRs, even though it had no significant overlap with the QWRs in the absence of disorder. Fabrication induced disorder can then be used as a means to even out the field distributions of supermodes, facilitating the coupling of emitters located inside the cavities to a maximum of modes of the CCA.

Finally, we demonstrated the coupling of two pyramidal QDs to the same delocalized optical mode of a photonic molecule. This was achieved by deterministically positioning a single site-controlled QD in the center of each cavity of the coupled cavity structure. This represents a first step in the realization of arrays of cavities incorporat-

ing two-level system like emitters, which have been proposed to construct quantum networks[291] or quantum simulators[322].

The next step of this study would be to increase the number of cavities, and consequently QDs, forming the array. Although site-controlled QDs enable the realisation of such complex structures, several problems arise when scaling up the system. Firstly, fabrication-induced disorder has to be minimized to obtain efficient mode delocalization in large scale cavity arrays. Secondly, as the number of QDs increases, ensuring a nearly identical emission energy for all the QDs is extremely challenging. This requires either to achieve a high level of uniformity during the QD growth, or to individually control the energy of each QD, for example by applying a local electric field[259, 324]. Thirdly, in a CCA, the amplitude of the electric field of a supermode varies from cavity to cavity. To achieve the same magnitude of coupling between each QD and a given supermode, the field envelop function has to be tailored. This can be achieved by modifying either the inter-cavity coupling strength or the cavity effective refractive index across the array and represents an interesting research direction.

7 Conclusions and outlook

During the course of this thesis, we studied systems of site-controlled quantum dots (QDs) integrated in photonic crystal (PhC) cavities. We relied on InGaAs/GaAs pyramidal QDs, grown in inverted pyramids defined by a combination of e-beam lithography and wet chemical etching on GaAs substrates. This deterministic fabrication method yields reproducible, symmetric QDs that can be positioned on the substrate with an accuracy higher than 50 nm . This allows a precise positioning of the QD inside the cavity, maximizing the overlap between the QD and the cavity mode (CM) electric field distribution. This method reduces the number of uncertainties in the QD-cavity coupling parameters, and enables a quantitative analysis of the coupled system photoluminescence. In addition, pyramidal QDs exhibit an inhomogeneous broadening well below 20 meV . Combined with the control of their position, this property enables the fabrication of larger scale photonic structures comprising multiple QDs and cavities. In particular, we investigated the coupling of two QDs to the CM of one PhC cavity and two coupled PhC cavities. The optical modes of larger arrays of coupled cavities were probed using site-controlled quantum wire (QWR) light sources.

In the first part of the study, we investigated the optical properties of single pyramidal QDs. The reproducibility of the QDs spectra, systematically showing three s-state features, was highlighted in this study. We reported the full correlation picture of the s-state transitions by performing photon correlation measurements. The transitions auto- and cross-correlation measurements were reproduced by a rate equation model, providing a clear identification of the QD excitonic species and evidencing single photon emission. In addition to single photon emission, most quantum computation schemes relying on quantum emitters also require photon indistinguishability[96, 325]. It could be useful to perform two-photon interference measurements with pyramidal QDs using a Hong-Ou-Mandel[326] optical setup to quantify the degree of indistinguishability of their emission. Obtaining a high degree of indistinguishability could be achieved by reducing the transition dephasing which is detrimental to the two-photon interference[327], or by coupling the transition to a CM, making use of the Purcell

effect to overcome the exciton fine-structure splitting[16].

By performing a statistical analysis of the QD exciton binding energies, we observed a transition from negative to positive biexciton (2X) binding energies with increasing neutral exciton (X) emission energy. This indicates the presence of internal piezoelectric fields induced by strain. Approximately 10% of the QDs investigated had vanishing 2X binding energies. We also presented time-resolved photoluminescence (PL) measurements of pyramidal QDs isolated using mesa etching. Differences up to a factor of two were observed between the decay times of two nominally identical QDs. Furthermore, the decay times of these QDs were found to be similar to decay times of QDs embedded in a PhC crystal. This indicates an important contribution of non-radiative recombinations, as confirmed by temperature dependent time-resolved measurements performed for a QD-coupled to a CM. To get access to the intrinsic QD radiative lifetime, additional measurements are required, preferably on a large number of isolated QDs to get a quantitative analysis of the impact of non-radiative decay channels on the QD decay rate and its dependence on the sample temperature.

In the second part of this work, we analysed polarization resolved PL measurements of a single pyramidal QD coupled to the fundamental mode of an L_3 PhC cavity. Although the QD was weakly coupled to the CM, rich polarization features were observed in the temperature dependent spectra. One of the important results of this thesis was the simulation of QD and CM spectral features on a large detuning range using a theoretical model that takes into account the influence of solid-state decoherence mechanisms on the QD-cavity coupling dynamic. This was made possible by the electronic properties of pyramidal QDs that resemble those of an ideal two-level system-like emitter. The absence of extended wetting layer states in the QD vicinity results in a background free QD emission even for high intensity incoherent pumping as was evidenced by excitation power dependent time-resolved PL measurements. By comparing the CM off-resonant emission with simulations, we identified the impact of pure dephasing and phonon scattering on the cavity feeding mechanism. In particular, we showed that pure dephasing efficiently contributes to the CM off-resonant emission for small detunings ($< 1 \text{ meV}$) and phonon scattering is the main cavity feeding mechanism for detunings ranging from 1 meV up to 3 meV . Identifying the source of the off-resonant CM emission and the detuning range of action of the corresponding decoherence mechanism is an important step towards the full comprehension of semiconductor QD-cavity interaction. The co-polarization of the QD feature for small detunings was found to result from the emission of cavity photons at the energy of the QD transition, resulting in an additional Lorentzian feature in the CM spectrum centered on the QD transition. This additional peak has the polarization properties of the CM and can lead to a strong co-polarization of the QD feature at resonance, together with a Purcell enhancement of its emission intensity. Additional measurements on QD-cavity structures with different dephasing rates and cavity quality factor could be useful to investigate different weak coupling regimes: for example the "good cavity" regime[224].

By comparing the experimental results to simulations, we extracted QD-cavity coupling strengths values of $\hbar g_0 = 20 \mu eV$ and $\hbar g_0 = 50 \mu eV$. To give a precise explanation for these small coupling strengths values, a study of the dipole moments of excitons in pyramidal QDs should be undertaken. The dipole moment orientation can be obtained from polarization resolved cross-sectional PL measurements. An important out-of-plane dipole moment component could explain the coupling strengths values reported here, as well as the Purcell factor of 17 obtained from time-resolved PL measurements which is far below its maximum value. Increasing the QD-cavity coupling strength, for example by modifying the aspect ratio of the QD to align the exciton dipole moment with the CM electric field, could also help to reach the strong-coupling regime. In addition, reducing the QD linewidth, increasing the cavity Q factor by optimizing the PhC fabrication process or increasing the wavelength of the CM to minimize absorption losses[173], and working with thinner membranes and thus smaller optical mode volumes, could also facilitate the observation of strong QD-cavity coupling in our system. Encouraging QD linewidths as low as $40 \mu eV$ have been obtained in recent sample using triethylgallium (TEGa) precursors during the QD growth process.

In the third part of this work we investigated systems of multiple QDs and cavities. We studied a structure comprising of two QDs simultaneously coupled to the same CM of an L_3 cavity. However, by comparing the structure's PL spectrum to simulations, we showed that no signs of collective effects were visible. Possible explanations for this absence of collective emission are the presence of important dephasing effects responsible for the large linewidths of the QDs ($> 100 \mu eV$) and the finite QD-cavity detunings that are enforced by the energy difference of $2 meV$ between the QDs transitions. Reducing QD pure dephasing and increasing the size homogeneity of the QDs could help achieving an ideal situation in which the transitions of both QDs are resonant with the CM, increasing the chances of observing collective effects. The optical modes of larger cavity arrays were probed by placing site-controlled quantum wire (QWR) light sources inside chosen cavities of the array. This enabled the first observation of mode delocalization in large coupled cavity arrays excited by site-controlled quantum emitters. The first observation of coupling between the supermode of a photonic molecule and two site-controlled QDs located in each cavity of the array was also demonstrated. This represents an important step towards the realization of quantum network devices[292], enabling the transfer of information, mediated by light, between distant emitters. These structures are also candidates to realize quantum simulators[322], although each QD should be strongly coupled to its host cavity which still represents an important challenge. Another interesting direction that is currently being explored is the deterministic integration of QDs into waveguides as illustrated in Fig. 7.1. Coupling multiple emitters to the same optical mode is easier in those structures due to the broader energy distribution of photonic waveguide modes. By embedding QDs of different sizes in those structures, wavelength multiplexing and signal propagation could be explored.

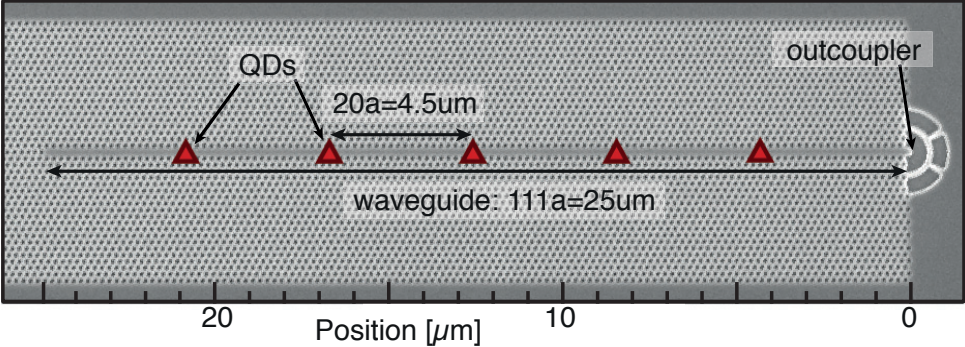


Figure 7.1: Scanning electron microscope image of a waveguide and an out-coupler incorporating site-controlled QDs. The position of the QDs is indicated by red triangles. Courtesy of B. Rigal.

A Appendix

A.1 Effective phonon density of states calculation

This is a complement to the derivation of the effective phonon density of states presented in chapter 3. The effective phonon density of states is given by [166, 220]

$$D(\Omega) = \pi \sum_{\mathbf{k}} |M_{\mathbf{k}}|^2 [n(\omega_{\mathbf{k}})\delta(\Omega + \omega_{\mathbf{k}}) + (n(\omega_{\mathbf{k}}) + 1)\delta(\Omega - \omega_{\mathbf{k}})] \quad (\text{A.1})$$

where $n(\omega_{\mathbf{k}}) = [\exp(\hbar\omega_{\mathbf{k}}/k_B T) - 1]^{-1}$ is the Bose-Einstein distribution and $\delta(\omega)$ the Dirac function. $M_{\mathbf{k}}$ is the electron-phonon interaction matrix element given by

$$M_{\mathbf{k}} = \sqrt{\frac{\hbar k}{2\rho c_s V}} D \int d^3\mathbf{r} |\phi(\mathbf{r})|^2 e^{-i\mathbf{k}\cdot\mathbf{r}} \quad (\text{A.2})$$

where ρ is the mass density, c_s is the speed of sound in the material and V is the phonon quantization volume. We assume here the same Gaussian wave function $\phi(\mathbf{r})$ for the ground and excited states, i.e., for a confined electron in the valance and conduction bands. $D = D_e - D_g$ is the difference of the two-level system excited and ground state deformation potentials.

We consider an isotropic confinement length l in the x-y plane and a confinement length l_z in the z-direction. The electronic wave function becomes

$$\phi(\mathbf{r}) = \frac{1}{\sqrt{\pi^{\frac{3}{2}} l^2 l_z}} e^{-(x^2+y^2)/2l^2} e^{-z^2/2l_z^2}. \quad (\text{A.3})$$

Appendix A. Appendix

The electron-phonon interaction matrix element then becomes

$$M_{\mathbf{k}} = \sqrt{\frac{\hbar D^2}{2\rho c_s V}} \frac{1}{\pi^{\frac{3}{2}} l^2 l_z} (\sqrt{\pi} l)^2 \sqrt{\pi} l_z \sqrt{k} e^{-(k_x^2 + k_y^2) l^2 / 4} e^{-k_z^2 l_z^2 / 4} \quad (\text{A.4})$$

$$= \sqrt{\frac{\hbar D^2}{2\rho c_s V}} \sqrt{k} e^{-(k_x^2 + k_y^2) l^2 / 4} e^{-k_z^2 l_z^2 / 4}. \quad (\text{A.5})$$

To compute the effective phonon density, the sum over \mathbf{k} is transformed into an integral. Cylindrical coordinates are used to account for the isotropic confinement in the x-y plane.

$$\sum_{\mathbf{k}} \rightarrow \frac{V}{(2\pi)^3} \int d^3 \mathbf{k} = \frac{V}{(2\pi)^3} \int_0^\infty \int_{-\infty}^\infty \int_0^{2\pi} u du dk_z d\theta = \frac{V}{(2\pi)^2} \int_0^\infty \int_{-\infty}^\infty u du dk_z \quad (\text{A.6})$$

with $u = \sqrt{k_x^2 + k_y^2}$. The effective phonon density can be written as follows

$$D(\Omega) = \frac{\hbar D^2}{2\rho c_s V} \frac{\pi V}{(2\pi)^2} \int_{-\infty}^\infty \int_0^\infty du dk_z u \sqrt{u^2 + k_z^2} e^{-u^2 l^2 / 2} e^{-k_z^2 l_z^2 / 2} \dots \quad (\text{A.7})$$

$$\dots [n(c_s k) \delta(\Omega + c_s k) + (n(c_s k) + 1) \delta(\Omega - c_s k)]$$

where we used $\omega_k = c_s k$. Lets rewrite the deltas as a function of the new integration variable u . We know that $\delta(f(u)) = \sum_i \frac{\delta(u - u_0)}{|f'(u_0)|}$. Here $f(u) = \Omega \pm c_s \sqrt{u^2 + k_z^2}$ and the zeros of the function are given by

$$\frac{\Omega}{c_s} = \mp \sqrt{u_0^2 + k_z^2} \Rightarrow u_0 = \pm \sqrt{\frac{\Omega^2}{c_s^2} - k_z^2} \quad (\text{A.8})$$

which gives

$$\delta\left(\frac{\Omega}{c_s} \pm k\right) = \sum_{\pm} \left| \frac{\sqrt{u_i^2 + k_z^2}}{u_i} \right| \delta(u - u_i). \quad (\text{A.9})$$

Since u is always positive, only the second term of the sum will contribute. Finally we get

$$\delta\left(\frac{\Omega}{c_s} \pm k\right) = \frac{|\frac{\Omega}{c_s}|}{\sqrt{\Omega^2 - c_s^2 k_z^2}} \delta\left(u - \sqrt{\frac{\Omega^2}{c_s^2} - k_z^2}\right) \quad (\text{A.10})$$

Since $u \in \Re$, we get the following condition on k_z : $\frac{\Omega^2}{c_s^2} > k_z^2 \Rightarrow -|\frac{\Omega}{c_s}| < k_z < |\frac{\Omega}{c_s}|$.

We can see in equation (A.7) that the term in $n(k) \delta(\frac{\Omega}{c_s} + k)$ will only contribute for

A.1. Effective phonon density of states calculation

$\Omega < 0$ and the term in $(n(k) + 1)\delta(\frac{\Omega}{c_s} - k)$ for $\Omega > 0$ (k is always positive). We will thus separate the computation for $\Omega > 0$ and $\Omega < 0$.

$\Omega < 0$

$$D(\Omega < 0) \propto \int_{-\infty}^{\infty} \int_0^{\infty} duk_z u \sqrt{u^2 + k_z^2} e^{-u^2 l^2 / 2} e^{-k_z^2 l_z^2 / 2} n(c_s k) \delta\left(\frac{\Omega}{c_s} + k\right) \quad (\text{A.11})$$

$$\begin{aligned} &\propto \int_{-\infty}^{\infty} \int_0^{\infty} duk_z u \sqrt{u^2 + k_z^2} e^{-(u^2)l^2/2} e^{-k_z^2 l_z^2 / 2} n(c_s \sqrt{u^2 + k_z^2}) \dots \\ &\dots \frac{|\frac{\Omega}{c_s}|}{c_s \sqrt{\frac{\Omega^2}{c_s^2} - k_z^2}} \delta\left(u - \sqrt{\frac{\Omega^2}{c_s^2} - k_z^2}\right) \end{aligned} \quad (\text{A.12})$$

$$\propto \left|\frac{\Omega}{c_s}\right|^2 n(|\Omega|) \int_{-\frac{|\Omega|}{c_s}}^{\frac{|\Omega|}{c_s}} dk_z e^{-\left(\frac{\Omega^2}{c_s^2} - k_z^2\right)l^2/2} e^{-k_z^2 l_z^2 / 2} \quad (\text{A.13})$$

$$\propto \sqrt{\pi} \left|\frac{\Omega}{c_s}\right|^2 n(|\Omega|) e^{-\Omega^2 l^2 / 2 c_s^2} \frac{\text{erf}\left[\frac{|\Omega|}{c_s} \sqrt{\frac{l_z^2 - l^2}{2}}\right]}{\sqrt{\frac{l_z^2 - l^2}{2}}} \quad (\text{A.14})$$

$$\propto \sqrt{\pi} \left|\frac{\Omega}{c_s}\right|^2 n(-\Omega) e^{-\Omega^2 l^2 / 2 c_s^2} \frac{\text{erf}\left[-\frac{\Omega}{c_s} \sqrt{\frac{l_z^2 - l^2}{2}}\right]}{\sqrt{\frac{l_z^2 - l^2}{2}}} \quad (\text{A.15})$$

$$\propto \sqrt{\pi} \frac{\Omega^2}{c_s^3} [-n(-\Omega)] e^{-\Omega^2 l^2 / 2 c_s^2} \frac{\text{erf}\left[\frac{\Omega}{c_s} \sqrt{\frac{l_z^2 - l^2}{2}}\right]}{\sqrt{\frac{l_z^2 - l^2}{2}}}. \quad (\text{A.16})$$

$\Omega > 0$

$$D(\Omega > 0) \propto \int_{-\infty}^{\infty} \int_0^{\infty} duk_z u \sqrt{u^2 + k_z^2} e^{-u^2 l^2 / 2} e^{-k_z^2 l_z^2 / 2} [n(c_s k) + 1] \delta\left(\frac{\Omega}{c_s} - k\right) \quad (\text{A.17})$$

$$\begin{aligned} &\propto \int_{-\infty}^{\infty} \int_0^{\infty} duk_z u \sqrt{u^2 + k_z^2} e^{-(u^2)l^2/2} e^{-k_z^2 l_z^2 / 2} [n(c_s \sqrt{u^2 + k_z^2}) + 1] \dots \\ &\dots \frac{|\frac{\Omega}{c_s}|}{c_s \sqrt{\frac{\Omega^2}{c_s^2} - k_z^2}} \delta\left(u - \sqrt{\frac{\Omega^2}{c_s^2} - k_z^2}\right) \end{aligned} \quad (\text{A.18})$$

Appendix A. Appendix

$$\propto \left| \frac{\Omega}{c_s^2} \right|^2 [n(|\Omega|) + 1] \int_{-|\frac{\Omega}{c_s}|}^{|\frac{\Omega}{c_s}|} dk_z e^{-(\frac{\Omega^2}{c_s^2} - k_z^2)l^2/2} e^{-k_z^2 l^2/2} \quad (\text{A.19})$$

$$\propto \sqrt{\pi} \frac{\Omega^2}{c_s^3} [n(\Omega) + 1] e^{-\Omega^2 l^2/2c_s^2} \frac{\text{erf}\left[\frac{\Omega}{c_s} \sqrt{\frac{l_z^2 - l^2}{2}}\right]}{\sqrt{\frac{l_z^2 - l^2}{2}}}. \quad (\text{A.20})$$

We now look for a unique expression describing the behavior of $D(\Omega)$. We start by showing that $\frac{1}{2}[n(\Omega) - n(-\Omega) + 1] = -n(-\Omega)$:

$$\begin{aligned} \frac{1}{2}[n(\Omega) - n(-\Omega) + 1] &= \frac{1}{2} \left(\frac{1}{e^{\Omega/T} - 1} + \frac{e^{\Omega/T}}{e^{\Omega/T} - 1} + \frac{e^{\Omega/T} - 1}{e^{\Omega/T} - 1} \right) \\ &= \frac{e^{\Omega/T}}{e^{\Omega/T} - 1} = e^{\Omega/T} n(\Omega) \end{aligned} \quad (\text{A.21})$$

$$n(-\Omega) = \frac{1}{e^{-\Omega/T} - 1} = -\frac{e^{\Omega/T}}{e^{\Omega/T} - 1} = -e^{\Omega/T} n(\Omega) \quad (\text{A.22})$$

By combining (A.21) and (A.22) we get

$$\frac{1}{2}[n(\Omega) - n(-\Omega) + 1] = -n(-\Omega). \quad (\text{A.23})$$

We can also show

$$n(\Omega) + 1 = n(\Omega) + 1 + n(-\Omega) - n(-\Omega) \quad (\text{A.24})$$

$$= n(\Omega) - n(-\Omega) + 1 - \frac{1}{2}\{n(\Omega) - n(-\Omega) + 1\} \quad (\text{A.25})$$

$$= \frac{1}{2}[n(\Omega) - n(-\Omega) + 1]. \quad (\text{A.26})$$

We now rewrite $D(\Omega > 0)$ and $D(\Omega < 0)$ using (A.23) and (A.26)

$$D(\Omega < 0) = \frac{\hbar D^2}{2\rho c_s V} \frac{\pi V}{(2\pi)^2} \sqrt{\pi} \frac{\Omega^2}{c_s^3} [-n(-\Omega)] e^{-\Omega^2 l^2 / 2c_s^2} \frac{\text{erf}\left[\frac{\Omega}{c_s} \sqrt{\frac{l_z^2 - l^2}{2}}\right]}{\sqrt{\frac{l_z^2 - l^2}{2}}} \quad (\text{A.27})$$

$$= \frac{\hbar D^2}{16\rho c_s^4 \sqrt{\pi}} \Omega^2 [n(\Omega) - n(-\Omega) + 1] e^{-\Omega^2 l^2 / 2c_s^2} \frac{\text{erf}\left[\frac{\Omega}{c_s} \sqrt{\frac{l_z^2 - l^2}{2}}\right]}{\sqrt{\frac{l_z^2 - l^2}{2}}} \quad (\text{A.28})$$

$$D(\Omega > 0) = \frac{\hbar D^2}{2\rho c_s V} \frac{\pi V}{(2\pi)^2} \sqrt{\pi} \frac{\Omega^2}{c_s^3} [n(\Omega) + 1] e^{-\Omega^2 l^2 / 2c_s^2} \frac{\text{erf}\left[\frac{\Omega}{c_s} \sqrt{l_z^2 - l^2}\right]}{\sqrt{l_z^2 - l^2}} \quad (\text{A.29})$$

$$= \frac{\hbar D^2}{16\rho c_s^4 \sqrt{\pi}} \Omega^2 [n(\Omega) - n(-\Omega) + 1] e^{-\Omega^2 l^2 / 2c_s^2} \frac{\text{erf}\left[\frac{\Omega}{c_s} \sqrt{\frac{l_z^2 - l^2}{2}}\right]}{\sqrt{\frac{l_z^2 - l^2}{2}}}. \quad (\text{A.30})$$

This provides a single expression for $D(\Omega)$

$$D(\Omega) = \frac{\hbar D^2}{16\rho c_s^4 \sqrt{\pi}} \Omega^2 [n(\Omega) - n(-\Omega) + 1] e^{-\Omega^2 l^2 / 2c_s^2} \frac{\text{erf}\left[\frac{\Omega}{c_s} \sqrt{\frac{l_z^2 - l^2}{2}}\right]}{\sqrt{\frac{l_z^2 - l^2}{2}}}. \quad (\text{A.31})$$

A.2 Contributions

The author, Clément Jarlov, did all the optical measurements and data analysis presented in this work, except for the studies presented in sections 5.2 and 6.2 that were conducted jointly with M. Calic and B. Rigal, respectively. The author did all the finite-difference time-domain modeling presented in this study using a Matlab code written by Dr. K. F. Karlsson. The physical model presented in section 3.4 was developed jointly with E. Wodey, based on well established results published in the literature, and implemented in Python by the author, relying on the quantum toolbox QuTip. The samples investigated in this work were fabricated by M. Calic, A. Lyasota and K. Atlasov, along with P. Gallo, L. Ferrier, I. Kulkova, B. Dwir and A. Rudra. The author participated in the elaboration of the sample's design and performed optical measurements during the quantum dot growth optimization process. The work presented in this thesis was conducted under the supervision of the thesis director, Professor E. Kapon.

Bibliography

1. Shen, Y. *et al.* Nanophotonics: Interactions, Materials, and Applications. *J. Phys. Chem. B* **104**, 7577–7587 (2000).
2. Gaponenko, S. V. *Introduction to Nanophotonics* (Cambridge University Press, 2010).
3. Liu, Y. & Zhang, X. Metamaterials: a new frontier of science and technology. *Chem. Soc. Rev.* **40**, 2494–2507 (2011).
4. Smith, D. R., Pendry, J. B. & Wiltshire, M. C. K. Metamaterials and Negative Refractive Index. *Science* **305**, 788–792 (2004).
5. Miyazaki, H. T. & Kurokawa, Y. Squeezing Visible Light Waves into a 3-nm-Thick and 55-nm-Long Plasmon Cavity. *Phys. Rev. Lett.* **96**, 097401 (2006).
6. Oulton, R. F. *et al.* Plasmon lasers at deep subwavelength scale. *Nature* **461**, 629–632 (2009).
7. Mühlischlegel, P., Eisler, H.-J., Martin, O. J. F., Hecht, B. & Pohl, D. W. Resonant Optical Antennas. *Science* **308**, 1607–1609 (2005).
8. Joannopoulos, J. D., Villeneuve, P. R. & Fan, S. Photonic crystals: putting a new twist on light. *Nature* **386**, 143–149 (1997).
9. Vlasov, Y. A., O’Boyle, M., Hamann, H. F. & McNab, S. J. Active control of slow light on a chip with photonic crystal waveguides. *Nature* **438**, 65–69 (2005).
10. Wang, Y.-C. *et al.* High efficiency silicon nanodisk laser based on colloidal Cd-Se/ZnS QDs. *Nano Reviews* **2** (2011).
11. Zhang, Y. & Lončar, M. Submicrometer diameter micropillar cavities with high quality factor and ultrasmall mode volume. *Optics Letters* **34**, 902 (2009).
12. Akahane, Y., Asano, T., Song, B.-S. & Noda, S. High-Q photonic nanocavity in a two-dimensional photonic crystal. *Nature* **425**, 944–947 (2003).
13. Kwon, S.-H., No, Y.-S. & Park, H.-G. Design of plasmonic cavities. *Nano Convergence* **1**, 8 (2014).
14. Faist, J. *et al.* Quantum Cascade Laser. *Science* **264**, 553–556 (1994).

Bibliography

15. Atlasov, K. A. *et al.* Photonic-crystal microcavity laser with site-controlled quantum-wire active medium. *Opt. Express* **17**, 18178–18183 (2009).
16. Gazzano, O. *et al.* Bright solid-state sources of indistinguishable single photons. *Nat Commun* **4**, 1425 (2013).
17. Purcell, E. M. Spontaneous Emission Probabilities at Radio Frequencies. *Phys. Rev.* **69**, 674–674 (1946).
18. Stehle, P. Atomic Radiation in a Cavity. *Phys. Rev. A* **2**, 102–106 (1970).
19. Barton, G. Quantum Electrodynamics of Spinless Particles between Conducting Plates. *Proceedings of the Royal Society of London. Series A, Mathematical and Physical Sciences* **320**, 251–275 (1970).
20. Miller, R *et al.* Trapped atoms in cavity QED: coupling quantized light and matter. *Journal of Physics B: Atomic, Molecular and Optical Physics* **38**, S551–S565 (2005).
21. Goy, P., Raimond, J. M., Gross, M. & Haroche, S. Observation of Cavity-Enhanced Single-Atom Spontaneous Emission. *Phys. Rev. Lett.* **50**, 1903–1906 (1983).
22. Hulet, R. G., Hilfer, E. S. & Kleppner, D. Inhibited Spontaneous Emission by a Rydberg Atom. *Phys. Rev. Lett.* **55**, 2137–2140 (1985).
23. Thompson, R. J., Rempe, G. & Kimble, H. J. Observation of normal-mode splitting for an atom in an optical cavity. *Phys. Rev. Lett.* **68**, 1132–1135 (1992).
24. Brune, M. *et al.* Quantum Rabi Oscillation: A Direct Test of Field Quantization in a Cavity. *Phys. Rev. Lett.* **76**, 1800–1803 (1996).
25. McKeever, J., Boca, A., Boozer, A. D., Buck, J. R. & Kimble, H. J. Experimental realization of a one-atom laser in the regime of strong coupling. *Nature* **425**, 268–271 (2003).
26. McKeever, J. *et al.* Deterministic Generation of Single Photons from One Atom Trapped in a Cavity. *Science* **303**, 1992–1994 (2004).
27. Ritsch, H., Domokos, P., Brennecke, F. & Esslinger, T. Cold atoms in cavity-generated dynamical optical potentials. *Rev. Mod. Phys.* **85**, 553–601 (2013).
28. Schoelkopf, R. J. & Girvin, S. M. Wiring up quantum systems. *Nature* **451**, 664–669 (2008).
29. Wallraff, A. *et al.* Strong coupling of a single photon to a superconducting qubit using circuit quantum electrodynamics. *Nature* **431**, 162–167 (2004).
30. Johansson, J. *et al.* Vacuum Rabi Oscillations in a Macroscopic Superconducting Qubit LC Oscillator System. *Phys. Rev. Lett.* **96**, 127006 (2006).
31. Houck, A. A. *et al.* Generating single microwave photons in a circuit. *Nature* **449**, 328–331 (2007).
32. Tame, M. S. *et al.* Quantum plasmonics. *Nat Phys* **9**, 329–340 (2013).

33. Kühn, S., Håkanson, U., Rogobete, L. & Sandoghdar, V. Enhancement of Single-Molecule Fluorescence Using a Gold Nanoparticle as an Optical Nanoantenna. *Phys. Rev. Lett.* **97**, 017402 (2006).
34. Ropp, C. *et al.* Nanoscale imaging and spontaneous emission control with a single nano-positioned quantum dot. *Nat Commun* **4**, 1447 (2013).
35. Huck, A., Kumar, S., Shakoor, A. & Andersen, U. L. Controlled Coupling of a Single Nitrogen-Vacancy Center to a Silver Nanowire. *Phys. Rev. Lett.* **106**, 096801 (2011).
36. Trügler, A. & Hohenester, U. Strong coupling between a metallic nanoparticle and a single molecule. *Phys. Rev. B* **77**, 115403 (2008).
37. Hümmer, T., García-Vidal, F. J., Martín-Moreno, L. & Zueco, D. Weak and strong coupling regimes in plasmonic QED. *Phys. Rev. B* **87**, 115419 (2013).
38. Vahala, K. J. Optical microcavities. *Nature* **424**, 839–846 (2003).
39. Reithmaier, J. P. *et al.* Strong coupling in a single quantum dot–semiconductor microcavity system. *Nature* **432**, 197–200 (2004).
40. Armani, D. K., Kippenberg, T. J., Spillane, S. M. & Vahala, K. J. Ultra-high-Q toroid microcavity on a chip. *Nature* **421**, 925–928 (2003).
41. Vora, P. M. *et al.* Spin-cavity interactions between a quantum dot molecule and a photonic crystal cavity. *Nat Commun* **6**, 7665 (2015).
42. Reitzenstein, S. *et al.* AlAs/GaAs micropillar cavities with quality factors exceeding 150.000. *Applied Physics Letters* **90**, 251109 (2007).
43. Gorodetsky, M. L., Savchenkov, A. A. & Ilchenko, V. S. Ultimate Q of optical microsphere resonators. *Optics Letters* **21**, 453 (1996).
44. Khitrova, G., Gibbs, H. M., Kira, M., Koch, S. W. & Scherer, A. Vacuum Rabi splitting in semiconductors. *Nat Phys* **2**, 81–90 (2006).
45. Imamoğlu, A. Cavity-QED Using Quantum Dots. *Opt. Photon. News* **13**, 22–25 (2002).
46. Lai, Y. *et al.* Genetically designed L3 photonic crystal nanocavities with measured quality factor exceeding one million. *Applied Physics Letters* **104**, 241101 (2014).
47. Gérard, J. M. *et al.* Enhanced Spontaneous Emission by Quantum Boxes in a Monolithic Optical Microcavity. *Phys. Rev. Lett.* **81**, 1110–1113 (1998).
48. Graham, L. A., Huffaker, D. L., Deng, Q. & Deppe, D. G. Controlled spontaneous lifetime in microcavity confined InGaAlAs/GaAs quantum dots. *Applied Physics Letters* **72**, 1670–1672 (1998).
49. Kiraz, A. *et al.* Cavity-quantum electrodynamics using a single InAs quantum dot in a microdisk structure. *Applied Physics Letters* **78**, 3932–3934 (2001).

Bibliography

50. Happ, T. D. *et al.* Enhanced light emission of $\text{In}_x\text{Ga}_{1-x}\text{As}$ quantum dots in a two-dimensional photonic-crystal defect microcavity. *Phys. Rev. B* **66**, 041303 (2002).
51. Peter, E. *et al.* Exciton-Photon Strong-Coupling Regime for a Single Quantum Dot Embedded in a Microcavity. *Phys. Rev. Lett.* **95**, 067401 (2005).
52. Yoshie, T. *et al.* Vacuum Rabi splitting with a single quantum dot in a photonic crystal nanocavity. *Nature* **432**, 200–203 (2004).
53. The many aspects of quantum dots. *Nat Nano* **5**, 381–381 (2010).
54. Rossetti, R., Nakahara, S. & Brus, L. E. Quantum size effects in the redox potentials, resonance Raman spectra, and electronic spectra of CdS crystallites in aqueous solution. *The Journal of Chemical Physics* **79**, 1086–1088 (1983).
55. Stokes, E. B., Stiff-Roberts, A. D. & Dameron, C. T. Quantum dots in semiconductor optoelectronic devices. *Electrochemical Society Interface* **15** (2006).
56. Wood, V. & Bulović, V. Colloidal quantum dot light-emitting devices. *Nano Rev* **1** (2010).
57. Shirasaki, Y., Supran, G. J., Bawendi, M. G. & Bulović, V. Emergence of colloidal quantum-dot light-emitting technologies. *Nat Photon* **7**, 13–23 (2013).
58. Sanderson, K. Quantum dots go large. *Nature News* **459**, 760–761 (2009).
59. Lodahl, P. *et al.* Controlling the dynamics of spontaneous emission from quantum dots by photonic crystals. *Nature* **430**, 654–657 (2004).
60. Ünlü, H., Karim, M. R., Gürel, H. H. & Akıncı, O. in *Low Dimensional Semiconductor Structures* (eds Ünlü, H. & Horing, N. J. M.) DOI: 10.1007/978-3-642-28424-3_1 1–17 (Springer Berlin Heidelberg, 2013).
61. Neamen, D. A. *Semiconductor physics and devices: basic principles* (McGraw-Hill, 2003).
62. Davies, J. H. *The Physics of Low-dimensional Semiconductors: An Introduction* (Cambridge University Press, 1998).
63. Luttinger, J. M. & Kohn, W. Motion of Electrons and Holes in Perturbed Periodic Fields. *Phys. Rev.* **97**, 869–883 (1955).
64. Yariv, A. *Quantum electronics* (Wiley, 1967).
65. Vegard, L. Die Konstitution der Mischkristalle und die Raumfüllung der Atome. *Z. Physik* **5**, 17–26 (1921).
66. Gywat, O., Krenner, H. J. & Berezovsky, J. *Spins in Optically Active Quantum Dots: Concepts and Methods* (John Wiley & Sons, 2010).
67. Mitin, V. V., Sementsov, D. I. & Vagidov, N. Z. *Quantum Mechanics for Nanostructures* (Cambridge University Press, 2010).

68. Badolato, A. Deterministic Coupling of Single Quantum Dots to Single Nanocavity Modes. *Science* **308**, 1158–1161 (2005).
69. Hennessy, K. *et al.* Quantum nature of a strongly coupled single quantum dot–cavity system. *Nature* **445**, 896–899 (2007).
70. Dousse, A. *et al.* Controlled Light-Matter Coupling for a Single Quantum Dot Embedded in a Pillar Microcavity Using Far-Field Optical Lithography. *Phys. Rev. Lett.* **101**, 267404 (2008).
71. Graf, A. *et al.* Excitonic states in GaAs quantum dots fabricated by local droplet etching. *Phys. Rev. B* **89**, 115314 (2014).
72. Hours, J., Senellart, P., Peter, E., Cavanna, A. & Bloch, J. Exciton radiative lifetime controlled by the lateral confinement energy in a single quantum dot. *Phys. Rev. B* **71**, 161306 (2005).
73. Helfrich, M. *et al.* Growth and characterization of site-selective quantum dots. *Phys. Status Solidi A* **209**, 2387–2401 (2012).
74. Huggenberger, A. *et al.* Site-controlled In(Ga)As/GaAs quantum dots for integration into optically and electrically operated devices. *Journal of Crystal Growth* **323**, 194–197 (2011).
75. Choi, K., Kako, S., Holmes, M. J., Arita, M. & Arakawa, Y. Strong exciton confinement in site-controlled GaN quantum dots embedded in nanowires. *Applied Physics Letters* **103**, 171907 (2013).
76. Tommila, J. *et al.* The influence of temperature on the photoluminescence properties of single InAs quantum dots grown on patterned GaAs. *Nanoscale Research Letters* **7**, 313 (2012).
77. Schneider, C. *et al.* Lithographic alignment to site-controlled quantum dots for device integration. *Applied Physics Letters* **92**, 183101 (2008).
78. Jöns, K. D. *et al.* Triggered Indistinguishable Single Photons with Narrow Line Widths from Site-Controlled Quantum Dots. *Nano Letters* **13**, 126–130 (2013).
79. Huggenberger, A. *et al.* Narrow spectral linewidth from single site-controlled In(Ga)As quantum dots with high uniformity. *Applied Physics Letters* **98**, 131104 (2011).
80. Zhang, L. *et al.* Single photon emission from site-controlled InGaN/GaN quantum dots. *Applied Physics Letters* **103**, 192114 (2013).
81. Felici, M. *et al.* Site-Controlled InGaAs Quantum Dots with Tunable Emission Energy. *Small* **5**, 938–943 (2009).
82. Mereni, L. O. *et al.* Fine-structure splitting in large-pitch pyramidal quantum dots. *Physical Review B* **85** (2012).

Bibliography

83. Hartmann, A., Loubies, L., Reinhardt, F. & Kapon, E. Self-limiting growth of quantum dot heterostructures on nonplanar {111}B substrates. *Applied Physics Letters* **71**, 1314 (1997).
84. Dimastrodonato, V., Pelucchi, E., Zestanakis, P. A. & Vvedensky, D. D. Transient and self-limited nanostructures on patterned surfaces. *Phys. Rev. B* **87**, 205422 (2013).
85. Mohan, A. *et al.* Record-Low Inhomogeneous Broadening of Site-Controlled Quantum Dots for Nanophotonics. *Small* **6**, 1268–1272 (2010).
86. Rigal, B. *et al.* Site-controlled InGaAs/GaAs pyramidal quantum dots grown by MOVPE on patterned substrates using triethylgallium. *Journal of Crystal Growth* **414**, 187–191 (2015).
87. Malko, A. *et al.* Single-photon emission from pyramidal quantum dots: The impact of hole thermalization on photon emission statistics. *Phys. Rev. B* **72**, 195332 (2005).
88. Gallo, P. *et al.* Integration of site-controlled pyramidal quantum dots and photonic crystal membrane cavities. *Applied Physics Letters* **92**, 263101 (2008).
89. Marquardt, F. *An introduction to the basics of dephasing* (tech. rep., University of Basel, 2001).
90. Berthelot, A. *et al.* From Random Telegraph to Gaussian Stochastic Noises: Decoherence and Spectral Diffusion in a Semiconductor Quantum Dot. *Advances in Mathematical Physics* **2010**, 1–13 (2010).
91. Türec, V. *et al.* Effect of random field fluctuations on excitonic transitions of individual CdSe quantum dots. *Phys. Rev. B* **61**, 9944–9947 (2000).
92. Seufert, J. *et al.* Spectral diffusion of the exciton transition in a single self-organized quantum dot. *Applied Physics Letters* **76**, 1872–1874 (2000).
93. Berthelot, A. *et al.* Unconventional motional narrowing in the optical spectrum of a semiconductor quantum dot. *Nat Phys* **2**, 759–764 (2006).
94. Favero, I. *et al.* Temperature dependence of the zero-phonon linewidth in quantum dots: An effect of the fluctuating environment. *Phys. Rev. B* **75**, 073308 (2007).
95. Uskov, A. V., Nishi, K. & Lang, R. Collisional broadening and shift of spectral lines in quantum dot lasers. *Applied Physics Letters* **74**, 3081–3083 (1999).
96. Santori, C., Fattal, D., Vučković, J., Solomon, G. S. & Yamamoto, Y. Indistinguishable photons from a single-photon device. *Nature* **419**, 594–597 (2002).
97. Cui, G. & Raymer, M. Emission spectra and quantum efficiency of single-photon sources in the cavity-QED strong-coupling regime. *Physical Review A* **73** (2006).
98. Naesby, A., Suhr, T., Kristensen, P. T. & Mørk, J. Influence of pure dephasing on emission spectra from single photon sources. *Phys. Rev. A* **78**, 045802 (2008).

99. Auffèves, A. *et al.* Controlling the dynamics of a coupled atom-cavity system by pure dephasing. *Physical Review B* **81** (2010).
100. Auffèves, A., Gérard, J.-M. & Poizat, J.-P. Pure emitter dephasing: A resource for advanced solid-state single-photon sources. *Phys. Rev. A* **79**, 053838 (2009).
101. Grange, T. *et al.* Cavity-Funneled Generation of Indistinguishable Single Photons from Strongly Dissipative Quantum Emitters. *Phys. Rev. Lett.* **114**, 193601 (2015).
102. Besombes, L., Kheng, K., Marsal, L. & Mariette, H. Acoustic phonon broadening mechanism in single quantum dot emission. *Phys. Rev. B* **63**, 155307 (2001).
103. Bayer, M. & Forchel, A. Temperature dependence of the exciton homogeneous linewidth in $\text{In}_{0.6}\text{Ga}_{0.4}\text{As}/\text{GaAs}$ self-assembled quantum dots. *Phys. Rev. B* **65**, 041308 (2002).
104. Kammerer, C. *et al.* Line narrowing in single semiconductor quantum dots: Toward the control of environment effects. *Phys. Rev. B* **66**, 041306 (2002).
105. Favero, I. *et al.* Acoustic phonon sidebands in the emission line of single InAs/GaAs quantum dots. *Phys. Rev. B* **68**, 233301 (2003).
106. Leosson, K., Birkedal, D., Magnúsdóttir, I., Langbein, W. & Hvam, J. M. Homogeneous linewidth of self-assembled III–V quantum dots observed in single-dot photoluminescence. *Physica E: Low-dimensional Systems and Nanostructures* **17**, 1–6 (2003).
107. Peter, E. *et al.* Non perturbative exciton-phonon coupling for a single GaAs quantum dot. *physica status solidi (c)* **1**, 438–441 (2004).
108. Fan, X., Takagahara, T., Cunningham, J. E. & Wang, H. Pure dephasing induced by exciton–phonon interactions in narrow GaAs quantum wells. *Solid State Communications* **108**, 857–861 (1998).
109. Muljarov, E. A. & Zimmermann, R. Dephasing in Quantum Dots: Quadratic Coupling to Acoustic Phonons. *Phys. Rev. Lett.* **93**, 237401 (2004).
110. Grosse, F., Muljarov, E. A. & Zimmermann, R. in *Semiconductor Nanostructures* (ed Bimberg, P. D. D.) DOI: 10.1007/978-3-540-77899-8_8 165–187 (Springer Berlin Heidelberg, 2008).
111. Hohenester, U. *et al.* Phonon-assisted transitions from quantum dot excitons to cavity photons. *Physical Review B* **80** (2009).
112. Kaer, P., Nielsen, T. R., Lodahl, P., Jauho, A.-P. & Mørk, J. Non-Markovian Model of Photon-Assisted Dephasing by Electron-Phonon Interactions in a Coupled Quantum-Dot–Cavity System. *Physical Review Letters* **104** (2010).
113. Calic, M. *et al.* Phonon-Mediated Coupling of $\text{InGaAs}/\text{GaAs}$ Quantum-Dot Excitons to Photonic Crystal Cavities. *Phys. Rev. Lett.* **106** (2011).

Bibliography

114. Hughes, S. *et al.* Influence of electron-acoustic phonon scattering on off-resonant cavity feeding within a strongly coupled quantum-dot cavity system. *Phys. Rev. B* **83**, 165313 (2011).
115. Majumdar, A., Kim, E. D., Gong, Y., Bajcsy, M. & Vučković, J. Phonon mediated off-resonant quantum dot–cavity coupling under resonant excitation of the quantum dot. *Physical Review B* **84** (2011).
116. Lord Rayleigh, S. XVII. On the maintenance of vibrations by forces of double frequency, and on the propagation of waves through a medium endowed with a periodic structure. *Philosophical Magazine Series 5* **24**, 145–159 (1887).
117. Bykov, V. P. Spontaneous Emission in a Periodic Structure. *Soviet Journal of Experimental and Theoretical Physics* **35**, 269 (1972).
118. Yablonovitch, E. Inhibited Spontaneous Emission in Solid-State Physics and Electronics. *Phys. Rev. Lett.* **58**, 2059–2062 (1987).
119. John, S. Strong localization of photons in certain disordered dielectric superlattices. *Phys. Rev. Lett.* **58**, 2486–2489 (1987).
120. Yablonovitch, E., Gmitter, T. J. & Leung, K. M. Photonic band structure: The face-centered-cubic case employing nonspherical atoms. *Phys. Rev. Lett.* **67**, 2295–2298 (1991).
121. Blanco, A. *et al.* Large-scale synthesis of a silicon photonic crystal with a complete three-dimensional bandgap near 1.5 micrometres. *Nature* **405**, 437–440 (2000).
122. Joannopoulos, J. D., Johnson, S. G., Winn, J. N. & Meade, R. D. *Photonic Crystals: Molding the Flow of Light (Second Edition)* (Princeton University Press, 2011).
123. Englund, D., Fushman, I. & Vučković, J. General recipe for designing photonic crystal cavities. *Opt. Express* **13**, 5961–5975 (2005).
124. Chalcraft, A. R. A. *et al.* Mode structure of the L3 photonic crystal cavity. *Applied Physics Letters* **90**, 241117–241117–3 (2007).
125. Englund, D. *et al.* Controlling the Spontaneous Emission Rate of Single Quantum Dots in a Two-Dimensional Photonic Crystal. *Physical Review Letters* **95** (2005).
126. Chang, W.-H. *et al.* Efficient Single-Photon Sources Based on Low-Density Quantum Dots in Photonic-Crystal Nanocavities. *Physical Review Letters* **96** (2006).
127. Gevaux, D. G. *et al.* Enhancement and suppression of spontaneous emission by temperature tuning InAs quantum dots to photonic crystal cavities. *Applied Physics Letters* **88**, 131101 (2006).
128. Balet, L. *et al.* Enhanced spontaneous emission rate from single InAs quantum dots in a photonic crystal nanocavity at telecom wavelengths. *Applied Physics Letters* **91**, 123115 (2007).

129. Noda, S., Fujita, M. & Asano, T. Spontaneous-emission control by photonic crystals and nanocavities. *Nat Photon* **1**, 449–458 (2007).
130. Luxmoore, I. J. *et al.* III-V quantum light source and cavity-QED on Silicon. *Sci. Rep.* **3** (2013).
131. Madsen, K. H. *et al.* Measuring the effective phonon density of states of a quantum dot in cavity quantum electrodynamics. *Phys. Rev. B* **88**, 045316 (2013).
132. Petruzzella, M. *et al.* in *CLEO: 2015 FW4B.2* (2015).
133. Munsch, M. *et al.* Continuous-wave versus time-resolved measurements of Purcell factors for quantum dots in semiconductor microcavities. *Physical Review B* **80** (2009).
134. Madsen, K. H. *et al.* Observation of Non-Markovian Dynamics of a Single Quantum Dot in a Micropillar Cavity. *Physical Review Letters* **106** (2011).
135. Jakubczyk, T. *et al.* Pronounced Purcell enhancement of spontaneous emission in CdTe/ZnTe quantum dots embedded in micropillar cavities. *Applied Physics Letters* **101**, 132105 (2012).
136. Jakubczyk, T. *et al.* Inhibition and Enhancement of the Spontaneous Emission of Quantum Dots in Micropillar Cavities with Radial-Distributed Bragg Reflectors. *ACS Nano* **8**, 9970–9978 (2014).
137. Unsleber, S. *et al.* Two-photon interference from a quantum dot–microcavity: Persistent pure-dephasing and suppression of time-jitter. *Physical Review B* **91**, arXiv: 1503.00931 (2015).
138. Balet, L. *Investigation into the coupling of quantum dots to photonic crystal nanocavities at telecommunication wavelengths* PhD thesis (ÉCOLE POLYTECHNIQUE FÉDÉRALE DE LAUSANNE, 2009).
139. Peretti, R., Seassal, C., Viktorovich, P. & Letartre, X. Inhibition of light emission in a 2.5D photonic structure. *Journal of Applied Physics* **116**, 023107 (2014).
140. Thon, S. M. *et al.* Strong coupling through optical positioning of a quantum dot in a photonic crystal cavity. *Applied Physics Letters* **94**, 111115 (2009).
141. Laucht, A. *et al.* Dephasing of Exciton Polaritons in Photoexcited InGaAs Quantum Dots in GaAs Nanocavities. *Physical Review Letters* **103** (2009).
142. Englund, D. *et al.* Resonant Excitation of a Quantum Dot Strongly Coupled to a Photonic Crystal Nanocavity. *Phys. Rev. Lett.* **104**, 073904 (2010).
143. Ota, Y., Ohta, R., Kumagai, N., Iwamoto, S. & Arakawa, Y. Vacuum Rabi Spectra of a Single Quantum Emitter. *Phys. Rev. Lett.* **114**, 143603 (2015).
144. Press, D. *et al.* Photon Antibunching from a Single Quantum-Dot-Microcavity System in the Strong Coupling Regime. *Phys. Rev. Lett.* **98**, 117402 (2007).

Bibliography

145. Münch, S. *et al.* The role of optical excitation power on the emission spectra of a strongly coupled quantum dot-micropillar system. *Opt. Express* **17**, 12821–12828 (2009).
146. Keldysh, L. V., Kulakovskii, V. D., Reitzenstein, S., Makhonin, M. N. & Forchel, A. Interference effects in the emission spectra of quantum dots in high-quality cavities. *Jetp Lett.* **84**, 494–499 (2007).
147. Kim, H., Sridharan, D., Shen, T. C., Solomon, G. S. & Waks, E. Strong coupling between two quantum dots and a photonic crystal cavity using magnetic field tuning. *Opt. Express* **19**, 2589–2598 (2011).
148. Kaniber, M. *et al.* Investigation of the nonresonant dot-cavity coupling in two-dimensional photonic crystal nanocavities. *Phys. Rev. B* **77**, 161303 (2008).
149. Suffczyński, J. *et al.* Origin of the Optical Emission within the Cavity Mode of Coupled Quantum Dot-Cavity Systems. *Physical Review Letters* **103**, 027401 (2009).
150. Ates, S. *et al.* Non-resonant dot-cavity coupling and its potential for resonant single-quantum-dot spectroscopy. *Nat Photon* **3**, 724–728 (2009).
151. Dalacu, D. *et al.* Deterministic emitter-cavity coupling using a single-site controlled quantum dot. *Phys. Rev. B* **82**, 033301 (2010).
152. Laucht, A. *et al.* Nonresonant feeding of photonic crystal nanocavity modes by quantum dots. *Journal of Applied Physics* **109**, 102404 (2011).
153. Winger, M. *et al.* Explanation of Photon Correlations in the Far-Off-Resonance Optical Emission from a Quantum-Dot-Cavity System. *Phys. Rev. Lett.* **103**, 207403 (2009).
154. Karrai, K. *et al.* Hybridization of electronic states in quantum dots through photon emission. *Nature* **427**, 135–138 (2004).
155. Settnes, M., Kaer, P., Moelbjerg, A. & Mork, J. Auger Processes Mediating the Nonresonant Optical Emission from a Semiconductor Quantum Dot Embedded Inside an Optical Cavity. *Phys. Rev. Lett.* **111**, 067403 (2013).
156. Chauvin, N. *et al.* Controlling the charge environment of single quantum dots in a photonic-crystal cavity. *Physical Review B* **80** (2009).
157. Jarlov, C. *et al.* Exciton dynamics in a site-controlled quantum dot coupled to a photonic crystal cavity. *Applied Physics Letters* **107**, 191101 (2015).
158. Gonzalez-Tudela, A. *et al.* Effect of pure dephasing on the Jaynes-Cummings nonlinearities. *Optics Express* **18**, 7002 (2010).
159. Yamaguchi, M., Asano, T. & Noda, S. Third emission mechanism in solid-state nanocavity quantum electrodynamics. *Rep Prog Phys* **75**, 096401 (2012).
160. Majumdar, A. *et al.* Linewidth broadening of a quantum dot coupled to an off-resonant cavity. *Phys. Rev. B* **82**, 045306 (2010).

161. Madsen, K. H. & Lodahl, P. Quantitative analysis of quantum dot dynamics and emission spectra in cavity quantum electrodynamics. *New J. Phys.* **15**, 025013 (2013).
162. Ota, Y., Iwamoto, S., Kumagai, N. & Arakawa, Y. Impact of electron-phonon interactions on quantum-dot cavity quantum electrodynamics. *arXiv:0908.0788 [cond-mat]* arXiv: 0908.0788 (2009).
163. Milde, F., Knorr, A. & Hughes, S. Role of electron-phonon scattering on the vacuum Rabi splitting of a single-quantum dot and a photonic crystal nanocavity. *Phys. Rev. B* **78**, 035330 (2008).
164. Hohenester, U. Cavity quantum electrodynamics with semiconductor quantum dots: Role of phonon-assisted cavity feeding. *Physical Review B* **81** (2010).
165. Tarel, G. & Savona, V. Linear spectrum of a quantum dot coupled to a nanocavity. *Physical Review B* **81** (2010).
166. Kaer, P., Nielsen, T. R., Lodahl, P., Jauho, A.-P. & Mørk, J. Microscopic theory of phonon-induced effects on semiconductor quantum dot decay dynamics in cavity QED. *Physical Review B* **86** (2012).
167. Roy, C. & Hughes, S. Polaron master equation theory of the quantum-dot Mollow triplet in a semiconductor cavity-QED system. *Phys. Rev. B* **85**, 115309 (2012).
168. Kaer, P., Lodahl, P., Jauho, A.-P. & Mørk, J. Microscopic theory of indistinguishable single-photon emission from a quantum dot coupled to a cavity: The role of non-Markovian phonon-induced decoherence. *Phys. Rev. B* **87**, 081308 (2013).
169. Kaer, P. & Mørk, J. Decoherence in semiconductor cavity QED systems due to phonon couplings. *Phys. Rev. B* **90**, 035312 (2014).
170. Roy-Choudhury, K. & Hughes, S. Theory of phonon-modified quantum dot photoluminescence intensity in structured photonic reservoirs. *Optics Letters* **40**, 1838 (2015).
171. Valente, D. *et al.* Frequency cavity pulling induced by a single semiconductor quantum dot. *Phys. Rev. B* **89**, 041302 (2014).
172. Portalupi, S. L. *et al.* Bright Phonon-Tuned Single-Photon Source. *Nano Lett.* **15**, 6290–6294 (2015).
173. Calic, M. *Cavity Quantum Electrodynamics with Site-Controlled Pyramidal Quantum Dots in Photonic Crystal Cavities* PhD thesis (ÉCOLE POLYTECHNIQUE FÉDÉRALE DE LAUSANNE, 2013).
174. Surrente, A. *et al.* Ordered systems of site-controlled pyramidal quantum dots incorporated in photonic crystal cavities. *Nanotechnology* **22**, 465203 (2011).
175. Lyasota, A. *et al.* Integration of multiple site-controlled pyramidal quantum dot systems with photonic-crystal membrane cavities. *Journal of Crystal Growth* **414**, 192–195 (2015).

Bibliography

176. Webster, L. *et al.* Coherent Control to Prepare an InAs Quantum Dot for Spin-Photon Entanglement. *Phys. Rev. Lett.* **112**, 126801 (2014).
177. Schwartz, I. *et al.* Deterministic Writing and Control of the Dark Exciton Spin Using Single Short Optical Pulses. *Phys. Rev. X* **5**, 011009 (2015).
178. Archer, M. D. & Nozik, A. J. *Nanostructured and Photoelectrochemical Systems for Solar Photon Conversion* (World Scientific, 2008).
179. Li, X.-Q., Nakayama, H. & Arakawa, Y. Phonon bottleneck in quantum dots: Role of lifetime of the confined optical phonons. *Phys. Rev. B* **59**, 5069–5073 (1999).
180. Zibik, E. A. *et al.* Intraband relaxation via polaron decay in InAs self-assembled quantum dots. *Phys. Rev. B* **70**, 161305 (2004).
181. Fox, M. *Quantum Optics : An Introduction* (OUP Oxford, 2006).
182. Walls, D. F. & Milburn, G. J. *Quantum Optics* (Springer Science & Business Media, 2012).
183. Zwiller, V. *et al.* Single quantum dots emit single photons at a time: Antibunching experiments. *Applied Physics Letters* **78**, 2476–2478 (2001).
184. Kiraz, A. *et al.* Photon correlation spectroscopy of a single quantum dot. *Phys. Rev. B* **65**, 161303 (2002).
185. Darquié, B. *et al.* Controlled single-photon emission from a single trapped two-level atom. *Science* **309**, 454–456 (2005).
186. Baier, M. H., Malko, A., Pelucchi, E., Oberli, D. Y. & Kapon, E. Quantum-dot exciton dynamics probed by photon-correlation spectroscopy. *Phys. Rev. B* **73**, 205321 (2006).
187. Brown, R. H. & Twiss, R. Q. Correlation between Photons in two Coherent Beams of Light. , *Published online: 07 January 1956*; | [doi:10.1038/177027a0](https://doi.org/10.1038/177027a0) **177**, 27–29 (1956).
188. Gökten, M., Elsherbeni, A. & Arvas, E. *Multiresolution Frequency Domain Technique for Electromagnetics* (Morgan & Claypool Publishers, 2012).
189. Yariv, A. *Optical Electronics* (Oxford University Press, 1990).
190. Jackson, J. D. *Classical Electrodynamics* (Wiley, 1998).
191. Prather, D. W. *Photonic Crystals, Theory, Applications and Fabrication* (John Wiley & Sons, 2009).
192. Mur, G. Absorbing Boundary Conditions for the Finite-Difference Approximation of the Time-Domain Electromagnetic-Field Equations. *IEEE Transactions on Electromagnetic Compatibility* **EMC-23**, 377–382 (1981).
193. Vuckovic, J., Loncar, M., Mabuchi, H. & Scherer, A. Optimization of the Q factor in photonic crystal microcavities. *IEEE Journal of Quantum Electronics* **38**, 850–856 (2002).

194. Surrente, A. *et al.* Dense arrays of ordered pyramidal quantum dots with narrow linewidth photoluminescence spectra. *Nanotechnology* **20**, 415205 (2009).
195. Pelucchi, E, Watanabe, S, Leifer, K, Dwir, B & Kapon, E Site-controlled quantum dots grown in inverted pyramids for photonic crystal applications. *Physica E: Low-dimensional Systems and Nanostructures* **23**, 476–481 (2004).
196. Pelucchi, E. *et al.* Mechanisms of Quantum Dot Energy Engineering by Metalorganic Vapor Phase Epitaxy on Patterned Nonplanar Substrates. *Nano Lett.* **7**, 1282–1285 (2007).
197. Surrente, A. *Epitaxial Growth and Optical Properties of Dense Arrays of Pyramidal Quantum Dots* PhD thesis (ÉCOLE POLYTECHNIQUE FÉDÉRALE DE LAUSANNE, 2013).
198. Biasiol, G. & Kapon, E. Mechanisms of self-ordering of quantum nanostructures grown on nonplanar surfaces. *Physical review letters* **81**, 2962–2965 (1998).
199. Karlsson, K. F. *et al.* Fine structure of exciton complexes in high-symmetry quantum dots: Effects of symmetry breaking and symmetry elevation. *Phys. Rev. B* **81**, 161307 (2010).
200. Karlsson, K. F. *et al.* Spectral signatures of high-symmetry quantum dots and effects of symmetry breaking. *New J. Phys.* **17**, 103017 (2015).
201. Dupertuis, M. A. *et al.* Symmetries and the Polarized Optical Spectra of Exciton Complexes in Quantum Dots. *Physical Review Letters* **107** (2011).
202. Lelarge, F. *et al.* Effect of indium segregation on optical properties of V-groove InGaAs/GaAs strained quantum wires. *Applied Physics Letters* **75**, 3300–3302 (1999).
203. Atlasov, K. *Light control and microcavity lasers based on quantum wires integrated in photonic-crystal cavities* PhD thesis (ÉCOLE POLYTECHNIQUE FÉDÉRALE DE LAUSANNE, 2009).
204. Gehrsitz, S. *et al.* The refractive index of $Al_xGa_{1-x}As$ below the band gap: Accurate determination and empirical modeling. *Journal of Applied Physics* **87**, 7825–7837 (2000).
205. Blakemore, J. S. Semiconducting and other major properties of gallium arsenide. *Journal of Applied Physics* **53**, R123–R181 (1982).
206. Mosor, S. *et al.* Scanning a photonic crystal slab nanocavity by condensation of xenon. *Applied Physics Letters* **87**, 141105 (2005).
207. Jaynes, E. & Cummings, F. Comparison of quantum and semiclassical radiation theories with application to the beam maser. *Proceedings of the IEEE* **51**, 89–109 (1963).
208. Kimble, H. J. Strong Interactions of Single Atoms and Photons in Cavity QED. *Physica Scripta* **T76**, 127 (1998).

Bibliography

209. Laussy, F, del Valle, E. & Tejedor, C. Strong Coupling of Quantum Dots in Microcavities. *Physical Review Letters* **101** (2008).
210. Grynberg, G., Aspect, A. & Fabre, C. *Introduction to Quantum Optics: From the Semi-classical Approach to Quantized Light* (Cambridge University Press, 2010).
211. Haroche, S. & Raimond, J.-M. *Exploring the Quantum: Atoms, Cavities, and Photons* (OUP Oxford, 2013).
212. Blanchard, P., Giulini, D., Joos, E., Kiefer, C. & Stamatescu, I.-O. *Decoherence: Theoretical, Experimental, and Conceptual Problems: Proceedings of a Workshop Held at Bielefeld Germany, 10–14 November 1998* (Springer, 2008).
213. Joos, E. *et al.* *Decoherence and the Appearance of a Classical World in Quantum Theory* (Springer Science & Business Media, 2013).
214. Schlosshauer, M. A. *Decoherence: And the Quantum-To-Classical Transition* (Springer Science & Business Media, 2007).
215. Johansson, J. R., Nation, P. D. & Nori, F. QuTiP: An open-source Python framework for the dynamics of open quantum systems. *Computer Physics Communications* **183**, 1760–1772 (2012).
216. Predojević, A. & Mitchell, M. W. *Engineering the Atom-Photon Interaction: Controlling Fundamental Processes with Photons, Atoms and Solids* (Springer, 2015).
217. Santori, C., Fattal, D. & Yamamoto, Y. *Single-photon devices and applications* (Wiley-VCH, 2010).
218. Skinner, J. L. Theory of Pure Dephasing in Crystals. *Annual Review of Physical Chemistry* **39**, 463–478 (1988).
219. Majumdar, A., Bajcsy, M., Rundquist, A., Kim, E. & Vučković, J. Phonon-mediated coupling between quantum dots through an off-resonant microcavity. *Physical Review B* **85** (2012).
220. Krummheuer, B., Axt, V. & Kuhn, T. Theory of pure dephasing and the resulting absorption line shape in semiconductor quantum dots. *Physical Review B* **65** (2002).
221. Karlsson, K. F. *et al.* Optical polarization anisotropy and hole states in pyramidal quantum dots. *Applied Physics Letters* **89**, 251113 (2006).
222. Dzhioev, R. I. *et al.* Optical orientation and alignment of excitons in quantum dots. *Phys. Solid State* **40**, 790–793 (1998).
223. Ohno, S., Adachi, S., Kaji, R., Muto, S. & Sasakura, H. Optical anisotropy and photoluminescence polarization in single InAlAs quantum dots. *Applied Physics Letters* **98**, 161912 (2011).
224. Auffèves, A., Besga, B., Gérard, J.-M. & Poizat, J.-P. Spontaneous emission spectrum of a two-level atom in a very-high-Q cavity. *Physical Review A* **77** (2008).

-
225. Tavis, M. & Cummings, F. W. Exact Solution for an N-Molecule-Radiation-Field Hamiltonian. *Phys. Rev.* **170**, 379–384 (1968).
226. Garraway, B. M. The Dicke model in quantum optics: Dicke model revisited. *Phil. Trans. R. Soc. A* **369**, 1137–1155 (2011).
227. Gross, M. & Haroche, S. Superradiance: An essay on the theory of collective spontaneous emission. *Physics Reports* **93**, 301–396 (1982).
228. Dicke, R. H. Coherence in Spontaneous Radiation Processes. *Phys. Rev.* **93**, 99–110 (1954).
229. Agarwal, G. S. Vacuum-Field Rabi Splittings in Microwave Absorption by Rydberg Atoms in a Cavity. *Phys. Rev. Lett.* **53**, 1732–1734 (1984).
230. Temnov, V. & Woggon, U. Superradiance and Subradiance in an Inhomogeneously Broadened Ensemble of Two-Level Systems Coupled to a Low-Q Cavity. *Physical Review Letters* **95** (2005).
231. Li, X. *et al.* An All-Optical Quantum Gate in a Semiconductor Quantum Dot. *Science* **301**, 809–811 (2003).
232. Avron, J. *et al.* Entanglement on Demand through Time Reordering. *Physical Review Letters* **100** (2008).
233. Takagahara, T. Effects of dielectric confinement and electron-hole exchange interaction on excitonic states in semiconductor quantum dots. *Phys. Rev. B* **47**, 4569–4584 (1993).
234. Lampert, M. A. Mobile and Immobile Effective-Mass-Particle Complexes in Nonmetallic Solids. *Phys. Rev. Lett.* **1**, 450–453 (1958).
235. Haynes, J. R. Experimental Observation of the Excitonic Molecule. *Phys. Rev. Lett.* **17**, 860–862 (1966).
236. Hu, Y. Z. *et al.* Biexcitons in semiconductor quantum dots. *Physical review letters* **64**, 1805–1807 (1990).
237. Reimer, M. E. *et al.* Electric Field Induced Removal of the Biexciton Binding Energy in a Single Quantum Dot. *Nano Letters* **11**, 645–650 (2011).
238. Rashba, E. Properties of semiconductors with an extremum loop. 1. Cyclotron and combinational resonance in a magnetic field perpendicular to the plane of the loop. *Sov. Phys. Solid State* **2**, 1224–1238 (1960).
239. Prabhakar, S., Melnik, R. V. N. & Bonilla, L. L. The influence of anisotropic gate potentials on the phonon induced spin-flip rate in GaAs quantum dots. *Applied Physics Letters* **100**, 023108 (2012).
240. Reimer, M. E., Dalacu, D., Poole, P. J. & Williams, R. L. Biexciton binding energy control in site-selected quantum dots. *Journal of Physics: Conference Series* **210**, 012019 (2010).

Bibliography

241. Amloy, S. *et al.* Size dependent biexciton binding energies in GaN quantum dots. *Applied Physics Letters* **99**, 251903 (2011).
242. Dal Savio, C. *et al.* Optical study of single InAs on In_{0.12}Ga_{0.88}As self-assembled quantum dots: biexciton binding energy dependence on the dots size. *Applied Physics B* **84**, 317–322 (2006).
243. Rodt, S. *et al.* Repulsive exciton-exciton interaction in quantum dots. *Physical Review B* **68** (2003).
244. Xiu-Ming, D. *et al.* Size dependence of biexciton binding energy in single InAs/-GaAs quantum dots. *Chinese Physics B* **18**, 2258 (2009).
245. Ding, F. *et al.* Tuning the Exciton Binding Energies in Single Self-Assembled InGaAs/GaAs Quantum Dots by Piezoelectric-Induced Biaxial Stress. *Physical Review Letters* **104** (2010).
246. Jarlov, C. *et al.* Bound and anti-bound biexciton in site-controlled pyramidal GaInAs/GaAs quantum dots. *Applied Physics Letters* **101**, 191101–191101–4 (2012).
247. Feucker, M., Seguin, R., Rodt, S., Hoffmann, A. & Bimberg, D. Decay dynamics of neutral and charged excitonic complexes in single InGa/InAs quantum dots. *Applied Physics Letters* **92**, 063116 (2008).
248. Amloy, S. *et al.* Dynamic characteristics of the exciton and the biexciton in a single InGaN quantum dot. *Applied Physics Letters* **101**, 061910–061910 (2012).
249. Brunner, K., Abstreiter, G., Böhm, G., Tränkle, G. & Weimann, G. Sharp-line photoluminescence and two-photon absorption of zero-dimensional biexcitons in a GaAs/AlGaAs structure. *Physical review letters* **73**, 1138–1141 (1994).
250. Ducommun, Y. *Semiconductor quantum dots grown in inverted pyramids* PhD thesis (ÉCOLE POLYTECHNIQUE FÉDÉRALE DE LAUSANNE, 2001).
251. Hartmann, A., Ducommun, Y., Kapon, E., Hohenester, U. & Molinari, E. Few-Particle Effects in Semiconductor Quantum Dots: Observation of Multicharged Excitons. *Phys. Rev. Lett.* **84**, 5648–5651 (2000).
252. Baier, M. H. *et al.* Single photon emission from site-controlled pyramidal quantum dots. *Applied Physics Letters* **84**, 648 (2004).
253. Baier, M. H., Watanabe, S., Pelucchi, E. & Kapon, E. High uniformity of site-controlled pyramidal quantum dots grown on prepatterned substrates. *Applied Physics Letters* **84**, 1943–1945 (2004).
254. Brouri, R., Beveratos, A., Poizat, J.-P. & Grangier, P. Photon antibunching in the fluorescence of individual color centers in diamond. *Optics Letters* **25**, 1294–1296 (2000).
255. Regelman, D. V. *et al.* Semiconductor Quantum Dot: A Quantum Light Source of Multicolor Photons with Tunable Statistics. *Phys. Rev. Lett.* **87**, 257401 (2001).

-
256. Takagahara, T. Biexciton states in semiconductor quantum dots and their non-linear optical properties. *Physical Review B* **39**, 10206 (1989).
257. Baier, M. H. *Correlated photon emission from pyramidal quantum dot heterostructures* PhD thesis (ÉCOLE POLYTECHNIQUE FÉDÉRALE DE LAUSANNE, 2005).
258. Stier, O., Schliwa, A., Heitz, R., Grundmann, M. & Bimberg, D. Stability of Biexcitons in Pyramidal InAs/GaAs Quantum Dots. *phys. stat. sol. (b)* **224**, 115–118 (2001).
259. Trotta, R., Zallo, E., Magerl, E., Schmidt, O. G. & Rastelli, A. Independent control of exciton and biexciton energies in single quantum dots via electroelastic fields. *Phys. Rev. B* **88**, 155312 (2013).
260. Ghali, M., Ohtani, K., Ohno, Y. & Ohno, H. Generation and control of polarization-entangled photons from GaAs island quantum dots by an electric field. *Nature Communications* **3**, 661 (2012).
261. Johansen, J., Julsgaard, B., Stobbe, S., Hvam, J. M. & Lodahl, P. Probing long-lived dark excitons in self-assembled quantum dots. *Phys. Rev. B* **81**, 081304 (2010).
262. Gallardo, E. *et al.* Emission polarization control in semiconductor quantum dots coupled to a photonic crystal microcavity. *Opt. Express* **18**, 13301–13308 (2010).
263. Bayer, M. *et al.* Fine structure of neutral and charged excitons in self-assembled In(Ga)As/(Al)GaAs quantum dots. *Phys. Rev. B* **65**, 195315 (2002).
264. Tischler, J. G., Bracker, A. S., Gammon, D. & Park, D. Fine structure of trions and excitons in single GaAs quantum dots. *Phys. Rev. B* **66**, 081310 (2002).
265. Heitz, R., Mukhametzhanov, I., Madhukar, A., Hoffmann, A. & Bimberg, D. Temperature dependent optical properties of self-organized InAs/GaAs quantum dots. *Journal of Electronic Materials* **28**, 520–527 (1999).
266. Bhattacharya, P. *et al.* In(Ga)As/GaAs self-organized quantum dot lasers: DC and small-signal modulation properties. *Electron Devices, IEEE Transactions on* **46**, 871–883 (1999).
267. Andreani, L. C., Panzarini, G. & Gérard, J.-M. Strong-coupling regime for quantum boxes in pillar microcavities: Theory. *Phys. Rev. B* **60**, 13276–13279 (1999).
268. Buckley, S., Rivoire, K. & Vučković, J. Engineered quantum dot single-photon sources. *Rep. Prog. Phys.* **75**, 126503 (2012).
269. Laucht, A. *et al.* Temporal monitoring of nonresonant feeding of semiconductor nanocavity modes by quantum dot multiexciton transitions. *Physical Review B* **81** (2010).
270. Elvira, D. *et al.* Single InAs_{1-x}P_x/InP quantum dots as telecommunications-band photon sources. *Phys. Rev. B* **84**, 195302 (2011).

Bibliography

271. Reimann, R. *et al.* Cavity-Modified Collective Rayleigh Scattering of Two Atoms. *Phys. Rev. Lett.* **114**, 023601 (2015).
272. Casabone, B. *et al.* Enhanced Quantum Interface with Collective Ion-Cavity Coupling. *Phys. Rev. Lett.* **114**, 023602 (2015).
273. Burkard, G. & Imamoglu, A. Ultra-long-distance interaction between spin qubits. *Phys. Rev. B* **74**, 041307 (2006).
274. Zheng, S.-B. & Guo, G.-C. Efficient Scheme for Two-Atom Entanglement and Quantum Information Processing in Cavity QED. *Phys. Rev. Lett.* **85**, 2392–2395 (2000).
275. Sridharan, D. & Waks, E. Generating entanglement between quantum dots with different resonant frequencies based on dipole-induced transparency. *Phys. Rev. A* **78**, 052321 (2008).
276. Pellizzari, T., Gardiner, S. A., Cirac, J. I. & Zoller, P. Decoherence, Continuous Observation, and Quantum Computing: A Cavity QED Model. *Phys. Rev. Lett.* **75**, 3788–3791 (1995).
277. Imamoglu, A. *et al.* Quantum Information Processing Using Quantum Dot Spins and Cavity QED. *Phys. Rev. Lett.* **83**, 4204–4207 (1999).
278. Noda, S. Seeking the Ultimate Nanolaser. *Science* **314**, 260–261 (2006).
279. Fink, J. M. *et al.* Dressed Collective Qubit States and the Tavis-Cummings Model in Circuit QED. *Phys. Rev. Lett.* **103**, 083601 (2009).
280. Mlynek, J. A. *et al.* Demonstrating W-type entanglement of Dicke states in resonant cavity quantum electrodynamics. *Phys. Rev. A* **86**, 053838 (2012).
281. Reitzenstein, S. *et al.* Coherent photonic coupling of semiconductor quantum dots. *Opt. Lett.* **31**, 1738–1740 (2006).
282. Gallardo, E. *et al.* Optical coupling of two distant InAs/GaAs quantum dots by a photonic-crystal microcavity. *Phys. Rev. B* **81**, 193301 (2010).
283. Laucht, A. *et al.* Mutual coupling of two semiconductor quantum dots via an optical nanocavity. *Phys. Rev. B* **82**, 075305 (2010).
284. Maragkou, M. *et al.* Bichromatic dressing of a quantum dot detected by a remote second quantum dot. *Phys. Rev. B* **88**, 075309 (2013).
285. Minkov, M. & Savona, V. Radiative coupling of quantum dots in photonic crystal structures. *Phys. Rev. B* **87**, 125306 (2013).
286. Lodahl, P. & Stobbe, S. Solid-state quantum optics with quantum dots in photonic nanostructures. *Nanophotonics* **2**, 39–55 (2013).
287. Stajic, J. The Future of Quantum Information Processing. *Science* **339**, 1163–1163 (2013).
288. Ladd, T. D. *et al.* Quantum computers. *Nature* **464**, 45–53 (2010).

-
289. Englund, D. *et al.* Ultrafast Photon-Photon Interaction in a Strongly Coupled Quantum Dot-Cavity System. *Phys. Rev. Lett.* **108** (2012).
290. Bajcsy, M, Majumdar, A, Rundquist, A & Vučković, J Photon blockade with a four-level quantum emitter coupled to a photonic-crystal nanocavity. *New J. Phys.* **15**, 025014 (2013).
291. Cirac, J. I., Zoller, P., Kimble, H. J. & Mabuchi, H. Quantum State Transfer and Entanglement Distribution among Distant Nodes in a Quantum Network. *Phys. Rev. Lett.* **78**, 3221–3224 (1997).
292. Ritter, S. *et al.* An elementary quantum network of single atoms in optical cavities. *Nature* **484**, 195–200 (2012).
293. Feynman, R. P. Simulating physics with computers. *Int J Theor Phys* **21**, 467–488 (1982).
294. Cirac, J. I. & Zoller, P. Goals and opportunities in quantum simulation. *Nat. Phys.* **8**, 264–266 (2012).
295. Greiner, M., Mandel, O., Esslinger, T., Hänsch, T. W. & Bloch, I. Quantum phase transition from a superfluid to a Mott insulator in a gas of ultracold atoms. *Nature* **415**, 39–44 (2002).
296. Bayer, M. *et al.* Optical Modes in Photonic Molecules. *Phys. Rev. Lett.* **81**, 2582–2585 (1998).
297. Karl, M. *et al.* Localized and delocalized modes in coupled optical micropillar cavities. *Opt. Express* **15**, 8191–8196 (2007).
298. Michaelis de Vasconcellos, S. *et al.* Spatial, spectral, and polarization properties of coupled micropillar cavities. *Appl. Phys. Lett.* **99**, 101103–101103–3 (2011).
299. Ishii, S., Nakagawa, A. & Baba, T. Modal characteristics and bistability in twin microdisk photonic molecule lasers. *IEEE J. Quantum Electron.* **12**, 71–77 (2006).
300. Englund, D., Faraon, A., Zhang, B., Yamamoto, Y. & Vučković, J. Generation and transfer of single photons on a photonic crystal chip. *Opt. Express* **15**, 5550–5558 (2007).
301. Atlasov, K. A., Karlsson, K. F., Rudra, A., Dwir, B. & Kapon, E. Wavelength and loss splitting in directly coupled photonic-crystal defect microcavities. *Opt. Express* **16**, 16255–16264 (2008).
302. Chalcraft, A. R. A. *et al.* Mode structure of coupled L3 photonic crystal cavities. *Opt. Express* **19**, 5670–5675 (2011).
303. Majumdar, A., Rundquist, A., Bajcsy, M. & Vučković, J. Cavity quantum electrodynamics with a single quantum dot coupled to a photonic molecule. *Phys. Rev. B* **86**, 045315 (2012).
304. Bose, R., Cai, T., Solomon, G. S. & Waks, E. All-optical tuning of a quantum dot in a coupled cavity system. *Appl. Phys. Lett.* **100**, 231107 (2012).

Bibliography

305. Cai, T., Bose, R., Solomon, G. S. & Waks, E. Controlled coupling of photonic crystal cavities using photochromic tuning. *Appl. Phys. Lett.* **102**, 141118 (2013).
306. O'Brien, D. *et al.* Coupled photonic crystal heterostructure nanocavities. *Opt. Express* **15**, 1228–1233 (2007).
307. Notomi, M., Kuramochi, E. & Tanabe, T. Large-scale arrays of ultrahigh-Q coupled nanocavities. *Nature Photon.* **2**, 741–747 (2008).
308. Majumdar, A. *et al.* Design and analysis of photonic crystal coupled cavity arrays for quantum simulation. *Phys. Rev. B* **86**, 195312 (2012).
309. Matthews, C. J. & Seviour, R. Effects of disorder on the frequency and field of photonic-crystal cavity resonators. *Appl. Phys. B* **94**, 381–388 (2009).
310. Vignolini, S. *et al.* Near-field imaging of coupled photonic-crystal microcavities. *Appl. Phys. Lett.* **94**, 151103 (2009).
311. Jarlov, C. *et al.* 1D and 2D arrays of coupled photonic crystal cavities with a site-controlled quantum wire light source. *Opt. Express* **21**, 31082–31091 (2013).
312. Atlasov, K. A., Gallo, P., Rudra, A., Dwir, B. & Kapon, E. Effect of sidewall passivation in BCl₃/N₂ inductively coupled plasma etching of two-dimensional GaAs photonic crystals. *J. Vac. Sci. Technol. B* **27**, L21–L24 (2009).
313. Hennessy, K. *et al.* Tuning photonic crystal nanocavity modes by wet chemical digital etching. *Appl. Phys. Lett.* **87**, 021108–021108–3 (2005).
314. Atlasov, K. A., Rudra, A., Dwir, B. & Kapon, E. Large mode splitting and lasing in optimally coupled photonic-crystal microcavities. *Opt. Express* **19**, 2619–2625 (2011).
315. Marcuse, D. Coupled mode theory of optical resonant cavities. *IEEE J. Quantum Electron.* **21**, 1819–1826 (1985).
316. Haus, H. A. & Huang, W. Coupled-mode theory. *Proc. IEEE* **79**, 1505–1518 (1991).
317. Ding, W., Chen, L., Tang, D., Li, W. & Liu, S. Supermodes of photonic crystal CCWs and multimode bistable switchings with uniform thresholds. *Opt. Commun.* **265**, 500–505 (2006).
318. Yoo, H.-J., Hayes, J. R., Paek, E. G., Scherer, A. & Kwon, Y.-S. Array mode analysis of two-dimension phased arrays of vertical cavity surface emitting lasers. *Quantum Electronics, IEEE Journal of* **26**, 1039–1051 (1990).
319. Lomascolo, M., Ciccarese, P., Cingolani, R., Rinaldi, R. & Reinhart, F. K. Free versus localized exciton in GaAs V-shaped quantum wires. *J. Appl. Phys.* **83**, 302–305 (1998).
320. Glennon, J. J. *et al.* Exciton localization and migration in individual CdSe quantum wires at low temperatures. *Phys. Rev. B* **80**, 081303 (2009).
321. Bockelmann, U. & Bastard, G. Interband Optical Transitions in Semiconductor Quantum Wires: Selection Rules and Absorption Spectra. *EPL* **15**, 215 (1991).

322. Greentree, A. D., Tahan, C., Cole, J. H. & Hollenberg, L. C. L. Quantum phase transitions of light. *Nat. Phys.* **2**, 856–861 (2006).
323. Hartmann, M. J., Brandão, F. G. S. L. & Plenio, M. B. Strongly interacting polaritons in coupled arrays of cavities. *Nat. Phys.* **2**, 849–855 (2006).
324. Bennett, A. J. *et al.* Electric-field-induced coherent coupling of the exciton states in a single quantum dot. *Nature Physics* **6**, 947–950 (2010).
325. Weiler, S. *et al.* Highly indistinguishable photons from a quantum dot in a microcavity. *physica status solidi (b)* **248**, 867–871 (2011).
326. Hong, C. K., Ou, Z. Y. & Mandel, L. Measurement of subpicosecond time intervals between two photons by interference. *Phys. Rev. Lett.* **59**, 2044–2046 (1987).
327. Close, T., Gauger, E. M. & Lovett, B. W. Overcoming phonon-induced dephasing for indistinguishable photon sources. *New Journal of Physics* **14**, 113004 (2012).

Publications and conferences

Journal publications

- B. Rigal, C. Jarlov, A. Rudra, P. Gallo, A. Lyasota, B. Dwir and E. Kapon, *Site-controlled InGaAs/GaAs pyramidal quantum dots grown by MOVPE on patterned substrates using triethylgallium*, [Journal of Crystal Growth](#) **414**, 187-191 (2015)
- B. Rigal, C. Jarlov, P. Gallo, B. Dwir, A. Rudra M. Calic and E. Kapon, *Site-controlled quantum dots coupled to a photonic crystal molecule*, [Appl. Phys. Lett.](#) **107**, 141103 (2015)
- A. Lyasota, S. Borghardt, C. Jarlov, B. Dwir, P. Gallo, A. Rudra and E. Kapon, *Integration of multiple site-controlled pyramidal quantum dot systems with photonic-crystal membrane cavities*, [Journal of Crystal Growth](#) **414**, 192-195 (2015)
- C. Jarlov, A. Lyasota, L. Ferrier, P. Gallo, B. Dwir, A. Rudra and E. Kapon, *Exciton dynamics in a site-controlled quantum dot coupled to a photonic crystal cavity*, [Appl. Phys. Lett.](#) **107**, 191101 (2015)
- C. Jarlov, K. A. Atlasov, L. Ferrier, M. Calic, P. Gallo, A. Rudra, B. Dwir, and E. Kapon, *1D and 2D arrays of coupled photonic crystal cavities with a site-controlled quantum wire light source*, [Opt. Express](#) **21**, 31082-31091 (2013)
- C. Jarlov, P. Gallo, M. Calic, B. Dwir, A. Rudra and E. Kapon, *Bound and anti-bound biexciton in site-controlled pyramidal GaInAs/GaAs quantum dots*, [Appl. Phys. Lett.](#) **101**, 191101 (2012)

Conference presentations

- C. Jarlov, E. Wodey, A. Lyasota, M. Calic, P. Gallo, A. Rudra, B. Dwir and E. Kapon, *Effect of Pure Dephasing and Phonon Scattering on the Coupling of Semiconductor Quantum Dots to Optical Cavities*, OECS 2015, Jerusalem, Israel, October 2015 (Contributed poster presentation)
- C. Jarlov, E. Wodey, A. Lyasota, M. Calic, P. Gallo, A. Rudra, B. Dwir and E. Kapon, *Effect of Pure Dephasing and Phonon Scattering on the Coupling of Semiconductor Quantum Dots to Optical Cavities*, CLEO 2015, San Jose, California, USA, June 2015 (Contributed oral presentation)
- C. Jarlov, E. Wodey, A. Lyasota, M. Calic, P. Gallo, A. Rudra, B. Dwir and E. Kapon, *Effect of Dephasing on the Coupling of Quantum Dot Excitons & Optical Cavities*, 32nd International Conference on the Physics of Semiconductors, ICPS 2014, Austin, Texas, USA, August 2014 (Contributed oral presentation)
- C. Jarlov, E. Wodey, A. Lyasota, M. Calic, P. Gallo, A. Rudra, B. Dwir and E. Kapon, *Effect of dephasing on the coupling of quantum dot excitons and optical cavities*, 8th International Conference on Quantum Dots, QD 2014, Pisa, Italy, May 2014 (Contributed poster presentation)
- C. Jarlov, L. Ferrier, M. Calic, P. Gallo, V. Belykh, A. Rudra, B. Dwir, N.N. Sibeldin and E. Kapon, *Observation of Purcell effect with a site-controlled pyramidal quantum dot coupled to a photonic crystal cavity mode*, 16th International Conference on Modulated Semiconductor Structures, MSS-16, Wroclaw, Poland, July 2013 (Contributed poster presentation)
- C. Jarlov, K. Atlasov, L. Ferrier, P. Gallo, A. Rudra, B. Dwir and E. Kapon, *1D and 2D arrays of coupled cavities with a site-controlled light source*, 4th International Topical Meeting on Nanophotonics and Metamaterials, Nanometa 2013, Seefeld, Austria, January 2013 (Contributed poster presentation)
- C. Jarlov, P. Gallo, M. Calic, B. Dwir, A. Rudra and E. Kapon, *Bound and Anti-Bound Biexcitons in site-controlled pyramidal quantum dots*, 7th International Conference on Quantum Dots, QD 2012, Santa Fe, New Mexico, USA, May 2012 (Contributed poster presentation)

Clément Jarlov

Route de Genève 103
1026 Denges
Canton de Vaud
Switzerland

French Citizen
Born April 14th 1989, Zimbabwe
Mobile: +41 (0)79 934 01 37
Email: clement.jarlov@epfl.ch



EDUCATION

2012 - 2016 **Swiss Federal Institute of Technology (EPFL)**, Lausanne, Switzerland

PhD, Physics (Thesis director: Prof. Eli Kapon)

- Experimental and theoretical study of systems of semiconductor site-controlled quantum dots and nanocavities.
- Measured optical spectra of quantum dots in cavities to study light-matter interactions at a fundamental level.
- Performed simulations with Matlab and Python to analyse experimental data.

2010 - 2012 **Swiss Federal Institute of Technology (EPFL)**, Lausanne, Switzerland

Master of Science MSc in Physics

- *Classes*: Quantum optics, Optics, Statistical physics, Solid-state physics, Experimental methods in physics.
- *Master project*: Performed optical experiments to study semiconductor quantum dots (Laboratory of Physics of Nanostructures)

2007 - 2010 **Swiss Federal Institute of Technology (EPFL)**, Lausanne, Switzerland

Bachelor of Science BSc in Physics

- *Classes*: Classical physics, Quantum physics, Solid-state physics, Optics, Numerical Physics, Mathematics (Algebra, Analysis).

2005 - 2007 **French International School of Singapore**

French baccalaureate, Scientific section, Physics speciality, with special honours (mention Très bien)

TECHNICAL SKILLS

Experimental	Optical spectroscopy: photoluminescence (PL) measurements, time-resolved PL measurements, photon correlation measurements, cryogenics.
Computer	Matlab and basic knowledge of Python and C++. Microsoft Office and Latex. Adobe illustrator and Blender

LANGUAGE SKILLS

French	Fluent (mother tongue)
English	Professional proficiency (C1)